

# Study of Structural, Magnetic and Transport Properties of Transition Metal Based Double Perovskites



THESIS SUBMITTED FOR THE DEGREE OF

DOCTOR OF PHILOSOPHY

IN PHYSICS

IN THE FACULTY OF NATURAL SCIENCE

GOA UNIVERSITY

GOA

538.4  
-----  
GAN/STU

By

SHRADDHA GANORKAR

DEPARTMENT OF PHYSICS

GOA UNIVERSITY

GOA 403 206

T-583

MARCH 2013

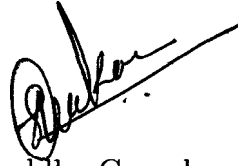
To

**Anna and Aai**

## DECLARATION

The author hereby declares that this thesis represents work which has been carried out by her and that it has not been submitted to any other University or Institution for the award of any Degree, Diploma, Associateship, Fellowship or any other such title.

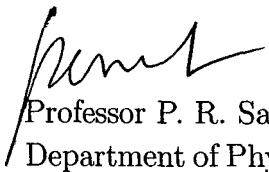
Place: Taleigao Plateau.  
Date : 2013- March-08



Shraddha Ganorkar

## CERTIFICATE

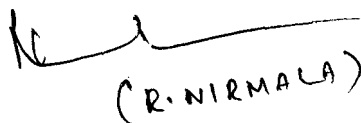
We hereby certify that the above Declaration of the candidate Shraddha Ganorkar is true and that this thesis represents her independent work.



Professor P. R. Sarode  
Department of Physics,  
Goa University, Goa.



Dr K. R. Priolkar  
Department of Physics  
Goa University, Goa.



(R. NIRMALA)

15/11/13

## Acknowledgements

The journey of doctoral thesis has been an interesting, inspiring and challenging experience for me. Completion of this doctoral dissertation was possible with the support of several people throughout my journey as a research scholar. I would like to express my sincere gratitude to all of them.

Foremost, I would like to express my deepest gratitude and appreciation to my supervisors *Prof. P.R. Sarode* and *Dr. K. R. Priolkar* for their continuous support, motivation, enthusiasm, and immense knowledge during my Ph.D. study. Their guidance helped me during my research work and writing of this thesis. This feat was possible only because of the unconditional support provided by my supervisors. Through their guidance, I have acquired a deep appreciation of the values and qualities required for a researcher and scholar. I am also thankful to *Dr. R. V. Pai* for his consistent encouragement I received throughout the research work.

I thank to Prof. S. Emura, Institute of Scientific and Industrial Research, Osaka University, Japan for his help to carry out EXAFS experiments at Photon Factory, Japan.

I am grateful to Centre Director, UGC-DAE consortium for Scientific Research, Indore for making facility available to carried out experiments.travel and local hospitality. I would like to thank Dr. Alok Banerjee for his valuable suggestions, guidance and encouragement received for magnetic measurements throughout this work. My sincere thank to Dr. Rajiv Rawat and Dr. V. G. Sathe for helping me for magnetoresistance and Raman Spectroscopy respectively.

I extend my acknowledgement to CSIR and DST, Govt. of India for funding fellowships and travel support.

I am thankful to Head of Department, Department of Physics, Goa University to make facilities available for research work. I am also grateful to all teaching, non teaching staff, research scholar and students - past and present at Department of Physics with whom I have shared these last few years. My experiences here good and bad, have taught me valuable lessons in life and will always be embedded in my mind.

Kapil Ingle, who has tolerated me as a friend, a companion and a labmate; and who has been a source of constant moral support to me for the last 8 years. The lengthy discussions, late night coffees, bike rides and impromptu breaks from the lab will always remain dear in my heart. The thesis would not have come to a successful completion without the help I received from him. I am thankful for his grate help and moral support during hard time of Ph.D. Thank you Kapil being there as my god father.

Elaine Dias, who has been always there for me in my all up and downs during research work and moral support. Thank you Elaine to bearing my all anger and scolding. Thank you for putting aside time and helping me sort out the few glitches I encountered toward the end.

My dearest friend Aruna - thanks for being there to show the way to life, and a strong moral support in hostel life. I am thankful to Shruti Naik and Family for their love and

care, a short but memorable days in hostel life will be remain deeply in my heart.

My thanks to Dr. Preeti, Dr. Teny, Dr. Efrem, Dr. Swati, Dr. Miskil, Dr. Ramu and Dr. Shweta who shared a short but memorable time of early reserve years and my research colleges Sir Nelson, Neelima, Bosco, Wilson, Reshma for support and joy of working together. I thanks to all friends- Shamshad, Beena, Lovina, Mamata, Pranav, Shilpa(Nagpur), Paresh, Nalini(Bhandara)... all of them those who help some or other way during this course of time.

My heartfelt thanks go out to Mrs. Mangla Sarode who has taken care of me as a daughter during the course of Ph.D. I have learnt many valuable things form you. My thanks to Dr. Ananya Das for her great care for me.

I am very much thankful to Bacchu(Mangesh) for his moral support, love and care which gave me strength to work harder. You were my lifeline during my darkest phase in life.

I owe a lot to my parents, who encouraged and helped me at every stage of my personal and academic life, and longed to see this achievement come true. I deeply miss my father, who is not with me to share this joy. I am very thankful to my lovely sis being there always to remind for time.

2013

Shraddha Ganorkar

# Contents

<b>1</b>	<b>Introduction</b>	<b>1</b>
1.1	Historical Background . . . . .	2
1.2	Cobaltites : Interest and Importance . . . . .	4
1.3	Crystal Field Theory . . . . .	6
1.3.1	Jahn-Teller Distortion . . . . .	9
1.4	Spin States of Cobalt . . . . .	10
1.5	Magnetic Interactions . . . . .	12
1.5.1	Goodenough-Kanamori rules . . . . .	18
1.6	Layered Cobaltites . . . . .	21
1.6.1	Composition and Structure . . . . .	22
1.6.2	Physical Properties . . . . .	25
1.7	Motivation, Aim and Objectives . . . . .	28
<b>2</b>	<b>Experimental Techniques</b>	<b>37</b>
2.1	Introduction . . . . .	37
2.2	Sample Preparation Technique . . . . .	38

2.2.1	Sol-Gel Method . . . . .	38
2.3	X-ray Diffraction(XRD) . . . . .	39
2.4	Thermogravimetric analysis . . . . .	41
2.4.1	TGA Measurements . . . . .	42
2.5	Iodometric Titration . . . . .	43
2.6	Magnetometry . . . . .	45
2.6.1	Vibrating Sample Magnetometer . . . . .	46
2.6.2	SQUID Magnetometer . . . . .	47
2.6.3	Magnetization Measurements . . . . .	49
2.7	Electrical Transport Properties : Resistivity Measurements . . . . .	49
2.7.1	Resistivity and Magnetoresistance Measurements . . . . .	51
2.8	Infra-red and Raman Spectroscopic Measurements . . . . .	52
2.9	X-ray Absorption Fine Structure Spectroscopy . . . . .	53
2.9.1	The Process of X-ray Absorption . . . . .	54
2.9.2	XAFS Measurements . . . . .	56
2.9.3	XAFS Data Reduction And Analysis . . . . .	58
	References . . . . .	63

<b>3</b>	<b>Correlation of Structural And Magnetic Properties of <math>\text{RBaCo}_2\text{O}_{5.5}</math>, R = Pr, Nd, Sm, Gd and Y</b>	<b>64</b>
3.1	Introduction . . . . .	64
3.2	X-ray Diffraction Studies . . . . .	67

3.3	Magnetization Measurements . . . . .	70
3.4	Transport Properties . . . . .	74
3.5	X-ray Absorption Spectroscopic Measurement . . . . .	76
3.5.1	X-ray Absorption Near Edge Structure (XANES) . . . . .	76
3.6	Discussion . . . . .	80
3.7	Conclusion . . . . .	82
	References . . . . .	83
<b>4</b>	<b>Unusual magnetic properties of <math>\text{SmBaCo}_2\text{O}_{5+\delta}</math>, (<math>0.12 \leq \delta \leq 0.65</math>)</b>	<b>87</b>
4.1	Introduction . . . . .	87
4.2	X-ray Diffraction Studies . . . . .	89
4.3	Oxygen rich region ( $\delta = 0.6$ and $0.65$ ) . . . . .	92
4.4	Orthorhombic region ( $\delta = 0.55$ and $0.39$ ) . . . . .	98
4.5	Oxygen deficient tetragonal region ( $\delta = 0.12$ ) . . . . .	102
4.6	X-ray Absorption Near Edge spectroscopic studies . . . . .	104
4.7	Conclusion . . . . .	110
	References . . . . .	111
<b>5</b>	<b>Effect of <math>\text{Co}3d\text{-O}2p</math> Hybridization on Magnetic and Transport Properties</b>	
	<b>of <math>\text{PrBaCo}_2\text{O}_{5.50}</math></b>	<b>114</b>
5.1	Introduction . . . . .	114
5.2	X-ray Diffraction Studies . . . . .	117



5.3	Magnetization Measurements . . . . .	118
5.4	Transport Properties : Electrical Resistivity Measurements . . . . .	120
5.5	Magneto-transport Properties : Magnetoresistance Measurements . . . . .	122
5.6	X-ray Absorption Spectroscopic Measurements . . . . .	123
5.6.1	X-ray Absorption Near Edge Structure (XANES) . . . . .	123
5.6.2	Extended X-ray Absorption Fine Structure . . . . .	128
5.7	Discussion . . . . .	132
5.8	Conclusions . . . . .	136
	References . . . . .	137
<b>6</b>	<b>Influence of local structure on magnetic properties of Layered Cobaltites</b>	
	<b>PrBaCo<sub>2</sub>O<sub>5+<math>\delta</math></sub>, <math>\delta &gt; 0.5</math></b>	<b>142</b>
6.1	Introduction . . . . .	142
6.2	Structural Study : XRD . . . . .	145
6.3	Magnetization Measurements . . . . .	148
6.4	Transport Properties : Electrical Resistivity Measurements . . . . .	157
6.5	Magneto-Transport Properties : Measurements of Magnetoresistance . . . . .	157
6.6	X-ray Absorption Spectroscopic Measurements . . . . .	161
6.6.1	Extended X-ray Absorption Fine Structure (EXAFS) . . . . .	162
6.7	Discussion . . . . .	165
6.8	Conclusions . . . . .	168
	References . . . . .	169

<b>7</b>	<b>Magnetic and Spectroscopic Studies of Oxygen Deficient Layered Cobaltites <math>\text{PrBaCo}_2\text{O}_{5+\delta}</math> (<math>\delta = 0.43, 0.35</math>)</b>	<b>173</b>
7.1	Introduction . . . . .	173
7.2	X-ray Diffraction Measurements . . . . .	175
7.3	Magnetization Measurements . . . . .	177
7.4	Transport Properties : Electrical Resistivity Measurements . . . . .	181
7.5	Magneto-Transport Properties : Magnetoresistance Measurements . . . . .	183
7.6	Infra-Red Spectroscopic Measurements . . . . .	184
7.7	Raman Spectroscopic Measurements . . . . .	188
7.8	X-ray Absorption Spectroscopic Measurements . . . . .	189
7.8.1	X-ray Absorption Near Edge Structure (XANES) . . . . .	189
7.8.2	Extended X-ray Absorption Fine Structure (EXAFS) . . . . .	191
7.9	Discussion . . . . .	196
7.10	Conclusion . . . . .	198
	References . . . . .	199
<b>8</b>	<b>Summary and Conclusions</b>	<b>203</b>
8.1	Summary and Conclusion . . . . .	203
8.2	Future Work . . . . .	207
<b>9</b>	<b>List of Publications</b>	<b>208</b>

# List of Figures

1.1	Angular dependence of the electron distribution in the 3d orbitals . . . .	8
1.2	Splitting of the free ion 3d energy levels in a cubic environment as provided by the oxygen octahedron. The elongation of the octahedra along some direction (here $z$ direction), splits the levels further. . . . .	9
1.3	The energy levels and the distribution of the six electrons of the $\text{Co}^{3+}$ ion are shown for a free ion, weak crystal field splitting ( $\Delta_{cf} < J_H$ , Hund's rule is obeyed) and strong crystal field splitting ( $\Delta_{cf} > J_H$ ) . . . . .	11
1.4	The possible spin states of Cobalt with total spin(S) and moment( $\mu$ ) in Bohr-magneton. . . . .	12
1.5	Superexchange in magnetic oxides, simplified to one electron per magnetic ion: the arrows represent the spins of the four electrons responsible for mediation of the exchange. Two excited states are shown ( $\Delta \gg U$ and $\Delta < U$ ). For AFM coupling the excited states can mix with the ground state, whereas for FM coupling the excited states are prohibited by the Pauli exclusion principles. . . . .	13

1.6	Double Exchange according to Zener [1, 2]. For the $\psi_+$ wavefunction the exchange is ferromagnetic and the delocalized electron leads to metallicity.	16
1.7	Double exchange mechanism gives ferromagnetic coupling between $Mn^{3+}$ and $Mn^{4+}$ ions participating in electron transfer. The single-centre exchange interaction favours hopping if (a) neighbouring ions are ferromagnetically aligned and not if (b) neighbouring ions are antiferromagnetically aligned.	17
1.8	Goodenough-Kanamori rules 1) Two half filled $e_g$ (e.g. $3d_{x^2-y^2}$ ) orbitals are coupled by an $O^{2-}$ , as is the case for two IS $Co^{3+}$ ions. 2) Two half filled $t_{2g}$ (e.g. $3d_{xy}$ ) orbitals are coupled by an $O^{2-}$ , as for two LS $Co^{4+}$ ions. 3) A half filled $t_{2g}$ and a half filled $e_g$ orbital are coupled by an O as for IS $Co^{3+}$ and LS $Co^{4+}$ . The FM coupling can be understood with Hund's rule, where parallel spins minimize energy.	20
1.9	Crystal structure of $RBaCo_2O_{5+\delta}$ with a) $a_p \times a_p \times 2a_p$ ( $\delta = 0$ ); b) $a_p \times 2a_p \times 2a_p$ ( $\delta = 0.5$ ); and c) $a_p \times a_p \times 2a_p$ ( $\delta = 1$ ) type unit cell.	23
1.10	Magnetic models (I) Different magnetic models, (a) $GdBaCo_2O_{5.5}$ , (b) $NdBaCo_2O_{5.47}$ , $TbBaCo_2O_{5.5}$ , (II) Small magnetic moment considered for LS octahedral Co ion which is ascribed to imperfect ordering of octahedra and square pyramids in $PrBaCo_2O_{5.5}$ . Figures are taken from reference [55, 64].	26
2.1	The Bragg condition, $2d\sin \theta = n\lambda$ .	40

2.2	TGA curves for $\text{PrBaCo}_2\text{O}_{5.80}$ and $\text{SmBaCo}_2\text{O}_{5.55}$ . . . . .	42
2.3	Vibrating Sample Magnetometer. . . . .	47
2.4	A cross-sectional schematic of a simple low-Tc SQUID system. . . . .	48
2.5	Basic flow diagram of resistivity measurement setup . . . . .	51
2.6	The photoelectric effect, in which an x-ray is absorbed and a core-level electron is promoted out of the atom. . . . .	55
2.7	The incident x-ray beam ( $I_0$ ) passing through a material of thickness $t$ . . . . .	56
2.8	Typical XAFS beamline (BL 7C at Photon Factory) (a) Experimental arrangement for low temperature transmission XAFS measurement (b) post mirror for rejection of higher order harmonics (c) monochromator drum consisting of Si (111) crystals. . . . .	57
2.9	(a) XAFS pre-edge subtraction and normalization. First, a pre-edge line (or simple polynomial) is fitted to the spectrum below the edge. The jump in the edge is approximated, and the spectrum is normalized by this value (b) XAFS $\mu(E)$ for $\text{PrBaCo}_2\text{O}_{5.5}$ , the measured XAFS spectrum is shown with the XANES and EXAFS regions identified. On the bottom, $\mu(E)$ is shown with smooth background function $\mu_0(E)$ and the edge-step $\Delta\mu_0(E_0)$ . . . . .	59
2.10	(a) Isolated EXAFS $\chi(k)$ for $\text{PrBaCo}_2\text{O}_{5.5}$ , (b) the $k$ -weighted XAFS, $k^2\chi(k)$ . . . . .	60
2.11	The Fourier Transformed XAFS, $\chi(R)$ , the magnitude $ \chi(R) $ is shown; this is the most common way to view the data. . . . .	61

3.1	Rietveld refined XRD patterns of $\text{RBaCo}_2\text{O}_{5.5}$ ( $\text{R} = \text{Pr, Nd, Sm, Gd}$ and $\text{Y}$ ). Circles represent experimental data, continuous line through the data is the fitted curve, vertical lines indicate Bragg positions and the difference pattern is shown at the bottom as solid line. . . . .	68
3.2	Variation of cell volume, orthorhombic distortion and Co-O-Co interpolyhedron angle with ionic radius for $\text{RBaCo}_2\text{O}_{5.5}$ ( $\text{R} = \text{Pr, Nd, Sm, Gd}$ and $\text{Y}$ ) . . . . .	69
3.3	Magnetization $M(T)$ as function of temperature in the field of 1T for $\text{RBaCo}_2\text{O}_{5.5}$ ( $\text{R} = \text{Pr, Nd, Sm, Gd}$ and $\text{Y}$ ). Inset shows 100Oe MT for $\text{R}=\text{Pr}$ and $\text{Sm}$ and 500Oe ZFC for $\text{R}=\text{Nd, Gd}$ and $\text{Y}$ (Innermost inset of $\text{R}=\text{Y}$ shows enlarged view of ZFC) . . . . .	71
3.4	Effect of rare earth ionic radius on various transition temperatures estimated from 1000 Oe ZFC magnetization data for $\text{RBaCo}_2\text{O}_{5.5}$ ( $\text{R} = \text{Pr, Nd, Sm, Gd}$ and $\text{Y}$ ) . . . . .	72
3.5	Hysteresis loops recorded at different temperatures for $\text{RBaCo}_2\text{O}_{5.5}$ ( $\text{R} = \text{Pr, Nd, Sm, Gd}$ and $\text{Y}$ ) . . . . .	73
3.6	Resistivity(left panel) and Isothermal Magnetoresistance (MR) (right panel) for $\text{RBaCo}_2\text{O}_{5.5}$ ( $\text{R} = \text{Pr, Nd, Sm, Gd}$ and $\text{Y}$ ) . . . . .	75
3.7	Normalised Co K XANES at room temperature with pre-edge encircled for $\text{RBaCo}_2\text{O}_{5.5}$ , $\text{R} = \text{Pr, Nd, Sm, Gd}$ and $\text{Y}$ . . . . .	77

3.8	Crystal field splitting with increasing rare earth ion radii for $\text{RBaCo}_2\text{O}_{5.5}$ (R = Pr, Nd, Sm, Gd and Y) . . . . .	78
3.9	Calculated Co K edge XANES for $\text{RBaCo}_2\text{O}_{5.5}$ (R = Pr, Sm and Y), for square pyramidal(Co1) and octahedral(Co2) site along with a comparison of calculated spectra(dotted line) and experimental(solid line) absorption curves. . . . .	80
4.1	Rietveld refined XRD patterns of $\text{SmBaCo}_2\text{O}_{5+\delta}$ . Circles represent experimental data, continuous line through the data is the fitted curve, vertical lines indicate Bragg positions and the difference pattern is shown at the bottom as solid line. . . . .	90
4.2	Lattice parameter and cell volume obtained from Rietveld refinement . . .	91
4.3	Magnetization as a function of temperature for $\text{SmBaCo}_2\text{O}_{5+\delta}$ compounds for $\delta = 0.65$ (a) 100Oe, (b) 1000 Oe and 1T, For $\delta = 0.60$ (d) 100 Oe, (e) 1000Oe and 1T. Insets of (a) and (d) show the enlarged view of ZFC curve. A plot of $1/\chi$ Vs temperature where in circles denote the experimental data along with Curie-Weiss fit indicated by solid line for (c) $\delta=0.65$ and (f) $\delta=0.60$	93
4.4	Isothermal magnetization curves recorded at (a)10 K, (b)50 K, (c)100 K, (d)130 K (e)200 K and (f)300 K for $\delta = 0.65$ (solid line) and (a) and (c) for $\delta = 0.60$ (dotted line). . . . .	95

4.5	(a)-(b) Plot of resistivity with temperature during cooling and warming cycles for $\delta=0.65$ and $0.60$ respectively. Isothermal magnetoresistance recorded at $100\text{ K}$ (c)-(e) and $200\text{ K}$ (d)-(f) for $\delta=0.65$ and $0.60$ respectively.	97
4.6	Magnetization as a function of temperature for $\text{SmBaCo}_2\text{O}_{5+\delta}$ compounds for $\delta = 0.55$ (a) $100\text{Oe}$ , (b) $1000\text{ Oe}$ and $1\text{T}$ , For $\delta = 0.39$ (c) $500\text{ Oe}$ , (d) $1000\text{Oe}$ and $1\text{T}$ .	99
4.7	Hysteresis loop for $\delta = 0.55$ recorded at (a) $10\text{ K}$ , (b) $180\text{ K}$ , (c) $250\text{ K}$ , inset in (c)shows $M$ Vs $H$ at $300\text{ K}$ and for $\delta = 0.39$ (d) $2\text{ K}$ , (e) $220\text{ K}$ , (f) $275\text{ K}$ .	100
4.8	(a)-(b) Plot of resistivity with temperature during cooling and warming cycles for $\delta=0.55$ and $0.39$ respectively. Isothermal magnetoresistance recorded at for $\delta=0.55$ at (c) $200\text{ K}$ and (d) $100\text{ K}$ .	101
4.9	Magnetization as a function of temperature for $\text{SmBaCo}_2\text{O}_{5.12}$ compounds (a) $100\text{Oe}$ , inset of (a) shows enlarged view of ZFC curve, (b) $1000\text{ Oe}$ .	103
4.10	(a)Plot of resistivity with temperature during cooling and warming cycles, inset (b) Isothermal magnetoresistance recorded at for $300\text{ K}$ for $\delta=0.12$ .	105
4.11	Normalised Co K XANES at room temperature with top inset shows pre-edge and down right inset shows enlarged region of XANES for $\text{SmBaCo}_2\text{O}_{5+\delta}$ , $\delta = 0.60, 0.55$ and $0.12$ .	106
4.12	Deconvolution of pre-edge peak, circles indicates XANES data along with best fit curves (solid lines) which is a sum of three constituent Gaussian peaks for (a) $\delta = 0.60$ , (b) $\delta = 0.55$ and (c) $\delta = 0.12$ .	107



4.13	Calculated Co K edge XANES for $\text{SmBaCo}_2\text{O}_{5+\delta}$ for square pyramidal(Co1), octahedral(Co2) site and experimental absorption curves for (a) $\delta = 0.60$ , (b) $\delta = 0.55$ and (c) $\delta = 0.12$ . . . . .	109
5.1	Rietveld refinement of XRD pattern of $\text{PrBaCo}_2\text{O}_{5.5}$ . Circles represent experimental data, a continuous line through the data is the fitted curve and the difference pattern is shown at the bottom as solid line. . . . .	117
5.2	Temperature dependent magnetization $M(T)$ (a) 100 Oe ZFC and FCW cycle indicated by circle and solid lines. Inset shows transition at 50 K by arrow. (b) 1000 Oe and (c) 10,000 Oe; for ZFC, FCC and FCW cycle indicated by circles, solid line and dashed line respectively. (d) Isothermal magnetization $M(H)$ curves of $\text{PrBaCo}_2\text{O}_{5.5}$ recorded at 10 K, 100 K, and 240 K. The initial magnetization curve at 300 K is shown in inset(d). . .	119
5.3	(a) Plot of resistivity with temperature in $H = 0\text{T}$ during cooling and warming cycles. Inset shows enlarged view of resistivity in the temperature range 100 K to 255 K. (b) Resistivity variation as a function of temperature in $H = 8\text{T}$ . Inset presents a plot of $\log \rho$ versus $T^{-1/4}$ . The arrow points to a anomaly indicating change in transport mechanism around 150 K. .	121
5.4	Magnetic-field-dependent isothermal magnetoresistance at 50 K and 100 K.	122
5.5	Normalized Co K XANES at room temperature with pre-edge peak encircle for $\text{PrCoO}_3$ , $\text{PrSrCoO}_4$ and $\text{PrBaCo}_2\text{O}_{5.5}$ . . . . .	124

5.6	Deconvolution of pre-edge peaks, circles indicates XANES data along with best fit curves (solid lines) which is a sum of two constituent Gaussian peaks at room temperature for (a)PrCoO <sub>3</sub> , (b)PrSrCoO <sub>4</sub> and (c)-(h) at various temperatures for PrBaCo <sub>2</sub> O <sub>5.5</sub> . . . . .	127
5.7	The atomic positions of two sites of cobalt along with oxygen. . . . .	129
5.8	First and second shell fit to the EXAFS of PrBaCo <sub>2</sub> O <sub>5.5</sub> . The $ \chi(R) $ of the data(open circles) and best-fit(solid lines through circles) are shown. . . . .	131
5.9	(a)EXAFS $\chi(k)$ data and best fit at 20 K, variation of Co-O bond distances (b)Octahedra Planer (c) Octahedra Apical, (d) Co-O-Co bond angle, Co-O bond distances (e) square pyramidal Planer (f) square pyramidal Apical at various temperatures for PrBaCo <sub>2</sub> O <sub>5.50</sub> . . . . .	133
6.1	Rietveld refinement of XRD patterns of PrBaCo <sub>2</sub> O <sub>5+<math>\delta</math></sub> , (a) $\delta = 0.80$ , (b) $\delta = 0.67$ and (c) $\delta = 0.58$ . Circles represent experimental data, the continuous line through data is the fitted curve, vertical line indicate Bragg's position and the difference pattern is shown at the bottom as solid line. . . . .	146
6.2	The (200) Bragg reflection and its splitting to (200) and (040) upon tetragonal to orthorhombic transition in PrBaCo <sub>2</sub> O <sub>5.58</sub> . . . . .	147
6.3	Temperature dependent magnetization M(T) (a) 100 Oe ZFC and FC cycle indicated by solid line and dashed lines. Inset shows transition at 50 K ( $T_{R1}$ ) by arrow. . . . .	150

6.4	Temperature dependance of magnetization recorded at 1000 Oe and 1 T for FCC and FCW cycles. The crossing FCC and FCW curves is presented more clearly in the insets. . . . .	151
6.5	Temperature dependent magnetization $M(T)$ in the field of 1000 Oe for ZFC and FC cycle indicated by open squares and triangles respectively. The magnetic transitions are indicated by arrows. Plot of $1/\chi$ Vs temperature where in circles denote the experimental data along with Curie-Weiss fit indicated by solid line. (a) $\delta = 0.80$ (b) $\delta = 0.67$ . . . . .	153
6.6	Hysteresis loops for $\text{PrBaCo}_2\text{O}_{5.80}$ recorded at (a) 10 K, (b) 100 K and (c) 150 K. The same data on a magnified scale is shown in the insets. M vs H data at 300 K is presented in inset(ii). . . . .	155
6.7	Isothermal magnetization curves of $\text{PrBaCo}_2\text{O}_{5.58}$ , recorded at 10 K, 100 K, and 240 K. The initial magnetization curve at 300 K is shown in inset. . . . .	156
6.8	(a) Plot of resistivity with temperature during cooling and warming cycles. (b) Logarithm of the resistivity verses $T^{-1/4}$ plot with arrows indicating different transitions. . . . .	158
6.9	Magnetic-field-dependent isothermal magnetoresistance at various temperatures for $\delta = 0.80$ . Inset shows enlarge view of positive going MR at 200 K. . . . .	159

6.10	Magnetic-field-dependent isothermal magnetoresistance at various temperatures for $\delta = 0.67$ , (a) 100 K, (b) 50 K; Inset shows an enlarged view of positive going MR at 50 K, (c) 30 K. . . . .	160
6.11	Magnetic-field-dependent isothermal magnetoresistance at various temperatures for $\delta = 0.58$ , (a) 100 K, (b) 50 K (c) 30 K. . . . .	161
6.12	(a) and (d) EXAFS $\chi(k)$ data and best fit, (b) and (e) variation of average Co-O bond distances planer and apical (c)and (f) Co-O-Co bond angle at various temperatures for $\text{PrBaCo}_2\text{O}_{5.80}$ and $\text{PrBaCo}_2\text{O}_{5.67}$ respectively. .	164
6.13	(a)EXAFS $\chi(k)$ data and best fit at 20 K, variation of Co-O bond distances (b)Octahedra Planer (c) Octahedra apical, (d) Co-O-Co bond angle, Co-O bond distances (e) square pyramidal planer (g) square pyramidal apical at various temperatures for $\text{PrBaCo}_2\text{O}_{5.58}$ . . . . .	166
7.1	Rietveld refinement of XRD patterns of $\text{PrBaCo}_2\text{O}_{5+\delta}$ for $\delta = 0.43$ and 0.35. Circles represent experimental data, the continuous line through the data is the fitted curve, vertical lines shows Bragg's reflections and the difference pattern is shown at the bottom as solid line. . . . .	176
7.2	Temperature dependent magnetization $M(T)$ for $\text{PrBaCo}_2\text{O}_{5.43}$ (a) 100 Oe ZFC and FC cycle indicated by solid line and dashed lines. Inset (i) shows transition at 140 K ( $T_{R2}$ ) by arrow (ii) shows transition at 300 K ( $T_{R1}$ ) by arrow (b) 1000 Oe ZFC and FC cycle indicated by solid line and dashed lines respectively. . . . .	178

7.3	Temperature dependent magnetization $M(T)$ for $\text{PrBaCo}_2\text{O}_{5.35}$ (a) 100 Oe ZFC and FC cycle indicated by solid line and dashed lines. Inset (i) shows transition at 60 K ( $T_{R2}$ ) by arrow (ii) shows transition at 300 K ( $T_{R1}$ ) by arrow (b) $M(T)$ recorded at 1000 Oe and 1 T for FCC and FCW cycles. The crossing FCC and FCW curves is presented more clearly in the insets(i) and (ii). . . . .	179
7.4	Magnetization as a function of magnetic field for $\text{PrBaCo}_2\text{O}_{5.35}$ recorded at (a) 250 K with the inset showing expanded view of the hysteresis loop and (b) the data recorded at 300 K. . . . .	180
7.5	(a)-(b) Plot of electrical resistivity verses temperature in $H = 0\text{T}$ during cooling and warming cycles for samples having $\delta = 0.43$ and $0.35$ respectively. (c)-(d) A plot of $\log \rho$ versus $T^{-1/4}$ . The arrow points to a anomaly indicating change in transport mechanism around $T_{R2}$ . . . . .	182
7.6	Magnetic-field-dependent isothermal magnetoresistance at (a)200 K for samples having $\delta = 0.43$ (b)100 K, (c)50 K and (d)30 K for $\delta = 0.35$ . . .	183
7.7	(a) Fourier transform IR absorption spectra of $\text{PrBaCo}_2\text{O}_{5.43}$ at 80 K and 375 K. Inset shows best fitted curve (solid line) which is a sum of four constituent Gaussian peaks. (b)-(e) Temperature evolution of IR stretching modes. . . . .	185

7.8	(a) Fourier transform IR absorption spectra of $\text{PrBaCO}_2\text{O}_{5.35}$ at 80 K and 375 K. Inset shows best fitted curve (solid line) which is a sum of five constituent Gaussian peaks. (b)-(e) Temperature evolution of IR stretching modes. . . . .	187
7.9	(a) Raman spectra of $\text{PrBaCO}_2\text{O}_{5.35}$ at 80 K.(b)-(f) Temperature evolution of Raman modes of different frequencies. . . . .	188
7.10	Normalized, Co K edge XANES for $\delta = 0.43$ (solid lines) and for $\delta = 0.35$ (dashed line), recorded at room temperature; inset (left top) shows pre-edge excluded region from baseline fitting. . . . .	190
7.11	(a)EXAFS $\chi(k)$ data and best fit at 325 K, variation of Co-O bond distances (b)Octahedra Planer (c) Octahedra Apical, (d) Co1-O-Co2 bond angle, Co-O bond distances (e) square pyramidal Planer (g) square pyramidal Apical at various temperatures for $\text{PrBaCO}_2\text{O}_{5.43}$ . . . . .	193
7.12	(a)EXAFS $\chi(k)$ data and best fit at 325 K, variation of Co-O bond distances (b)Octahedra planer (c) Octahedra apical, (d) Co1-O-Co2 bond angle, Co-O bond distances (e) square pyramidal planer (g) square pyramidal apical at various temperatures for $\text{PrBaCO}_2\text{O}_{5.35}$ . . . . .	195
8.1	Phase diagram constructed from magnetic transition observed in magnetization curves recorded at 100 Oe for $\text{SmBaCO}_2\text{O}_{5+\delta}$ . . . . .	204
8.2	Phase diagram constructed from magnetic transition observed in magnetization curves recorded at 100 Oe for $\text{PrBaCO}_2\text{O}_{5+\delta}$ . . . . .	204

# List of Tables

1.1	Properties and Applications of Perovskites. . . . .	4
2.1	Final annealing temperature and annealing atmosphere used in preparation of $\text{RBaCo}_2\text{O}_{5+\delta}$ compounds. The oxygen content $\delta$ as determined from iodometric titration is also reported. . . . .	39
3.1	Lattice parameters of $\text{RBaCo}_2\text{O}_{5.5}$ . Figures in parentheses indicate uncertainties in the last digit . . . . .	69
4.1	XANES fitting parameters for $\text{SmBaCo}_2\text{O}_{5+\delta}$ , $\delta = 0.60, 0.55, 0.12$ . . . .	108
5.1	XANES fitting parameters for $\text{PrCoO}_3$ , $\text{PrSrCoO}_4$ and $\text{PrBaCo}_2\text{O}_{5.5}$ . . .	126
5.2	EXAFS model parameters for $\text{PrBaCo}_2\text{O}_{5.5}$ . . . . .	130
6.1	Lattice parameters for $\text{PrBaCo}_2\text{O}_{5+\delta}$ . . . . .	148
7.1	Lattice parameters and magnetic transition temperatures for $\text{PrBaCo}_2\text{O}_{5+\delta}$ .177	

# Chapter 1

## Introduction

Materials are probably more deep-seated in our culture than most of us realize. Era of simple material is gone, modern life demands new materials with extraordinary properties.

Historically, the development and advancement of societies have been intimately tied to the members' ability to produce and manipulate materials to fill their needs. For technological development and to meet new demands of the tomorrows society there is a constant need for new materials with new and improved properties. An advancement in the understanding of a material type is often the forerunner to the stepwise progression of a technology. Earlier, materials utilization was totally a selection process, that is, deciding from a given, rather limited set of materials the one that was best suited for an application by virtue of its characteristics. It was not until relatively recent times that scientists came to understand the relationships between the structural elements of materials and their properties. This knowledge, has empowered them to fashion, to a large degree, the characteristics of materials.



## 1.1 Historical Background

*It's a perovskite material world!*

The extraordinary materials often possess complex structure, one such material is known as *Perovskites*. The perovskite as a mineral was described for the first time by G. Rose in the 1830's and was named so in the honour of the Russian mineralogist A. von Perovski. Long after, from the 1940's, a tremendous work was carried out on the perovskite materials and their derivatives, for both their structural, chemical and physical properties. The perovskite structure continues to attract interest, since properties suitable for applications can be found for compounds with this or closely related structures. The decade between 1950<sup>1</sup> and 1960 was extremely rich for the discovery of perovskite relatives. During the same period a large contribution was brought to the study of the magnetic and transport properties of the perovskite oxides as shown by the pioneering studies performed by Zener [1, 2] on double exchange in manganites and by Goodenough [3], Jonker and Van Santen [4] on the role of Jahn-Teller effect, superexchange interactions, orbital and charge ordering in the magnetic properties of numerous perovskites especially those of copper, manganese, cobalt and nickel oxides. The concepts introduced by Zener and Goodenough at that time remain today the basis for the understanding of the magnetotransport properties of these materials, as exemplified by the double exchange and the famous Kanamori-Goodenough rules.

Since the pioneering work of Mott [5], that recognized the electron-electron interactions as the origin for the insulating behaviour of many class is of transition oxides, the

research in Condensed Matter Physics has shown the properties of a new class of materials called the strongly correlated electron systems. Strongly correlated electron systems are a class of compounds where the effect of correlations among electrons plays a central role in such a way that the theoretical approaches based on the perturbative methods fail to describe even their very basic properties [6]. In this prospective the current status of investigation of these systems must be considered in the broader context of complexity [6]. Perovskites are one of the huge family belongs to strongly correlated electronic system which has been intensively studied over the last decades. Many compounds with perovskite structure exhibit strong electronic correlations and have been extensively studied over last few decades.

The perovskite structure with the formulation  $ABO_3$  is often represented as a simple cubic structure built up of  $BO_6$  octahedra. The large numbers of perovskite type compounds are described by the general formula  $A^{+2}B^{+4}O_3$ . The ionic radius of A cation is normally found to be somewhat larger than that of the B cation. Three main factors identified as being responsible for the distortion are: size effects (Goldschmidt Tolerance Factor), deviation from the ideal composition and Jahn-Teller effect [7, 8, 9]. Rarely a distortion of a certain perovskite compound can be assigned to a single effect. The unique range of responses, coupled with the flexibility of perovskites in accommodating a broad spectrum of atomic substitutions, provides a robust platform for probing correlations between structure, bulk chemistry, and physical properties [7]. When the A- or B-sites contain mixtures of two (or more) different atoms, control of the positional ordering of the

ordering of the cations in a complex perovskite provides an additional tool for mediating the bulk electronic response [8, 10]. As a result of the combination of different elements, the materials may present insulating, semiconducting, ionic conducting, superconducting, magnetoresistive and many other behaviours [11] that are useful for technological applications. Most popular perovskites and their applications are listed in Table 1.1.

Table 1.1: Properties and Applications of Perovskites.

Material	Property	Applications
$\text{CaTiO}_3$	Dielectric	Microwave application
$\text{BaTiO}_3$	Ferroelectric	Non volatile computer memories
$\text{Pb}(\text{Zr}_{1-x}\text{Ti}_x)\text{O}_3$	Piezoelectric	Sensors
$(\text{Ba}_{1-x}\text{La}_x)\text{O}_3$	Semiconductor	Semiconductor applications
$(\text{Y}_{1/2}\text{Ba}_{2/3})\text{CuO}_{3-x}$	Superconductor	Detectors of magnetic signals
$\text{SrCeO}_3$	H-protonic	Gas diffusion conductor
$\text{BaInO}_{2.5}$	Ionic Conductors	SOFC
$\text{LaMnO}_{3-x}$	GMR	Read heads for hard disks
$\text{RBaM}_2\text{O}_6$	Ionic conductor/GMR	SOFC, Gas absorber, Read heads for hard disks

## 1.2 Cobaltites : Interest and Importance

Like most first row transition metal ions, cobalt too exhibits several possible oxidation states  $\text{Co}^{2+}$ ,  $\text{Co}^{3+}$ , and  $\text{Co}^{4+}$  and several types of coordinations, that is, tetrahedral, pyramidal, and octahedral. Consequently, cobalt oxides offer a wide field for the creation of many frameworks, not only stoichiometric oxides but also non-stoichiometric oxides, involving a mixed valency of cobalt and/or the presence of oxygen vacancies.

High-temperature superconductivity in layered cuprates stimulated tremendous interest in other perovskite-structured oxides of 3d metals; like ruthenates, manganites and cobaltites. The most common feature to most of them is that they belong to strong electron correlation systems [12]. This results in a dielectric ground state of undoped  $\text{La}_2\text{CuO}_4$  (cuprates),  $\text{LaMnO}_3$  (manganites), and  $\text{LaCoO}_3$  (cobaltites). Doping in cuprates gives rise to an unusual pseudogap state and high-temperature superconductivity [13, 14]. In manganites, doping leads to competition of the antiferromagnetic (AFM) and ferromagnetic (FM) exchange interactions and to colossal magnetoresistance [15] while in ruthenates, exotic superconductivity in the case of  $\text{Sr}_2\text{RuO}_4$  and metal-dielectric transitions in the system  $\text{Ca}_{2-x}\text{Sr}_x\text{RuO}_4$  [16]. For cobaltites one can find all the phenomena known in cuprates and manganites: metal-insulator transition, superconductivity [17], competition between antiferromagnetic and ferromagnetic exchanges, giant magnetoresistance, high ionic conductivity and anomalously high thermoelectric emf [12, 17, 18, 19, 20, 21, 22, 23]. Cobaltites thus demonstrate a very rich collection of properties, some of which belong exclusively to them. Strong electron correlations effects, so crucial in 3d elements are definitely present in cobaltites, which not only enrich the underlying physics but also make their understanding complicated. Above mentioned properties have their origin in the strong interplay between crystallographic, magnetic and transport properties, which lead to very rich phase diagrams as a function of temperature, magnetic field, pressure, oxygen content and size of lanthanide ions. A property which distinguishes the cobaltites from other 3d metal oxides is the following: the crystal

field splitting  $\Delta_{cf}$  of the 3d energy level of the Co ion in cobaltites is of the same order of magnitude as the Hund's rule intra-atomic exchange energy  $J_H$ . Spin state transitions can therefore easily be provoked by either varying temperature, applying a magnetic field or pressure, and/or by tuning the structural parameters (oxygen content, type of lanthanide) of the material. The number of electrons in the 3d shell in Co (or also in Fe) allows for three spin states instead of two. Like other doped transition metal oxides, cobaltites can accommodate oxygen vacancies, which result in varying the ratio of  $\text{Co}^{2+}$ ,  $\text{Co}^{3+}$  and  $\text{Co}^{4+}$ . This has a strong influence on the structural, magnetic and transport properties.

### 1.3 Crystal Field Theory

For an isolated transition metal ion the  $d$ -levels are fivefold degenerated ( $2l+1$ , where  $l=2$ ). They are degenerate meaning each orbital has the same energy. This situation changes when Mn or Co cations are bound in a solid state material on specific positions in a crystal lattice. Crystal field theory is concerned with examining the effect of the electric field of symmetrically arranged neighbouring atoms (O) on a particular lattice atom (Co). If an outside force is brought near to the atom, the different orientations of the specific  $d$  orbitals cause them to interact differently with this force. Many  $d$ -electron metal oxides have a perovskite-like structure where a transition metal ion is situated at the center of an octahedron surrounded by six oxygen ions at each corner. Knowledge of the energy scheme is important, as it directly influences the spin states of the Co ion

and thereby affects the possible magnetic interactions in the system. In the presence of a crystal field the 3d-orbital degeneracy can be removed and the 3d levels are split. Crystal field theory shows that the splitting of 3d energy levels depends strongly on the symmetry of the crystallographic site. As the crystal field is produced by the electric charge distribution around 3d metal, the symmetry of the crystal field is given by the symmetry of the lattice site. To calculate this effect all electrons of the incomplete shell of the Co ion have to be considered. The relevant Hamiltonian( $H$ ) [24] is given by-

$$H = H_o + H_{el-el} + H_{SO} + H_{CF}, \quad (1.1)$$

where  $H_o$  is the kinetic energy of the electrons of the Co atom and their interactions with the nucleus,  $H_{el-el}$  is the electron-electron interaction in the Co atom,  $H_{SO}$  is the spin-orbit interaction and  $H_{CF}$  is the influence of the crystal field (repulsion between electrons of the Co atom and the surrounding O atoms).  $H_{el-el}$ ,  $H_{SO}$  and  $H_{CF}$  can be considered as perturbations of  $H_o$ . Let us define a coordination system xyz which is connected to the oxygen octahedron. The angular dependences of the electron density of  $d$ -orbitals are shown in Figure 1.1.

The crystal field energy in the case of a Co ion sitting in an octahedral oxygen environment arises from the electrostatic interaction between the electrons sitting in the 3d orbital of the Co ion and the electrons in the oxygen 2p orbitals. Depending on the symmetry of the filled 3d orbitals, the orbital overlap of the Co electrons with the O electrons can significantly differ. The 3d orbitals denoted as  $3d_{x^2-y^2}$  and  $3d_{z^2-r^2}$  point directly toward the oxygens. Other three orbitals ( $3d_{xy}$ ,  $3d_{xz}$ ,  $3d_{yz}$ ) are directed in between the

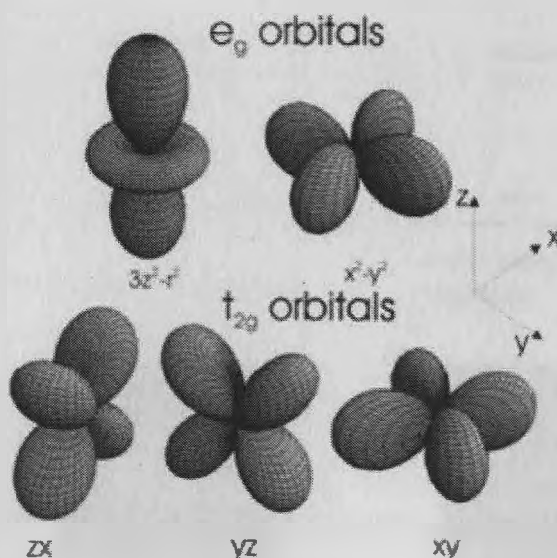


Figure 1.1: Angular dependence of the electron distribution in the 3d orbitals [70].

oxygens. According to the crystal field theory the energies of  $3d_{x^2-y^2}$  and  $3d_{z^2-r^2}$  orbitals are higher than those of the  $3d_{xy}$ ,  $3d_{xz}$ ,  $3d_{yz}$  orbitals. The lower energy levels, i.e.  $3d_{xy}$ ,  $3d_{xz}$ ,  $3d_{yz}$  are called  $t_{2g}$  and the higher energy levels i.e.  $3d_{x^2-y^2}$  and  $3d_{z^2-r^2}$  are called  $e_g$ . This is because the overlap of the  $p$  orbitals with the  $t_{2g}$  orbitals is smaller than with the  $e_g$  orbitals, causing the  $t_{2g}$  orbitals to have lower energy compared to the  $e_g$  orbitals (Figure 1.2 middle).

The energy difference between these two levels is called the crystal field (CF) energy  $\Delta_{cf}$ . Further splitting of the orbitals can occur if the octahedra are elongated along a certain direction, for example by the *Jahn-Teller effect* (Figure 1.2 right). The cubic environment is then transformed into a tetragonal one and the  $3d_{z^2-r^2}$  orbital lowered in energy. Usually the elongation along the  $z$  direction will lead to a simultaneous shrinking in the  $xy$ -plane, also changing the energy of the  $t_{2g}$  orbitals. The magnitude of the crystal

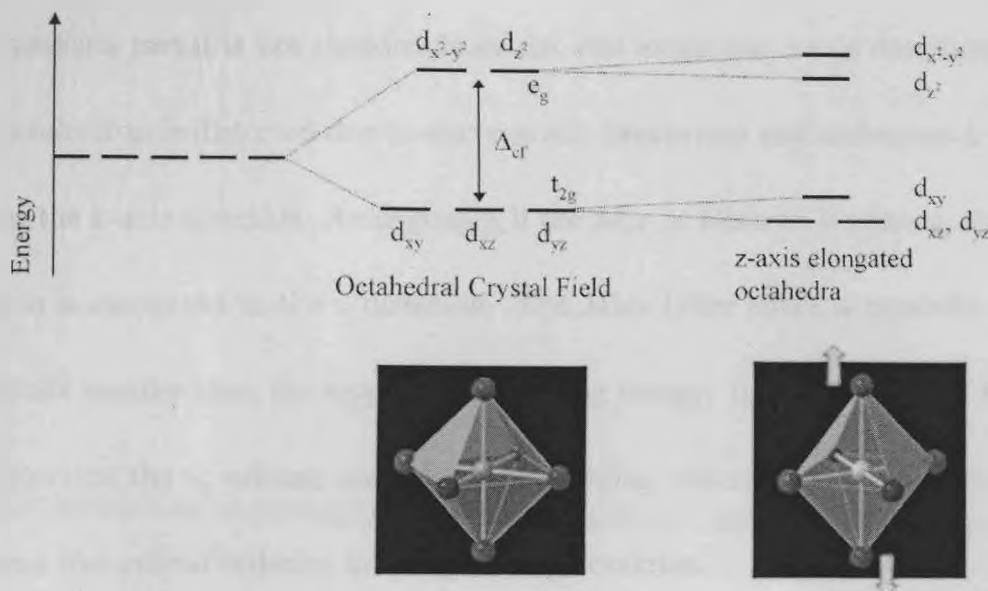


Figure 1.2: Splitting of the free ion 3d energy levels in a cubic environment as provided by the oxygen octahedron. The elongation of the octahedra along some direction (here z direction), splits the levels further.

field splitting  $\Delta_{cf}$  depends on the transition metal element, its charge and the number of ligands. In cobaltites, the magnitude of CF splitting being similar to spin orbit energy, realises Co ions to have different spin states which are discussed later in the Chapter.

### 1.3.1 Jahn-Teller Distortion

According to Jahn Teller theorem “any non-linear molecular system in a degenerate electronic state will be unstable and will undergo distortion to form a system of lower symmetry and lower energy thereby removing the degeneracy.” Therefore, systems with transition metals in octahedral surrounding and degenerated energy levels exhibit spontaneous distortion of octahedron and a lowering of the crystal field symmetry which is accompanied with splitting of energy levels. This effect is called Jahn-Teller effect and



Jahn-Teller distortion. When, for example, the  $3d_{z^2-r^2}$  orbital is unoccupied the nucleus of the transition metal is not shielded from the ions along the  $z$ -axis direction and the oxygen octahedron is distorted due to electrostatic interaction and undergoes a compression along the  $z$ -axis direction. Analogously, if the  $3d_{x^2-y^2}$  electron is missing, the oxygen octahedron is elongated in the  $z$  direction. The Jahn-Teller effect is typically an order of magnitude smaller than the crystal field splitting energy. In the presence of the Jahn-Teller distortion the  $e_g$  orbitals have different energies, which leads to many interesting phenomena like orbital ordering in manganese perovskites.

## 1.4 Spin States of Cobalt

For a transition metal ion the electron filling scheme of the  $t_{2g}$  and  $e_g$  orbitals depends on a competition between the crystal field and the Coulomb repulsion between  $d$ -electrons. The magnitude of the crystal field splitting  $\Delta_{cf}$  depends on the transition metal element, its charge and the number of ligands. The 3d transition metal ions are special because their  $d$ -orbitals are only partially filled.  $H_{el-el} > H_{CF}$  results in weak crystal fields (electrons obey the Pauli exclusion principle) while for strong crystal field arises due to  $H_{CF} > H_{el-el}$ . For a weak crystal field the levels are filled according to Hund's rule (obeying the Pauli exclusion principle), which requires that the total spin is maximized. This means that the intra-atomic exchange energy  $J_H$  (resulting from the electron-electron interaction) separating the spin up and spin down energy levels is large compared to the crystal field splitting  $\Delta_{cf}$  (Figure 1.3 middle).

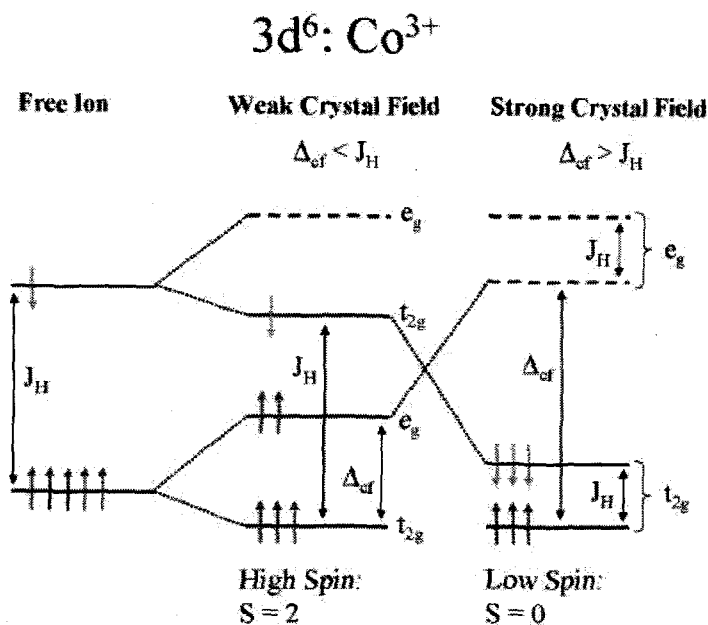


Figure 1.3: The energy levels and the distribution of the six electrons of the  $\text{Co}^{3+}$  ion are shown for a free ion, weak crystal field splitting ( $\Delta_{cf} < J_H$ , Hund's rule is obeyed) and strong crystal field splitting ( $\Delta_{cf} > J_H$ )[71].

If the crystal field splitting becomes larger than the intra-atomic exchange energy (as can be the case for Co), it may energetically be more favourable to fill the  $t_{2g}$  orbitals first, even though the electron spins are antiparallel (Figure 1.3 right). For  $\text{Co}^{3+}$  and  $\Delta_{cf} < J_H$  this will result in a spin configuration which is called a high spin configuration (HS,  $t_{2g}^4 e_g^2$ ,  $S = 2$ ), whereas for  $\text{Co}^{3+}$  and  $\Delta_{cf} > J_H$  a low spin state (LS,  $t_{2g}^6 e_g^0$ ,  $S = 0$ ) will be adopted. For  $\text{Co}^{3+}$  with 6 electrons in the 3d shell, a third possibility exists, namely the intermediate spin state (IS,  $t_{2g}^5 e_g^1$ ,  $S = 1$ ). A schematic way to illustrate the different spin states is shown in Figure 1.4. The possible spin states and their total spin  $S$  are shown for  $\text{Co}^{4+}$ ,  $\text{Co}^{3+}$  and  $\text{Co}^{2+}$  (for which the IS state does not exist).

**Possible scenario: Low spin vs. High spin state**

<sup>27</sup>  
Co

**Ground state electron configuration: [Ar].3d<sup>7</sup>.4s<sup>2</sup>**

	Low spin state	Intermediate spin state	High spin state
<b>Co<sup>2+</sup> (3d<sup>7</sup>)</b>	$\uparrow -$ $S=1/2$ $\uparrow\downarrow\uparrow\downarrow$ $\mu=1\mu_B$		$\uparrow\uparrow$ $S=3/2$ $\uparrow\downarrow\uparrow$ $\mu=3\mu_B$
<b>Co<sup>3+</sup> (3d<sup>6</sup>)</b>	$--$ $S=0$ $\uparrow\downarrow\uparrow\downarrow$ $\mu=0\mu_B$	$\uparrow -$ $S=1$ $\uparrow\downarrow\uparrow$ $\mu=2\mu_B$	$\uparrow\uparrow$ $S=2$ $\uparrow\downarrow\uparrow$ $\mu=4\mu_B$
<b>Co<sup>4+</sup> (3d<sup>5</sup>)</b>	$--$ $S=1/2$ $\uparrow\downarrow\uparrow$ $\mu=1/2\mu_B$	$\uparrow -$ $S=3/2$ $\uparrow\downarrow\uparrow$ $\mu=3\mu_B$	$\uparrow\uparrow$ $S=5/2$ $\uparrow\downarrow\uparrow$ $\mu=5\mu_B$

Figure 1.4: The possible spin states of Cobalt with total spin(S) and moment( $\mu$ ) in Bohr-magneton.

## 1.5 Magnetic Interactions

Exchange interactions lie at the heart of the phenomenon of long range magnetic order. These interactions are nothing more than electrostatic interactions, arising because charges of the same sign cost energy when they are close together and save energy when they are apart. Magnetic interactions between transition metal ions are of the special interest since they can cause long range magnetic order in oxides. To achieve a long range magnetic ordering the magnetic moments need to be able to "communicate" with each other. Long range magnetic order may set in, if the interactions between the magnetic moments are strong enough. In 3d metal oxides, the long range order is mainly due to exchange interactions, which are basically of electrostatic origin. Electrostatic interactions are due to the repulsion between charges of the same sign, resulting in an

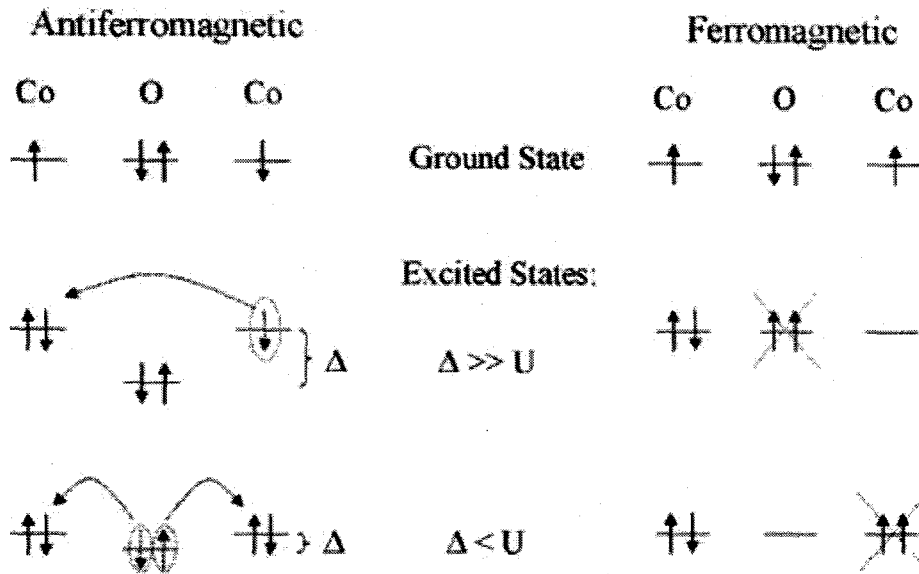


Figure 1.5: Superexchange in magnetic oxides, simplified to one electron per magnetic ion: the arrows represent the spins of the four electrons responsible for mediation of the exchange. Two excited states are shown ( $\Delta \gg U$  and  $\Delta < U$ ). For AFM coupling the excited states can mix with the ground state, whereas for FM coupling the excited states are prohibited by the Pauli exclusion principles [71].

energy cost for such charges to be close together and in a gain of energy when they are far apart. The exchange interaction is normally very short-ranged so that the longer ranged interaction that is operating in this case must be in some sense 'super'. Kramers and later Anderson [25, 26, 27] proposed a type of indirect exchange interaction which is called super-exchange interaction leading to antiferromagnetic order as a virtual hopping of electrons with antiparallel spins. It can be defined as an indirect exchange interaction between non-neighbouring magnetic ions which is mediated by a non-magnetic ion which is placed in between the magnetic ions. It arises because there is a kinetic energy advantage for antiferromagnetism which can be understood by reference to Figure 1.5 which shows two transition metal ions separated by an oxygen ion.

For simplicity we will assume that the magnetic moment on the transition metal ion is due to a single unpaired electron (more complicated cases can be dealt with in analogous ways). Hence if this system were perfectly ionic, each metal ion would have a single unpaired electron in a  $d$ -orbital and the oxygen would have two  $p$  electrons in its outermost occupied states, the Figure 1.5 demonstrates that antiferromagnetic coupling lowers the energy of the system by allowing these electrons to become delocalised over the whole structure, thus lowering the kinetic energy. Because super-exchange involves the oxygen orbitals as well as the metal atom, it is a second-order process and is derived from second-order perturbation theory. A general consequence of second-order perturbation theory is that the energy involved is approximately given by the square of the matrix element of the transition divided by the energy cost of making the excited state. Here the transition matrix element is controlled by a parameter called the hopping integral 't', which is proportional to the energy width of the conduction band (i.e. the bandwidth) in a simple tight-binding approach. The energy cost of making an excited state is given by the Coulomb energy  $U$ . This process can be treated as a perturbation in the Heisenberg Hamiltonian  $H = \sum_{ij} J_{ij} S_i S_j$ , where  $S_i$  and  $S_j$  are the localized moments on the Co ions. The value of the exchange interaction  $J_{ij}$  is difficult to calculate and its sign depends on the geometry of the involved Co/O orbitals.  $J_{ij}$  can be approximated to  $t^2/U$ , where  $t$  is the hopping integral for a transfer of an electron from the oxygen to a neighbouring Co ion and  $U$  is the Coulomb energy which has to be paid in order to add an electron to a singly occupied Co orbital. The coupling between the two magnetic ions can either be

antiferromagnetic (AFM,  $J_{ij} < 0$ ) or ferromagnetic (FM,  $J_{ij} > 0$ ). The exchange integral consists of two parts. The first is a potential exchange term which represents the electron repulsion and favours ferromagnetic ground states, but is small when the ions are well separated. The second is a kinetic exchange term which dominates here and is the effect discussed above. It depends on the degree of overlap of orbitals and thus super-exchange is strongly dependent upon the angle of the M-O-M bond. Hopping of the  $3d$  Co electrons occurs via the the  $2p$  oxygen orbitals. If  $\Delta = \epsilon_d - \epsilon_p$  is the energy difference between the  $3d$  and  $2p$  orbitals (charge transfer energy), then one can distinguish two cases (Figure 1.5): In the first case ( $\Delta \gg U$ ), the  $2p$  orbital lies below the  $3d$  orbitals. The excited states are those corresponding to the transfer of a  $3d$  electron from one Co site to another:  $d^n + d^n \rightarrow d^{n-1} + d^{n+1}$ . In the second case ( $\Delta < U$ ), the excited state will correspond to the transfer of an oxygen electron to a transition metal:  $d^n p^6 \rightarrow d^{n-1} p^5$ . The two cases are shown in Figure 1.5 for the simple case of one spin on each Co  $3d$  orbital and for AFM (left) and FM (right) coupling of the Co ions. Obviously, the excited states in the FM case are prohibited by the Pauli exclusion principle. The AFM coupling is therefore energetically favoured, because it results in a delocalization of the electrons (mixing of ground state with excited states), which lowers the kinetic energy of the system.

Another type of exchange interaction commonly found in the transition metal oxides is called double exchange interaction. It is possible to have a ferromagnetic exchange interaction which occurs because the magnetic ion can show mixed valency, that is it can exist in more than one oxidation state. The double exchange [1, 2, 28, 29, 30] in-

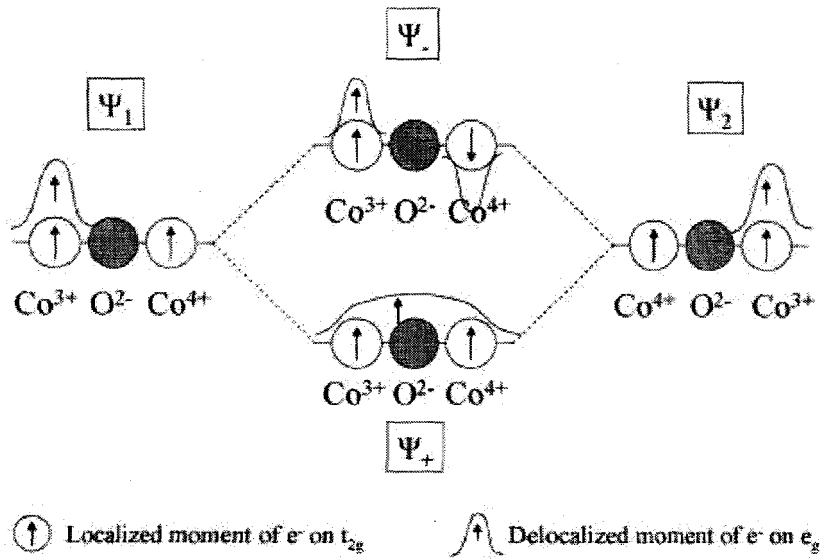


Figure 1.6: Double Exchange according to Zener [1, 2]. For the  $\psi_+$  wavefunction the exchange is ferromagnetic and the delocalized electron leads to metallicity [71].

interaction correlates magnetic and electronic properties, more specifically ferromagnetism and metallicity. In cobaltites, double exchange can be introduced by decreasing oxygen content, introducing  $\text{Co}^{4+}$  at the place of  $\text{Co}^{3+}$  ions due to charge neutrality. This leads to two degenerate electronic states, which can symbolically be represented by the two wave functions  $\psi_1 = \text{Co}^{3+} - \text{O}^{2-} - \text{Co}^{4+}$  and  $\psi_2 = \text{Co}^{4+} - \text{O}^{2-} - \text{Co}^{3+}$ . Zener showed [1, 2] that a magnetic interaction leads to lifting of the degeneracy of these two states by creating two resonant wave functions  $\psi_+ = \psi_1 + \psi_2$  and  $\psi_- = \psi_1 - \psi_2$  (Figure 1.6).

Double exchange associates the appearance of ferromagnetic coupling of the localized magnetic moments (in the  $t_{2g}$  energy level) to the delocalisation of an  $e_g$  electron. A strong Hund's rule coupling  $J_H$  is necessary, which makes an electron transfer from one Co ion to another energetically favourable, if the magnetic moments on the  $t_{2g}$  energy levels of the two Co ions coupled via an intermittent  $\text{O}^{2-}$  ion which are parallel to the spin

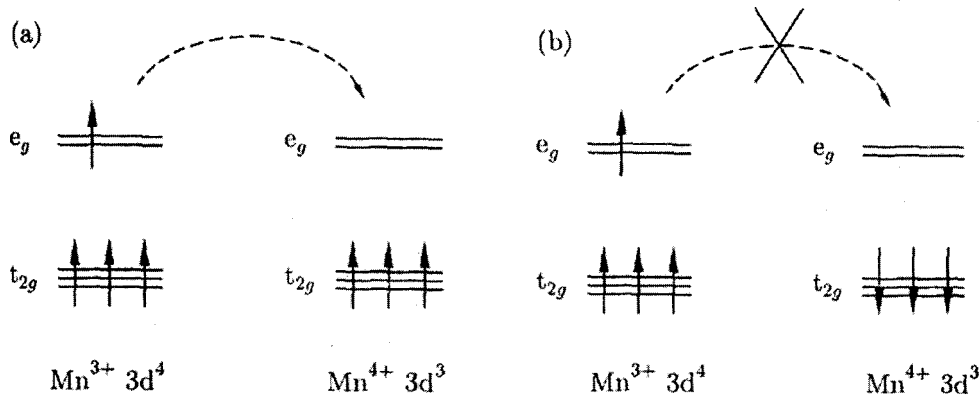


Figure 1.7: Double exchange mechanism gives ferromagnetic coupling between  $Mn^{3+}$  and  $Mn^{4+}$  ions participating in electron transfer. The single-centre exchange interaction favours hopping if (a) neighbouring ions are ferromagnetically aligned and not if (b) neighbouring ions are antiferromagnetically aligned.

of the delocalized electron (Figure 1.6). In a charge ordered material DE is forbidden, because the wave functions  $\psi_1$  and  $\psi_2$  are distinguishable.

This has been observed in  $La_{0.5}Ca_{0.5}MnO_3$  where 50%  $Mn^{3+}$  and 50%  $Mn^{4+}$  are ordered below the charge ordering temperature ( $T_{CO}$ ). The material undergoes a magnetic transition from ferromagnetic to antiferromagnetic at  $T_N = T_{CO}$ , since DE is no longer allowed and is replaced by superexchange [31, 32, 33, 34]. The ferromagnetic alignment is due to the double exchange mechanism which can be understood with reference to Figure 1.7. The  $e_g$  electron on a  $Mn^{3+}$  ion can hop to a neighbouring site only if there is a vacancy there of the same spin (since hopping proceeds without spin-flip of the hopping electron). If the neighbour is a  $Mn^{4+}$  which has no electrons in its  $e_g$  shell, this should present no problem. However, there is a strong single-centre (Hund's rule number 1) exchange interaction between the  $e_g$  electron and the three electrons in the  $t_{2g}$  level which wants to keep them all aligned. Thus it is not energetically favourable for an  $e_g$  electron



to hop to a neighbouring ion in which the  $t_{2g}$  spins will be antiparallel to the  $e_g$  electron (Figure 1.7(b)). Ferromagnetic alignment of neighbouring ions is therefore required to maintain the high-spin arrangement on both the donating and receiving ion. Because the ability to hop gives a kinetic energy saving, allowing the hopping process shown in Figure 1.7(a) reduces the overall energy. Thus the system ferromagnetically aligns to save energy. Moreover, the ferromagnetic alignment then allows the  $e_g$  electrons to hop through the crystal and the material becomes metallic.

### 1.5.1 Goodenough-Kanamori rules

The Goodenough-Kanamori rule, first formulated by Goodenough in 1955 [3] and subsequently provided more rigorous mathematical underpinning by Kanamori (1959) [35], applies to interatomic spin-spin interactions between two atoms, each carrying a net spin, that are mediated by virtual electron transfers between the atoms (**superexchange**) and/or between a shared anion and the two atoms (**semicovalent exchange**). A virtual electron transfer occurs between overlapping orbitals of electronic states that are separated by an energy  $\Delta E$ ; and a spin-spin interaction mediated by an electron transfer, virtual (or real as in ferromagnetic **double exchange**), is a kinetic exchange. Orthogonal orbitals do not overlap, so there is no electron transfer and the exchange interaction between spins in orthogonal orbitals is a ferromagnetic potential exchange; it is responsible for the Hund highest-spin rule for the free atom or ion. Goodenough-Kanamori rule has given three different ways by which two  $\text{Co}^{3+}$   $3d$ -orbitals can be coupled via the oxygen  $2p$ -orbital (when the angle of the  $\text{Co-O-Co}$  bond is  $180^\circ$ ).

(Figure 1.8) :

- Coupling between cations with half filled  $e_g$  orbitals: AFM
- Coupling between cations with half filled  $t_{2g}$  orbitals: weak AFM
- Coupling between a cation with a half filled  $t_{2g}$  to one with a half filled  $e_g$  orbital:  
FM

The first two cases result in the above described AFM coupling of the two cations.

The difference lies in the direction of the half filled  $e_g$  and  $t_{2g}$  orbitals with respect to the oxygen  $2p$  orbital. Since the exchange integral is larger for larger orbital overlap, the AFM coupling for the second case will be weaker (Figure 1.8). In the third case two different orbitals ( $e_g$  and  $t_{2g}$ ) are occupied at the Co ion sites. Due to the symmetry of the corresponding wave functions, these orbitals are orthogonal and no hopping can occur between them. However, the electron of the  $t_{2g}$  orbital (IS  $\text{Co}^{3+}$  in Figure 1.8) can hop into an empty  $t_{2g}$  orbital on the second ion (LS  $\text{Co}^{4+}$ ) which has the same symmetry. Following Hund's rule (minimizing the intra-atomic exchange energy), it is energetically more favourable, if the spin of the electron transferred to the empty orbital is parallel to the electron spin in this ion. This leads to FM coupling between the two magnetic Co ions. The FM coupling is weaker than the AFM one, since for FM coupling the electrons cannot become delocalized (Figure 1.5).

## Goodenough-Kanamori Rules

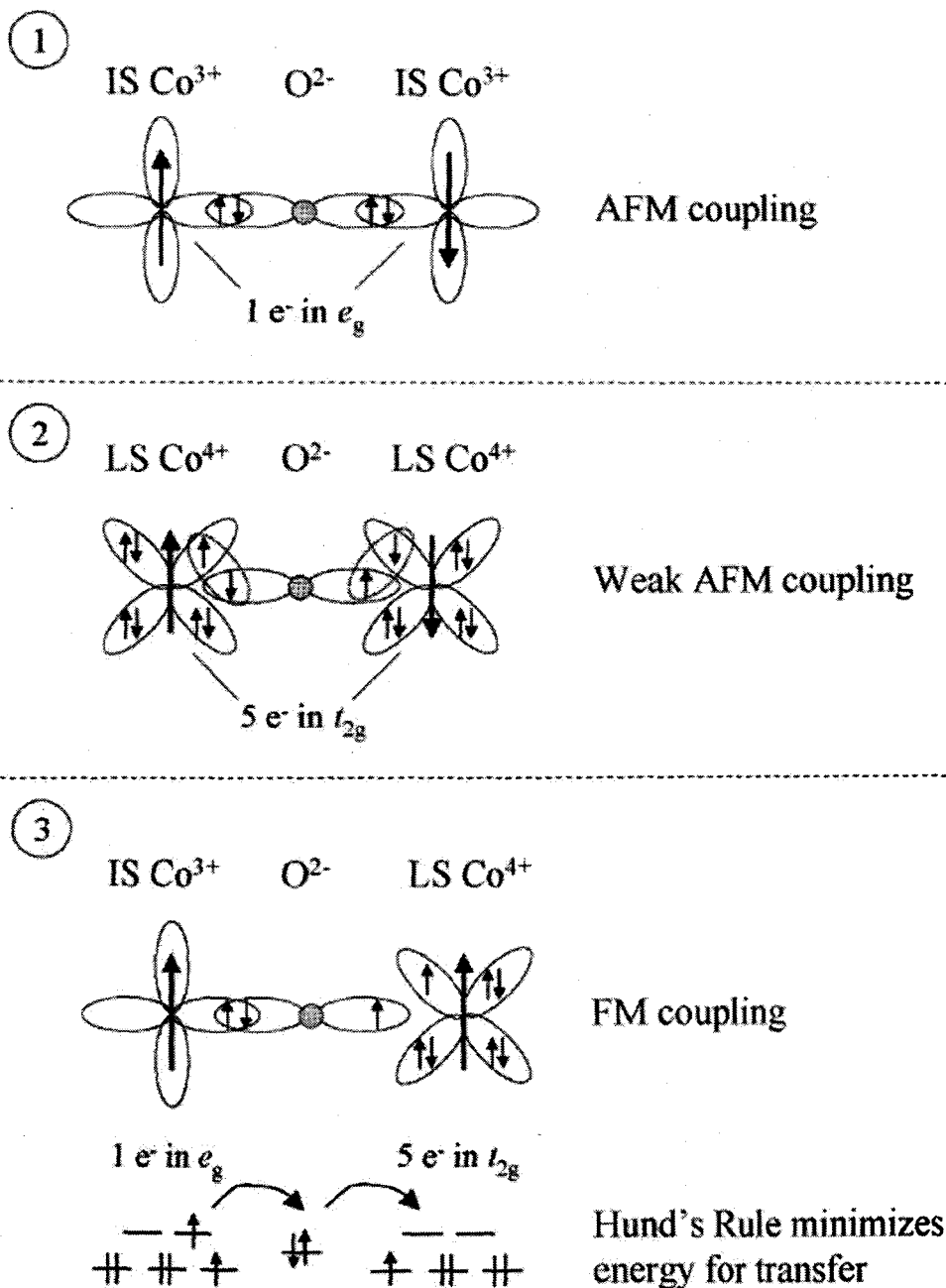


Figure 1.8: Goodenough-Kanamori rules [35, 36]. 1) Two half filled  $e_g$  (e.g.  $3d_{x^2-y^2}$ ) orbitals are coupled by an  $\text{O}^{2-}$ , as is the case for two IS  $\text{Co}^{3+}$  ions. 2) Two half filled  $t_{2g}$  (e.g.  $3d_{xy}$ ) orbitals are coupled by an  $\text{O}^{2-}$ , as for two LS  $\text{Co}^{4+}$  ions. 3) A half filled  $t_{2g}$  and a half filled  $e_g$  orbital are coupled by an O as for IS  $\text{Co}^{3+}$  and LS  $\text{Co}^{4+}$ . The FM coupling can be understood with Hund's rule, where parallel spins minimize energy [71].

## 1.6 Layered Cobaltites

Changing the nature of the A cation of the perovskite cage leads to a dramatic modification of the homogeneity range of this structure. The substitution of a divalent cation such as  $\text{Ca}^{2+}$ ,  $\text{Sr}^{2+}$ , or  $\text{Ba}^{2+}$  for  $\text{R}^{3+}$  in the  $\text{RCoO}_3$  perovskites is of great interest since it allows the mixed valence  $\text{Co}^{3+}/\text{Co}^{4+}$  to be generated. When the size difference between  $\text{R}^{3+}$  and  $\text{A}^{2+}$  cations becomes large in  $\text{R}_{1-x}\text{A}_x\text{CoO}_{3-\delta}$  perovskites, one observes a tendency of these two cations to order in the form of alternate layers, inducing simultaneously an ordering of the oxygen vacancies in the structure. This is the case for a series of cobaltites with  $\text{A}=\text{Ba}$  and  $\text{R}=\text{rare earth or Y}$  for  $x=1$ . Doping of Ba results in layer perovskites of the type  $\text{RBaCo}_2\text{O}_{5+\delta}$ . The structural degree of freedom of this family of compounds provides a strong playground to explore the interrelation between electronic, magnetic, and structural properties.

“Non-stoichiometry” and “doping” are important concepts in layered perovskites like  $\text{RBaCo}_2\text{O}_{5+\delta}$  ( $\text{R}=\text{rare earth}$ ). “Oxygen Engineering” is therefore one of the most important tool for on-demand tailoring functional oxides to get desired properties. A strong overlap of the unfilled, and therefore magnetic,  $3d$  electron orbitals with oxygen  $2p$  orbitals in these compounds makes them display strong correlation between crystallographic, magnetic and transport properties.

It is well known that the crystal structure and the bulk physics of correlated materials, such as band gap, orbital, charge ordering and magnetic properties, are often coupled [37, 38, 39, 40]. It may also happen, on the other hand, that electronic and magnetic,

phase transitions are associated to somewhat hardly detectable structural distortions, that nevertheless may imply important symmetry changes. This is just the case of the cobaltites of general formula  $\text{RBaCo}_2\text{O}_{5+\delta}$ , where  $0 < \delta < 1$  and R may be a trivalent lanthanide ion or yttrium. Such compounds, in the last decade, have raised a great deal of interest due to their intriguing magnetic and transport properties, [40, 41, 42, 43, 44] which can furthermore be varied as a function of temperature [43, 44, 45] or even pressure [43]. Recently, these compounds turned out to be attractive candidates also for the development of new intermediate-temperature solid oxides fuel cells (IT SOFC) [46, 47].

### 1.6.1 Composition and Structure

Most of the advances in the knowledge of the properties of materials have been the outcome of a systematic observation of the properties of closely related materials, this is because of the fact that often small crystal or microstructural differences are associated with marked changes in physical properties. Thus, prior to the investigation of physical properties, it is very essential to pay attention to the structural features and the relationship between crystal structure and electronic properties.

The crystal structure of  $\text{RBaCo}_2\text{O}_{5+\delta}$  consists of a sequence of  $[\text{CoO}_2]$ - $[\text{BaO}]$ - $[\text{CoO}_2]$ - $[\text{RO}_{5+\delta}]$  layers in the  $c$ -direction which involves a doubling of the unit cell in this direction [48]. These ordered oxygen-deficient perovskites are characterized by a 1 : 1 ordering of the  $\text{Ba}^{2+}$  and  $\text{R}^{3+}$  cations in the form of alternating planes. As a consequence, the ideal crystallographic description consists of layers of  $\text{CoO}_6$  octahedra along the  $(a-c)$  planes. These layers are interconnected by two-leg ladders along the  $a$ -direction of the rows of

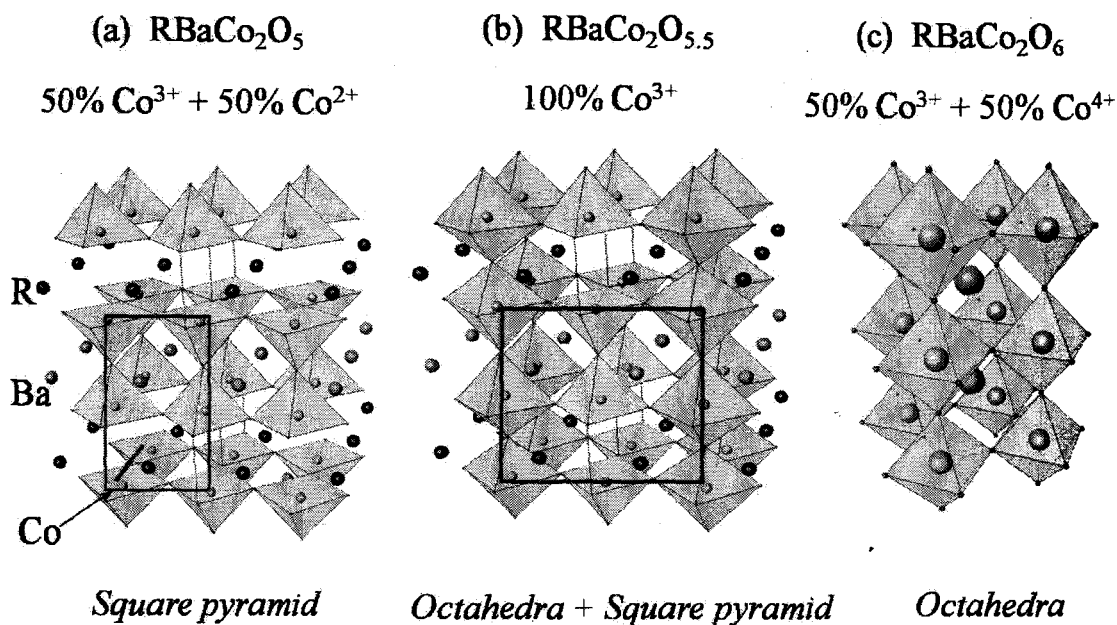


Figure 1.9: Crystal structure of  $\text{RBaCo}_2\text{O}_{5+\delta}$  with a)  $a_p \times a_p \times 2a_p$  ( $\delta = 0$ ); b)  $a_p \times 2a_p \times 2a_p$  ( $\delta = 0.5$ ); and c)  $a_p \times a_p \times 2a_p$  ( $\delta = 1$ ) type unit cell [72].

$\text{CoO}_5$  pyramids. In between these ladders, the six-sided tunnels are occupied by  $\text{R}^{3+}$  cation. Such a structure is very flexible, that is, sensitive to tiny variations in the oxygen content and to the size of the  $\text{R}^{3+}$  cation, so that long-range ordered superstructure or even local distortions can be obtained, leading to dramatic variations in the magnetic properties from one sample to the other.

In these compounds there is a strong interplay between the change in oxygen content ( $5 + \delta$ ), rare-earth ionic radius and valence state of cobalt. Depending on the  $5 + \delta$  value the valence state of cobalt can be  $2^+$ ,  $3^+$  or  $4^+$ . The Co-ion coordination changes from purely  $\text{CoO}_5$ -pyramidal (when  $\delta = 0$ ) “oxygen deficient” to a  $\text{CoO}_6$ -octahedra (when  $\delta = 1$ ) “oxygen rich” or a mixture of both when  $5 + \delta$  takes an intermediate value (see Figure 1.9).

The crystallographic structure of the stoichiometric compound  $\text{RBaCo}_2\text{O}_5$  was found to be tetragonal with  $P4/mmm$  symmetry and unit cell  $a_p \times a_p \times 2a_p$ , where  $a_p$  refers to the cubic perovskite lattice parameter [49, 50, 51]. In this structure all the cobalt cations (mixture of  $\text{Co}^{2+}$  and  $\text{Co}^{3+}$  in 1:1 ratio) are enclosed within square base pyramids formed by -ve oxygen ligands. The same  $P4/mmm$  symmetry with a doubling along  $c$ -direction was found for the case when the  $\text{RBaCo}_2\text{O}_6$  is formed. Here the  $\text{Co}^{3+}$  and  $\text{Co}^{4+}$  in ratio 1:1 are present. The compounds with the highest oxygen content are, however, difficult or even not at all possible to synthesize. For the only known case of  $\text{LaBaCo}_2\text{O}_6$  neutron diffraction measurements revealed a cubic structure where the La and Ba cations are randomly distributed on the same site [52]. Particularly interesting are the compounds with  $\delta = 0.5$  where the Co ions nominally possess a charge of  $3^+$ . For this composition the  $\text{Co}^{3+}$  ions exist in the structure in two different environments, namely  $\text{CoO}_5$  square pyramids and  $\text{CoO}_6$  octahedra which create alternating chains. For intermediate oxygen compositions possible ordering of the oxygen vacancies can introduce crystallographic superstructures. As a rule, higher oxygen contents were obtained for the compounds with higher ionic radius of the rare earth cation R when prepared at the same conditions [19, 53]. Maignan et al [19] showed that synthesizing  $\text{RBaCo}_2\text{O}_{5+\delta}$  in air gives different oxygen contents for different R= Pr, Nd, Sm, Eu, Gd, Tb, Dy, and Ho. It was found that as the size of the lanthanide decreases, the oxygen content ( $5 + \delta$ ) decreases from  $\delta = 0.7$  for R= Pr and Nd to  $\delta = 0.4$  for R= Sm, Eu, Gd, and Tb to  $\delta = 0.3$  for R= Dy and Ho. In the two mostly studied classes of cobaltites  $(\text{RB})\text{CoO}_{3-\delta}$  and  $\text{RBCo}_2\text{O}_{5+\delta}$

R= different rare earth cations and B= Ca, Sr, Ba), structure, electrical and magnetic properties strongly depend not only on composition (R and B cations) but also on the oxygen content. Oxygen stoichiometry strongly affects the crystal structure and the magnetic properties and a controlled processing is needed if reproducible results have to be obtained. Structural and sometimes electronic transitions are reflected in an alteration of the lattice parameters.

### 1.6.2 Physical Properties

Valance and spin states of Co ion changes with oxygen content and temperature/pressure. As is known different spin states corresponds to different ionic radius of cobalt cations or to different bond lengths Co-O [54]. The fact that the Co ion can be stabilized in several different electronic configurations, plays a crucial role in magnetic and transport properties of layered perovskites. Therefore, questions concerning stability of different cobalt spin states and their influence on bulk physical properties are extremely important and still can not be fully answered. Spin states of cobalt in octahedral and square pyramidal site are in debate. Spin state of Co ions critically affects the magnetic properties of these compounds. As it is the magnetic properties of these layered cobaltites are quite complex and the compounds display both ferromagnetic and antiferromagnetic transitions [55, 56, 57]. Just below  $T_{MI}$  the compounds undergo a paramagnetic (PM) to ferro(ferri)magnetic (FM) transition followed by a FM to antiferromagnetic (AFM1) transition which is accompanied by an onset of strong anisotropic magneto-resistive effects. There is also an AFM1 to second antiferromagnetic (AMF2) phase transition. The



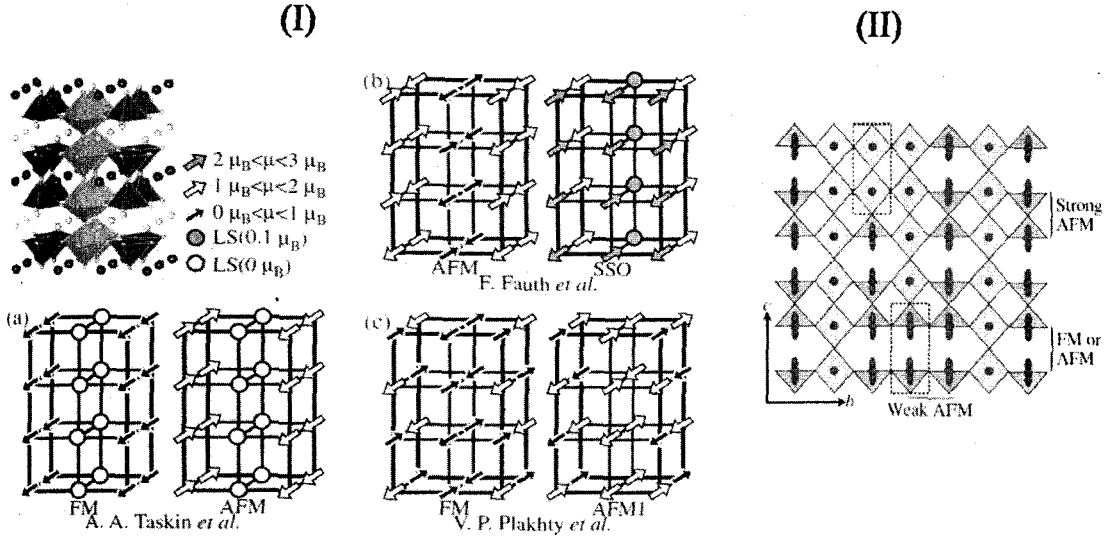


Figure 1.10: Magnetic models (I) Different magnetic models, (a) GdBaCo<sub>2</sub>O<sub>5.5</sub>, (b) NdBaCo<sub>2</sub>O<sub>5.47</sub>, TbBaCo<sub>2</sub>O<sub>5.5</sub>, (II) Small magnetic moment considered for LS octahedral Co ion which is ascribed to imperfect ordering of octahedra and square pyramids in PrBaCo<sub>2</sub>O<sub>5.5</sub>. Figures are taken from reference [55, 64].

mechanism of such magnetic transformations at low temperatures is still not properly understood. It is also not clear why subtle changes in oxygen content should cause drastic changes in magnetic properties [58, 59]. On the basis of neutron diffraction [60, 61, 62, 63] and macroscopic measurements [21], various contradicting magnetic structures, different spin states of Co<sup>3+</sup> ions as well as spin state ordering (SSO) have been proposed. Some of these structures are shown in Figure 1.10 (a) [64].

Neutron diffraction studies on PrBaCo<sub>2</sub>O<sub>5.5</sub> [55] reveal Co<sup>3+</sup> ions occupying square pyramidal sites to be in IS state and those occupying octahedral sites to be in LS state. Such an arrangement sustains two types of magnetic interactions along the *c*-axis, a strong AFM superexchange interaction between pyramidal Co ions that share an oxygen ion between them and a weak AFM direct exchange interaction between two pyramids connected through an oxide ion vacancy. However, the best fit to the experimental data considers [55]

a small magnetic moment for LS octahedral Co ion which is ascribed to imperfect ordering of octahedra and square pyramids in the compound (Figure 1.10 (b)). This surprising result is reconciled by invoking partial disorder in the arrangement of  $\text{CoO}_6$  octahedra and  $\text{CoO}_5$  square pyramids. Similar studies on  $\text{NdBaCo}_2\text{O}_{5.47}$  show that all Co ions in octahedral position cannot be in LS state for  $T \leq T_{MI}$ . Here, some of the octahedral Co ions undergoes first order HS to IS transition occurs at  $T_{MI}$ , followed by gradual IS-LS crossover when further cooling down [61]. Muon spin relaxation studies indicate that all square pyramidal Co ions are in IS spin state while Co at different octahedral sites have different spin states. In FM phase octahedral Co are in HS and IS state while in the AFM phase there is a spin state ordering (SSO) with octahedral Co ions in HS, IS and LS mixed state [56].

The cobaltites show metal insulator transition (MIT) above room temperatures. Unlike manganites the MIT takes place in the paramagnetic region followed by ferromagnetic ordering in the insulating phase. It was found that  $\text{YBaCo}_2\text{O}_{5.5}$  is the only compound for which the MIT coincides exactly with the onset of paramagnetic-ferromagnetic transition  $T_C$ . On the other hand, an application of an external magnetic field shifts  $T_C$  to higher temperatures without affecting  $T_{MI}$  [50]. Thus, different scenarios for the MIT were proposed involving a spin state ordering or a spin state transition [41, 53]. Additionally, it is believed that the MIT is presumably driven by a spin-state/orbital ordering of the  $\text{Co}^{3+}$  ions [65].

Layered cobaltites have also attracted a special interest due to their unusual behaviour

upon the application of external magnetic fields. Usually magnetoresistance (MR) is positive for AFM compounds and negative MR is a signal for ferromagnetic interactions. For  $\text{RBaCo}_2\text{O}_{5.4}$  (where  $\text{R} = \text{Gd, Eu}$ ) the effect was observed for the first time in 1997 by Martin et al. [41] who reported a giant negative magnetoresistance of about 10% in the presence of external magnetic field of seven tesla at  $T_{N1} = 240$  K. The temperature at which the GMR was observed coincides with a transition to antiferromagnetic ordering of the cobalt moments. An explanation of the GMR was given by Taskin et al. [42] who observed that in presence of external magnetic field the antiferromagnetic ordering enhances the resistivity, while the applied external magnetic field prevents establishing of the antiferromagnetic order. In the presence of a weakly coupled ferromagnetic ladders, an applied magnetic field aligns the FM ladders reducing the insulating gap and therefore an increase of the charge carriers.

The recent density functional calculations [66, 67] and resonant photoemission studies [68] suggest that there is a strong hybridization between O-2p and Co-3d orbitals with a narrow charge transfer gap near Fermi level. With increasing temperature, the  $pd\sigma$  hybridized hole in the O-2p valence band suffers a gradual delocalization leading to successive magnetic transitions and spin reorientations.

## 1.7 Motivation, Aim and Objectives

From the above, it is clear that physical properties of these layered cobaltites critically depend on the spin state of Co ion and the type of interactions between neighbouring

Co ions as a result of their spin states. The spin state of Co ion is directly controlled by oxygen stoichiometry as it not only affects the formal valence of Co ion ( $2^+ / 3^+ / 4^+$ ) but also its local environment (octahedral/square pyramidal). The second aspect that has an indirect effect on the spin state of Co ion is the diameter of the rare-earth ion [69]. The size of the rare-earth ion can affect the hybridization between nearest neighbour Co  $3d$  and O  $2p$ , which in turn affects the magnetic and transport properties of these materials. However, all the  $\text{RBaCo}_2\text{O}_{5.5}$  irrespective of the rare-earth ion have similar physical properties. Therefore a thorough study of these layered double perovskites by variation of oxygen stoichiometry and rare-earth size is necessary. In particular, it is important to understand the changes in local coordination of Co ion and its influence on the physical properties of resultant material. It is with this motivation the present work was taken up.

With the objective listed above, the aim of the thesis is

- to study the role of oxygen content on structural, magnetic and transport properties of Co-based double perovskites.
- to study the effect of rare earth size which plays an important role in stability of the structure.
- study the changes in local coordination of Co ion and understand its effect on physical properties of these materials.

To realise this aim, it was planned to study the physical properties of double per-

ovskites  $\text{RBaCo}_2\text{O}_{5.5}$ . Study the effect of variation of oxygen content in atleast two different series of layered perovskites  $\text{RBaCo}_2\text{O}_{5+\delta}$ . The two series chosen were  $\text{SmBaCo}_2\text{O}_{5+\delta}$  and  $\text{PrBaCo}_2\text{O}_{5+\delta}$ . These were chosen because (a) wide variation of oxygen content is possible in these materials. (b)  $\text{SmBaCo}_2\text{O}_{5+\delta}$  is reported to show slightly different properties as compared to other similar perovskites. (c) Study of Co K EXAFS is possible in  $\text{PrBaCo}_2\text{O}_{5+\delta}$  due to non interference of Pr L edges. All the samples studied here were prepared by sol-gel method. The oxygen content was carefully monitored by subjecting them to different final annealing treatment decided based on thermogravimetric analysis (TGA) studies. These materials were characterized and studied by several techniques for their structural, magnetic, transport and spectroscopic properties.

The thesis is divided in eight chapters. The main principle and instrumentation of the techniques used is briefly described in Chapter 2. Chapter 3 to 7 describe the results of our studies on different  $\text{RBaCo}_2\text{O}_{5+\delta}$  while Chapter 8 gives a brief summary of the work done and scope for future work.

# References

- [1] Zener C 1951 *Phys. Rev.* **81** 440
- [2] Zener C 1951 *Phys. Rev.* **82** 403
- [3] Goodenough J B 1958 *J. Phys. Chem. Solids* **6** 287
- [4] Jonker G H and Van Santen J H 1953 *Physica* **19** 120
- [5] Mott N F 1949 *Proc. Phys. Soc. London A* **62** 416
- [6] Dagotto E 2005 *Science* **309** 257
- [7] Goodenough J B 2004 *Rep. Prog. Phys.* **67** 191593
- [8] Davies P K, Wu H, Borisevich A Y, Molodetsky I E, and Farber L 2008 *Annu. Rev. Mater. Res.* **38** 369-401
- [9] Goldschmidt V M 1926, 1927 *Geochemische Verteilungsgesetze der Elemente 8: Untersuchungen über Bau und Eigenschaften von Krystallen. Norsk. Vid. Akad., Math.-Naturvid Kl* **8**
- [10] King G and Woodward P M 2010 *Mater. Chem.* **20** 578596

- [11] de Souza E C C and Muccillo R 2010 *Materials Research* **13** 385-394 and references therein
- [12] Maekawa S et al. 2004 *Physics of Transition Metal Oxides* Berlin:Springer
- [13] Wu M K, Ashburn J R, Torng C J, Hor P H, Meng R L, Gao L, Huang Z J, Wang Y Q, and Chu C W 1987 *Phys. Rev. Lett.* **58** 908
- [14] Chu C W, Gao L, Chen F, HUANG Z J, Meng R L and Xue Y Y 1993 *Nature* **365** 323 - 325
- [15] Raveau B, Maignan A, Martin C, and Hervieu M 1998 *Chem. Mater.* **10** 2641-2652
- [16] Nakatsuji S and Maeno Y 2000 *Phys. Rev. Lett.* **84** 2666
- [17] Takada K et al. 2003 *Nature* **422** 53
- [18] Briceño G et al. 1995 *Science* **270** 273
- [19] Maignan A et al. 1999 *J. Solid State Chem.* **142** 247
- [20] Jirák Z et al. 2008 *Phys. Rev. B* **78** 014432
- [21] Taskin A A, Lavrov A N, Ando Y 2006 *Phys. Rev. B* **73** 121101(R)
- [22] Teraoka Y, Nobunaga T, Okamoto K, Miura N, and Yamazoe N 1991 *Solid State Ionics* **48**:207
- [23] Kruidhof H, Bouwmeester H J M, van Doorn R H E, and Burggraaf A J 1993 *Solid State Ionics* **63-65**:816

- [24] Madelung O 1978 *Introduction to Solid-State Theory* Springer-Verlag Berlin Heidelberg
- [25] Kramers H A 1934 *Physica* **1** 182
- [26] Anderson P W 1950 *Phys. Rev.* **79** 350
- [27] Anderson P W 1950 *Phys. Rev.* **80** 922
- [28] Anderson P W and Hasegawa H 1955 *Phys. Rev.* **100** 675
- [29] de Gennes P G 1960 *Phys. Rev.* **118** 141
- [30] Blundell S 2001 *Magnetism in Condensed Matter* Oxford University Press, New York
- [31] Schiffer P, Ramirez A P, Bao W, and Cheong S W 1995 *Phys. Rev. Lett.*, **75** 3336
- [32] Ramirez A P 1997 *J. Phys.: Condens. Mat* **9** 8171
- [33] Rao C N R, Arulraj A, Santosh P N, and Cheetham A K 1998 *Chem. Mater.* **10** 2714
- [34] González-Calbet J M, Herrero E, Rangavittal N, Alonso J M, Martínez J L, and Vallet-Regí M 1999 *J. Solid State Chem.* **148** 158
- [35] Kanamori J 1959 *J. Phys. Chem. Solids*, **10** 87
- [36] Goodenough J B 1995 *Phys. Rev. B* **100** 564



- [37] Meinert M, Schmalhorst J M and Reiss G 2010 *Appl. Phys. Lett.* **97** 012501
- [38] Jrgensen J E and Keller L 2008 *Eur. Phys. J. B* **66** 445
- [39] Reehuis M, Ulrich C, Pattison P, Miyasaka M, Tokura Y and Keimer B 2008 *Eur. Phys. J. B* **64** 27
- [40] Fauth F, Suard E, Caignaert V, Domengès B, Mirabeau I and Keller L 2001 *Eur. Phys. J. B* **21** 163
- [41] Martin C, Maignan A, Pelloquin D, Nguyen N, and Raveau B 1997 *Appl. Phys. Lett.* **71** 1421
- [42] Taskin A A, Lavrov A N and Ando Y *Phys. Rev. Lett.* 2003 **90** 227201
- [43] Liao D, Lees M R, Balakrishnan G and Paul D McK 2010 *J. Phys. Conf. Ser.* **200** 012104
- [44] Raveau B, Seikh MD M, Pralong V and Caignaert V 2009 *Bull. Mater. Sci.* **32** 305
- [45] Frontera C, Garcia-Muoz J L, Llobet A, Aranda M A G, Rodriguez-Carvajal J, Respaud M, Broto J M, Raquet B, Rakoto H and Goiran M 2001 *Journal of Alloys and Compounds* **468** 323-324
- [46] Wang W, Peh T S, Chan S H and Zhang T S, 2009 *ECS Transactions* **25** 2277
- [47] Chavez E, Mueller M, Mogni L and Caneiro A 2009 *J. Phys. Conf. Ser.* **167** 012043
- [48] Fauth F, Suard E and Caignaert V 2001 *Phys. Rev. B* **65** 060401

- [49] Vogt T, Woodward P M, Karen P, Hunter B A, Henning P and Moodenbaugh A R, 2000 *Phys. Rev. Lett.* **84** 2969
- [50] Akahoshi D and Ueda Y 2001 *J. Solid State Chem.* **156** 355
- [51] Suard E, Fauth F, Caignaert V, Mirebeau I and Baldinozzi G 2000 *Phys. Rev. B* **61** R11871
- [52] Suard E, Fauth F and Caignaert V 2000 *Physica B* **254** 276
- [53] Roy S, Dubenko I S, Khan M, Condon E M , Craig J, Ali N, Liu W and Mitchell B S 2005 *Phys. Rev. B* **71** 024419
- [54] Raccah P M and Goodenough J B 1967 *Phys. Rev. B* **155** 932
- [55] Frontera C, Luis J, Muoz G, and Carrillo A E, Aranda M A G, Margiolaki I and Caneiro A 2006 *Phys. Rev. B* **74** 054406
- [56] Lutkenes H, Stingaciu M, Pashkevich Yu G, Conder K, Pomjakushina E, Gusev A A, Lamonova K V, Lemmens P, and Klauss H H 2008 *Phys. Rev. Lett* **101** 017601
- [57] Frontera C, García-Muñoz J L and Carrillo A 2004 *Phys. Rev. B* **70** 184428
- [58] Kim W, Chi E, Choi H, Hur N, Oh S, and Ri C 2000 *Solid State Commu.* **116** 609
- [59] Burley J, Mitchell J F, Short S, Millar D and Tang Y 2003 *J. Solid State Chem.* **170** 339

- [60] Frontera C, García-Munoz J L, Castaño O, Ritter C and Caneiro A 2008 *J. Phys:Cond Matter* **20** 104228
- [61] Fauth F, Suard E, Caignaert V, and Mirebeau I 2002 *Phys. Rev. B* **66** 184421
- [62] Plakhty V, Chernenkov P, Barilo S, Podlesnyak E, Pomjakushina E, Moskvina E and Gavrilov S 2005 *Phys. Rev. B* **71** 214407
- [63] Soda M, Yasui Y, Ito M, Iikubo S and Sato M 2003 *J. Phys. Soc. Japan* **72** 1729
- [64] Soda M, Yasui Y, Kobayashi Y, Fujita T, Sato M and Kakurai K 2006 *J. Phys. Soc. Jpn.* **175** 104708
- [65] Zhao G, Conder K, Keller H and Müller K A 1996 *Nature* **381** 676
- [66] Wu H 2001 *Phys. Rev. B* **64** 92413
- [67] Wu H 2003 *J. Phys.: Condens. Matter* **15** 503
- [68] Flavell W, Thomas A, Tsoutsou D, Mallick A, North M, Seddon E, Cacho C, Malins A, et al 2004 *Phys. Rev. B* **70** 224427
- [69] Raveau B 2008 *Phil. Trans. R. Soc. A* 366
- [70] Fletcher S 2010 *J. Solid State Electrochem.* **14** 705-739
- [71] Bodner G M : <http://chemed.chem.purdue.edu/genchem/topicreview/bp/ch12/crystal.php>.
- [72] Conder K, Podlesnyak A, Pomjakushina E and Stingaciu M 2007 *Acta. Phys. Pol. A* **111** 7-14

# Chapter 2

## Experimental Techniques

*Different experimental methods contribute in making progress in research and only the combination of all of them will lead to unambiguous results.*

### 2.1 Introduction

This chapter describes all the experimental techniques which are used in this research with regard to the study of cobalt based double perovskites. Alongwith the sample preparation technique, the method adopted for measurements, basic principle involved and the instruments used for all the experiments, are discussed below. In particular, to study the crystal structure, technique like X-ray diffraction was used. The transport and magnetic properties were investigated using four-probe resistivity and magnetization as a function of temperature and magnetic field. In order to gain an insight into changes occurring in the local structure of constituent atoms, spectroscopic measurements like Infra-red, Raman and X-ray absorption fine structure (XAFS) spectroscopic studies have been undertaken.

## 2.2 Sample Preparation Technique

There are several techniques available that allow obtaining single-phase double perovskite samples. One can use wet chemistry methods (sol-gel) or solid-state reaction method for preparation of these materials. The physical properties of the samples synthesized with different methods can differ. The disadvantage of solid state reaction method is as it based on heat and beat technique, which needs high temperature. Hence sol-gel method is applied for more homogeneity and low temperature synthesis. The properties of these cobaltites not only depend on oxygen content but also on the synthesis history [1].

### 2.2.1 Sol-Gel Method

All the polycrystalline samples were synthesized by sol-gel method. Stoichiometric amounts of rare-earth oxides,  $\text{BaCO}_3$  and  $\text{Co}_2(\text{NO}_3)_2 \cdot 6\text{H}_2\text{O}$  were dissolved in nitric acid. Citric acid was added to the above solution as a complexing agent. The solution was then heated at 353 K to form a gel which was subsequently dried at 433 K to remove the solvent. The precursor thus obtained was ground, pelletized and heated at 1073 K for 4 hours followed by annealing at 1323 K for 24 hours and “slow cooling” at the rate of  $1^\circ\text{C}/\text{min}$  to room temperature to get the required sample. This as-prepared sample is used to prepare another member of the respective rare earth series in different atmosphere and temperature to get desire oxygen content  $(5 + \delta)$ . “Very slow cooling” ( $0.2^\circ\text{C}/\text{min}$ ) rate used to get higher  $\delta$ . Table 2.1 gives the details of annealing conditions and temperatures. The value of  $\delta$  given Table 2.1 were determined from iodometric analysis

which will be discussed in detailed later in this chapter.

Table 2.1: Final annealing temperature and annealing atmosphere used in preparation of  $\text{RBaCo}_2\text{O}_{5+\delta}$  compounds. The oxygen content ( $5 + \delta$ ) determined from iodometric titration. The  $\delta$  values are also reported.

Sample name	Final annealing condition	$\delta$ ( $\pm 0.01$ )
$\text{PrBaCo}_2\text{O}_{5.50}$	1073 K, 36h Ar, Ice Quench	0.50
$\text{NdBaCo}_2\text{O}_{5.56}$	873 K, 36h Ar, Ice Quench	0.56
$\text{SmBaCo}_2\text{O}_{5.55}$	1323 K, 24h Air, Slow Cooled	0.55
$\text{GdBaCo}_2\text{O}_{5.50}$	1323 K, 24h Air, Slow Cooled	0.50
$\text{YBaCo}_2\text{O}_{5.51}$	1323 K, 24h Oxygen, Slow Cooled	0.51
$\text{PrBaCo}_2\text{O}_{5.80}$	1323 K, 24h Air, Slow Cooled	0.80
$\text{PrBaCo}_2\text{O}_{5.67}$	673 K, 36h Ar, Ice Quench	0.67
$\text{PrBaCo}_2\text{O}_{5.58}$	873 K, 36h Ar, Ice Quench	0.58
$\text{PrBaCo}_2\text{O}_{5.43}$	1173 K, 36h Ar, Ice Quench	0.43
$\text{PrBaCo}_2\text{O}_{5.35}$	1073 K, 36h Ar, Ice Quench(twice)	0.35
$\text{SmBaCo}_2\text{O}_{5.65}$	973 K, 36h Oxygen, Very Slow Cooled	0.65
$\text{SmBaCo}_2\text{O}_{5.60}$	873 K, 36h Oxygen, Very Slow Cooled	0.60
$\text{SmBaCo}_2\text{O}_{5.39}$	873 K, 36h Ar, Ice Quench	0.39
$\text{SmBaCo}_2\text{O}_{5.12}$	1173 K, 36h Ar, Ice Quench	0.12

## 2.3 X-ray Diffraction(XRD)

X-rays have wavelength ( $\lambda$ ) in the range from 0.1-10 Å which, correspond to typical values of interatomic distances. This makes the X-rays an ideal probe to study the crystal structure of materials. When a beam of X-rays passes through a screen containing a regular pattern of slits, interference phenomenon is observed if the distance between successive slits is of the same order as the wavelength of the incident X-rays. According to the Bragg, X-ray diffraction(XRD)[2] of the crystal is the reflection obtained from the ordered atomic planes of the crystal as seen in the Figure 2.1.

For constructive interference of the scattered X-rays (the appearance of a diffraction

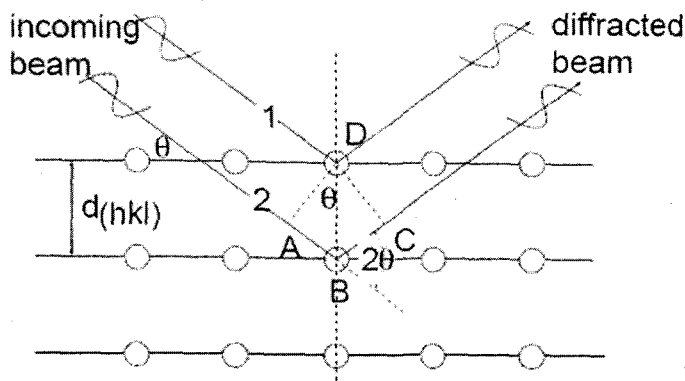


Figure 2.1: The Bragg condition,  $2d\sin\theta = n\lambda$ .

peak) it is required that the beams, scattered on successive planes, be in phase (have again a common wave front) after they leave the surface of the crystal. In terms of the beams labelled 1 and 2 in Figure 2.1 requires that the distance  $\vec{AB} + \vec{BC}$  be equal to an integral number of wavelengths of the incident radiation. Accordingly:

$$\vec{AB} + \vec{BC} = n\lambda \quad (2.1)$$

Where  $n = 1, 2, 3..$

Since  $\vec{AB} = \vec{BC}$  and  $\sin\theta = \frac{\vec{AB}}{d_{hkl}}$

$$n\lambda = 2d_{hkl}\sin\theta \quad (2.2)$$

This relation is referred to as Bragg's Law and describes the angular position of the diffracted beam in terms of  $\lambda$  and  $d_{hkl}$ . In most instances of interest we deal with first order diffraction ( $n = 1$ ) and, accordingly, Bragg's law is:

$$\lambda = 2d_{hkl}\sin\theta \quad (2.3)$$

X-ray diffraction measurements can be carried out on the polycrystalline (powder) samples or single crystals. The XRD pattern is a plot of the intensity of diffracted rays

versus Bragg angle and contains information about the structure and composition of the material. This information needs to be extracted from the pattern by employing a proper analysis procedure. In the present study, the powder method is made use of wherein the samples were crushed into fine powder in an agate pestle and mortar and placed in a beam of monochromatic X-rays. The measurements are performed on powder samples thus prepared using an in house Rigaku D-MaxIIIC X-ray diffractometer system. The intensity of the copper  $K_{\alpha}$  ( $\lambda = 1.5418 \text{ \AA}$ ) radiation diffracted from the powdered specimen was detected by a scintillation counter and recorded as a function of  $2\theta$ , where  $\theta$  is the angle of incidence. The patterns were recorded in continuous mode in the  $2\theta$  range of  $20^{\circ} \leq 2\theta \leq 80^{\circ}$  with a step size of  $0.02^{\circ}$  at a speed of  $1^{\circ}/\text{min}$ . The X-ray diffraction patterns were Rietveld refined using FULLPROF suite for phase purity and structural parameters were obtained. The starting parameters were taken from those reported from neutron diffraction measurements [3]. The parameters like scale, background, lattice parameter and atomic positions of Co, Ba and R(rare earth) were varied while that of oxygen positions were fixed. Total 13 parameters were varied. Typical values of R factors and chi square obtained.

## 2.4 Thermogravimetric analysis

Thermogravimetric analysis (TGA) is an analytical technique used to determine a material's thermal stability and its fraction of volatile components by monitoring the weight change that occurs as a specimen is heated. The measurement is normally carried out in



air or in an inert atmosphere, and the weight is recorded as a function of increasing temperature. TGA experiments were carried out using vertical type Shimadzu's DTA+TGA model No DTA60.

### 2.4.1 TGA Measurements

The sample is heated in a reducing atmosphere and the change in its mass is recorded. This weight loss corresponds to the weight of volatile components. Here we have used this method to estimate the heat treatment required to be given to a cobaltite sample in order to modulate its oxygen content. The method can be used for all the cobaltites, independent on the average cobalt valence in the starting material.

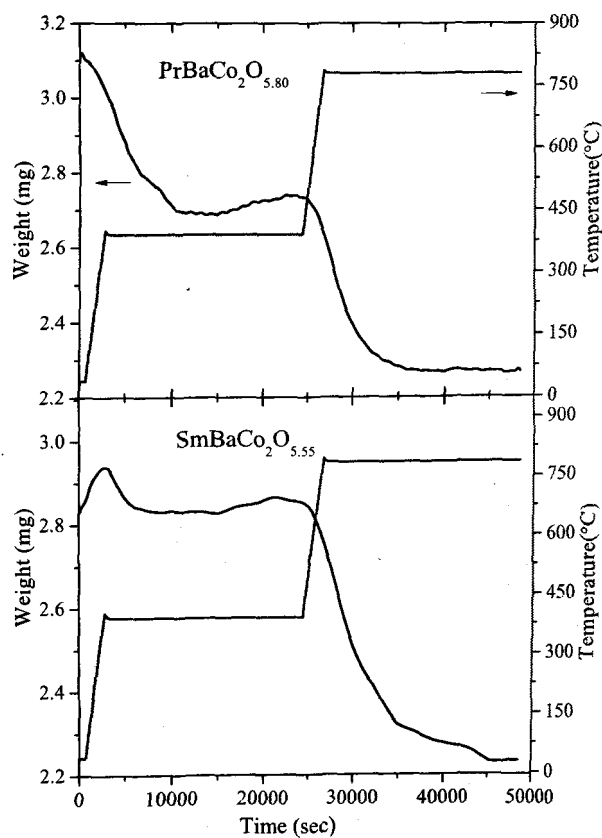


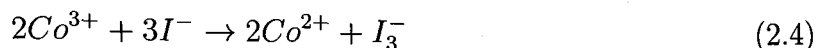
Figure 2.2: TGA curves for  $\text{PrBaCo}_2\text{O}_{5.80}$  and  $\text{SmBaCo}_2\text{O}_{5.55}$ .

In order to ascertain the nature of heat treatment required to control oxygen content ( $5 + \delta$ ), TGA of the air annealed sample was carried out in nitrogen atmosphere. Figure 2.2 shows weight loss as function of time and along with heating schedule used. The sample was heated from room temperature to  $400^\circ\text{C}$  at the rate of  $10^\circ\text{C}$  and held there for 6 hrs, again heated at the same rate to  $800^\circ\text{C}$  and held there again for another 6 hrs. From the observed weight loss oxygen content of  $\text{PrBaCo}_2\text{O}_{5.80}$  at  $400^\circ\text{C}$  after 6 hrs was estimated to be 5.4(1) and at  $800^\circ\text{C}$  after 6 hrs was 4.9(1). In case of  $\text{SmBaCo}_2\text{O}_{5.55}$  at  $400^\circ\text{C}$  after 6 hrs there was not much change observed in weight loss while at  $800^\circ\text{C}$  after 6 hrs was 5.1(1). From this analysis, final heat treatment to be given to a sample was decided and is presented earlier in Table 2.1

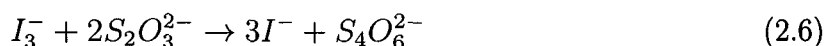
## 2.5 Iodometric Titration

The most accurate methods for establishing the precise oxygen contents of transition metal oxides are all based on redox reactions. In these methods, the high-valent cation(s) of the studied sample are reduced by a suitable reductant, e.g.  $\text{I}^-$ ,  $\text{Fe}^{2+}$ ,  $\text{Cu}^+$  or  $\text{H}_2$ , followed by the determination of the exact amount of reductant left over or the oxidized form of the reductant formed, or even the weight change related to the reduction reaction, using an appropriate analysis technique. Iodometry, also known as iodometric titration, is a method of volumetric chemical analysis, a redox titration where the appearance or disappearance of elementary iodine indicates the end point. By dissolving the  $\text{LnBaCo}_2\text{O}_{5+\delta}$  sample in dilute hydrochloric acid (1M HCl) containing potassium iodide (solid KI) the

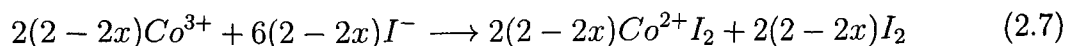
following reduction-oxidation reactions are taking place:

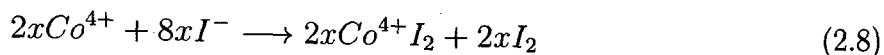


Thus, the oxygen content in the cobaltate's structure, balances the  $Co^{3+}$  and  $Co^{4+}$  charge and can be calculated from the obtained amount of iodine. The amount of liberated iodine is determined by titration with sodium thiosulfate:

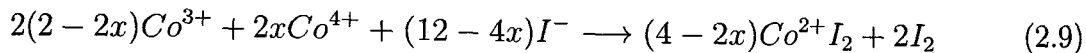


The sample (15-20 mg) is dissolved in a two-step process. After the sample is placed in a conical flask, 1 g solid KI is added. After a few minutes 25 ml of 1 M HCl is added to dissolve the sample. At this stage the air from the conical flask over KI solution is removed by adding 1 g  $NaCO_3$  producing  $CO_2$  gas. The liberated iodine (Eqs. 2.4 and 2.5) is titrated with 0.01 mol/l  $Na_2S_2O_3$  using 10 ml microburet ( $\pm 0.02$  ml), all the time keeping the conical flask under inert atmosphere. Sodium thiosulfate has been always standardized against  $KIO_3$  before each series of titration. The end-point of the titration is detected using a starch-indicator, introduced to the solution just before the end of the titration. All the reagents used were of the analytical grade. In blank titration (without the sample) it was checked that in our experiments atmospheric oxygen does not influence the results. The oxygen content were obtained using formula as given below.

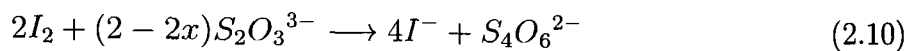




Adding and simplifying above two equations, we get



$I_2$  thus liberated will react with thio to give



From the above equations a formula was derived to calculate oxygen content  $\delta$  using molecular weight(MW) of  $RBaCo_2O_{5.5}$  is:

$$\delta = \frac{(MW)vy - 2w}{2w - 15.999vy} \quad (2.11)$$

Where,

$y$  = Normality of thio sulphate solution (N)

$w$  = weight of sample in mg

$v$  = Volume of added titrant (ml)

Oxygen content of each of the prepared sample was determined as an average value of at least three titrations. The values obtained were accurate within an error bar of  $\pm 0.01$ . All compounds are henceforth referred with final values of oxygen content obtained from iodometric titration.

## 2.6 Magnetometry

The Magnetization experiments have been performed on all the samples as a function of temperature and magnetic field. The measurements were made using Superconduct-

ing Quantum Interference Device (SQUID) magnetometer and an 14T Vibrating sample magnetometer (VSM). The basic principle for both the magnetometers is given below.

### 2.6.1 Vibrating Sample Magnetometer

The vibrating sample magnetometer(VSM) is very versatile and sensitive. It may be used for measurements on both weakly and strongly magnetic substances, and standard versions can detect a magnetic moment of about  $10^5$  emu = erg/Oe or  $10^8$  A-m<sup>2</sup>. The vibrating sample method which may be regarded as kind of partial extraction method, is very common. It is based on the flux change in a coil when a magnetized sample is vibrated near it. The sample, commonly a small disk, is attached to the end of a non-magnetic rod, the other end of which is fixed to a loudspeaker cone Figure 2.3 or to some other kind of mechanical vibrator.

The oscillating magnetic field of the moving sample induces an alternating emf in the detection coils, whose magnitude is proportional to the magnetic moment of the sample. The (small) alternating emf is amplified, usually with a lock-in amplifier which is sensitive only to signals at the vibration frequency. The lock-in amplifier must be provided with a reference signal at the frequency of vibration, which can come from an optical, magnetic, or capacitive sensor coupled to the driving system. The detection-coil arrangement shown in Figure 2.3 is only one of several possible ones described by Foner, all of which involve balanced pairs of coils that cancel signals due to variation in the applied field. The coil arrangement of Figure 2.3 is very commonly used. The apparatus is calibrated with a specimen of known magnetic moment, which must be of the same size and shape as the

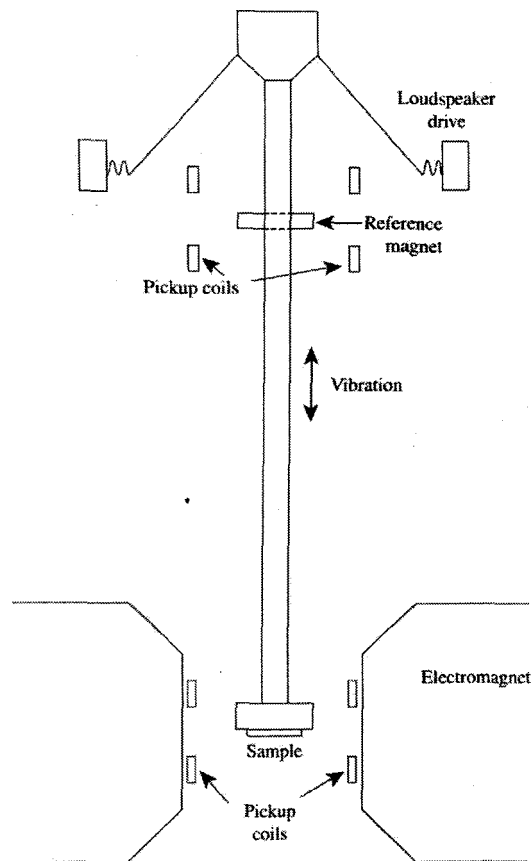


Figure 2.3: Vibrating Sample Magnetometer [5].

sample to be measured, and should also be of similar permeability.

## 2.6.2 SQUID Magnetometer

Superconducting Quantum Interference Devices (SQUID) are the most sensitive detectors of magnetic flux available. A SQUID is in essence, a flux to voltage transducer, providing an output voltage that is periodic in applied flux with a period of one flux quantum,  $\Phi_0 = h/2e \approx 2.07 \times 10^{-15} \text{Wb}$ . One is generally able to detect an output signal corresponding to a flux change much less than  $\Phi_0$ . A typical SQUID instrument is depicted in Figure 2.4.

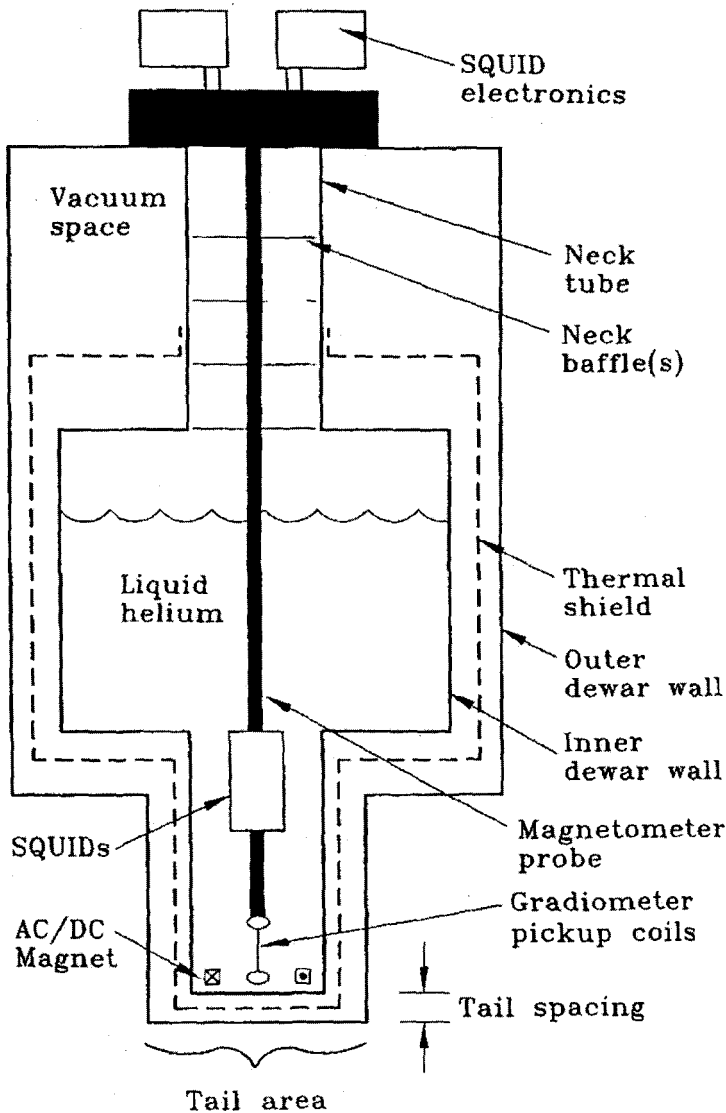


Figure 2.4: A cross-sectional schematic of a simple low- $T_c$  SQUID system. The SQUID and input coil are housed in a superconducting niobium cylinder; they are inductively coupled to an axial gradiometer near the tail of the Dewar. The flux-locked loop is housed in the SQUID electronics box above the Dewar and linked to the SQUID through the magnetometer probe. The Dewar is filled with liquid helium (boiling point 4.2 K) to cool the superconducting SQUID, niobium canister, and pickup coils. The Dewar is insulated by a vacuum space between the inner and outer walls. The instrument may be used to sense the intrinsic magnetic field of a sample or, with the magnet energized, it can measure the response of the sample to an ac or a dc magnetic field. [4]

### 2.6.3 Magnetization Measurements

Quantum Design 7T MPMS SQUID magnetometer and 14T PPMS VSM magnetometer is used to carry out the magnetic measurements. The sample was cooled at 10 K in zero applied field. Magnetization  $M(T)$  was recorded while warming under an applied field (zero-field cooled (ZFC)) and subsequent cooling field-cooled cooling (FCC) and warming (FCW) cycles in the temperature range 10-300 K. The isothermal magnetization  $M(H)$  is recorded at various temperatures in the field of  $\pm 7T$  or  $\pm 14T$ . The care has been taken while reducing field that the program set to oscillatory zero to achieve minimum remnant field.

## 2.7 Electrical Transport Properties : Resistivity Measurements

One of the most important properties of a material is its resistivity which for a given material is affected by many factors. The quantitative measure of this property is of great importance, the actual resistance of a material depends on its shape and its resistivity.

For a material of uniform cross-section, resistivity  $\rho$  is given by the equation

$$\rho = \frac{RA}{l} \quad (2.12)$$

where  $R$  is the resistance of the sample,  $A$  is the cross-section area and  $l$  is the length across which current is passed. Resistivity measurements on all the samples were done by conventional D.C. four probe technique in the temperature interval of 10 K to 325 K using a Closed Cycle Refrigerator(CCR). General description of CCR is as below:



Janis closed cycle refrigerator (CCR) system provides a convenient means of cooling samples to temperatures below 10 K, and can be used to perform a wide variety of optical and electrical experiments between  $\sim 10$  K and 325 K. CCR system requires no liquid helium or liquid nitrogen as a source of cooling. Instead, a closed loop of helium gas is compressed and expanded, based on the Gifford-McMahon (G-M) thermodynamic cycle. During the expansion phase of each cycle, heat is removed from the cold finger, on which the sample is mounted. A heater and thermometer are installed on the cold finger and are used to precisely control the sample temperature [5].

The resistivity setup developed in the Department uses a Keithley 224 Constant Current Source to pass a desired current through the outer two contacts on the sample. The potential developed across the sample is measured using a Keithley 2182 Nanovoltmeter. The temperature was measured using a calibrated Si diode with an accuracy of 0.01K using a Lakeshore 325 temperature controller. All the instruments were interfaced using a Keithley IEEE 488 card (CEC 488PC) with a PC. A program written in QBASIC was used to collect the data and store it on the hard disk. The basic flow diagram of the program is given in Figure 2.5.

The controller (PC) through the IEEE card instructs the temperature controller to raise the temperature of the system to a predetermined temperature (set point). A sufficiently long delay is given in the program so that the temperature of the system stabilizes to the set point. Then it instructs the constant current source to pass the predetermined current through the sample and the voltage developed is measured by

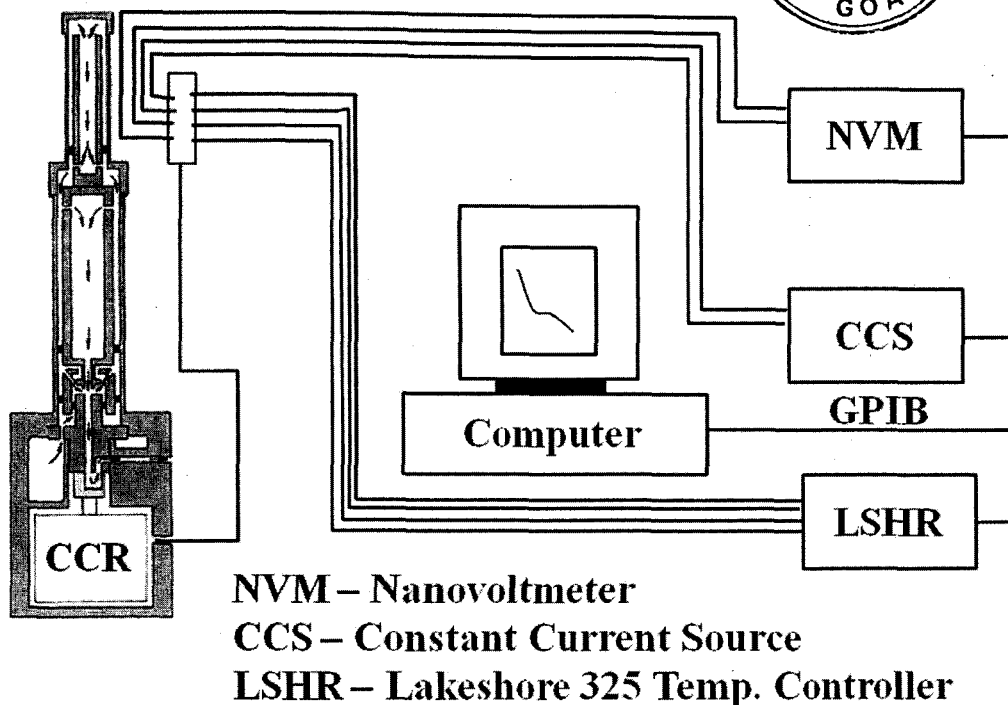


Figure 2.5: Basic flow diagram of resistivity measurement setup

the voltmeter. The direction of the current is reversed and the voltage is measured again. The reversal of the current is done to take care of the thermoelectric voltages or rectification developed across the sample due to inhomogeneities, rectifying boundaries or other defects. The basic flow diagram is shown in Figure 2.5

### 2.7.1 Resistivity and Magnetoresistance Measurements

Resistivity ( $R(T)$ ) was measured in zero and 8T applied fields in the temperature range 300 K - 10 K during cooling and warming cycles. Magnetotransport studies were carried out in longitudinal geometry using OXFORD Spectromag 10T magnet. Resistance as a function of temperature  $R(T)$  was measured in the range 10 K - 300 K in 0T and 8T during warming and cooling cycles. Isothermal magneto-resistance (MR) was measured at selected temperatures by ramping the field in the range  $\pm 8T$ .

## 2.8 Infra-red and Raman Spectroscopic Measurements

After absorption of radiation, the molecules of the chemical substance vibrate at many rates of vibration giving rise to closely packed absorption bands called as IR or Raman absorption spectra. Absorption of low energy radiation is restricted to compounds with small energy differences in the possible vibrational and rotational states. Vibrations fall into two main categories of stretching and bending. Bond lengths and bond angles are continuously changing due to these vibrations.

For a molecule to absorb IR, the vibrations or rotations within the molecule must cause a net change in the dipole moment of the molecule. To generate the IR spectrum, radiation containing all frequencies in the IR region is passed through the sample. The molecule absorbs specific frequency of radiation. IR radiation can only be absorbed by the bonds within the molecule, if the radiation has exactly the right amount of energy to induce vibrations of the bond, thus causing a change in the amplitude of molecular vibrations. This is the reason only specific frequencies are absorbed. The frequencies which are absorbed appear with decreased intensity in the detected signal.

In case of Raman effect, a change in the molecular polarization potential-or amount of deformation of the electron cloud-with respect to the vibrational coordinate is required for a molecule to exhibit a Raman effect. The amount of the polarizability change will determine the Raman scattering intensity. The pattern of shifted frequencies is determined by the rotational and vibrational states of the sample.

IR spectra recorded on FTIR-8900 Shimadzu spectrophotometer with Oxford OP-TIDIVA Cryostat with KRS5 window in the temperature range of 80 K to 375 K. The samples were prepared by mixing finely ground powders of sample and dried KBr in 1:150 ratio and pelletizing this mixture in 20mm diameter thin disks. The spectra were recorded in absorption mode and the deconvolution of IR peaks were done using Origin7 software.

HORIBA JOBIN YVON HR-800 Raman spectrometer with 488nm laser was used for Raman spectrometry in the temperature range 80 K-350 K. The sample chamber is flushed with nitrogen vapour for 30min to ensure the removal of air. The surface of the sample was etched just before its exposure to LASER beam.

## **2.9 X-ray Absorption Fine Structure Spectroscopy**

X-ray Absorption Fine Structure commonly known as XAFS is a technique employed to study the local environment of the atoms in a crystal. When a high energy X-ray photon is absorbed, a core level electron is ejected if the incident energy of the photons exceeds its binding energy. This causes a sharp dip in the transmitted intensity which is called as "absorption edge". XAFS refers to modulations in x-ray absorption coefficient around an x-ray absorption edge. The outgoing photo-electron can be thought of as a spherical wave expanding in all directions. When such a wave reaches the neighbouring atoms, it will be partially back-scattered. The back-scattered wave interferes with the outgoing electron wave causing a constructive or destructive interference. The net effect is the

modulation of the transmitted X-rays through the absorber upto about 1000 eV from the absorption edge. The interference pattern depends mainly on the number, nature and distance of the surrounding atoms. Thus XAFS proves to be a useful tool for the study of the atoms in a solid. XAFS spectra are especially sensitive to the formal oxidation state, coordination chemistry, and the distances, coordination number and species of the atoms immediately surrounding the selected element. Because of this dependence, XAFS provides a practical, and relatively simple, way to determine the chemical state and local atomic structure for a selected atomic species. XAFS can be used in a variety of systems and bulk physical environment.

XAFS is often divided (somewhat arbitrarily) into “EXAFS” (Extended X-ray Absorption Fine Structure) and “XANES” (X-ray Absorption Near Edge Structure). The physical origin of EXAFS and XANES is basically the same, but several simplifying approximations are applicable in the EXAFS range, which permits a simpler quantitative analysis. XANES and EXAFS provide complementary information.

### 2.9.1 The Process of X-ray Absorption

The interaction of X-rays with matter results in a number of interesting phenomena such as, scattering, photoelectron absorption, pair production (in the case of X-rays of energy  $> 1.02$  MeV), secondary emission, Auger emission etc. The analysis of the attenuation, therefore requires, the segregation of the various processes involved, of which the photoelectric absorption is usually the most important and is referred to as the true absorption. X-rays are light with energies ranging from  $\sim 500$  eV to 500 keV, or

wavelengths from  $\sim 25 \text{ \AA}$  to  $0.25 \text{ \AA}$ . At this energy regime, light is absorbed by all matter through the photo-electric effect. In this process, an x-ray photon is absorbed by an electron in a tightly bound quantum core level (such as the  $1s$  or  $2p$  level) of an atom

Figure 2.6

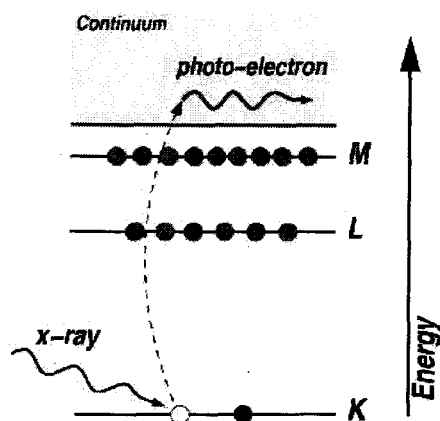


Figure 2.6: The photoelectric effect, in which an x-ray is absorbed and a core-level electron is promoted out of the atom.

In order for a particular electronic core level to participate in the absorption, the binding energy of this core level must be less than the energy of the incident x-ray. If the binding energy is greater than the energy of the x-ray, the bound electron will not be perturbed from the well-defined quantum state and will not absorb the x-ray. If the binding energy of the electron is less than that of the x-ray, the electron may be removed from its quantum level. In this case, the x-ray is destroyed (i.e., absorbed) and any energy in excess of the electronic binding energy is given to a photo-electron that is ejected from the atom.

When discussing x-ray absorption, we are primarily concerned with the absorption coefficient,  $\mu$  which gives the probability that x-rays will be absorbed according to Beer's

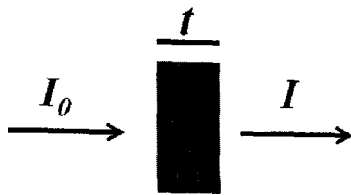


Figure 2.7: The incident x-ray beam ( $I_0$ ) passing through a material of thickness  $t$ .

Law:

$$I = I_0 e^{-\mu t} \quad (2.13)$$

where  $I_0$  is the x-ray intensity incident on a sample,  $t$  is the sample thickness, and  $I$  is the intensity transmitted through the sample, as shown in Figure 2.7. For x-rays, as for all light, the x-ray intensity is proportional to the number of x-ray photons.

At most x-ray energies, the absorption coefficient  $\mu$  is a smooth function of energy, with a value that depends on the sample density  $\rho$ , the atomic number  $Z$ , atomic mass  $A$ , and the x-ray energy  $E$  roughly as:

$$\mu \approx \frac{\rho Z^4}{AE^3} \quad (2.14)$$

## 2.9.2 XAFS Measurements

All XAFS measurements on Co  $K$ -edge in this thesis were carried out using in transmission mode in the temperature range 20 K-325 K using the beamline BL7C at the Photon Factory, Tsukuba, Japan. The synchrotron energy ranges from 2-2.5 GeV with injection current of ranges from 430 to 440 mA. This beamline is equipped with a double-crystal monochromator. Wide horizontal acceptance, 4 mrad, can be realized by using sagittal focusing when Si(111) crystal is used. Vertical focusing can be achieved by using

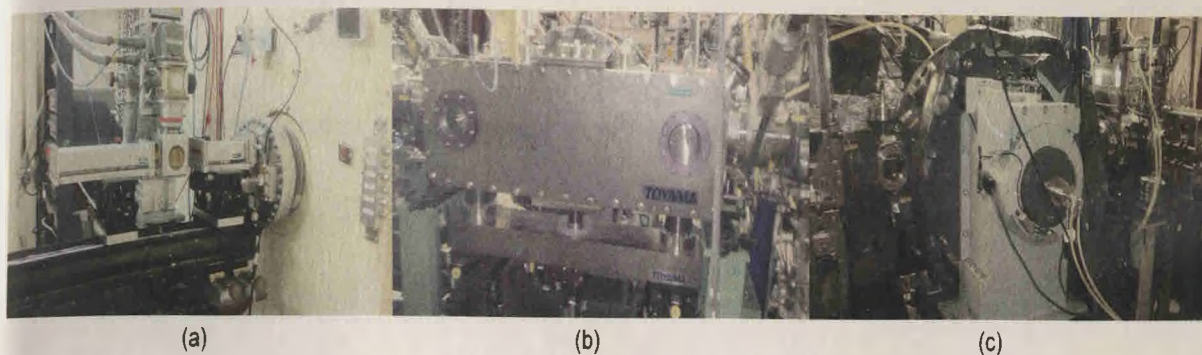


Figure 2.8: Typical XAFS beamline (BL 7C at Photon Factory) (a) Experimental arrangement for low temperature transmission XAFS measurement (b) post mirror for rejection of higher order harmonics (c) monochromator drum consisting of Si (111) crystals.

a focusing double mirror, which is usually used to reduce the higher order reflections.

Intense, higher-order free, and monochromatic X-rays can be obtained at this station.

The important parts of this beam line are shown in Figure 2.8.

The most important characteristics of an XAFS sample are its thickness, homogeneity and purity. The sample thickness is determined by optimizing the signal to noise ratio. This corresponds to an edge step absorption coefficient of about 1.0 while total absorption coefficient does not exceed 2.5. The homogeneity of the sample is important because the XAFS signal gets attenuated if part of the X-rays do not pass through the sample. The particle size of the powder sample should be fairly uniform.

Taking into consideration all these factors, absorbers for the XAFS experiments were made by spreading very fine powder of the sample on a scotch tape avoiding any sort of sample inhomogeneity and pin holes. Small strips of the sample coated tape were cut and were held one on top of the other. This assembly of the sample coated tape was sandwiched in between the scotch tape and held onto the sample holder plate. Enough



number of such strips were adjusted to give absorption edge jump,  $\Delta \mu_x \leq 1$ . XAFS at Co *K*-edge were recorded in the transmission mode using Si(111) as monochromator. The *K*-edge energy of Co is 7709 eV.

The measurements were carried out at room temperature and low temperature measurements were carried out on cold cycle refrigerator (CCR). The incident ( $I_0$ ) and transmitted ( $I$ ) photon intensities were simultaneously recorded using gas-ionization chambers filled with pure  $N_2$  and mixtures of Ar(15%)- $N_2$ (85%) respectively for Co edge. Measurements were carried out from 300 eV below the edge energy to 1000 eV above it with a 5 eV step in the pre-edge region (-300 eV to -50 eV) 0.3 eV in the edge region (-50 eV to +50 eV) followed by 1 eV step upto 100 eV and thereafter with a step of 2.5 eV.

### 2.9.3 XAFS Data Reduction And Analysis

A typical XAFS spectrum (measured in the transmission geometry at room temperature for a powder of  $PrBaCo_2O_{5.5}$ ) is shown in Figure 2.9. First the raw data ( $\mu$  v/s  $E$ ) converted to  $\chi(k)$  v/s  $k$  through series of steps, which is then analyzed using the XAFS equation.

The sharp rise in  $\mu(E)$  due to the Co 1s electron level (at 7723eV) is clearly visible in the spectra, as are the oscillations in  $\mu(E)$  that are the XAFS. As mentioned in the introduction, the XAFS is generally thought of in two distinct portions: the near-edge spectra (XANES)-typically within 30 eV of the main absorption edge, and the extended fine-structure (EXAFS).

For the EXAFS, we are interested in the oscillations well above the absorption edge,

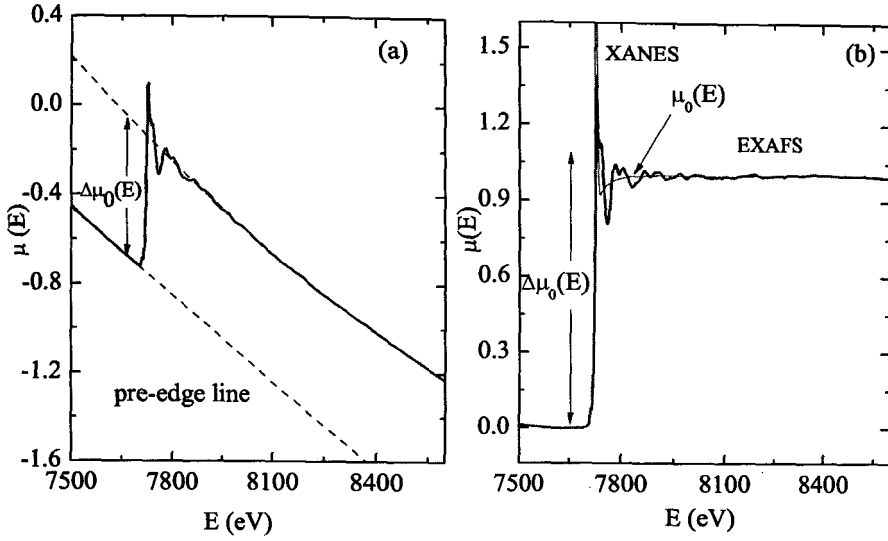


Figure 2.9: (a) XAFS pre-edge subtraction and normalization. First, a pre-edge line (or simple polynomial) is fitted to the spectrum below the edge. The jump in the edge is approximated, and the spectrum is normalized by this value (b) XAFS  $\mu(E)$  for  $\text{PrBaCo}_2\text{O}_{5.5}$ , the measured XAFS spectrum is shown with the XANES and EXAFS regions identified. On the bottom,  $\mu(E)$  is shown with smooth background function  $\mu_0(E)$  and the edge-step  $\Delta\mu_0(E_0)$ .

and define the EXAFS fine-structure function  $\chi(E)$ , as:

$$\chi(E) = \frac{\mu(E) - \mu_0(E)}{\Delta\mu_0 E} \quad (2.15)$$

where  $\mu(E)$  is the measured absorption coefficient,  $\mu_0(E)$  is a smooth background function representing the absorption of an isolated atom, and  $\Delta\mu_0$  is the measured jump in the absorption  $\mu(E)$  at the threshold energy  $E_0$  (Figure 2.9(b)).

EXAFS is best understood in terms of the wave behaviour of the photo-electron created in the absorption process. Because of this, it is common to convert the x-ray energy to  $k$ , the wave number of the photo-electron, which has dimensions of 1/distance and is defined as

$$k = \sqrt{\frac{2m(E - E_0)}{\hbar^2}} \quad (2.16)$$

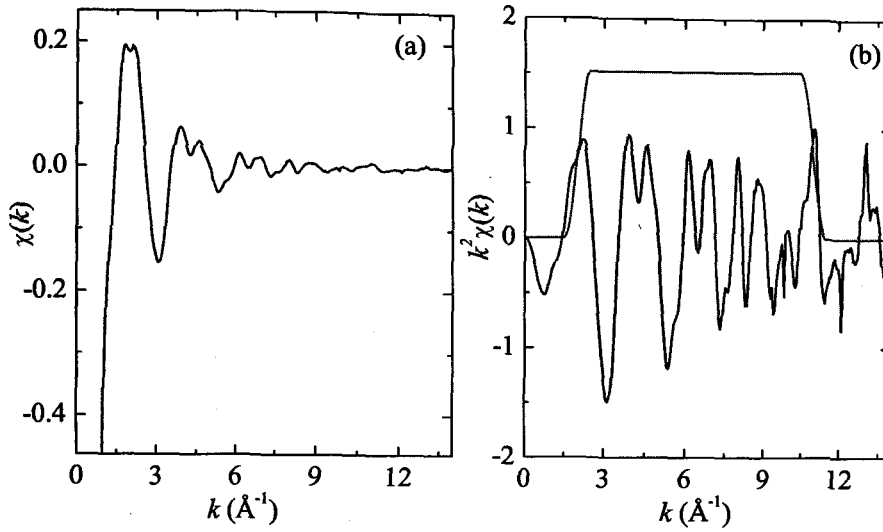


Figure 2.10: (a) Isolated EXAFS  $\chi(k)$  for PrBaCo<sub>2</sub>O<sub>5.5</sub>, (b) the  $k$ -weighted XAFS,  $k^2\chi(k)$ .

where  $E_0$  is the absorption edge energy and  $m$  is the electron mass. The primary quantity for EXAFS is then  $\chi(k)$ , the oscillations as a function of photo-electron wave number, and  $\chi(k)$  is often referred to simply as “the EXAFS”. In this way, the EXAFS extracted from the Co  $K$ -edge for PrBaCo<sub>2</sub>O<sub>5.5</sub> is shown in Figure 2.10(a). As can be seen, the EXAFS is oscillatory and decays quickly with  $k$ . To emphasize the oscillations,  $\chi(k)$  is often multiplied by a power of  $k$  typically  $k^2$  or  $k^3$ , as shown in Figure 2.10(b).

The different frequencies apparent in the oscillations in  $\chi(k)$  correspond to different near-neighbour coordination shells which can be described and modelled according to the EXAFS Equation,

$$\chi(k) = \frac{me}{4\pi\hbar^2k} \sum_j \frac{N_j}{R_j^2} F_j(k) \exp(-2R_j/\lambda_e) \exp(-2\sigma^2k^2) \sin[2Rk_j + \phi_j(k)] \quad (2.17)$$

where  $k$  is the electron wave factor,  $N_j$  is the number of atoms in the  $j^{\text{th}}$  coordination sphere,  $R_j$  is the average radial distance to the  $j^{\text{th}}$  atoms,  $F_j(k)$  is the back scattering

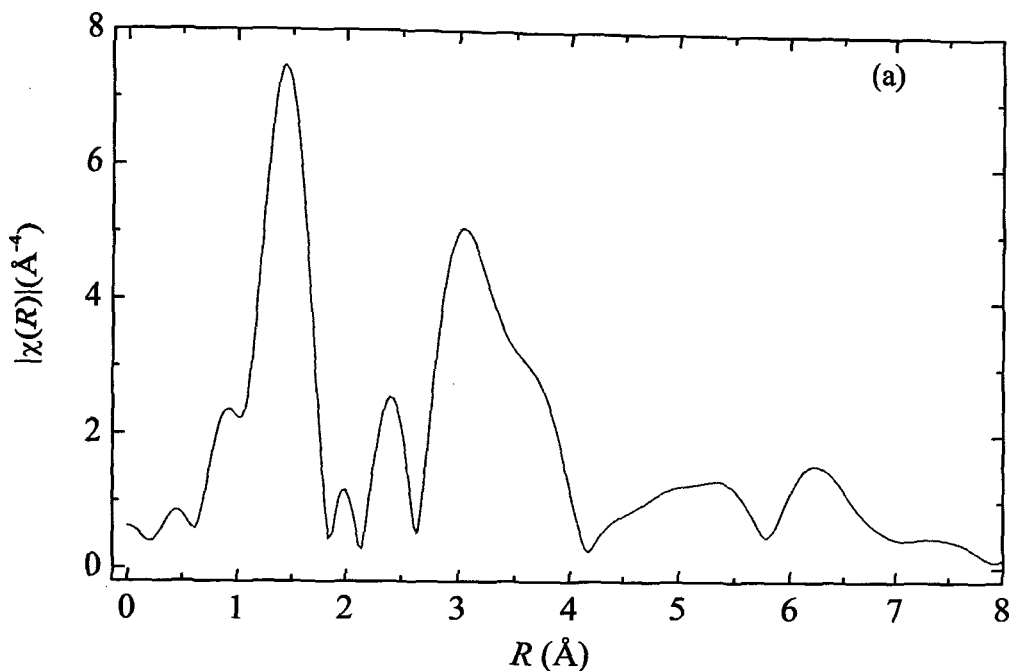


Figure 2.11: The Fourier Transformed XAFS,  $\chi(R)$ , the magnitude  $|\chi(R)|$  is shown; this is the most common way to view the data.

amplitude of electrons,  $\lambda$  is the mean free path of the electron, the second exponential containing  $\sigma_j^2$  is a Debye-Waller type term where  $\sigma_j$  is the rms fluctuations of the atom about  $R_j$ , and  $\phi_j(k)$  is the phase shift due to varying potential of central atom and backscattered atom. The form of this equation is a sine like scattering from each shell of atoms at  $R_j$  with the EXAFS signal proportional to the number of atoms surrounding the absorbing atom and inversely proportional to  $R_j^2$ . The EXAFS data fitted as per above equation is then Fourier Transformed as shown in Figure 2.11

A decrease in temperature has the effect of sharpening the EXAFS. Each coordination sphere contributes a sine like term of period  $2kR_j$ . The total result is a summation over all the coordination spheres within range of the effect.

The resulting spectrum then fitted to a chosen theoretical model to obtain local structural parameters. The EXAFS data were treated using IFEFFIT software [6]. The absorption data were first processed using Athena to extract the EXAFS signal  $\chi(k)$  from  $\mu$  v/s E data[7]. The  $\chi(k)$  v/s k data were Fourier transformed (FT) and fitted with theoretically calculated EXAFS signal for the known crystal structure in Artemis [8]. EXAFS data in the range  $k = 2\text{\AA}^{-1}$  to  $14\text{\AA}^{-1}$  and the corresponding data in R-space in the range of  $1\text{\AA}$  to  $4\text{\AA}$  was used for fitting. The various single scattering and multiple scattering correlations were obtained using FEFF6.01 program [9] and lattice parameter obtained from XRD.

# References

- [1] Streule S, Podlesnyak A, Mesot J, Medared M, Conder K, Pomjakushina E, Mitberg E and Kozhevnikov V 2005 *J. Phys: Condens. Matter* **17** 3317
- [2] Cullity B D 1956 *Elements of X-ray Diffraction* Addison Wesley Publishing Co.
- [3] Frontera C, Garc J L ía-Muñoz, A. Carrillo, M. A. G. Aranda, I. Margiolaki and A. Caneiro 2006 *Phys. Rev. B* **74** 054406
- [4] Jenks W G, Thomas I M, and Wiksow J P 1997 *Encyclopedia of Applied Physics*, **19** VCR Publishers, Inc.
- [5] Cullity B D and Graham C D 2009 *Introduction to Magnetic Materials* John Wiley & Son's, Inc.,Publication.
- [6] Janis Closed Cycle Refrigerator(CCR) system Manual
- [7] Newville M 2001 *J. Synchrotron Radiat.* **8** 322
- [8] Ravel B, and Newville M 2005 *J. Synchrotron Radiat.* **12** 537
- [9] Ravel B 2001 *J. Synchrotron Radiat.* **8** 314
- [10] Zabinsky S I, Rehr J J, Ankudinov A et al 1995 *Phys. Rev. B* **52** 2995

# Chapter 3

## Correlation of Structural And Magnetic Properties of $\text{RBaCo}_2\text{O}_{5.5}$ , $\text{R} = \text{Pr, Nd, Sm, Gd and Y}$

### 3.1 Introduction

Rare-earth based perovskites with generic formula  $\text{RBO}_3$  (R - rare-earth ion, B - Transition metal ion) exhibit a variety of physical properties due to their ability in realizing different stable structures by accommodating dopants either at R site or B site. One of the derivatives of these compounds are the layered perovskites with general formula  $\text{RBaCo}_2\text{O}_{5+\delta}$ , ( $0 \leq \delta \leq 1$ ). A large interest in these layered perovskites has arisen due to their ever surprising properties like metal insulator transition (MIT), spin state transition, charge ordering and giant magnetoresistance (MR), etc. [1, 2, 3, 4, 5, 6, 7]. However, a clear understanding of these properties is still elusive.

$\text{RBaCo}_2\text{O}_{5.5}$ , in particular, demonstrates a unique combination of physical properties. The structure consists of stacking of  $[\text{CoO}_2]$ - $[\text{BaO}]$ - $[\text{CoO}_2]$ - $[\text{RO}_{0.5}]$  along  $c$ -axis. Doubling of  $b$  axis results due to alternation of  $\text{CoO}_5$  square pyramids and  $\text{CoO}_6$  octahedra. These polyhedra are known to be heavily distorted [8, 9]. Complexities in these compounds

arise due to size difference of R and Ba and different local environment around  $\text{Co}^{3+}$  ions. Competition between crystal splitting of the  $\text{Co}^{3+}$   $3d$  level, the Hund's rule intra-atomic exchange energy and the on-site Coulomb correlation gives rise to different spin state transitions.  $\text{Co}^{3+}$  ion can have three possible spin states: the low spin state (LS,  $t_{2g}^6 e_g^0$ ,  $S=0$ ), the intermediate spin state (IS,  $t_{2g}^5 e_g^1$ ,  $S=1$ ) and high spin state (HS,  $t_{2g}^4 e_g^2$ ,  $S=2$ ). These spin state transitions, along with phenomena like charge and orbital ordering, phase separation are believed to play a key role in the exclusive properties of  $\text{RBaCo}_2\text{O}_{5.5}$  [1, 3, 4, 8, 10, 11, 12, 13, 14, 15, 16, 17, 18, 19].

One of the most important factor in deciding the magnetic properties of these layered perovskites is the oxygen content. A change in oxygen content from the meta-stable  $\text{RBaCo}_2\text{O}_{5.5}$  composition results in a change in magnetic and magnetotransport properties of these compounds [16, 17, 20, 21]. Therefore it is needed to control the oxygen content carefully during synthesis. Usually air synthesis of compounds with lighter rare-earth ions result in oxygen rich compositions and have to be annealed in reducing atmospheres to arrive at desired oxygen content, that is  $\delta \sim 0.5$ . While oxygen deficient phases are realized when layered perovskites with heavier rare-earths are synthesized and therefore have to be annealed in oxygen for desired composition.

Another important aspect is the role of the rare-earth (R) ion in magnetic properties of these layered perovskite. Several reports indicate a strong dependence of R ion on nature and type of magnetic transitions [10, 21, 22, 23]. Compounds with R ions like Sm and Eu have been reported to show complex magnetic phase diagram [22]. A recent study



on  $\text{RBaCo}_2\text{O}_{5.5}$  with  $\text{R} = \text{La} - \text{Ho}$  and  $\text{Y}$  has highlighted the role of A site cation disorder especially in compounds with larger rare-earth ions [20]. On the other hand studies based on  $\mu\text{SR}$  spectroscopy [24], neutron diffraction [10, 11, 18, 25] and nuclear magnetic resonance [19] have indicated presence of similar magnetic transitions irrespective of the R ion in these layered perovskites. For example, neutron diffraction studies on several layered perovskites with different R ion have shown that these compounds undergo a paramagnetic (PM) to antiferromagnetic (AFM) transition even though magnetization shows a sharp rise akin to PM to ferromagnetic transition (FM) [10, 11, 18, 25]. However, the reason for the presence of such a spontaneous magnetic moment in an antiferromagnetic state is not yet clearly understood. However, a correlation of magnetic and transport properties with structure, especially the local structure around Co ion and its spin state is missing.

In this Chapter we present a systematic study to establish a correlation between the structural, especially local structural parameters and the magnetic and transport properties of  $\text{RBaCo}_2\text{O}_{5.5}$  ( $\text{R} = \text{Pr}, \text{Nd}, \text{Sm}, \text{Gd}$  and  $\text{Y}$ ) compounds as a function of rare-earth ionic radii where  $\delta$  is carefully controlled to  $\sim 0.5$ . It is observed that, though there is a similarity in the nature of magnetic interactions exhibited by different  $\text{RBaCo}_2\text{O}_{5.5}$ , the strength of these magnetic interactions depend on the structural distortions around the Co ion and these interaction are affected by the size of the rare-earth ion. The samples were prepared as described in section 2.1 and the oxygen content was determined by iodometric titration are given in Table 2.1.

## 3.2 X-ray Diffraction Studies

Rietveld refinement of room temperature XRD patterns of  $\text{RBaCo}_2\text{O}_{5+\delta}$   $\delta \sim 0.5$  for  $\text{R} = \text{Pr, Nd, Sm, Gd}$  and  $\text{Y}$  confirm the formation of single phase samples with  $a_p \times 2a_p \times 2a_p$  type orthorhombic unit cell belonging to Pmmm space group. It can be seen from Figure 3.1 a very minor impurity phase is detected with peaks around  $2\theta \sim 29^\circ$  and  $31^\circ$  which can be ascribed to unreacted R-oxides ( $\text{R}_2\text{O}_3$ ).

The cell volume plotted in Figure 3.2(a) shows expected variation in accordance with Vegard's law. The lattice parameters obtained from Rietveld refinement are presented in Table 3.1. A good agreement is noticed between our values and those reported in Ref. [20]. Orthorhombic distortion,  $O_s = |(a-b)/(a+b)|$  (where  $a$  and  $b$  are lattice parameter) was calculated and is presented as a function of rare-earth ionic radius in Figure 3.2(b). Expectedly,  $O_s$  decreases with decreasing ionic radius. It may be remarked here that some structural reports have ascribed a tetragonal unit cell to  $\text{YBaCo}_2\text{O}_{5.5}$  compound [28]. It can be seen here that compound with  $\text{R} = \text{Y}$  has the least  $O_s$  and its value is very close to zero. Another noticeable feature is the presence of a distinct anomaly for  $\text{R} = \text{Sm}$ .

A close inspection of lattice parameters presented in Table 3.1 reveals that this anomaly is due to sudden contraction of  $b$  axis in  $\text{R} = \text{Sm}$  based compound. This could be due to slight deviation of oxygen content from 5.5 to 5.56 in this compound. However, this deviation in oxygen content is found to be too small to account for the observed variation in the value of lattice parameter  $b$ . Moreover, a similar deviation in

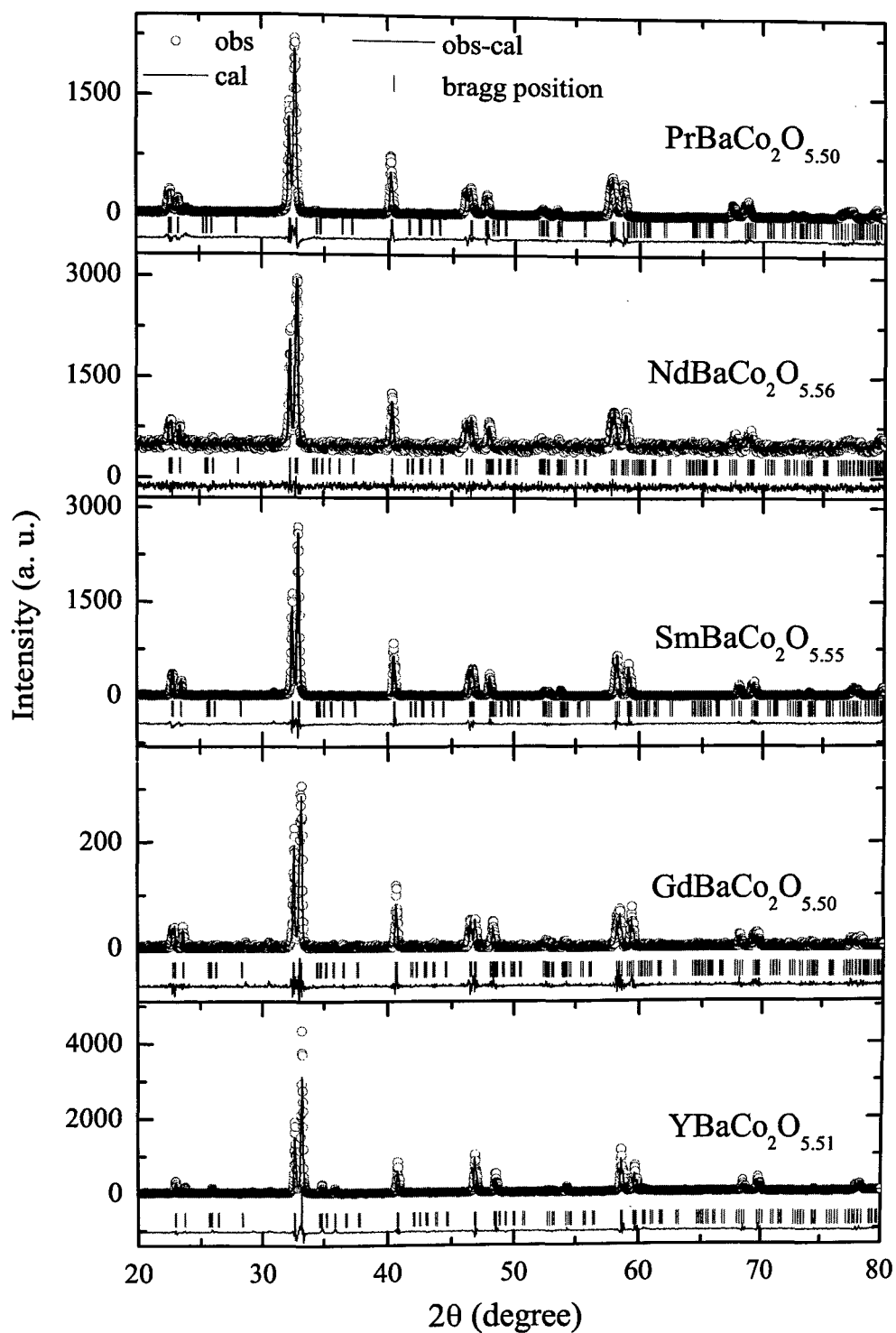


Figure 3.1: Rietveld refined XRD patterns of  $\text{RBaCo}_2\text{O}_{5.5}$  ( $R = \text{Pr, Nd, Sm, Gd}$  and  $\text{Y}$ ). Circles represent experimental data, continuous line through the data is the fitted curve, vertical lines indicate Bragg positions and the difference pattern is shown at the bottom as solid line.

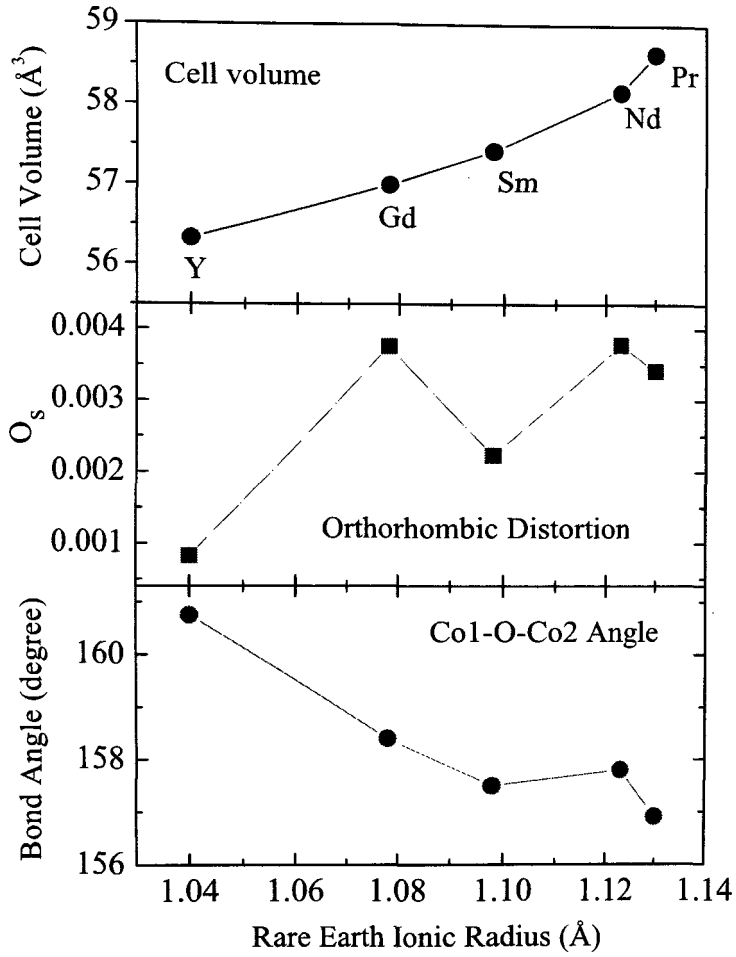


Figure 3.2: Variation of cell volume, orthorhombic distortion and Co-O-Co interpolyhedron angle with ionic radius for  $\text{RBaCo}_2\text{O}_{5.5}$  ( $\text{R} = \text{Pr, Nd, Sm, Gd}$  and  $\text{Y}$ )

Table 3.1: Lattice parameters of  $\text{RBaCo}_2\text{O}_{5.5}$ . Figures in parentheses indicate uncertainties in the last digit

Rare Earth (R)	$a(\text{Å})$	$b/2(\text{Å})$	$c/2(\text{Å})$
Pr	3.9087(1)	3.9355(1)	3.8122(1)
Nd	3.9013(1)	3.9309(1)	3.7925(1)
Sm	3.8869(2)	3.9043(1)	3.8783(2)
Gd	3.8751(2)	3.9034(1)	3.7670(2)
Y	3.8778(2)	3.8714(2)	3.7520(1)

oxygen content is observed in layered perovskite containing Nd (Table 2.1) but its lattice parameters obtained from Rietveld refinement (Table 3.1) agree with those reported for  $\text{NdBaCo}_2\text{O}_{5.5}$  in literature [20]. Such anomalies in lattice parameters have also been reported in other  $\text{RBaCo}_2\text{O}_{5.5}$  compounds ( $R = \text{Eu}$  and  $\text{Gd}$ ) [20]. These anomalies in lattice parameters can affect the inter-polyhedron bond angle,  $\text{Co}(1)\text{-O-Co}(2)$  which, as can be seen in Figure 3.2(c), exhibits an anomaly for  $R = \text{Sm}$ . This will have an effect on Co  $3d\text{-O } 2p$  hybridization and could therefore influence the magnetic and transport properties of these compounds.

### 3.3 Magnetization Measurements

Results of temperature dependant magnetization  $M(T)$  for  $\text{RBaCo}_2\text{O}_{5.5}$ , measured in two different fields  $10000\text{Oe}=1\text{T}$  and  $100\text{Oe}/500\text{Oe}$  during ZFC and FC cycles are presented in Figure 3.3. Except in case of  $\text{YBaCo}_2\text{O}_{5.5}$ , a bifurcation is seen between the ZFC and FC curves at lower temperatures indicating complex magnetic ground state. This difference between ZFC and FC curves increases with increasing rare-earth ionic radius.  $M(T)$  for  $\text{GdBaCo}_2\text{O}_{5.5}$  is restricted down to 50 K due to large paramagnetic contribution coming from Gd ion [21]. Two transitions from PM to AFM1 at  $T_{N1}$  followed by AFM1 to AFM2 at  $T_{N2}$  can be clearly seen from these plots. Besides  $T_{N1}$  and  $T_{N2}$ , two other AFM transitions  $T_{R1}$  and  $T_{R2}$  are also seen for  $\text{RBaCo}_2\text{O}_{5.5}$  [24]. It is noticed that the transition at  $T_{R2}$  is quite strong in  $\text{SmBaCo}_2\text{O}_{5.5}$  while it is quite subtle in all other compounds.

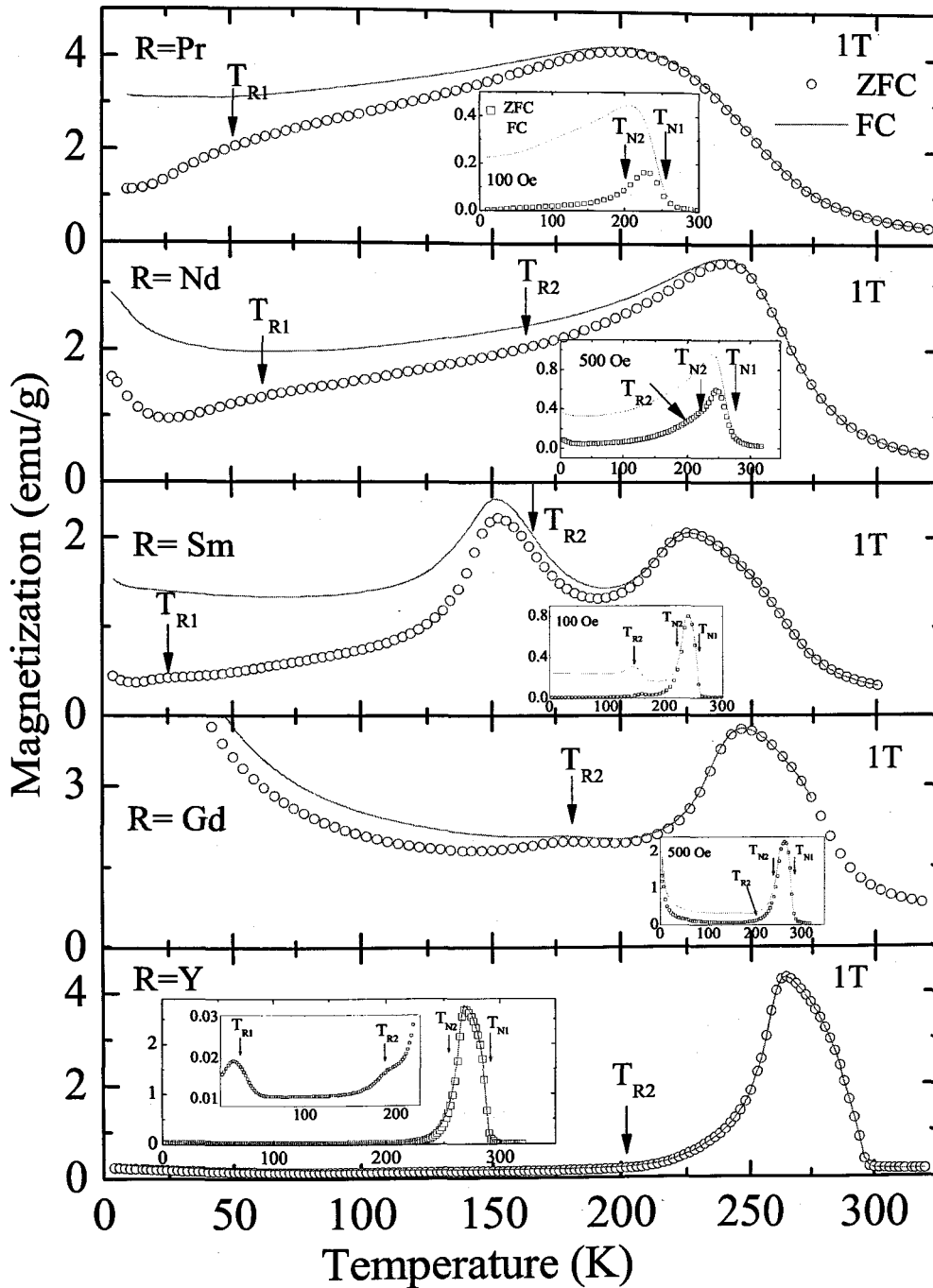


Figure 3.3: Magnetization  $M(T)$  as function of temperature in the field of 1T for  $\text{RBaCo}_2\text{O}_{5.5}$  ( $R = \text{Pr, Nd, Sm, Gd}$  and  $\text{Y}$ ). Inset shows 100Oe MT for  $R = \text{Pr}$  and  $\text{Sm}$  and 500Oe ZFC for  $R = \text{Nd, Gd}$  and  $\text{Y}$  (Innermost inset of  $R = \text{Y}$  shows enlarged view of ZFC)

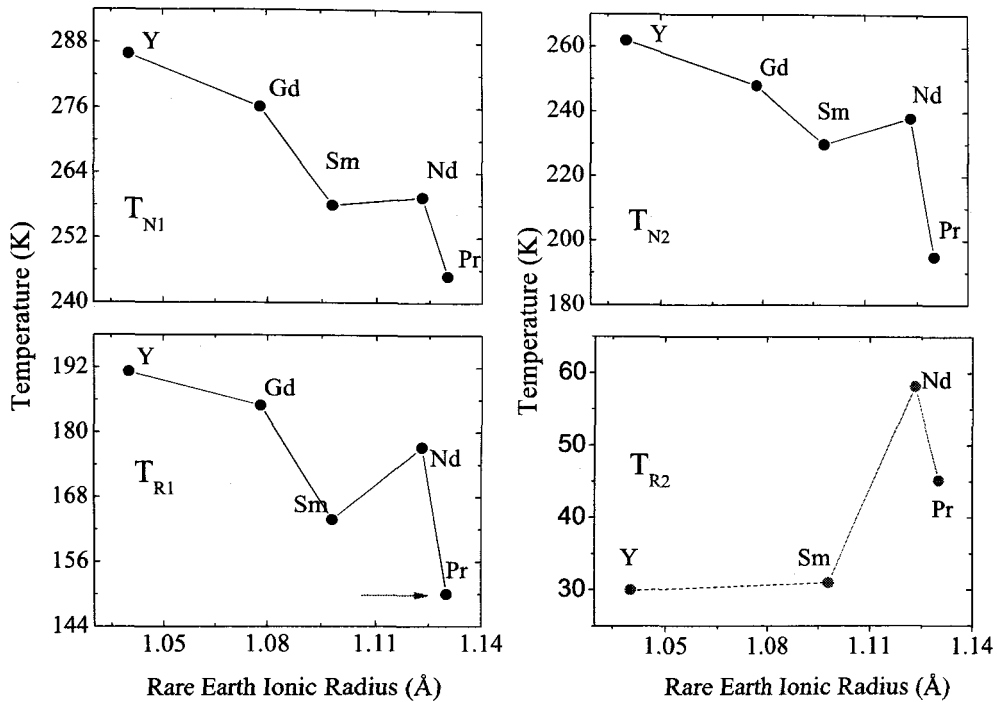


Figure 3.4: Effect of rare earth ionic radius on various transition temperatures estimated from 1000 Oe ZFC magnetization data for  $\text{RBaCo}_2\text{O}_{5.5}$  ( $R = \text{Pr, Nd, Sm, Gd}$  and  $\text{Y}$ )

Furthermore, the transition temperatures,  $T_{N1}$ ,  $T_{N2}$ ,  $T_{R1}$  and  $T_{R2}$  show an interesting variation with rare-earth ionic radius (Figure 3.4). It can be seen that as ionic radius decreases the transition temperatures  $T_{N1}$ ,  $T_{N2}$  and  $T_{R1}$  show an increase except in case of  $\text{SmBaCo}_2\text{O}_{5.5}$ . All these transition temperatures exhibit a decrease in case of compound with  $R = \text{Sm}$ . This decrease compares well with the anomalies seen in  $O_s$  and  $\text{Co}(1)\text{-O-Co}(2)$  bond angle. Due to interfering paramagnetic contribution of Gd,  $T_{R2}$  could not be determined for  $\text{GdBaCo}_2\text{O}_{5.5}$  and therefore we cannot comment on its variation with rare-earth ionic radii unambiguously. However, a decrease in  $T_{R2}$  is noted in case of  $\text{SmBaCo}_2\text{O}_{5.5}$  beyond which it appears to remain constant.

To investigate the magnetic properties further, isothermal magnetization  $M(H)$  curves

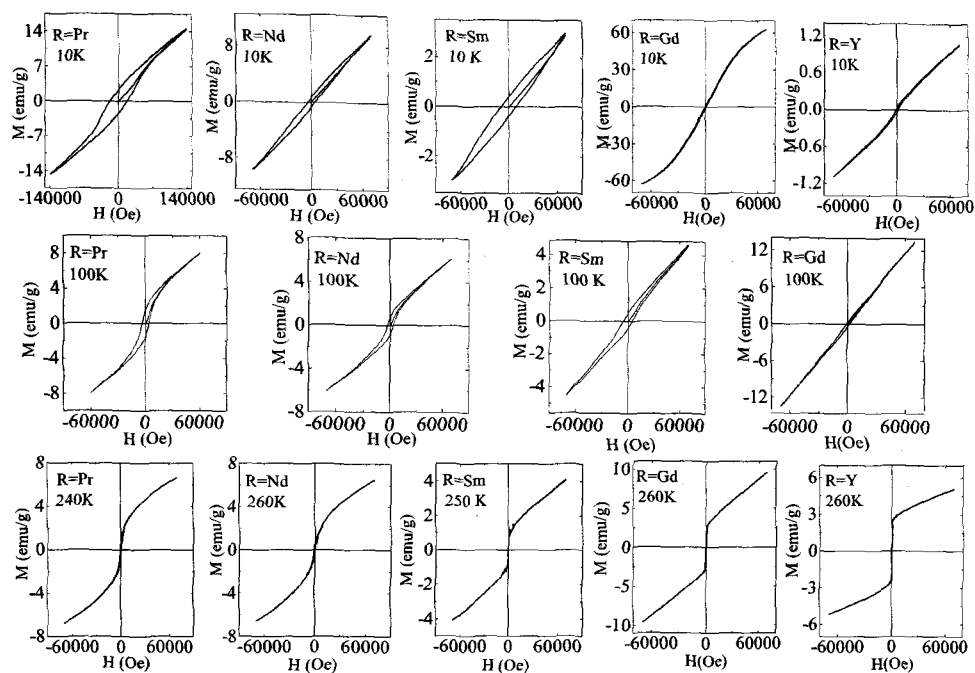


Figure 3.5: Hysteresis loops recorded at different temperatures for  $\text{RBaCo}_2\text{O}_{5.5}$  ( $R = \text{Pr}$ ,  $\text{Nd}$ ,  $\text{Sm}$ ,  $\text{Gd}$  and  $\text{Y}$ )

have been recorded at several temperatures (10 K, 100 K,  $\sim 250$  K) and are presented in Figure 3.5.

While  $M(H)$  at 10 K shows clear hysteresis for compound with  $R = \text{Pr}$ , it diminishes with decrease in ionic radius of the rare-earth ion. Further, none of the compounds exhibit saturation of  $M(H)$  value even in an applied field of 7T indicating presence of competing magnetic interactions. Further, the value of magnetization at 7T shows a gradual decrease as the rare-earth ion is changed from Pr to Y. The only exception is the Gd containing compound which has a large paramagnetic contribution of the Gd ion as can be seen in  $M(T)$  curve. Therefore, it appears that with decrease in rare-earth ionic radius, antiferromagnetic interactions dominate over ferromagnetic interactions. This is



A similar situation exists at  $T = 100$  K which lies in between  $T_{R2}$  and  $T_{R1}$ . With decreasing rare-earth ionic radii the ferromagnetic interactions seem to be weakened. While in the vicinity of 250 K, which is close to  $T_{N1}$ , the effect of spontaneous magnetic moment is clearly seen in  $M(H)$  loops. There is a sudden change in the value of magnetization at very low fields. It is also noticed that this change in magnetization depends on the type of rare-earth ion. In general, larger the rare-earth ion less sudden is the change.

### 3.4 Transport Properties

Resistivity curves recorded in applied magnetic fields of 0T and 8T and in the temperature range 300 K to 10 K are presented in Figure 3.6(a). Resistivity measurements shows a semiconductor type behaviour with  $\text{NdBaCo}_2\text{O}_{5.5}$  exhibiting highest resistance. There is very little or no change in resistivity measured in the field of 8T. Compound with  $R = \text{Y}$  shows a MIT around 300 K while for other samples MIT is reported to occur at temperatures  $> 300$  K [1]. One interesting observation is that the sample with  $R = \text{Sm}$  exhibits minimum magnitude of resistivity. The measured resistivity in  $\text{SmBaCo}_2\text{O}_{5.5}$  is lower by more than an order of magnitude as compared to other  $\text{RBaCo}_2\text{O}_{5.5}$ . Although resistance of a polycrystalline material depends largely on the grain size and grain boundaries, these may not account for such large changes in resistance. This could be due to lower Co(1)-O-Co(2) bond angle. The lower interpolyhedron bond angle results in increased Co-O-Co band overlap and hence a greater mobility of the charge carriers.

Isothermal magnetoresistance (MR) measured at 200 K in the field of  $\pm 8$ T are shown

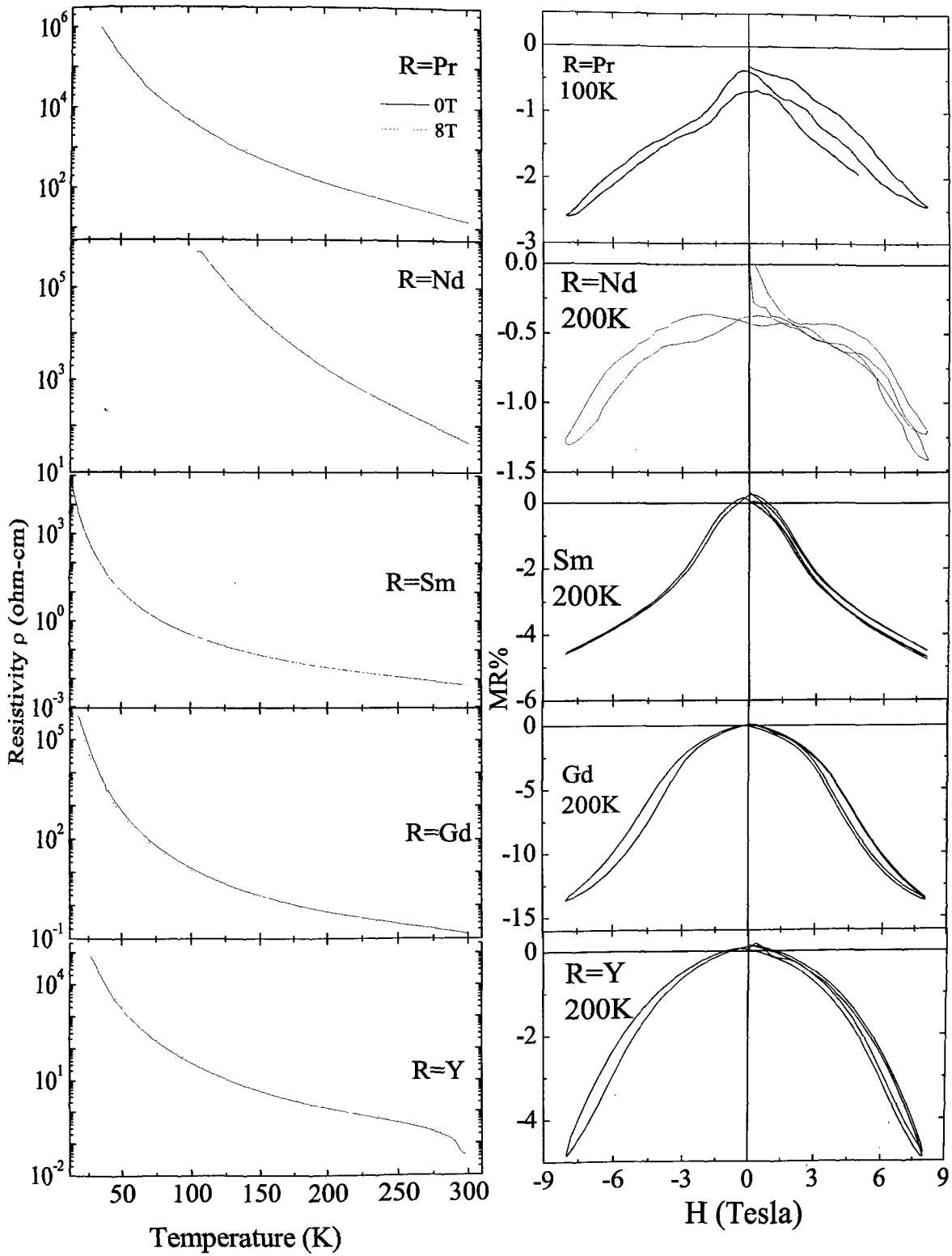


Figure 3.6: Resistivity(left panel) and Isothermal Magnetoresistance (MR) (right panel) for  $\text{R}\text{BaCo}_2\text{O}_{5.5}$  ( $\text{R} = \text{Pr}, \text{Nd}, \text{Sm}, \text{Gd}$  and  $\text{Y}$ )

in Figure 3.6(b). MR is small. In the case of  $\text{PrBaCo}_2\text{O}_{5.5}$ , it was too small to be measured at 200 K and hence data recorded at 100 K is shown. All samples exhibit negative MR with a quadratic dependence on magnetic field which results mainly due to spin disorder scattering [29]. One noticeable feature however, is the shape of the MR curve in case of  $\text{SmBaCo}_2\text{O}_{5.5}$ . Compared to the other  $\text{RBaCo}_2\text{O}_{5.5}$ , the MR has a bell shaped curve which is typically observed in materials exhibiting spin valve effect [10]. We can only speculate that such a change in MR behaviour is due to decrease in spin disorder scattering perhaps arising due to higher degree of Co  $3d$ -O  $2p$  band overlap.

## 3.5 X-ray Absorption Spectroscopic Measurement

The above variation of magnetic and transport properties and their correlation with orthorhombic distortion and Co1-O-Co2 bond angle hints at Co-O hybridization to be one of the important factors in deciding magnetic and transport properties of these layered cobaltites. Co K edge XANES spectroscopy is a valuable tool in probing the local structure around Co ion and can give information about the nature of Co-O hybridization.

### 3.5.1 X-ray Absorption Near Edge Structure (XANES)

The XAFS raw data were processed as given in Chapter 2. Normalized XANES spectra for all  $\text{RBaCo}_2\text{O}_{5.5}$  are shown in Figure 3.7. All the edges are normalized to an average absorption between +55 to +60 eV beyond the absorption edge. XANES features in all the samples are almost similar consisting of the pre-edge peak at about 7710 eV, a shoulder on the rising part of the absorption curve at about 7720 eV, the main resonance

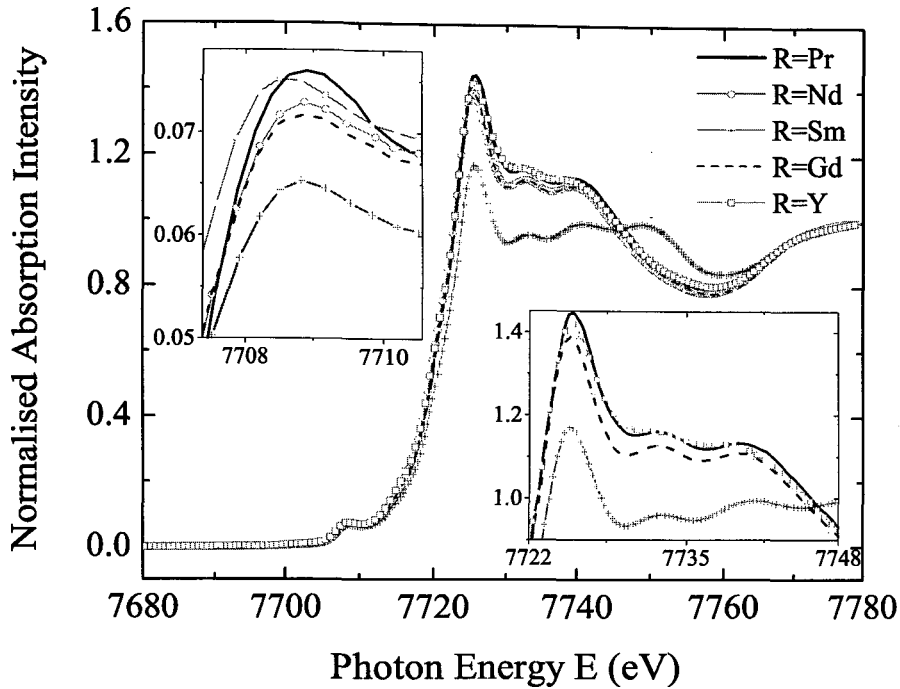


Figure 3.7: Normalised Co K XANES at room temperature with pre-edge encircled for  $\text{RBaCo}_2\text{O}_{5.5}$ ,  $R = \text{Pr, Nd, Sm, Gd, and Y}$

peak around 7725 eV followed by two maxima at about 7733 eV and 7740 eV. In case of  $\text{SmBaCo}_2\text{O}_{5.5}$  a third maximum at about 7750 eV is seen due to interfering Sm  $L_1$  edge which occurs at 7745 eV. Another difference in case of  $\text{SmBaCo}_2\text{O}_{5.5}$  is that area under the absorption edge is quite low. One reason for this could be the interfering Sm  $L_1$  edge which affects normalization. However,  $L_1$  edges in general have a very low transition probability so as to cause such a large change. Therefore this can be ascribed to a decrease in hole density as a result of greater degree of hybridization between Co and O states.

Pre-edge feature which represents an electronic transition  $1s \rightarrow 3d$  made allowed due to quadrupolar splitting or due to hybridization of ligand  $p$  states, was extracted by

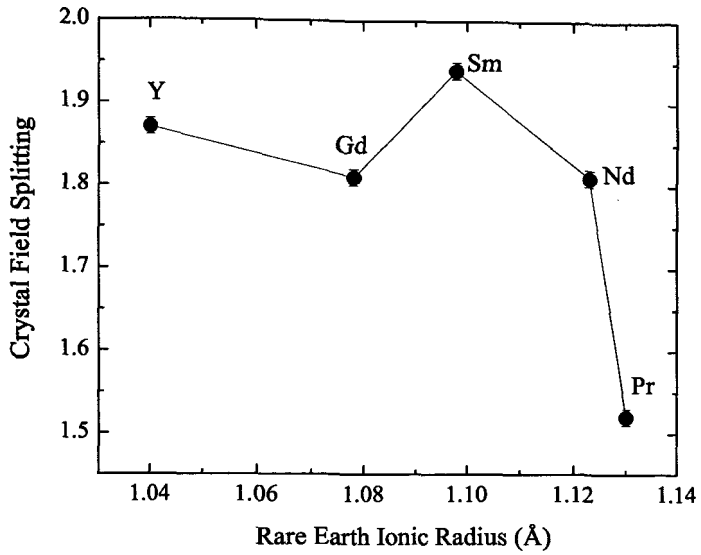


Figure 3.8: Crystal field splitting with increasing rare earth ion radii for  $\text{RBaCo}_2\text{O}_{5.5}$  ( $R = \text{Pr, Nd, Sm, Gd and Y}$ )

subtracting a spline curve as base line from near edge data and is shown in top inset of Figure 3.7. This data was used to extract the value of crystal field (CF) splitting of the 3d orbital in each of these layered perovskite. The values of CF splitting estimated from the pre-edge peak are plotted as a function of rare-earth ionic radii in Figure 3.8. It can be seen that while CF splitting is nearly same in all compounds, it is slightly higher in case of  $\text{SmBaCo}_2\text{O}_{5.5}$ . A higher CF splitting augurs well with structural anomalies exhibited by this compound.

The lower inset of Figure 3.7 shows an expanded view of XANES features. It can be seen that with change in rare-earth ionic radius, the relative positions and intensities of the XANES features change with respect to main resonance peak. In  $\text{RCoO}_3$  compounds such changes are ascribed to a orthorhombic distortion of the  $\text{CoO}_6$  octahedra [30]. In these layered perovskites, the Co ion has two different local coordinations, octa-

hedral and square pyramidal and distortions are possible at both Co sites. In order to extract this information, Co K XANES spectra have been calculated in three compounds of  $\text{RBaCo}_2\text{O}_{5.5}$  ( $\text{R} = \text{Pr}, \text{Sm}$  and  $\text{Y}$ ) using FEFF8.4 [31]. These full multiple scattering calculations were performed for Co ion at square pyramidal site (Co1) and at octahedral site (Co2) in each of the above three layered perovskites. Structural parameters obtained from Rietveld refinement of room temperature XRD profile were used as input parameters in ATOMS to generate input file for FEFF calculations. The spherical muffin tin potentials were self consistently calculated over a radius of  $9\text{\AA}$ . A default overlapping muffin tin potentials and Hedin-Lunqvist exchange correlations were used to calculate X-ray absorption transitions to a fully relaxed final state in presence of a core hole. An energy shift of 2 eV was applied to achieve a better description of pre-edge absorption at the Co K edge. A comparison of calculated spectra with the experimentally absorption curves is presented in Figure 3.9. The individual spectra calculated for Co1 and Co2 are shifted along y-axis for clarity. All the XANES features seen in experimental data are reproduced in the FEFF calculated curves. It can be seen that the feature at 7720 eV is entirely due to Co ion at octahedral site, while the peak at 7733 eV is more prominent in the XANES spectra of Co in square pyramidal coordination. In analogy with  $\text{RCoO}_3$  compounds [30] the XANES features at 7733 eV and 7740 eV tend to be weakened with decreasing orthorhombic distortion. The calculations suggest that the feature at 7733 eV has contribution from unoccupied  $p$  states of R/Ba ions, Co  $4p$  states and O  $2p$  states, whereas, the peak at 7740 eV is a result of hybridization between Co  $4p$  and O  $2p$  states.

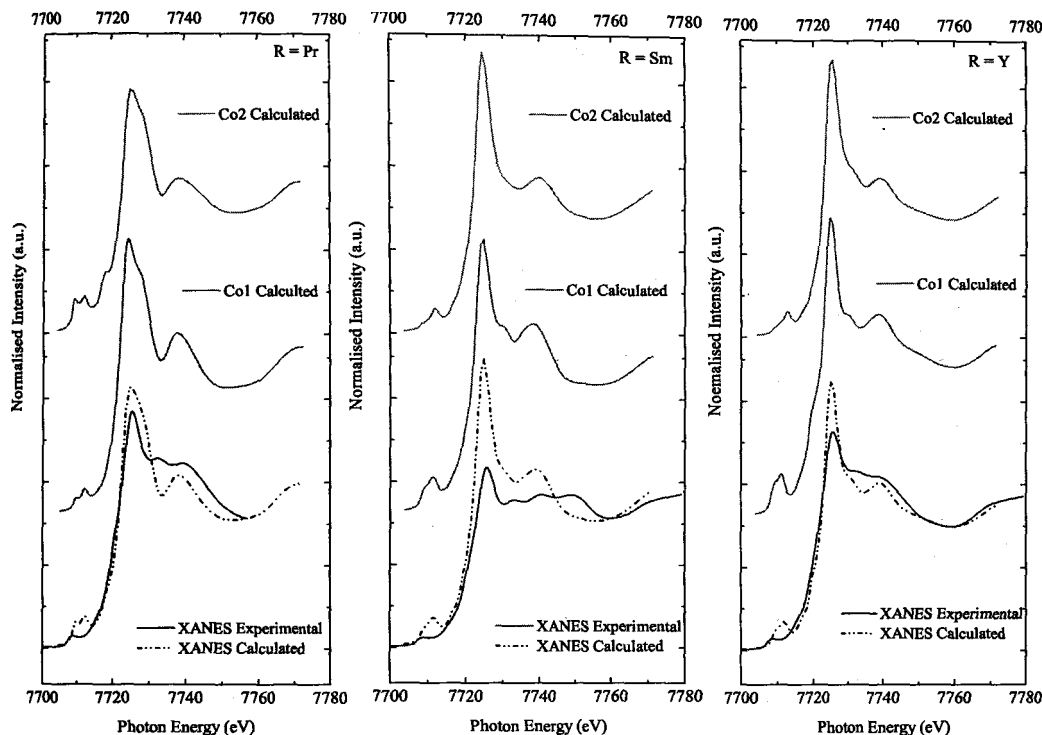


Figure 3.9: Calculated Co K edge XANES for  $\text{R BaCo}_2\text{O}_{5.5}$  ( $\text{R} = \text{Pr}, \text{Sm}$  and  $\text{Y}$ ), for square pyramidal(Co1) and octahedral(Co2) site along with a comparison of calculated spectra(dotted line) and experimental(solid line) absorption curves.

Again the post-edge XANES features have lower intensity in  $\text{SmBaCo}_2\text{O}_{5.5}$  indicating at greater hybridization of Co and O orbitals.

### 3.6 Discussion

The layered cobaltites  $\text{R BaCo}_2\text{O}_{5.5}$  ( $\text{R} = \text{Pr}, \text{Nd}, \text{Sm}, \text{Gd}$  and  $\text{Y}$ ) as mentioned earlier crystallize in orthorhombic unit cell with  $Pmmm$  structure. Though a linear variation of cell volume with ionic radii is seen, anomalies in orthorhombic distortion and interpolyhedron bond angle are observed especially in compound containing Sm. Such structural anomalies have also been observed in earlier reports in compounds with larger rare-earth ions [20]. The differences in magnetic and transport properties observed in  $\text{SmBaCo}_2\text{O}_{5.5}$

point towards the role of structural anomalies in magnetic and transport properties. In present case, although magnetic transition temperatures tend to increase with decreasing rare-earth ionic radii, the compound with Sm has lower transition temperatures and stands out as different from the observed trend. Moreover, resistivity of Sm containing compound is about one order of magnitude lower than other rare-earth counterparts. Magnetization as a function of temperature indicates increasing dominance of ferromagnetic interactions with increase in size of the rare-earth ion. Here too the compound with Sm tends to stand out. The transition at  $T_{R2}$ , which is quite subtle in other compounds, is quite strong in  $\text{SmBaCo}_2\text{O}_{5.5}$ .

Co K edge XANES analysis performed in all the layered perovskites studied here indicates that the most probable cause of anomalous magnetic and transport properties of  $\text{SmBaCo}_2\text{O}_{5.5}$  is the higher degree of hybridization of Co and the O orbitals. The higher CF splitting, lower hole density and weaker post-edge XANES features support this claim. Further, theoretical calculations of Co K XANES performed separately for square pyramidal and octahedrally coordinated Co ions show that features of both Co ions are equally affected with changing rare-earth radius. It is generally believed that, in  $\text{RBaCo}_2\text{O}_{5.5}$  compounds, the square pyramidal Co ion is in intermediate spin state while the octahedral Co ion prefers low spin state. The changes observed in XANES features of both Co sites questions the assignment of low spin state to octahedral Co ion. Recent reports on  $\text{RBaCo}_2\text{O}_{5.5}$  have indicated presence of high spin Co ions along with low spin Co ions in octahedral coordination [32].



### 3.7 Conclusion

In summary, the ionic radius of rare earth ion plays a distinct role in the unique properties of layered perovskites. The larger rare earth results in a complex magnetic ground state while AFM interactions tend to dominate in compounds with smaller rare earths. The crossover happens for larger rare-earths, near about  $R = \text{Sm}$ . The most probable cause of anomalous properties is the higher degree of Co-O hybridization in which both, square pyramidal and octahedral Co ions participate.

# References

- [1] Maignan A, Martin C, Pelloquin D, Nguyen N, and Raveau B 1999 *J. Solid State Chem.* **142** 247
- [2] Martin C, Maignan A, Pelloquin D, Nguyen N, and Raveau B 1997 *Appl. Phys. Lett.* **71** 1421
- [3] Moritomo Y, Akimoto T, Takeo M, Machida A, Nishibori E, Takata M, Sakata M, Ohoyama K and Nakamura A 2000 *Phys. Rev. B* **61** R13325
- [4] Respaud M, Frontera C, García-Muñoz J, Aranda A G M, Raquet B, Broto J, Rakoto H, Goiran M, Llobet A, and Carvajal J 2001 *Phys. Rev. B* **64** 214401
- [5] Vogt T, Woodward P M, Karen P, Hunter B A, Henning P, and Moodenbaugh A R 2000 *Phys. Rev. Lett.* **84** 2969
- [6] Suard E, Fauth F, Caignaert V, Mirebeau I and Baldinozziet G 2000 *Phys. Rev. B* **61** R11871
- [7] Troyanchuk I, Kasper N, and Khalyavin D D 1998 *Phys. Rev. Lett.* **80** 3380

- [8] Khalyavin D D, Barilo S, Shiryaev S, Bychkov G, Troyanchuk I, Furrer A, Al-lenspach P, Szymczak S and Szymczak R 2003 *Phys. Rev. B* **67** 214421
- [9] Pomjakushina E, Conder K and Pomjakushin V 2006 *Phys. Rev. B* **73** 113105
- [10] Taskin A A, Lavrov A N and Ando Y 2003 *Phys. Rev. Lett.* **90** 227201
- [11] Taskin, A A, Lavrov, A N, Ando, Y 2005 *Phys. Rev. B* **71** 134414
- [12] Baran, M, Gatalskaya, V I, Szymczak, R, Shiryaev, S V, Barilo, S N, Bychkov, G L, Szymczak, H J, 2005 *J. Phys.: Condens. Matter* **17** 5613
- [13] Chernenkov, Y P, Plakhty, V P, Fedorov, V I, Barilo, S N, Shiryaev, S V, Bychkov, G L 2005 *Phys. Rev. B* **71** 184105
- [14] Maignan, A, Caignaert, V, Raveau, B, Khomskii, D, Sawatzky, G 2004 *Phys. Rev. Lett.* **93** 26401.
- [15] Zhou, H D, Goodenough, J B 2004 *J. Solid State Chem.* **177** 3339.
- [16] Roy, S, Dubenko, I S, Khan M, Condon, E M, Craig, J, Ali, N, Liu, W, Mitchell B S 2005 *Phys. Rev. B* **71**, 024419.
- [17] Burley, J C, Mitchell, J F, Short, S, Miller, D, Tang, Y J 2003 *Solid State Chem.* **170** 339
- [18] Plakhty, V P, Chernenkov, Y P, Barilo, S N, Podlesnyak, A, Pomjakushina, E, Moskvina, E V, Gavrilov, S V 2005 *Phys. Rev. B* **71** 214407

- [19] Soda M, Yasui Y, Kobayashi Y, Fujita T, Sato M and Kakurai K 2006 *J. Phys. Soc. Jpn* **75** 104708
- [20] Rautama E L, Caignaert V, Boullay P, Kundu A K, Pralong V, Karppinen M, Ritter C, Raveau B 2009 *Chem. Mater* **21** 102
- [21] Frontera C, García-Muñoz J L, Carrillo A, Aranda M A G, Margiolaki I and Caneiro A 2006 *Phys. Rev. B* **74** 054406
- [22] Seikh Md M, Simon Ch, Caignaert V, Pralong V, Lepetit M B, Boudin S, and Raveau B 2008 *Chem. Mater.* **20** 231238
- [23] Kundu A K, Reveau B, Caignaert V, Rautama E-L and Pralong V 2009 *J. Phys. Condens. Matter* **21** 056007
- [24] Jarry A, Luetkens H, Pashkevich Y, Stingaciu M, Pomjakushina E, Conder K, Lemmens P and Klaus H 2009 *Physica B* **404** 765
- [25] Fauth F, Suard E, Caignaert V and Mirebeau I 2002 *Phys. Rev. B* **66** 184421
- [26] Ganorkar S, Priolkar K R, Sarode P R, and Banerjee A 2011 *J. Appl. Phys.* **110** 053923
- [27] Conder K, Pomjakushina E, Soldatov A and Mitberg E 2005 *Mater. Res. Bull.* **40** 257
- [28] Aksenovaa T V, Gavrilovaa L Ya, Tsvetkova D S, Voroninb V I, and Cherepanova V A 2011 *Russ. J Phys. Chem.* **85** 427-432

- [29] Raveau B 2008 *Phil. Trans. R. Soc. A* 366
- [30] Pandey S K, Kumar A, Patil S, Medicherla V R R, Singh R, Maiti K, Prabhakaran D, Boothroyd A, and Pimpale A V 2008 *Phys. Rev. B* **77** 045123
- [31] Ankudinov A L, Nesvizhskii A I and Rehr J J 2003 *Phys. Rev. B* **67** 115120
- [32] Hu Z, Wu H, Koethe T C, Barilo S N, Shiryaev S V, Bychkov G L, Schüler-Langeheine C, Lorenz T, Tanaka A, Hsieh H H, Lin H-J, Chen C T, Brookes N B, Agrestini S, Chin Y-Y, Rotter M and Tjeng L H 2012 *New J. Phys.* **14** 123025

# Chapter 4

## Unusual magnetic properties of $\text{SmBaCo}_2\text{O}_{5+\delta}$ , ( $0.12 \leq \delta \leq 0.65$ )

### 4.1 Introduction

Modifications of the ideal cubic perovskite structure are often caused by a size mismatch of the corresponding ions. One of such distorted layered perovskites is  $\text{RBaCo}_2\text{O}_{5+\delta}$ , ( $0 \leq \delta \leq 1$ ) (R - rare-earth element). The size difference cause the layers of  $\text{CoO}_2$  -  $\text{BaO}$  -  $\text{RO}_{0.5}$  -  $\text{CoO}_2$  stack along the  $c$ -axis. Cobalt as a transition metal ion plays an important role in these system which are characterized by metal insulator transition (MIT), spin state transition, charge ordering and giant magnetoresistance (MR) [1, 2, 3, 4, 5, 6, 7]. These fascinating physical properties originate from strong variations in electronic configurations of Co ions due to changes in composition, charge, crystal field, structural symmetry, spin and angular momentum and electronic correlations [8, 9, 10, 11, 12, 13]. Based on the oxygen content which can be varied from  $\text{O}_6$  ( $\delta = 1$ ) to  $\text{O}_5$  ( $\delta = 0$ ). Such a large variation in oxygen content is possible due to flexibility of the layered structure which in turn depends on the size of the rare-earth ion. Therefore the rare-earth ion also plays an indirect role in magnetic and transport properties of these layered perovskites.

Several magnetic transitions have been reported for these compounds. Below MIT the compounds undergo a paramagnetic (PM) to ferro(ferri)magnetic (FM) transition followed by a FM to antiferromagnetic (AFM1) transition along with an onset of strong anisotropic magneto-resistive effects and AFM1 to second antiferromagnetic (AMF2) phase transition. The mechanism behind such magnetic transformations at low temperature is still to be clearly understood. Various contradicting magnetic structure with different spin state of  $\text{Co}^{3+}$  ions and also spin state ordering (SSO) have been proposed, based on neutron diffraction [14, 15, 16, 17] and macroscopic measurements [18]. Muon-spin relaxation ( $\mu\text{SR}$ ) studies show that irrespective of the rare earth ion, a homogeneous FM phase with ferrimagnetic SSO of IS and HS states develops through two first order phase transitions into phase separated AFM1 and AFM2 phases with different types of antiferromagnetic SSO [19]. Density functional calculations suggest that there is a strong hybridization between O-2p and Co-3d orbitals with a narrow charge transfer gap near Fermi level, which gives rise to  $\text{pd}\sigma$  hybridized hole in the O-2p valence band. With increasing temperature, a gradual delocalization of the  $\text{pd}\sigma$  holes in the almost HS  $\text{Co}^{3+}$  is responsible for the successive magnetic transitions accompanied by spin reorientation in a spin-canted structure due to competing FM and AFM interactions [20]. Resonant photoemission studies also support this picture [21].

Further, tiny variations in oxygen content result in large changes in magnetic properties and hence method of synthesis, oxygen content and size of rare earth ion play a crucial role [11]. Though several studies exist on these compounds with different rare-earth ions,

there are still some open issues especially concerning complex magnetic transitions and their relation to oxygen stoichiometry, nanoscopic phase separation, etc. that have to be understood. These effects are more prominent in compounds with rare-earth ions like Sm, Eu, Gd which tend to form compositions with  $\delta \approx 0.5$  without any additional annealing treatment. It is also reported that  $R = \text{Sm}$  shows very different low temperature magnetic behaviour as compared to other  $\text{RBaCo}_2\text{O}_{5.5}$  [22]. This Chapter presents a systematic investigation of magnetic, transport and X-ray spectroscopic properties of  $\text{SmBaCo}_2\text{O}_{5+\delta}$  ( $0.12 \leq \delta \leq 0.65$ ). It is seen that oxygen content plays a crucial role in influencing the magnetic properties of these compounds. Oxygen vacancies or excess with respect to  $\text{SmBaCo}_2\text{O}_{5.5}$  induces a transition from orthorhombic to tetragonal structure accompanied by magnetic compensation. Structural symmetry influences the crystal field splitting of the Co 3d states as well as the Co 3d - O 2p hybridization. The samples were prepared as described in section 2.1 and the oxygen content was determined by iodometric titration are given in Table 2.1.

## 4.2 X-ray Diffraction Studies

Room temperature XRD confirms the formation of  $\text{SmBaCo}_2\text{O}_{5+\delta}$  samples in single phase. Rietveld refinement XRD patterns are presented in Figure 4.1. Few of the compounds show presence of very minor impurity phases ( $\sim 1\%$ ) with peaks around  $2\theta \sim 31^\circ$  which can be ascribed to unreacted  $\text{Sm}_2\text{O}_3$ .

The variation in lattice parameters as a function of oxygen content is presented in



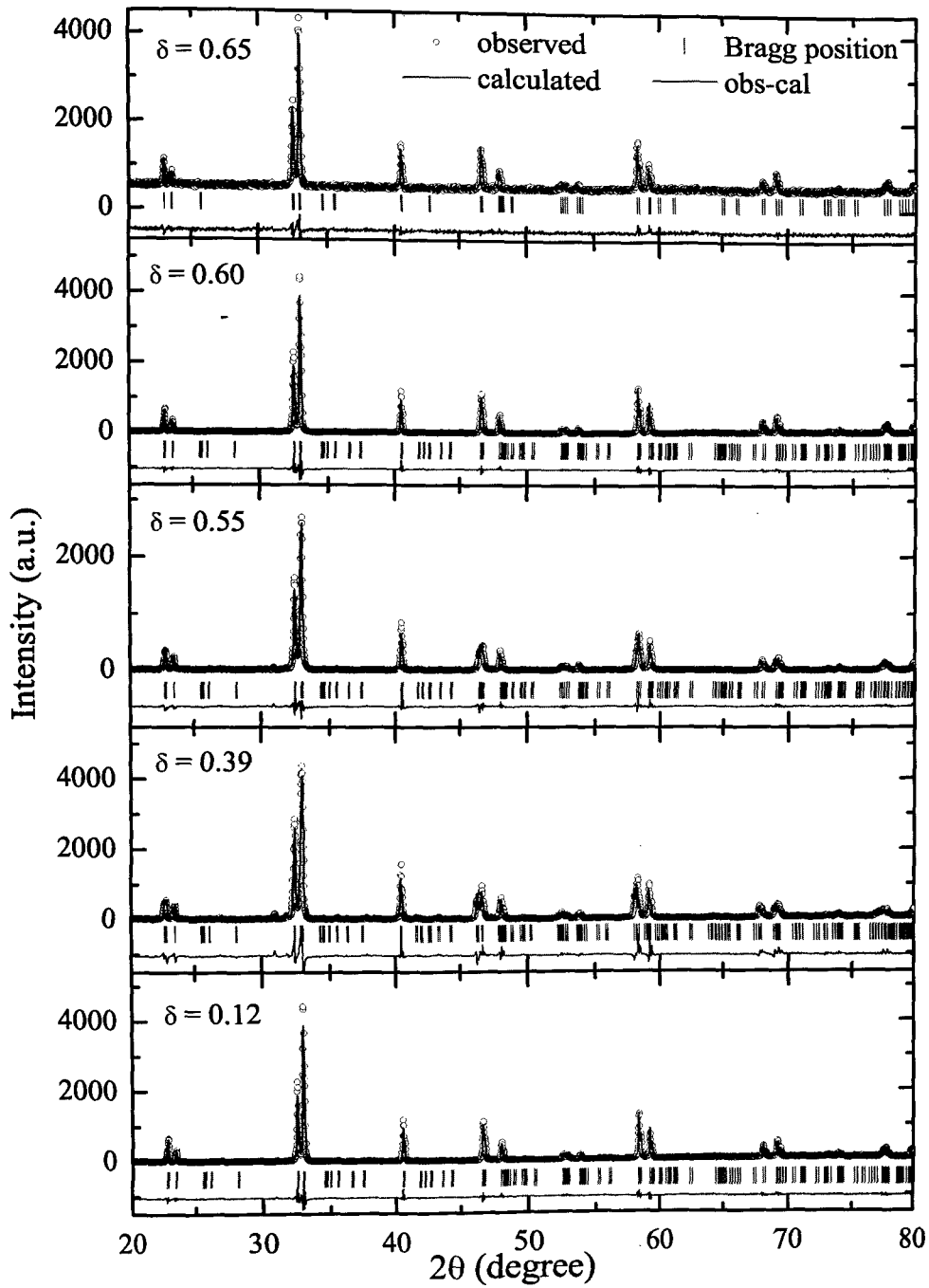


Figure 4.1: Rietveld refined XRD patterns of  $\text{SmBaCo}_2\text{O}_{5+\delta}$ . Circles represent experimental data, continuous line through the data is the fitted curve, vertical lines indicate Bragg positions and the difference pattern is shown at the bottom as solid line.

Tetragonal to orthorhombic transition can be clearly observed. The end members on both sides of  $\delta = 0.5$  crystallize in  $P4/mmm$  tetragonal unit cell while all other intermediate members have orthorhombic structure with  $Pmmm$  space group. Such a structural crossover from tetragonal to orthorhombic unit cell is also reported for  $R = \text{Pr}$  [13, 24]. We therefore present the results of magnetic and transport properties split in three different regions: (i) orthorhombic region ( $\delta = 0.5$  and  $0.39$ ), (ii) oxygen rich region ( $\delta \geq 0.6$ ) and (iii) oxygen deficient tetragonal region ( $\delta = 0.12$ ).

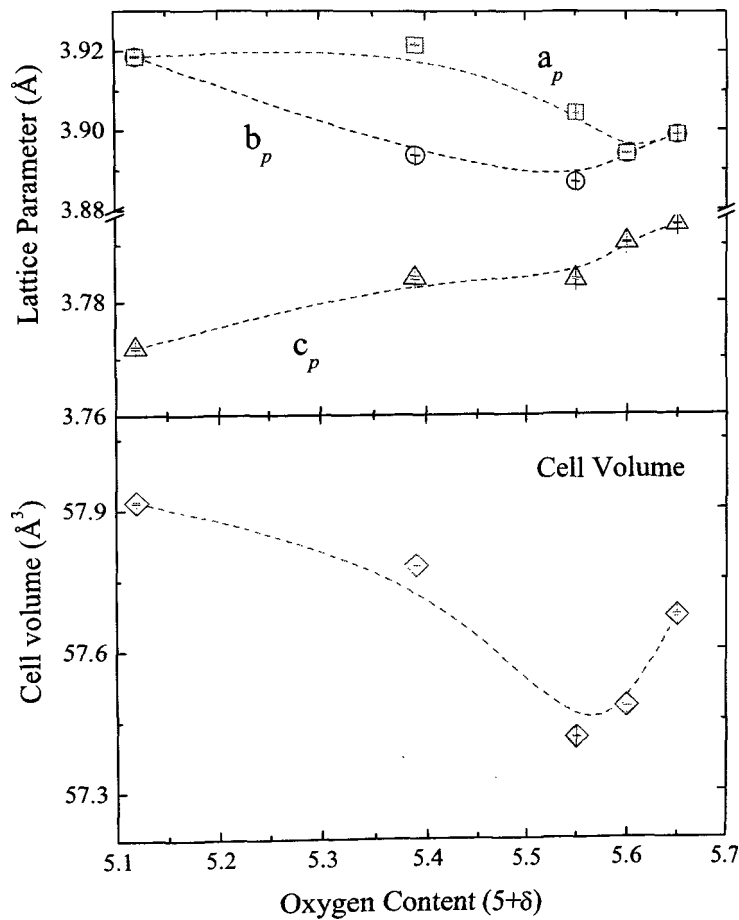


Figure 4.2: Lattice parameter and cell volume obtained from Rietveld refinement

### 4.3 Oxygen rich region ( $\delta = 0.6$ and $0.65$ )

These samples were annealed in oxygen atmosphere. Presence of oxygen content higher than  $\delta = 0.5$  leads to formation of mixed valent  $\text{Co}^{3+}$  and  $\text{Co}^{4+}$  ions. The temperature dependence of magnetization  $M(T)$  measured in different applied magnetic fields is shown in Figure 4.3 (a-d). Magnetization rises steeply below  $T_C = 150$  K indicating ferromagnetic ordering and then drops at lower temperatures indicating a transition to antiferromagnetic state. There is also a wide difference between ZFC and FC curves right down to the lowest temperature of measurement. Such a behaviour of magnetization points towards presence of competing magnetic interactions in these compounds.

A cross-over to negative values of magnetization is also visible in ZFC curves recorded in 100 Oe in both the samples. Magnetic compensation and magnetization reversal can occur in ferrimagnets or in samples which have a minor magnetic phase competing with major phase. Presence of competing magnetic phases in these layered perovskites can be expected due to existence of  $\text{Co}^{4+}$  ions.  $\text{Co}^{3+} - \text{O} - \text{Co}^{4+}$  interaction is known to be ferromagnetic superexchange type as per Goodenough Kanamori rules [25]. While antiferromagnetism can arise due to interactions between  $\text{Co}^{3+}$  ions. A possibility of ferrimagnetic order due to different spin states of  $\text{Co}^{3+}$  ions also cannot be ruled out.

Effect of magnetic field on magnetization of the two oxygen rich samples can be seen in Figures 4.3(c) and (d). It can be seen that just below 150 K, the difference between ZFC and FC magnetization decreases with increasing magnetic field. This difference

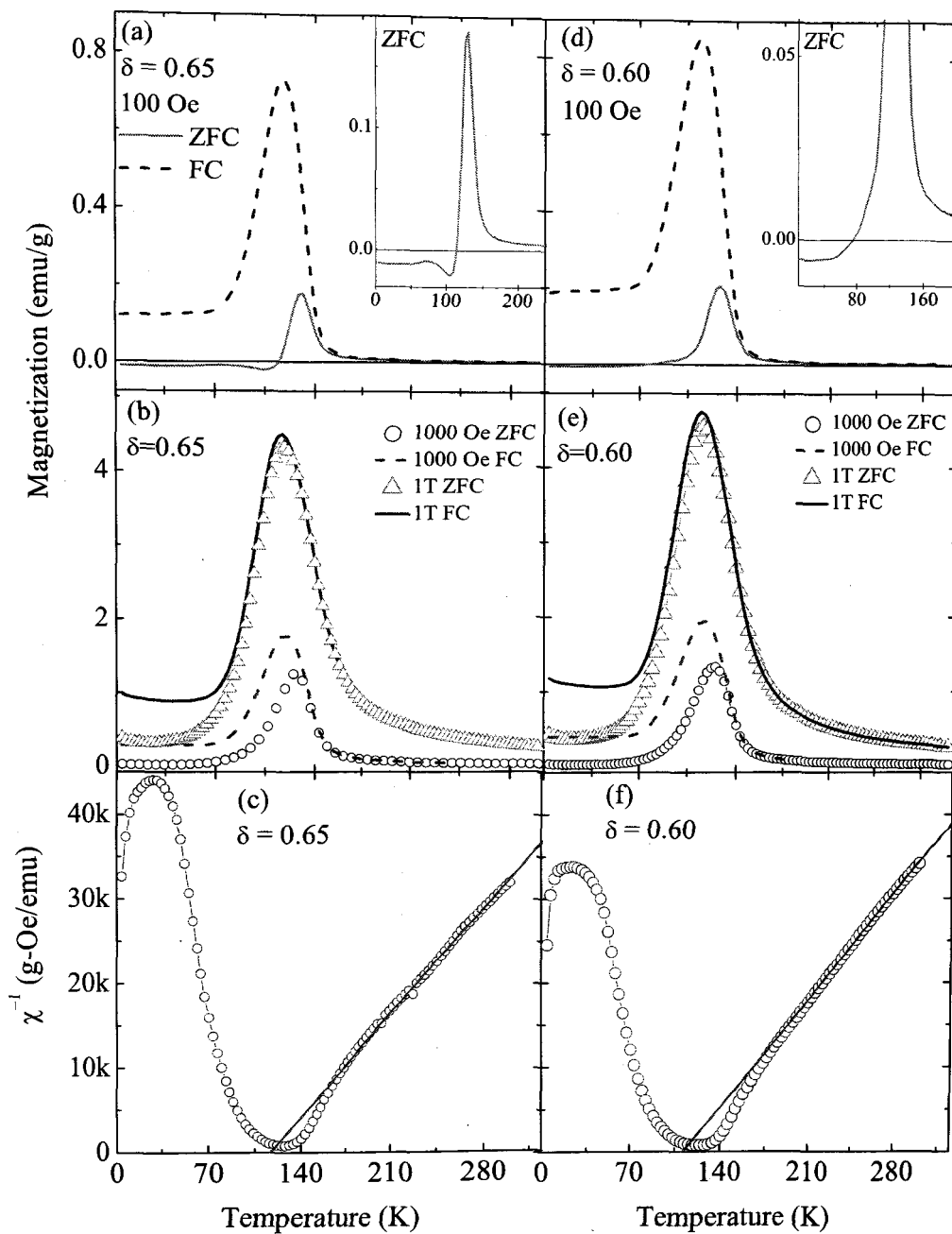


Figure 4.3: Magnetization as a function of temperature for  $\text{SmBaCo}_2\text{O}_{5+\delta}$  compounds for  $\delta = 0.65$  (a) 100Oe, (b) 1000 Oe and 1T, For  $\delta = 0.60$  (d) 100 Oe, (e) 1000Oe and 1T. Insets of (a) and (d) show the enlarged view of ZFC curve. A plot of  $1/\chi$  Vs temperature where in circles denote the experimental data along with Curie-Weiss fit indicated by solid line for (c) $\delta=0.65$  and (f) $\delta=0.60$

almost disappears in magnetization measured in 1T applied field only to reappear again at temperatures below 70 K. Such a behaviour of magnetization as a function of temperature and magnetic field adds weight to the presence of competing magnetic phases in these compounds.

To further discount the possibility of ferrimagnetic order, inverse of magnetic susceptibility  $\chi = M/H$  calculated from magnetization has been plotted against temperature in Figures 4.3(e) and (f) for the two compounds. In both compounds,  $\chi^{-1}$  vs T exhibits a linear behaviour in the high temperature region ( $T > 250$  K) which in agreement with earlier report [27]. This region between 300 K to 250 K was fitted to a Curie-Weiss equation and the values of paramagnetic Curie temperature,  $\theta_p$  and effective magnetic moment  $\mu_{eff}$  were calculated. The values obtained for both compounds were expectedly quite similar with  $\theta_p = 116$  K and 112 K and  $\mu_{eff} = 4.72 \mu_B/f.u.$  and  $4.66 \mu_B/f.u.$  for compounds with  $\delta = 0.65$  and 0.6 respectively. Though our values of  $\mu_{eff}$  are much higher than those reported earlier [27], these are much closer to those obtained in case of other oxygen rich layered perovskites [17, 24]. Furthermore, calculated value of  $\mu_{eff}$  based on assignment of LS state for  $Co^{4+}$  ions and HS/IS state for  $Co^{3+}$  ions is also in much better agreement with those obtained from Curie-Weiss fit. Positive values of  $\theta_p$  indicates presence of ferromagnetic interactions thus strengthening the possibility of competing magnetic phases to be the cause of observed magnetic compensation.

M(H) curves presented in in Figure 4.4 for compounds with  $\delta = 0.6$  and 0.65 also show presence of ferromagnetism right down to 10 K riding on antiferromagnetic background.

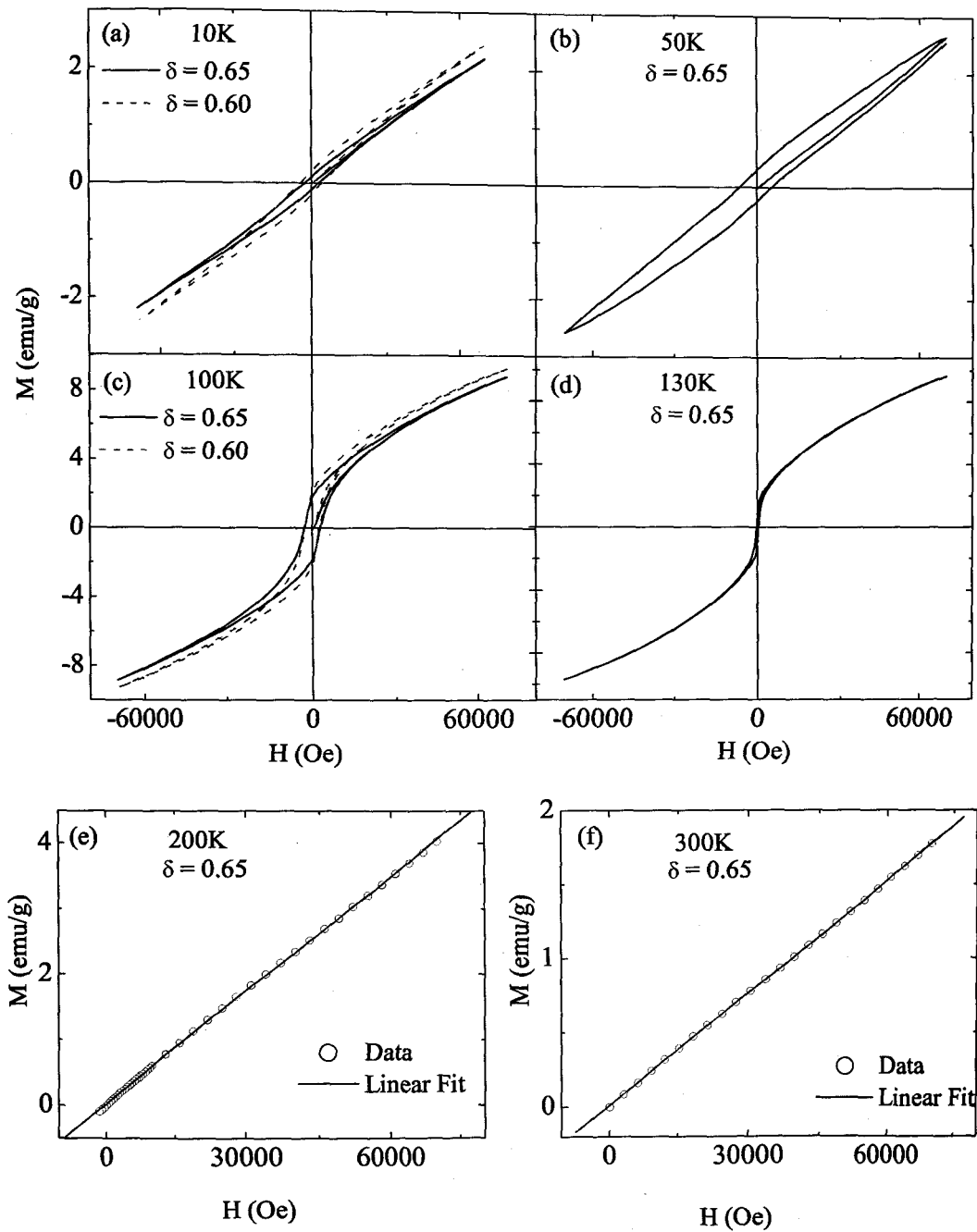


Figure 4.4: Isothermal magnetization curves recorded at (a)10 K, (b)50 K, (c)100 K, (d)130 K (e)200 K and (f)300 K for  $\delta = 0.65$ (solid line) and (a) and (c) for  $\delta = 0.60$ (dotted line).

Hysteresis in magnetization is clearly visible at 10 K. So also the hysteresis loops recorded at 100 K and 130 K exhibit ferromagnetic behavior. At 50 K however, the non closure of hysteresis loop is indicative of strongly competing FM and AFM interactions. This behavior of  $M(H)$  loops is in agreement with high field ( $H = 1T$ )  $M(T)$  curves. From figure 4.3 it can be seen that difference between ZFC and FC magnetization observed below 150 K, reduces with increase in applied magnetic field. At 1T, this difference is significant only below 70 K. It is around this temperature, magnetic compensation and magnetization reversal is observed. Thus field dependent magnetization, magnetic compensation and behavior of  $M(H)$  loops indicate presence of a minor ferromagnetic phase and an antiferromagnetic phase competing against each other in these two oxygen rich  $\text{SmBaCo}_2\text{O}_{5+\delta}$  compounds. Above 150 K magnetization exhibits typical paramagnetic behavior (Figure 4.4(e) and (f)).

The competition between ferromagnetic and antiferromagnetic interactions is also visible in transport and magnetotransport properties. In both the compounds electrical resistivity exhibits semiconducting behaviour in the entire temperature range (10 K - 330 K) with negligible hysteresis between cooling and warming curves (Figure 4.5(a) and (b)). Isothermal magnetoresistance (MR) for  $\text{SmBaCo}_2\text{O}_{5+\delta}$ ,  $\delta = 0.65, 0.60$  measured at 100 K and 200 K in the field range of  $\pm 8T$  are shown in Figure 4.5(c - f). MR is negative but exhibits a crossover to positive values at smaller values of magnetic fields. Similarly, MR recorded during the two directions of ramping of magnetic field is not symmetric. Such a behaviour is usually observed in materials with competing magnetic

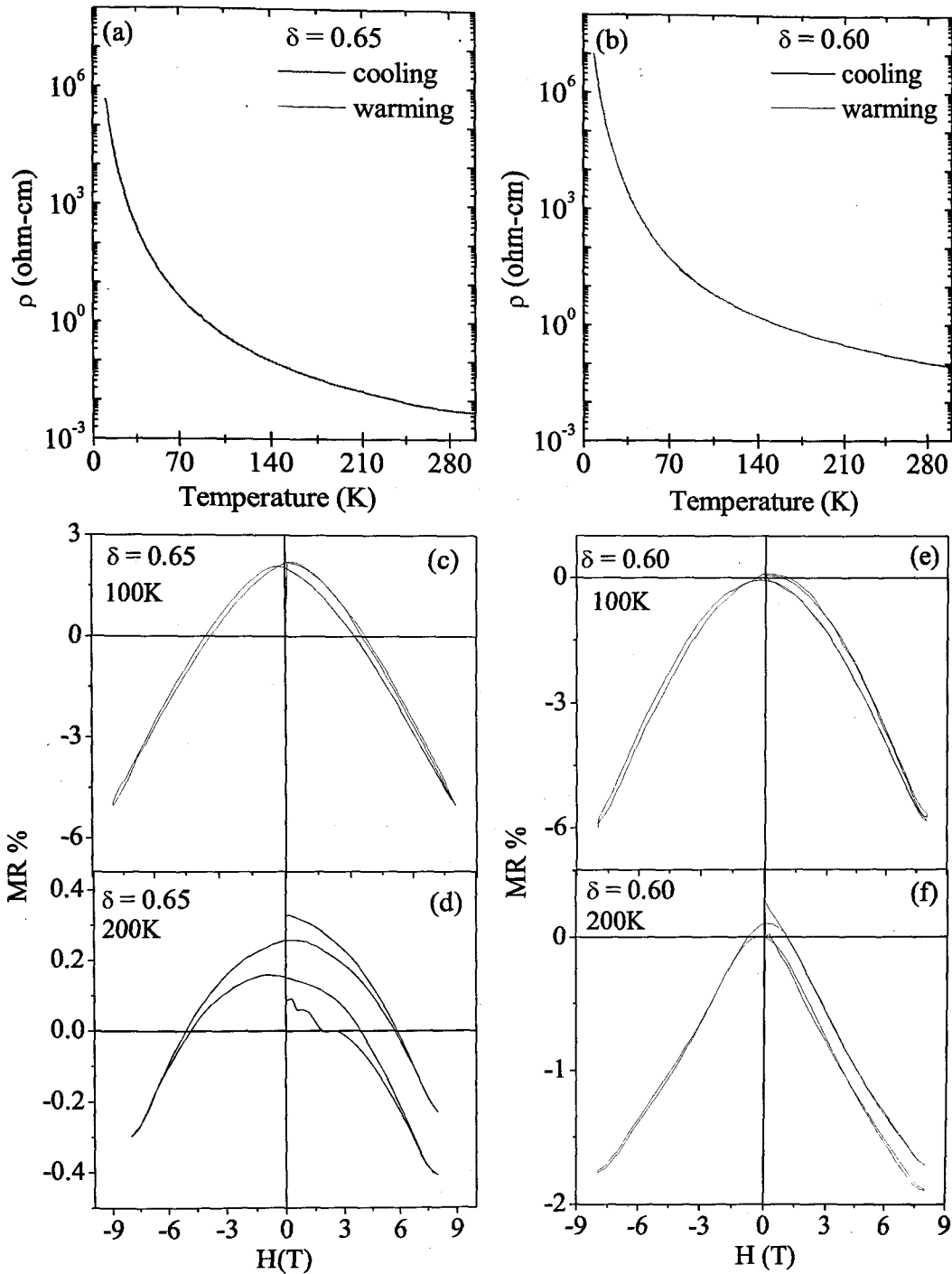


Figure 4.5: (a)-(b) Plot of resistivity with temperature during cooling and warming cycles for  $\delta=0.65$  and  $0.60$  respectively. Isothermal magnetoresistance recorded at 100 K (c)-(e) and 200 K (d)-(f) for  $\delta=0.65$  and  $0.60$  respectively.



interactions. Further, it is interesting to note that compound ( $\delta = 0.65$ ) exhibiting larger magnetization reversal has crossover of MR at higher magnetic fields.

#### 4.4 Orthorhombic region ( $\delta = 0.55$ and $0.39$ )

The samples in the intermediate range of oxygen content form with orthorhombic structure of the type  $2a_p \times 2a_p \times c$ . With change in structure, the physical properties also change. Even though  $\text{Co}^{4+}$  ions are absent, temperature dependent magnetization,  $M(T)$  depicted in Figure 4.6, measured in different applied fields shows a sharp increase at about  $T_{N1} = 255$  K. Neutron diffraction studies on several  $\text{RBaCo}_2\text{O}_{5.5}$  compounds have reported this transition to be antiferromagnetic in nature and the presence of spontaneous magnetic moment is attributed to presence of HS and LS  $\text{Co}^{3+}$  ions in octahedral sites. A equally sharp drop in magnetization just below  $T_{N1}$  confirms the transition to antiferromagnetic state at  $T_{N2} = 200$  K. Another magnetic transition can be seen at around  $T_{R1} = 164$  K. This transition is magnetic field dependent and is also seen in other  $\text{RBaCo}_2\text{O}_{5.5}$  compounds [14, 19, 26, 28]. Wide difference between ZFC and FC magnetization curves at low temperatures indicates complex magnetic ordering in these compounds too. Another important feature to be noted is absence of magnetic compensation and magnetization reversal which was seen in oxygen rich compounds. Such a dramatic change in magnetic properties of these layered perovskites with small changes in oxygen content, though not new has not been clearly understood. It is envisaged that local structure around Co ions plays an important role and will be discussed further in

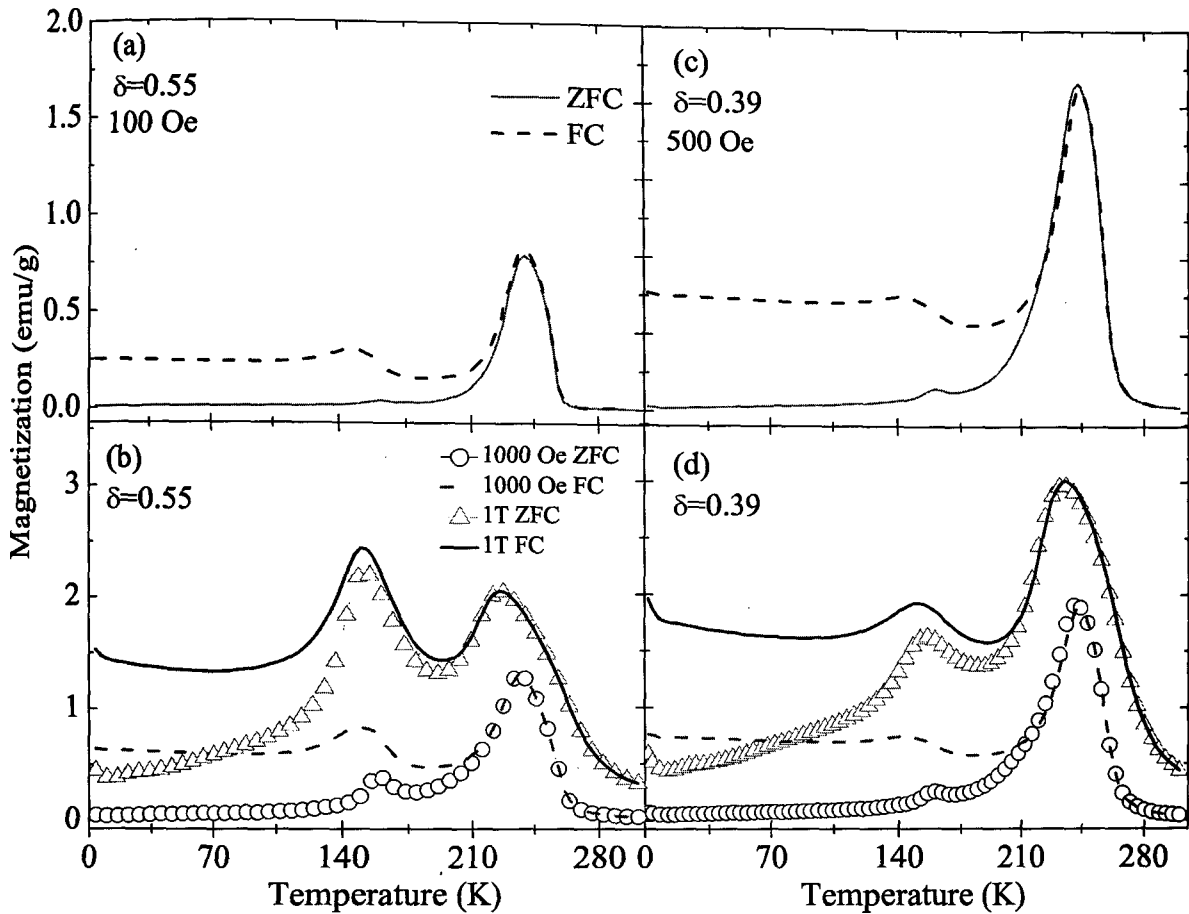


Figure 4.6: Magnetization as a function of temperature for  $\text{SmBaCo}_2\text{O}_{5+\delta}$  compounds for  $\delta = 0.55$  (a) 100Oe, (b) 1000 Oe and 1T, For  $\delta = 0.39$  (c) 500 Oe, (d) 1000Oe and 1T.

this Chapter.

$M(H)$  recorded at various temperatures for  $\delta = 0.55$  and  $0.39$  are depicted in Figure 4.7(a)-(f). Unlike tetragonal oxygen rich samples,  $M(H)$  at 10 K of compound with  $\delta = 0.55$ , does not show the typical bending of magnetization as expected for a ferromagnet. The loops are fairly linear which is a signature of dominant antiferromagnetic interactions but broad indicating presence of other competing magnetic interactions. It may be noted that  $M(H)$  loop for  $\delta = 0.39$  compound recorded at 2 K and in 14 T magnetic field (Figure 4.7(d)) does not show any tendency of saturation confirming presence of strong

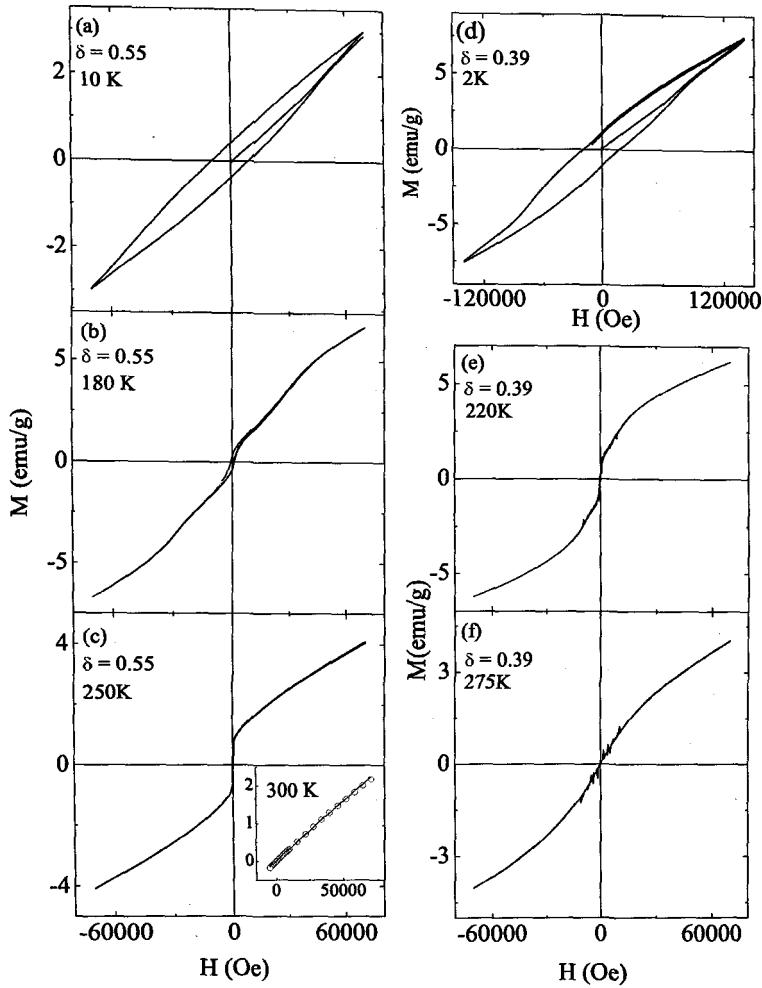


Figure 4.7: Hysteresis loop for  $\delta = 0.55$  recorded at (a) 10 K, (b) 180 K, (c) 250 K, inset in (c) shows  $M$  Vs  $H$  at 300 K and for  $\delta = 0.39$  (d) 2 K, (e) 220 K, (f) 275 K.

antiferromagnetic interactions. At temperatures close to  $T_{R1}$ , step-like behaviour of  $M(H)$  loop is visible (Figure 4.7(b) and (e)) which is indicative of metamagnetic transition. Furthermore,  $M(H)$  loop at 250 K clearly shows presence of spontaneous magnetic moment in very low values of magnetic field and linear increase of magnetization thereafter suggesting antiferromagnetic order.

Electrical resistivity exhibits semiconducting behaviour in the entire temperature range (10 K - 330 K) for both the compounds as shown in Figure 4.8(a) and (b). These

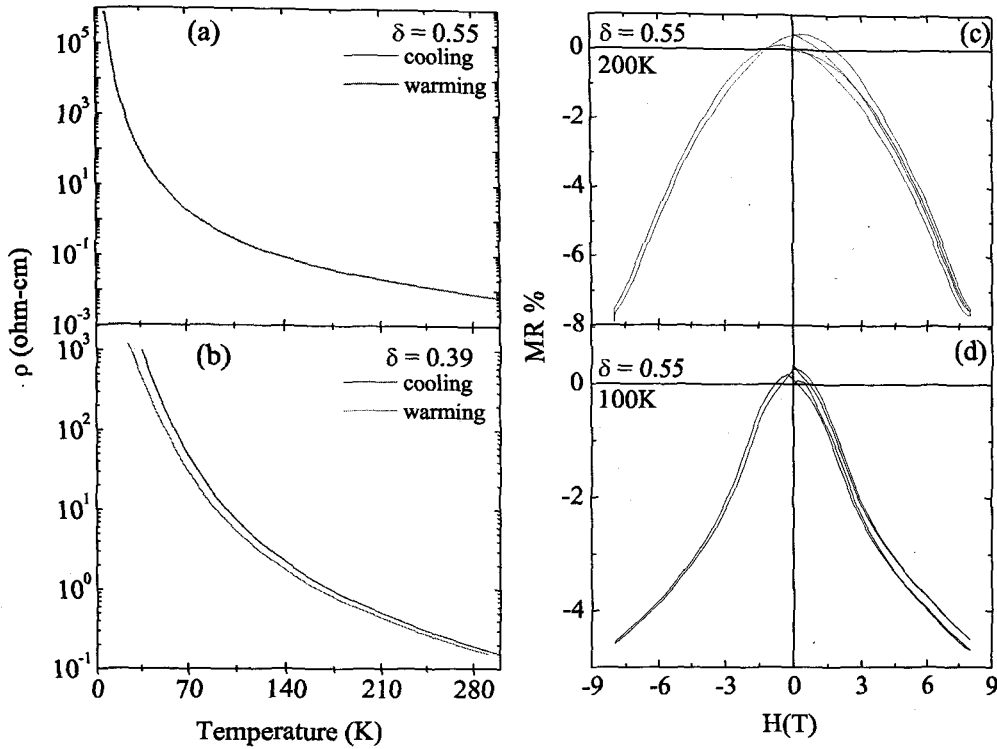


Figure 4.8: (a)-(b) Plot of resistivity with temperature during cooling and warming cycles for  $\delta=0.55$  and  $0.39$  respectively. Isothermal magnetoresistance recorded at for  $\delta=0.55$  at (c) 200 K and (d) 100 K.

compounds are known to exhibit metal insulator transition at temperatures above 340 K [27]. This transition cannot be seen here due to limitation of our temperature range. A comparison of resistivity curves shows that room temperature resistivity is higher than an order in case of  $\delta = 0.39$ . The change in resistivity with decreasing temperature is higher for the sample with  $\delta = 0.39$ . Due to high resistance the data for  $\delta = 0.39$  can not be recorded below 25 K.

Isothermal magnetoresistance (MR) for  $\text{SmBaCo}_2\text{O}_{5.5}$ , measured at 200 K and 100 K in the field range of  $\pm 8$  T is shown in Figures 4.8(c) and (d) respectively. MR is negative which is typical of these layered perovskites [18] even though Co spins align antiferromagnetically. MR in these samples mainly arises due to spin disorder scattering,

the contribution of which decreases with increasing magnetic field. Irreversibility in MR measured during increasing and decreasing field cycles is also seen at both temperatures and in an indication of presence of complex magnetic interactions in the compounds. MR for compound with  $\delta = 0.39$  though very small is similar in trend with that of  $\delta = 0.55$  and hence is not presented here.

## 4.5 Oxygen deficient tetragonal region ( $\delta = 0.12$ )

Further decreasing in oxygen content results in a structural change from orthorhombic to tetragonal. The temperature dependence of magnetization  $M(T)$  measured in applied fields of 100Oe and 1000Oe is shown in Figure 4.9(a) and (b) respectively. A para to ferromagnetic transition can be clearly seen at  $T_C = 278$  K. Though there is a decrease in magnetization below the transition temperature indicating onset of antiferromagnetic transition, it is quite gradual as compared to orthorhombic compounds. This decrease is even more gradual in the field cooled magnetization curve. Such a behaviour of magnetization suggests presence of ferromagnetic component even at low temperatures. The temperature evolution of field cooled magnetization curve and magnetization measured at 1000 Oe indicate strengthening of ferromagnetic interactions under applied magnetic field. Furthermore, as in case of oxygen rich tetragonal samples, magnetic compensation and magnetization reversal is visible also in this compound. Strongly competing ferromagnetic and antiferromagnetic interactions could be responsible for this magnetic compensation. Magnetic compensation occurs at about 250 K and at all lower temper-

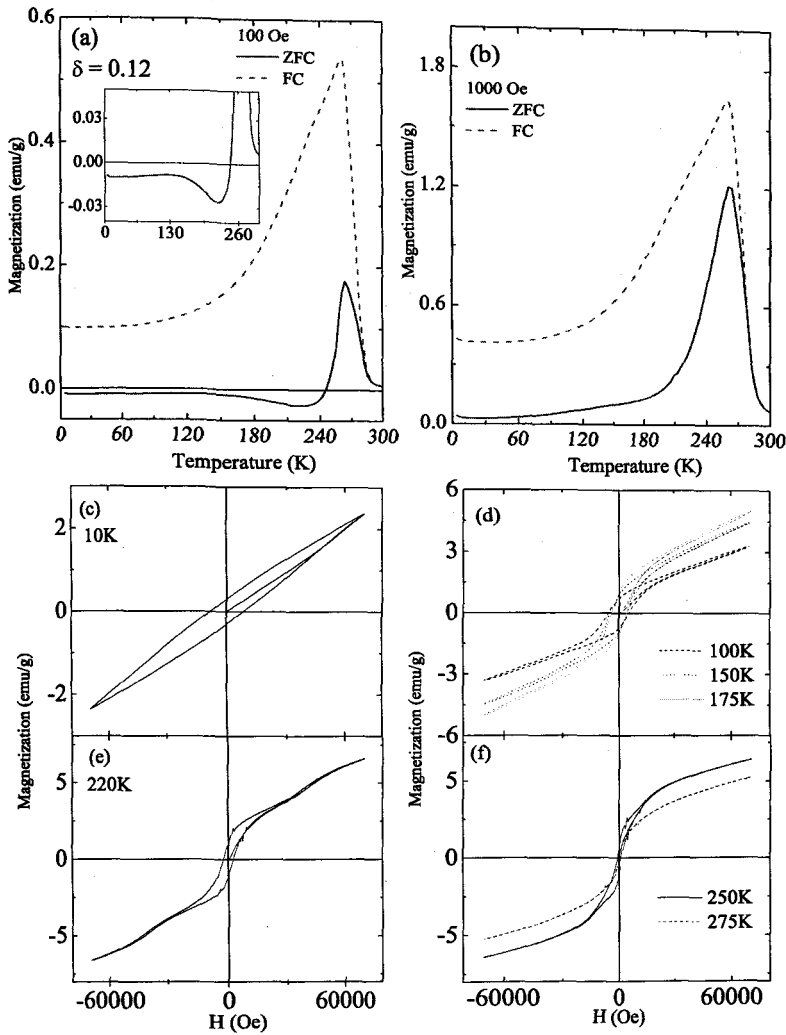


Figure 4.9: Magnetization as a function of temperature for  $\text{SmBaCo}_2\text{O}_{5.12}$  compounds (a) 100Oe, inset of (a) shows enlarged view of ZFC curve, (b) 1000 Oe

ature magnetization has negative values. Second point of distinction from orthorhombic compounds is the transition at 164 K. However it must be mentioned that a small hump at about 120 K is visible in data recorded under 1000 Oe magnetic field. Around the same temperature, magnetization at 100 Oe also shows a maxima (see inset of Figure 4.9(a)).

$M(H)$  recorded at various temperatures for  $\delta = 0.12$  are presented in Figure 4.9(c - f). Though a broad hysteresis loop is seen at 10 K, comparatively smaller magnitude of

magnetization and nearly linear evolution of magnetization with magnetic field suggests strong competition between ferro and antiferromagnetic interactions. FM phase appears to be dominant in the range range of 100 K to 175 K (Figure 4.9(d)). A field induced metamagnetic transition is visible at about 3T in the hysteresis loop recorded at 220 K. Metamagnetic transition is also visible at 250 K but at much lower field. It may be recalled that magnetization suffers a reversal in this temperature range with a minima around 220 K. At 275 K hysteresis presented is of a typical ferromagnet with very weak coercivity. This is expected as this temperature is very close to  $T_C$ .

Electrical resistivity measured in the temperature range 120 K to 330 K exhibits semiconducting behaviour as can be seen in Figure 4.10(a). The resistivity values are quite high and hence data below 120 K could not be recorded. It may be mentioned here that this compound shows highest value of room temperature resistance. In general the resistivity increases with decreasing oxygen content.

## 4.6 X-ray Absorption Near Edge spectroscopic studies

Co K edge XANES spectroscopy is a valuable tool in probing the local structure around Co ion and can shed light on the reasons behind complex magnetic behaviour exhibited by these layered perovskites. Normalized XANES spectra for three compositions of  $\text{SmBaCo}_2\text{O}_{5+\delta}$ , ( $\delta = 0.12, 0.55$  and  $0.60$ ) one each belonging to the three groups discussed above are presented in Figure 4.11. All the edges are normalized to an average absorption between +55 to +60 eV beyond the absorption edge. XANES features in all the samples

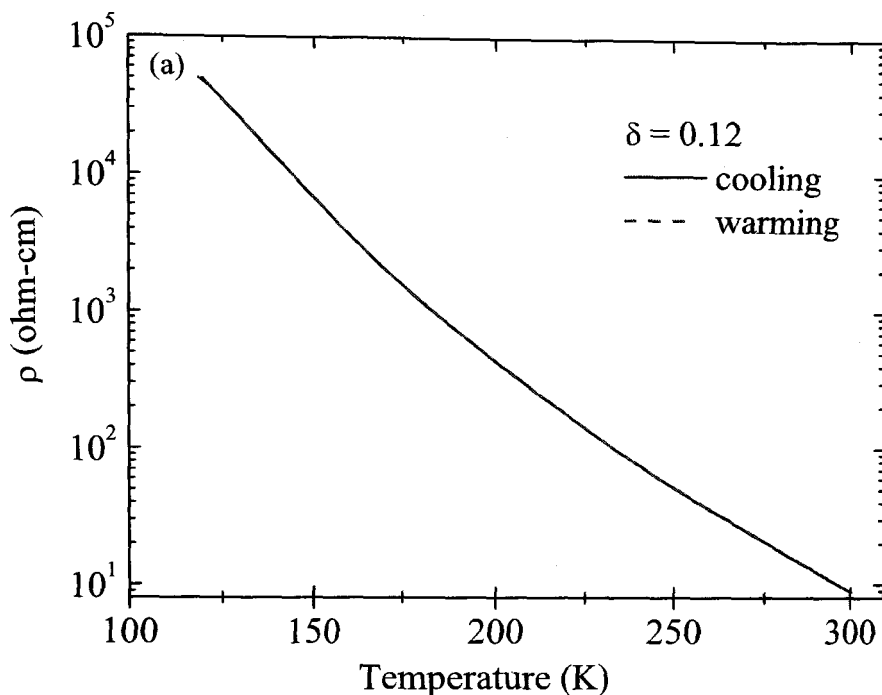


Figure 4.10: (a) Plot of resistivity with temperature during cooling and warming cycles, inset (b) Isothermal magnetoresistance recorded at for 300 K for  $\delta=0.12$ .

part of the absorption curve at about 7720 eV, the main resonance peak around 7725 eV followed by two maxima at about 7733 eV and 7740 eV. A third maxima at about 7750 eV is seen due to interfering Sm  $L_1$  edge which occurs at 7745 eV. Another difference that can be readily seen is the shift in edge energy in  $\text{SmBaCo}_2\text{O}_{5.12}$  and the other two compounds. In the oxygen deficient compound, Co is in  $2+/3+$  state and as a result there is a higher screening of the nuclear charge by the electronic charge as compared to the other two compounds.

Pre-edge feature (top inset of Figure 4.11) represents a selection rule disallowed transition from  $1s \rightarrow 3d$  states, made allowed due to quadrupolar splitting or due to hybridization of  $3d$  states with ligand  $p$  states. Its contribution to the XANES spectra was



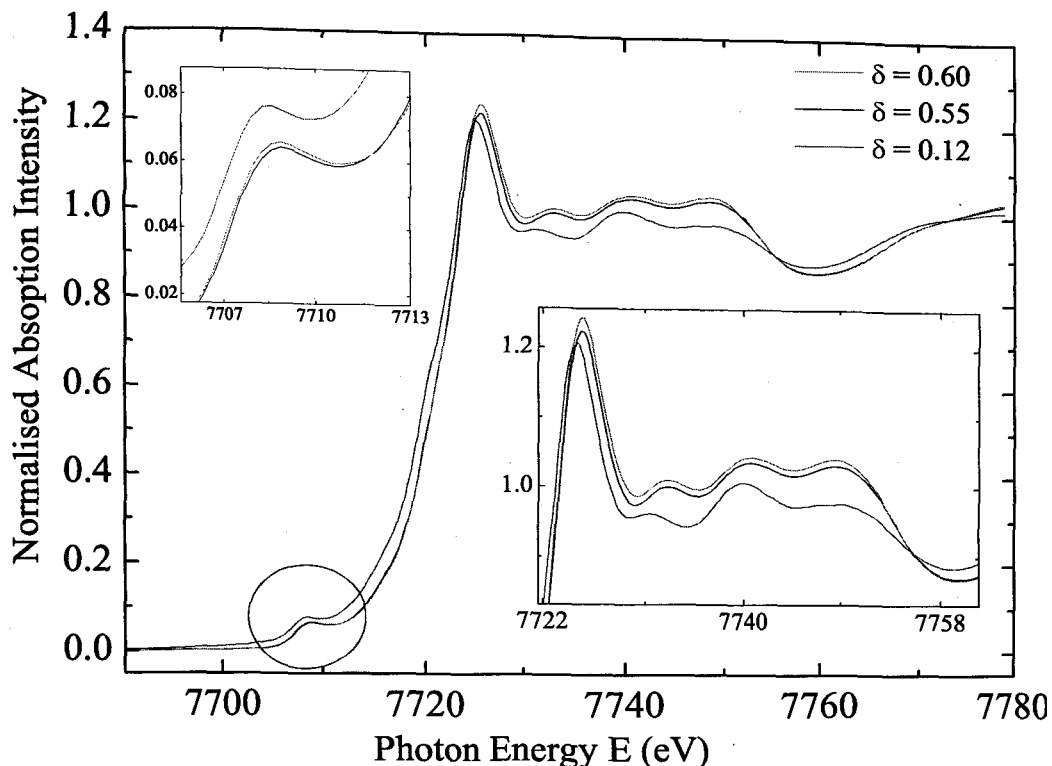


Figure 4.11: Normalised Co K XANES at room temperature with top inset shows pre-edge and down right inset shows enlarged region of XANES for  $\text{SmBaCo}_2\text{O}_{5+\delta}$ ,  $\delta = 0.60$ , 0.55 and 0.12

bridization of  $3d$  states with ligand  $p$  states. Its contribution to the XANES spectra was extracted by subtracting a spline curve as base line from near edge data. The resultant spectra was used to extract the value of crystal field (CF) splitting of the  $3d$  orbital in each of the three compounds. In all of them the pre-edge peak can be deconvoluted into three peaks corresponding to transition of core electron to  $e_{g\uparrow}$ ,  $t_{2g\downarrow}$  and  $e_{g\downarrow}$  respectively. The fitting parameters for pre-edge peaks are given in Table 4.1. The CF splitting was estimated to be around 1 to 1.5 eV with a maximum of 1.5 eV in compound with  $\delta = 0.55$ . This could be the reason for presence of low spin Co ions in octahedral sites in  $\text{SmBaCo}_2\text{O}_{5.55}$ .

XANES features arise due to multiple scattering of the ejected photoelectron by the

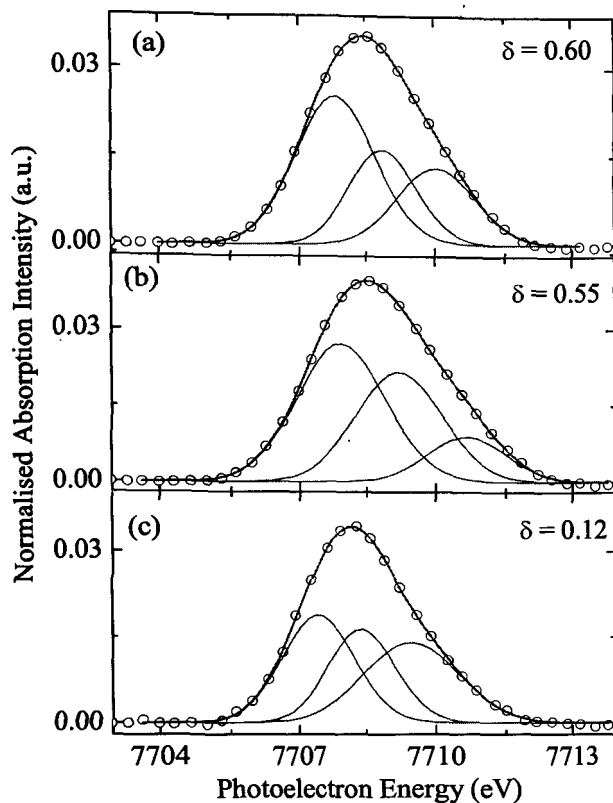


Figure 4.12: Deconvolution of pre-edge peak, circles indicates XANES data along with best fit curves (solid lines) which is a sum of three constituent Gaussian peaks for (a)  $\delta = 0.60$ , (b)  $\delta = 0.55$  and (c)  $\delta = 0.12$

continuum states and therefore their relative position and intensity give a clue about physical properties of the compounds. An expanded view of XANES features is presented in the lower inset of Figure 4.11. It can be seen that with increase in oxygen content the relative position of the first XANES feature with respect to main resonance peak changes. This feature arises due to hybridization between Co  $4p$  and O  $2p$  states. In order to understand the relative contribution of each ion to the XANES features an attempt has been made to calculate Co K edges in all these three compounds. Full scale multiple scattering calculations to calculate the absorption edge and partial density of states contribution of each ion to the XANES features were performed using FEFF8.4 [29]. These calculations

attempt has been made to calculate Co K edges in all these three compounds. Full scale multiple scattering calculations to calculate the absorption edge and partial density of states contribution of each ion to the XANES features were performed using FEFF8.4 [29]. These calculations were performed for (i) tetragonal structure for fully oxygenated compound ( $\text{SmBaCo}_2\text{O}_6$ ), (ii)  $\text{SmBaCo}_2\text{O}_5$  representing the oxygen deficient structure and (iii) orthorhombic  $\text{SmBaCo}_2\text{O}_{5.5}$  structure. In case of orthorhombic compound, the calculations were performed by setting both Co ions at square pyramidal site (Co1) and the octahedral site (Co2). These calculated spectra were respectively compared with Co K edges recorded in  $\text{SmBaCo}_2\text{O}_{5.65}$ ,  $\text{SmBaCo}_2\text{O}_{5.12}$  and  $\text{SmBaCo}_2\text{O}_{5.55}$ . The spherical muffin tin potentials were self consistently calculated over a radius of 9Å. A default overlapping muffin tin potentials and Hedin-Lunqvist exchange correlations were used to calculate X-ray absorption transitions to a fully relaxed final state in presence of a core hole. An energy shift of 2 eV was applied to achieve a better description of pre-edge absorption at the Co K edge. A comparison of calculated spectra and experimental absorption curves along with partial density of states (pDOS) of each of the contributing ion is presented in Figure 4.13.

Calculated spectra are rigidly shifted up for clarity. It can be seen that all the XANES features are well reproduced in the FEFF calculated curves. As earlier stated the third feature at 7750 eV is due to contribution from Sm  $L_1$  edge and hence cannot be seen in the calculated spectra. The calculations suggest that the feature at 7733 eV has contribution from unoccupied  $p$  states of Sm/Ba ions, Co  $4p$  states and O  $2p$  states. Whereas, the

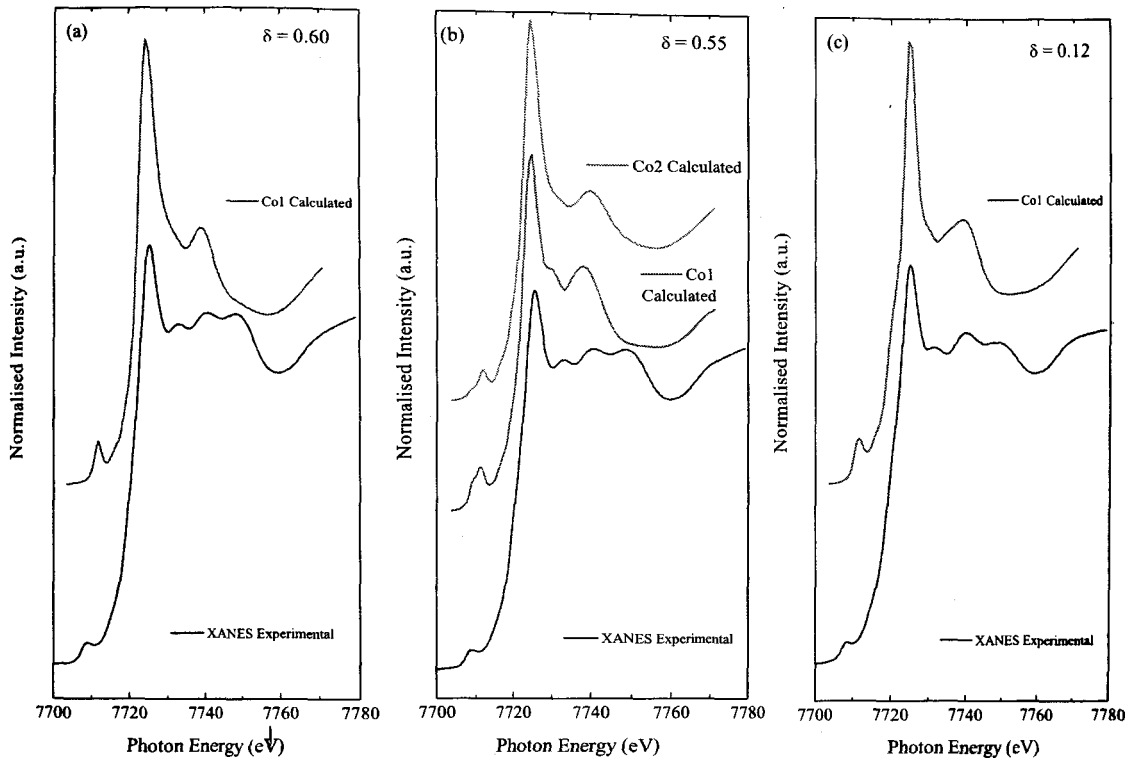


Figure 4.13: Calculated Co K edge XANES for  $\text{SmBaCo}_2\text{O}_{5+\delta}$  for square pyramidal (Co1), octahedral (Co2) site and experimental absorption curves for (a)  $\delta = 0.60$ , (b)  $\delta = 0.55$  and (c)  $\delta = 0.12$ .

peak at 7740 eV is a result of hybridization between Co 4p and O 2p states. The pDOS contributions indicate that maximum Co-O hybridization occurs in compound with least oxygen content while the oxygen rich compound has the least hybridization. Higher hybridization in oxygen deficient compounds leads to localization of the charge carriers which result in higher resistivity. In fact there is a systematic decrease in the room temperature value of resistance with increase in  $\delta$  which correlates well with the observed changes in Co-O hybridization.

## 4.7 Conclusion

Study of sol-gel synthesized layered perovskites,  $\text{SmBaCo}_2\text{O}_{5+\delta}$  shows that these compounds exhibit several magnetic transitions and exhibit a complex magnetic ground state. Compounds with excess or deficient oxygen compared to  $\delta = 0.5$  show have tetragonal structure and exhibit phenomena of magnetic compensation and magnetization reversal. Change in structural symmetry is seen to affect the crystal field splitting of the Co 3d state. The orthorhombic compounds exhibit higher crystal field splitting compared to oxygen rich or oxygen deficient tetragonal compounds. Lower crystal field implies  $\text{Co}^{3+}$  ions in  $S \neq 0$  spin state and therefore participating in magnetic interactions. This results in competing magnetic interactions which can lead to magnetic compensation and negative net magnetization. In case of orthorhombic compounds, crystal field splitting is higher which can drive  $\text{Co}^{3+}$  ions in LS state. Indeed magnetization studies show dominance of antiferromagnetic interactions and no magnetic compensation. In compounds involving  $\text{Co}^{2+}/\text{Co}^{3+}$  mixed valency, a higher degree of Co - O hybridization can be seen from XANES calculations. The hybridization decreases with increasing oxygen content and so also the resistivity. Our studies therefore show that oxygen content greatly influences the local structure around Co ions which in turn plays an important role in magnetic and transport properties of these layered perovskites.

# References

- [1] Maignan A, Martin C, Pelloquin D, Nguyen N, and Raveau B 1999 *J. Solid State Chem.* **142** 247
- [2] Martin C, Maignan A, Pelloquin D, Nguyen N, and Raveau B 1997 *Appl. Phys. Lett.* **71** 1421
- [3] Moritomo Y, Akimoto T, Takeo M, Machida A, Nishibori E, Takata M, Sakata M, Ohoyama K and Nakamura A 2000 *Phys. Rev. B* **61** R13325
- [4] Respaud M, Frontera C, García-Muñoz J, Aranda A G M, Raquet B, Broto J, Rakoto H, Goiran M, Llobet A, and Carvajal J 2001 *Phys. Rev. B* **64** 214401
- [5] Vogt T, Woodward P M, Karen P, Hunter B A, Henning P, and Moodenbaugh A R 2000 *Phys. Rev. Lett.* **84** 2969
- [6] Suard E, Fauth F, Caignaert V, Mirebeau I and Baldinozziet G 2000 *Phys. Rev. B* **61** R11871
- [7] Troyanchuk I, Kasper N, and Khalyavin D D 1998 *Phys. Rev. Lett.* **80** 3380
- [8] Frontera C, García-Muñoz J, Llobet A, and Aranda M 2002 *Phys. Rev. B* **65** 180405

- [9] Khalyavin D D, Barilo S, Shiryaev S, Bychkov G, Troyanchuk I, Furrer A, Alenspach P, Szymczak S and Szymczak R 2003 *Phys. Rev. B* **67** 214421
- [10] Pomjakushina E, Conder K and Pomjakushin V 2006 *Phys. Rev. B* **73** 113105
- [11] Streule S, Podlesnyak A, Mesot J, Medared M, Conder K, Pomjakushina E, Mitberg E and Kozhevnikov V 2005 *J. Phys: Condens. Matter* **17** 3317
- [12] Diaz-Fernandez Y, Malavasi L and Mozzati M C 2008 *Phys. Rev. B* **78** 144405
- [13] Frontera C, Carrillo A, Oró-Solé J and García-Muñoz J L 2005 *Chem. Mater* **17** 5439-5445
- [14] Plakhty V, Chernenkov P, Barilo S, Podlesnyak E, Pomjakushina E, Moskvina E and Gavrilov S 2005 *Phys. Rev. B* **71** 214407
- [15] Fauth F, Suard E, Caignaert V and Mirebeau I 2002 *Phys. Rev. B* **66** 184421
- [16] Soda M, Yasui Y, Ito M, Iikubo S and Sato M 2003 *J. Phys. Soc. Jpn.* **72** 1729
- [17] Frontera C, García-Muñoz J L, Carrillo A, Aranda M A G, Margiolaki I and Caneiro A 2006 *Phys. Rev. B* **74** 054406
- [18] Taskin A , Lavrov A N and Ando 2003 *Phys. Rev. Lett.* **90** 227201
- [19] Luetkens H, Stingaciu M, Pashkevich Y, Conder K, Pomjakushina E, Gusev A, Lamonova K, Lemmens P and Klauss H 2008 *Phys. Rev. Lett.* **101** 017601
- [20] Wu H 2003 *J. Phys.: Condens. Matter* **15** 503

- [21] Flavell W, Thomas A, Tsoutsou D, Mallick A, North M, Seddon E, Cacho C, Malins A, Patel S, Stockbauer R, Kurtz R, Sprunger P, Barilo S, Shiryaev S, and Bychkov G 2004 *Phys. Rev. B* **70** 224427
- [22] Raveau B, Seikh M M, Pralong V and Caignaert V 2009 *Bull. Mater. Sci.* **32** 305-312
- [23] Conder K, Pomjakushina E, Soldatov A and Mitberg E 2005 *Mater. Res. Bull.* **40** 257
- [24] Ganorkar S, Priolkar K R, Sarode P R, and Banerjee A 2011 *J. Appl. Phys.* **110** 053923
- [25] Goodenough J 1963 *Magnetism and the Chemical Bond*; Wiley-Interscience:New York
- [26] Jarry A, Luetkens H, Pashkevich Y, Stingaciu M, Pomjakushina E, Conder K, Lemmens P and Klaus H 2009 *Physica B* **404** 765
- [27] Seikh M M, Simon Ch, Caignaert V, Pralong V, Lepetit M B, Boudin S, and Raveau B 2008 *Chem. Mater.* **20** 231-238
- [28] Zhou Z X, McCall S, Alexander C S, Crow J E, and Schlottmann P 2004 *Phys. Rev. B* **70** 024425
- [29] Zabinsky S I, Rehr J J, Ankudinov A, Albers R C and Eller M J 1995



## Chapter 5

# Effect of $Co3d-O2p$ Hybridization on Magnetic and Transport Properties of $PrBaCo_2O_{5.50}$

### 5.1 Introduction

The layered perovskites  $RBaCo_2O_{5+\delta}$ , ( $R$  = rare earth elements;  $0 \leq \delta \leq 1$ ) which are well known for strong electronic correlations gained importance due to their unique properties like metal insulator transition (MIT), spin state transitions, charge ordering and giant magnetoresistance [1, 2, 3, 4, 5, 6, 7]. A complete understanding of factors responsible for the above properties is still elusive. Oxygen non-stoichiometry is one of the important factor in deciding their structural, magnetic and transport properties [8, 9]. Tailoring of oxygen not only gives rise to various valance states ( $2^+$ ,  $3^+$ ,  $4^+$ ) of cobalt ion but also to different local environments (octahedral, square pyramidal). Furthermore, Co ion can undergo spin state transitions. All these factors are believed to play a crucial role in the physical properties of these compounds.

Particularly special is  $RBaCo_2O_{5.5}$  because it undergoes many different transitions as a function of temperature like the MIT, followed by paramagnetic(PM) to Ferromag-

netic(FM), and FM to Antiferromagnetic (AFM) transitions [10, 11, 12]. Although all Co ions are in trivalent state, they are surrounded alternately by octahedral and square pyramidal oxygen environment. Ionic differences between the R and Ba ions cause distortions in oxygen cages leading  $\text{Co}^{3+}$  ion to have any of the three possible spin states: the low spin state (LS,  $t_{2g}^6 e_g^0$ ,  $S=0$ ), the intermediate spin state (IS,  $t_{2g}^5 e_g^1$ ,  $S=1$ ) and high spin state (HS,  $t_{2g}^4 e_g^2$ ,  $S=2$ ) [13, 14, 15]. Magnetic properties and the nature of magnetic transitions are therefore described to be dependent of the size of the rare-earth ions [16]. Neutron diffraction studies on  $\text{PrBaCo}_2\text{O}_{5.5}$  [10] reveal  $\text{Co}^{3+}$  ions occupying square pyramidal sites to be in IS state and those occupying octahedral sites to be in LS state. Such a arrangement sustains two types of magnetic interactions along the  $c$ -axis, a strong AFM superexchange interaction between pyramidal Co ions that share a oxygen ion between them and a weak AFM direct exchange interaction between two pyramids connected through a oxide ion vacancy. However, the best fit to the experimental data considers a small magnetic moment for LS octahedral Co ion which is ascribed to imperfect ordering of octahedra and square pyramids in the compound. Similar studies on  $\text{NdBaCo}_2\text{O}_{5.47}$  suggest a spin state ordering (SSO) below 230 K, with one of the octahedral Co ion switching from LS to HS state [17]. SSO is also invoked to explain magnetic properties of  $\text{YBaCo}_2\text{O}_{5.5}$  [18]. Such SSO transitions are also observed in  $\text{TbBaCo}_2\text{O}_{5.5}$  and  $\text{LaBaCo}_2\text{O}_{5.5}$  at low temperatures [19, 20]. Muon spin relaxation studies ( $\mu\text{SR}$ ) show presence of two AFM phases with different SSO and these are independent of the rare earth ion [12]. Resonant photoemission studies [21] and density functional calculations

[22, 23] suggest HS  $\text{Co}^{3+}$  ions in octahedral sites. Successive magnetic transitions and spin reorientations are interpreted as a result of strong hybridization between  $\text{O}2p$  and  $\text{Co}3d$  orbitals. Furthermore, the transport and magneto-transport properties of these layered cobaltites are also closely related to the magnetic properties indicating a strong correlation between the magnetic and charge degrees of freedom. In particular, a giant negative magnetoresistance (MR) in  $\text{GdBaCo}_2\text{O}_{5.5}$  [2] and strong irreversibility of MR in  $\text{LaBaCo}_2\text{O}_{5.5}$  [20] are observed near the FM - AFM phase boundary. Therefore a detailed study of the spin state of Co ion and its interaction with neighboring oxygen ions is necessary to derive a complete understanding of magnetic and transport properties of these layered perovskites especially below MIT.

$\text{RBaCo}_2\text{O}_{5.5}$  are structural derivatives of  $\text{RCoO}_3$  with an alternate arrangement of  $\text{CoO}_6$  octahedra and  $\text{CoO}_5$  square pyramids. However, the Co polyhedra are more distorted in the double perovskites [14, 15] as compared to those in  $\text{RCoO}_3$  [24, 25, 26, 27]. X-ray absorption fine structure spectroscopy (XAFS) at the Co K-edge has been successfully used to investigate the local structural disorder, electronic properties and the spin state of Co ion in  $\text{RCoO}_3$  compounds [29, 30, 31]. In this Chapter, we focus our attention on studying the temperature evolution of local environment of Co ions and their spin states in  $\text{PrBaCo}_2\text{O}_{5.5}$  using XAFS. We have concentrated on temperatures below MIT and in particular in the temperature range  $100 \text{ K} \leq T \leq 325 \text{ K}$ . Pr  $L$  absorption edges occur at much lower energies as compared to Co  $K$  edge hence do not interfere in the near edge structure or the fine structure of Co  $K$  edge. The sample was prepared as

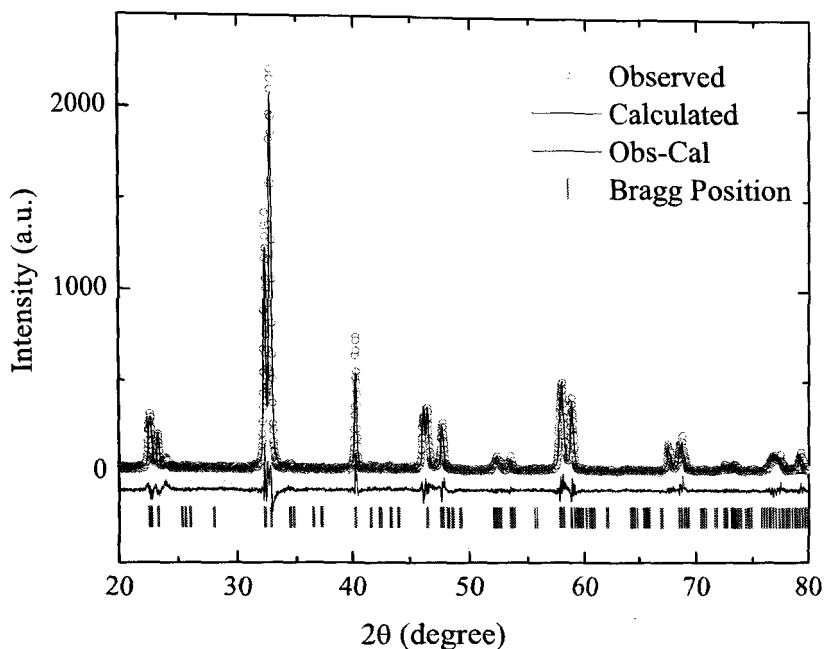


Figure 5.1: Rietveld refinement of XRD pattern of  $\text{PrBaCo}_2\text{O}_{5.5}$ . Circles represent experimental data, a continuous line through the data is the fitted curve and the difference pattern is shown at the bottom as solid line.

described in section 2.2 and the oxygen content was determined by iodometric titration.

Its value was found to be  $0.50 \pm 0.01$ .

## 5.2 X-ray Diffraction Studies

Rietveld refinement of XRD pattern of  $\text{PrBaCo}_2\text{O}_{5.50}$  confirms the formation of single phase sample with 122 type orthorhombic unit cell belonging to Pmmm space group and is presented in Figure 5.1. The lattice parameters obtained from the fitting are  $a=3.9355(1)\text{\AA}$ ,  $b=7.8175(3)\text{\AA}$  and  $c=7.6245(2)\text{\AA}$ .

### 5.3 Magnetization Measurements

The temperature dependence of magnetization  $M(T)$  measured at 100 Oe is shown in Figure 5.2(a). The curves show PM-FM like transition characterized by an increase in magnetization at  $T_C = 246$  K followed by a decrease in magnetization which is designated as FM-AFM transition at  $T_N = 200$  K. It must be mentioned here that neutron diffraction measurements ascribe both these transitions at 246 K and 200 K as antiferromagnetic in nature [10]. A closer examination of  $M(T)$  curves indicates presence of few more magnetic transitions at low temperatures. Apart from the PM to FM transition another transition is visible at  $T_{R1} \sim 50$  K which has not been hitherto reported as indicated by an arrow in Figure 5.2(a). Muon spin relaxation ( $\mu$ SR) studies on  $\text{NdBaCo}_2\text{O}_{5.5}$  attribute the transition around 50 K to a magnetic phase transition [16].

To investigate the effect of magnetic field on the above magnetic transition temperatures and magnetization in general,  $M(T)$  have been recorded at 1000 Oe and 1 T during ZFC, FCC and FCW cycles (see Figure 5.2(b) and (c)). It is clear from the Figure 5.2(b) and (c) ferromagnetism seems to strengthen with the application of field. This lends weight to the hypothesis of electronic phase separation in these compounds. A small amount of thermal hysteresis that increases with decreasing  $\delta$  is still observed below  $T_C$  even in fields of 1 T confirming the presence of a complex magnetic ground state as was evident from magnetization curves at 100 Oe. One can also notice a crossover between FCC and FCW magnetization curves at around 225 K. At lower temperature ( $50 \text{ K} \leq T \leq 225 \text{ K}$ ), the FCW magnetization curve lies below the FCC curve while above  $T \geq 225$

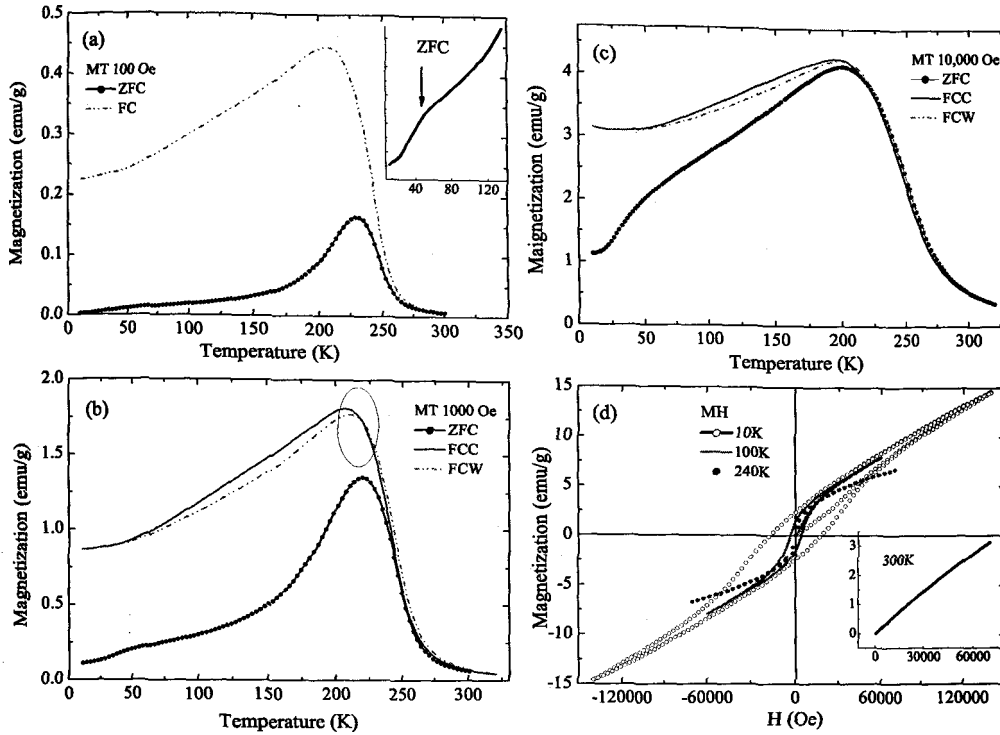


Figure 5.2: Temperature dependent magnetization  $M(T)$  (a) 100 Oe ZFC and FCW cycle indicated by circle and solid lines. Inset shows transition at 50 K by arrow. (b) 1000 Oe and (c) 10,000 Oe; for ZFC, FCC and FCW cycle indicated by circles, solid line and dashed line respectively. (d) Isothermal magnetization  $M(H)$  curves of PrBaCo<sub>2</sub>O<sub>5.5</sub> recorded at 10 K, 100 K, and 240 K. The initial magnetization curve at 300 K is shown in inset(d).

K, the FCW curve lies above FCC curve. It has been shown that this compound has a complex magnetic ground state with competing magnetic interactions present right down to 10 K [33].

Isothermal magnetization  $M(H)$  recorded at various temperature is presented in Figure 5.2(d). The main point is that although the samples are reported to undergo AFM transition, ferromagnetic hysteresis loop is observed at all temperatures below  $T_C$ . Further, isothermal magnetization measured at 300 K (Inset in Figure 5.2(d)) shows a slight curvature indicating presence of short range ferromagnetic interactions well above  $T_C$ .

The coercive field increases with decrease in temperature indicating strengthening of FM interactions. However, no saturation of magnetization is observed even at lowest temperature and maximum field of measurement for this compounds. The continuous increase in magnetization with field could also be attributed to paramagnetic contribution of Pr ions. However, this contribution would have been reversible, in contrast to the observed result. The hysteresis loop at 10 K shows a clear irreversibility right up to fields = 14T. This indicates presence of competing ferro and antiferromagnetic interactions in this sample. Moreover, it is clear that the magnetization is induced by the applied field rather than being of spontaneous nature.

## 5.4 Transport Properties : Electrical Resistivity Measurements

The electrical resistivity in zero field has been plotted in Figure 5.3(a). Data was recorded for cooling and warming cycles in the temperature range  $10 \text{ K} \leq T \leq 325 \text{ K}$  and it exhibits semiconducting behaviour. Hysteresis between the cooling and warming curves can be seen in the temperature region between 100 K and 200 K which coincides with the difference in magnetization seen in FCC and FCW curves in Figure 5.2. This is a clear indication of coupling between spin and charge degrees of freedom. A plot of  $\ln \rho$  versus  $T^{-1/4}$  shown as inset in Figure 5.3(a) indicates a distinct anomaly around 150 K indicating a change in the mechanism of charge transport around this temperature. Similar anomaly in resistivity around the same temperature has been also observed in  $\text{GdBaCo}_2\text{O}_{5.5}$  [34]. In  $\text{RBaCo}_2\text{O}_{5.5}$  with  $R = \text{Tb}$  and  $\text{Y}$ , a magnetic transition due to

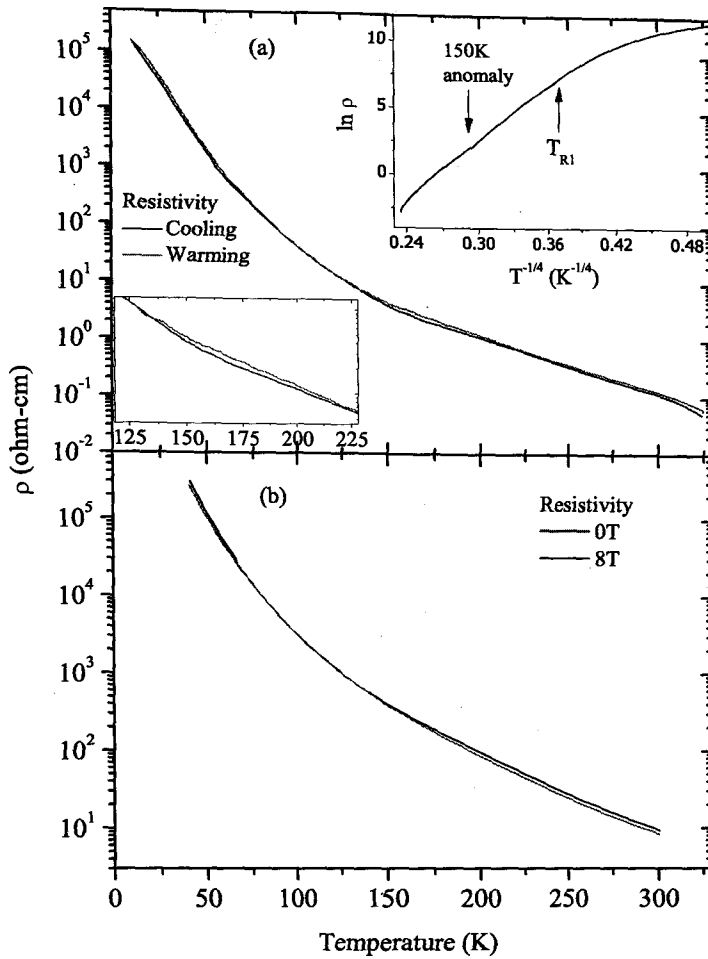


Figure 5.3: (a) Plot of resistivity with temperature in  $H = 0T$  during cooling and warming cycles. Inset shows enlarged view of resistivity in the temperature range 100 K to 255 K. (b) Resistivity variation as a function of temperature in  $H = 8T$ . Inset presents a plot of  $\log \rho$  versus  $T^{-1/4}$ . The arrow points to a anomaly indicating change in transport mechanism around 150 K.

reorientation of antiferromagnetic Co spins has been reported around this temperature [18, 19].

Resistivity measured in applied field of 8T had a similar temperature dependency with very little difference from the zero field value in the entire temperature range as can be seen in Figure 5.3(b). The only noticeable difference in the two curves is in the temperature range 200 K to 100 K, the same region wherein large difference between



FCC and FCW magnetization curves was also seen.

## 5.5 Magneto-transport Properties : Magnetoresistance Measurements

Isothermal magnetoresistance (MR) at 100 K and 50 K were recorded and are presented in Figure 5.4. Interestingly MR is negative at both these temperatures.

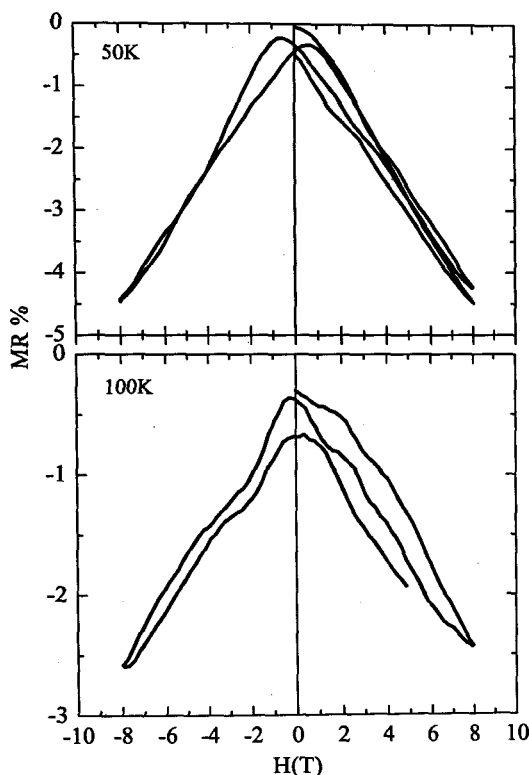


Figure 5.4: Magnetic-field-dependent isothermal magnetoresistance at 50 K and 100 K.

For  $T > 100$  K MR is too small to be measured. Usually MR is positive for AFM compounds and negative MR is a signal for ferromagnetic interactions. The observed negative MR could therefore be either due to presence of both FM and AFM interactions or due to a magnetic frustration resulting from a reorientation of AFM Co spins. As mentioned earlier some of the double perovskites do show additional magnetic transition

at  $T \sim 150$  K due to a SSO transition that leads to reorientation of magnetic spins [18, 19]. The reorientation of spins alleviates magnetic frustration. While no such magnetic transition is seen in magnetic properties of  $\text{PrBaCo}_2\text{O}_{5.5}$ , strong irreversibility noticed in FCC and FCW magnetization curves indicates the presence of magnetic frustration. With decrease in temperature, the negative contribution to MR increases as also indicated by the data recorded at 50 K. The presence of magnetic frustration is further supported by the strong irreversibility observed in MR at 50 K.

## 5.6 X-ray Absorption Spectroscopic Measurements

The above studies clearly bring out the presence of competing magnetic interactions and coupling between spin and charge degrees of freedom in  $\text{PrBaCo}_2\text{O}_{5.5}$  which could be due to SSO transitions of  $\text{Co}^{3+}$  ions. To understand the role of  $\text{Co}^{3+}$  spin state and local coordination around it in the transport and magnetic properties of  $\text{PrBaCo}_2\text{O}_{5.5}$ , XANES and EXAFS measurements at the Co K edge have been carried out at several temperatures in the range  $20 \text{ K} \leq T \leq 300 \text{ K}$ .

### 5.6.1 X-ray Absorption Near Edge Structure (XANES)

Co K edge XANES in this double perovskite has been compared with the Co XANES in two model compounds,  $\text{PrCoO}_3$  and  $\text{PrSrCoO}_4$  recorded at 300 K. In both these compounds Co is in  $3^+$  state and octahedral environment. In  $\text{PrCoO}_3$ , cobalt is known to be in HS state for  $200 \text{ K} < T < 600 \text{ K}$  [35] whereas in  $\text{PrSrCoO}_4$  it is in the IS state [36]. The comparison of normalized Co K edge XANES spectra in  $\text{PrCoO}_3$ ,  $\text{PrSrCoO}_4$  and

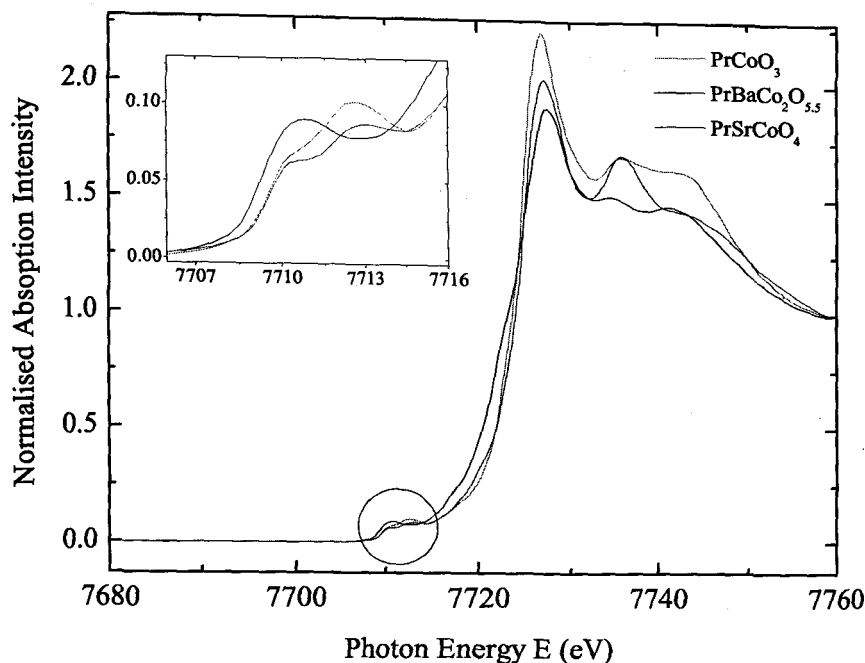


Figure 5.5: Normalized Co K XANES at room temperature with pre-edge peak encircle for  $\text{PrCoO}_3$ ,  $\text{PrSrCoO}_4$  and  $\text{PrBaCo}_2\text{O}_{5.5}$

$\text{PrBaCo}_2\text{O}_{5.5}$  is depicted in Figure 5.5. The spectra in all three compounds are similar with the main resonance peak followed by a broad structure consisting of a doublet extending between 10 to 20 eV above the main resonance peak. There is also a pre edge structure which arises from  $1s \rightarrow 3d$  transition made allowed due to admixture of oxygen  $2p$  orbitals. The pre-edge region is enlarged and shown in the inset of Figure 5.5. One can clearly see the splitting of pre edge corresponding to transitions to  $t_{2g}$  and  $e_g$  crystal field (CF) split  $3d$  states of Co. The CF splitting can be clearly seen in case of  $\text{PrCoO}_3$  and  $\text{PrSrCoO}_4$  while the energy splitting is comparatively smaller in  $\text{PrBaCo}_2\text{O}_{5.5}$ .

In order to obtain more information about the CF splitting and spin state of Co ion in these compounds, a spline curve calculated excluding the pre-edge region (7700 eV

to 7720 eV) was subtracted from the normalized XANES spectra. The resulting curves for the two model compounds,  $\text{PrCoO}_3$  and  $\text{PrSrCoO}_4$  are presented in Figure 5.6(a). The intensity of the pre-edge peak gives an indication of hybridization of CF split  $3d$  orbitals with  $\text{O}2p$  orbitals [31]. A comparison of intensity of pre-edge peak in  $\text{PrSrCoO}_4$  and  $\text{PrBaCo}_2\text{O}_{5.5}$  with that in  $\text{PrCoO}_3$  indicates a stronger hybridization of in the former compounds. To obtain CF splitting and understand more about hybridization especially in case of  $\text{PrBaCo}_2\text{O}_{5.5}$ , the pre-edge region was fitted with two Gaussians corresponding to transitions from  $1s$  level to  $t_{2g} \downarrow$ , and  $e_g \downarrow$  centered around 7709 eV and 7711 eV. Attempts were made to deconvolute the spectra in three Gaussian peaks corresponding to  $t_{2g} \downarrow$ ,  $e_g \uparrow$  and  $e_g \downarrow$  respectively. However, only two peaks could be fitted which were labelled as  $t_{2g} \downarrow$  and  $e_g \downarrow$ . This could be due to smaller energy separation between  $e_g \uparrow$  and  $t_{2g} \downarrow$ . The transitions to unoccupied part of  $e_g \uparrow$  also contribute to the first peak at 7709 eV. It may be mentioned here that in literature, the pre-edge region of  $\text{PrCoO}_3$  has been deconvoluted in three peaks corresponding to transitions to  $t_{2g} \downarrow$ ,  $e_g \uparrow$  and  $e_g \downarrow$  with the intensity of  $e_g \uparrow$  having maximum intensity [37]. This is contrary to general understanding that relative intensity of these transitions will be proportional to available electronic states in the  $t_{2g}$  and  $e_g$  orbitals. For  $\text{Co}^{3+}$  ion in HS state  $e_g \uparrow$  is fully occupied and hence should have minimum intensity. Even if a strong hybridization of  $e_g$  states with  $\text{O}2p$  is considered, it will only lower the intensity further [31]. Furthermore, the two peak deconvolution of the pre-edge region in  $\text{PrCoO}_3$  gives a CF splitting of about 2 eV which is good agreement with values reported in literature. Therefore only a two peak

Table 5.1: XANES fitting parameters for  $\text{PrCoO}_3$ ,  $\text{PrSrCoO}_4$  and  $\text{PrBaCo}_2\text{O}_{5.5}$ .

Compound	Peak Position		Peak Width		Peak Area	
$\text{PrCoO}_3$ (RT)	7709.02(2)	7711.81(2)	1.43(4)	2.38(4)	0.054(3)	0.176(3)
$\text{PrSrCoO}_4$ (RT)	7709.63(1)	7711.83(2)	1.37(2)	2.21(4)	0.055(1)	0.104(2)
$\text{PrBaCo}_2\text{O}_{5.5}$						
325 K	7710.0(1)	7711.0(1)	1.5(3)	2.1(3)	0.02(3)	0.06(4)
RT	7709.9(6)	7711.1(1)	1.54(8)	2.05(1)	0.02(1)	0.06(1)
250 K	7710.50(5)	7712.1(1)	1.97(6)	1.54(9)	0.093(5)	0.25(5)
200 K	7710.1(1)	7711.1(3)	1.5(2)	2.0(2)	0.02(2)	0.06(2)
150 K	7710.18(1)	7711.40(2)	1.72(2)	1.8(2)	0.05(1)	0.03(1)
100 K	7709.90(8)	7711.0(2)	1.5(1)	2.0(1)	0.02(1)	0.06(1)

deconvolution is carried out for all the spectra studied here. Table 5.1 gives the values of peak position, peak area and peak width obtained from deconvolution corresponding to  $t_{2g}$  and  $e_g$  transitions in all compounds. The value of CF splitting obtained for  $\text{PrSrCoO}_4$  is similar to that in  $\text{PrCoO}_3$  while the room temperature CF splitting in  $\text{PrBaCo}_2\text{O}_{5.5}$  is slightly lower.

In  $\text{PrBaCo}_2\text{O}_{5.5}$ , the  $\text{Co}^{3+}$  ion in octahedral coordination is reported to be in LS state while the one in square pyramidal state is in IS state [10]. The observed profile of the pre edge peak will therefore be a average of LS and IS states. In case of LS state, the  $e_g$  level is completely vacant and the transition corresponding to  $e_g \downarrow$  state will have maximum intensity. Hence the intensity ratio of  $e_g/t_{2g}$  should be higher in the double perovskite compared to that in  $\text{PrCoO}_3$  or  $\text{PrSrCoO}_4$ . Indeed it can be seen that at 300 K, this ratio is about 3 as compared to  $\sim 2$  in  $\text{PrSrCoO}_4$ . The temperature variation of this ratio is even more interesting. Especially at 250 K and 150 K, the area under the  $t_{2g}$  peak is more than the  $e_g$  peak. Such a change in the ratio of area under  $e_g$  and  $t_{2g}$  peaks signifies

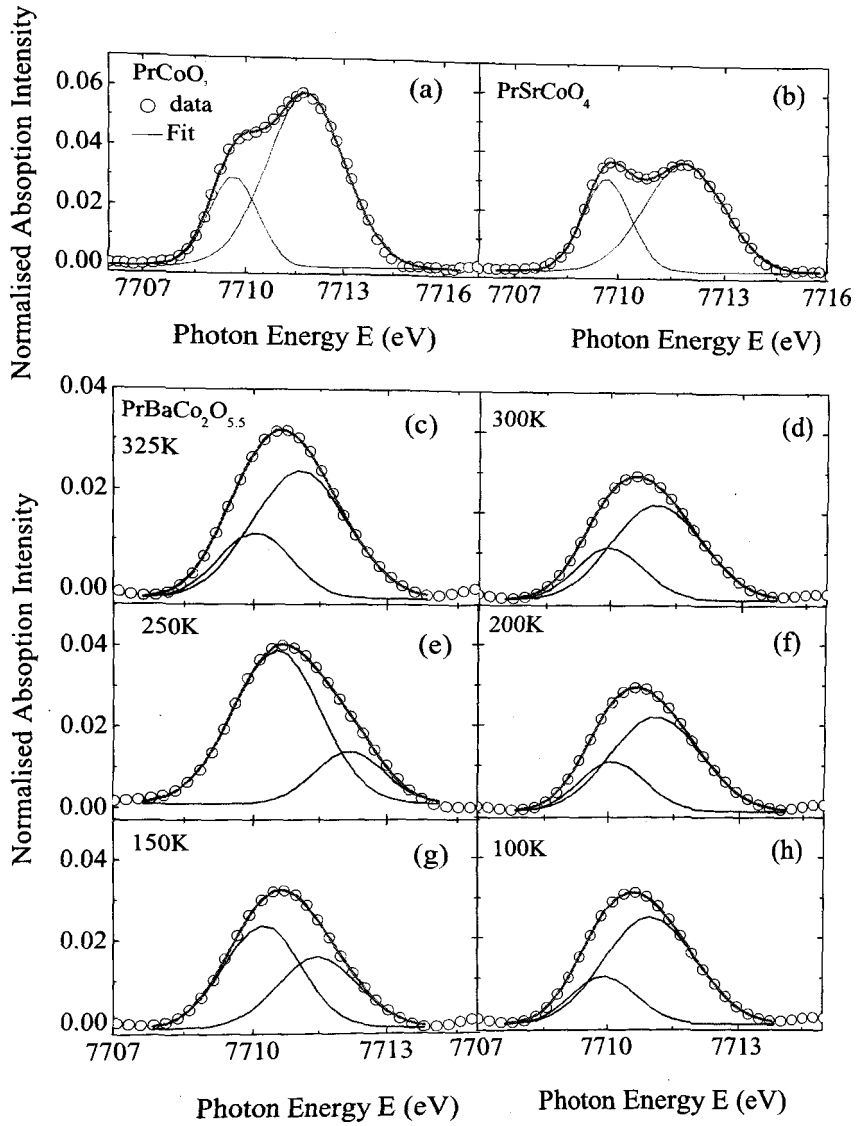


Figure 5.6: Deconvolution of pre-edge peaks, circles indicates XANES data along with best fit curves (solid lines) which is a sum of two constituent Gaussian peaks at room temperature for (a)PrCoO<sub>3</sub>, (b)PrSrCoO<sub>4</sub> and (c)-(h) at various temperatures for PrBaCo<sub>2</sub>O<sub>5.5</sub>

stronger hybridization of the Co  $3d_{e_g}$  orbitals with O $2p$  orbitals. This increase in Co $3d$  - O $2p$  hybridization, most likely occurs at the square pyramidal positions and will have a effect on the magnetic and transport properties of the double perovskite. It may be noted that the temperatures 250 K and 150 K correspond to two of the transition temperatures of PrBaCo $_2$ O $_{5.5}$ .

### 5.6.2 Extended X-ray Absorption Fine Structure

There is an empirical relation between the distance of absorber atom from its nearest neighbour and the pre-edge spectral features. Therefore the admixture of Co $3d$  - O $2p$  states should significantly affect the nearest neighbour Co-O bond distances. In order to glean an insight on this hybridization, Co  $K$  EXAFS spectra recorded at several temperatures in the range  $20 \text{ K} \leq T \leq 325 \text{ K}$ . The EXAFS raw data reduction is carried out as per the steps given in Chapter 2. The reduced data obtained is fitted to a model. The detailed of the EXAFS data modelling and analysis is given below.

#### EXAFS Data Modelling

The EXAFS spectra were fitted to a model based on its crystal structure wherein the Co-O and Co-Co bond distances and Co-O-Co bond angle were expressed in terms of lattice constants obtained from XRD. These expressions reduced the number of variables considerably thereby improving the reliability of the fitted parameters. Furthermore, same variable parameters were used to describe the nearly equal Co-O bond distances, for example, the apical Co-O bond distances in octahedral and square pyramids. Low

temperature neutron diffraction studies on  $\text{PrBaCo}_2\text{O}_{5.5}$  [10] shows that there is a minimum change in lattice constant along  $x$ -axis hence it was kept fixed during refinement. FEFF calculation was individually performed on both Co sites, Co1 for square pyramids and Co2 for octahedral site. The positions of the atoms are shown in Figure 5.7. The details of these parameters are given in Table 5.2.

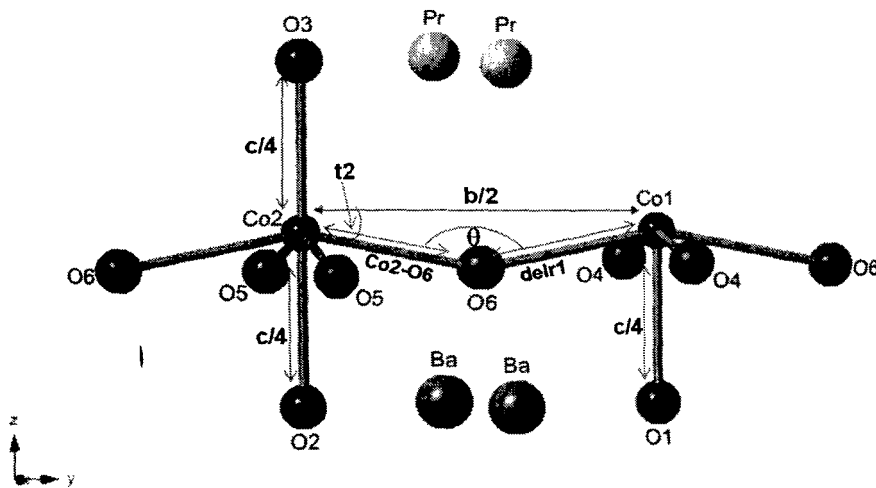


Figure 5.7: The atomic positions of two sites of cobalt along with oxygen.

$R_1$  is defined as  $1.8959 \text{ \AA}$  (from FEFF calculations) which is  $R_{\text{eff}}$  for Co1-O6, change in  $R_1$  is given by variable  $\text{delr1}$ . The Co-O-Co bond angle ( $\theta$ ) along  $y$ -axis was calculated from angle  $t_2$  ( $\text{Co1} - \text{Co2} - \text{O}$ ). The angle  $t_1$  is defined in the similar way along  $x$ -axis, so that calculated  $\theta$  along  $x$ -axis is  $180 - 2 * t_1 = 166^\circ$ . Similar model is used for the compounds with  $\delta = 0.58, 0.43$  and  $0.35$  while in case  $\delta = 0.80$  and  $0.67$  the FEFF calculations were carried out assuming all Co in octahedral environment.

The EXAFS data at various temperatures in  $R$ -space in the range of  $1 \text{ \AA}$  to  $4 \text{ \AA}$  were used for fitting. Magnitude of Fourier Transform of EXAFS data recorded at several



Table 5.2: EXAFS model parameters for PrBaCo<sub>2</sub>O<sub>5.5</sub>.

Bond Distance	Variable equation	$\sigma^2$
Square Pyramid		
Co1-O6	delr1	ss1
Co1-O1	$c/4 - R_{\text{eff}}$	ss2
Co1-O4	$\sqrt{(R1 + delr1)^2 + a^2 - 2 * a * (R1 + delr1) * \cos(t1)} - R_{\text{eff}}$	ss1
Co1-Br	delr3	ss4
Co1-Pr	delr4	ss5
Octahera		
Co2-O6	$\sqrt{(R1 + delr1)^2 + (b/2)^2 - 2 * (b/2) * (R1 + delr1) * \cos(t2)} - R_{\text{eff}}$	ss1
Co2-O5	$\sqrt{(R1 + delr1)^2 + a^2 - 2 * a * (R1 + delr1) * \cos(t1)} - R_{\text{eff}}$	ss2
Co1-O4	$c/4 - R_{\text{eff}}$	ss2
Co1-Br	delr3	ss4
Co1-Pr	delr4	ss5

temperatures in the range 100 K - 325 K along with best fit is shown in Figure 5.8 while EXAFS data at 20 K along with its best fit is presented in Figure 5.9(a). Similar fits were obtained for all other samples of PrBaCo<sub>2</sub>O<sub>5+ $\delta$</sub> . These data analyses are presented in following chapters. For avoiding repetitiveness, data at 20 K only is presented.

One can notice that at magnetic transition temperatures the fits are of relatively poor quality and the parameters obtained have higher error bars. Neutron and X-ray diffraction studies have not indicated any major change in structure at these temperatures. This indicates a strong coupling between the local structural and magnetic degrees of freedom. The variation of Co-O bond lengths for the octahedra and square pyramids along with Co-O-Co inter-polyhedron bond angle are plotted in Figure 5.9(b-f). As can be seen from Figure 5.9(b) there appears to be hardly any change in planar Co-O bond distances of the octahedral site in the entire temperature range. This could be due to

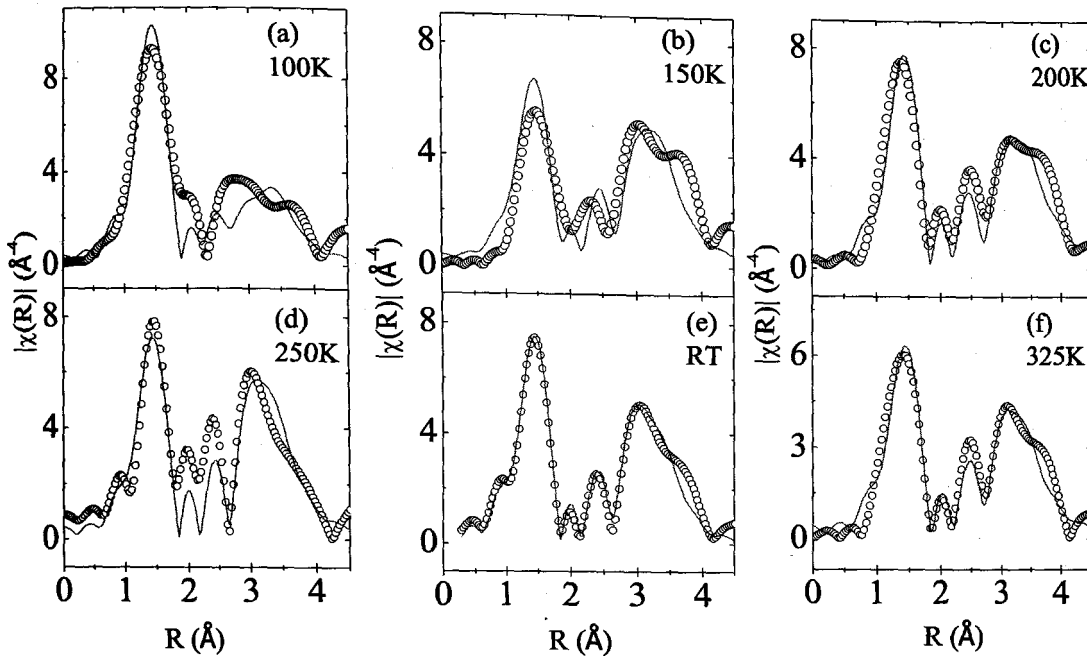


Figure 5.8: First and second shell fit to the EXAFS of  $\text{PrBaCo}_2\text{O}_{5.5}$ . The  $|\chi(R)|$  of the data (open circles) and best-fit (solid lines through circles) are shown.

LS state of  $\text{Co}^{3+}$  ions occupying the octahedral sites. However, in case of square pyramids, although the Co-O bond distance along  $a$  axis remains nearly constant in the entire temperature range, that along  $b$  axis shows a strong temperature dependence (see Figure 5.9(e)). It must be mentioned here that amongst the lattice parameters,  $a$  shows the least change as a function of temperature [13]. Most dramatic effects in local structural parameters are seen at about  $T = 250$  K. The Co-O bond distance along  $b$  axis shows a local maxima while the same along  $c$  axis has a distinct minima. The inter-polyhedron, Co-O-Co bond angle (depicted in Figure 5.9(d)) also exhibits a minimum around 250 K. It is of interest to note that the analysis of the pre-edge peak in XANES spectra indicated increased Co3d - O2p hybridization at around 250 K. This also happens to be the

temperature around which the material orders antiferromagnetically with a spontaneous magnetic moment. Such anomalies in the Co-O bond distance and bond angle are also seen around  $T = 150$  K where the resistivity measurements show an anomaly. Though magnetization of  $\text{PrBaCo}_2\text{O}_{5.5}$  shows only a irreversibility in FCC and FCW curves, other such double perovskites containing Sm, Tb or Y exhibit a distinct magnetic transition around 150 K [18, 19]. EXAFS analysis therefore, clearly suggests that this increase in  $3d - 2p$  admixture occurs in the Co ions occupying square pyramidal sites.

## 5.7 Discussion

The double perovskite  $\text{PrBaCo}_2\text{O}_{5.5}$  undergoes several magnetic and electronic transitions as a function of temperature in the insulating phase. These transitions are believed to be intimately related to spin state of Co ions and the hybridization of Co  $3d$  band with O  $2p$  orbitals. Magnetization depicts a PM to FM like transition at 246 K followed by another transition to AFM state at 200 K. Neutron diffraction measurements classify both the above transitions to be antiferromagnetic in nature arising due to the canted ordering of square pyramidal Co spins along the  $c$  axis [10]. These measurements ascribe IS state to square pyramidal Co ions while octahedral Co are believed to be in LS state. Antiferromagnetic nature of the above transitions has also been confirmed in other members of  $\text{RBaCo}_2\text{O}_{5.5}$  family even though there are varied explanations to ferromagnetic nature of the first transition [10, 17, 18, 19]. Apart from these, another magnetic transition at  $T_{R1} = 50$  K has also been observed. This transition appears to be related to orthorhombic

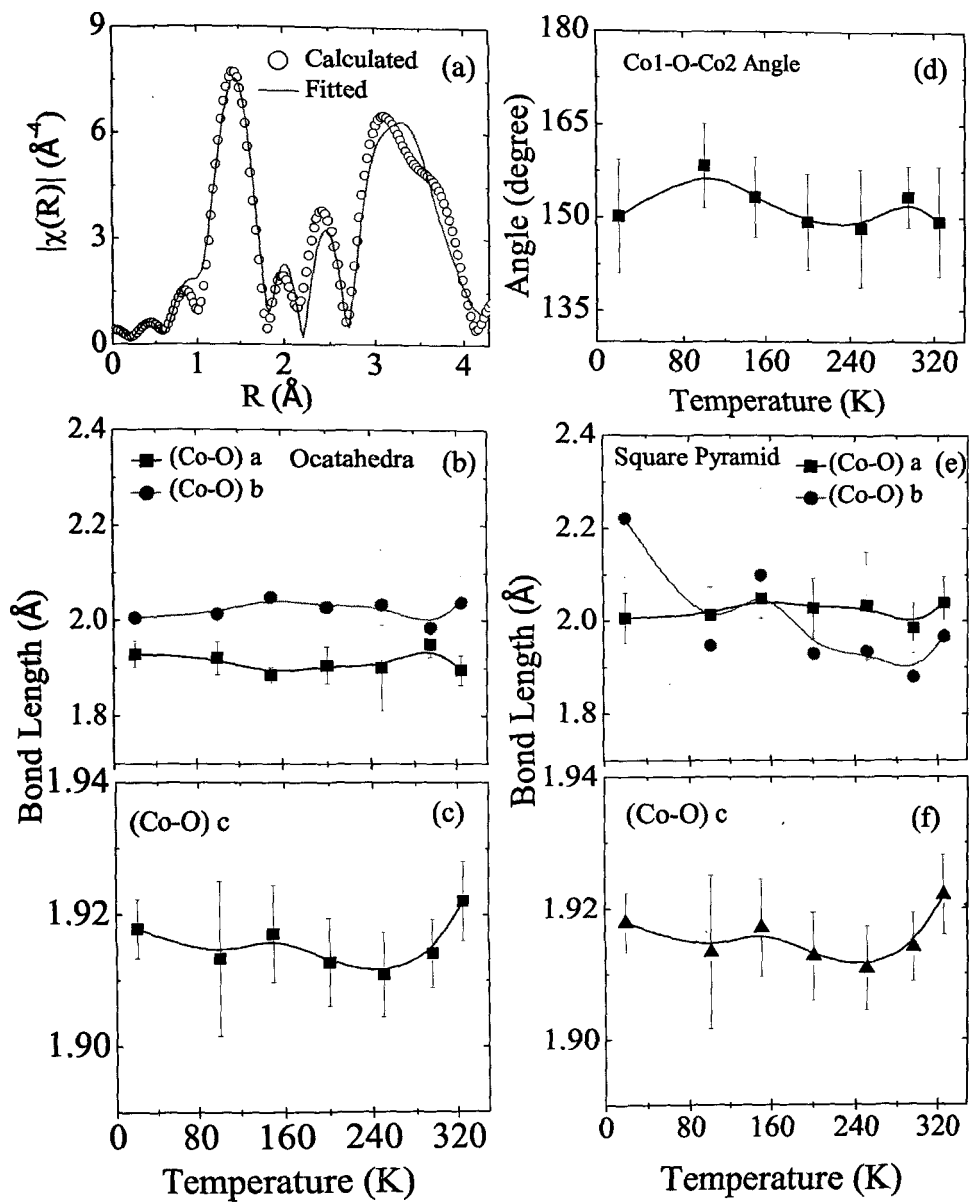


Figure 5.9: (a) EXAFS  $\chi(k)$  data and best fit at 20 K, variation of Co-O bond distances (b) Octahedra Planer (c) Octahedra Apical, (d) Co-O-Co bond angle, Co-O bond distances (e) square pyramidal Planer (g) square pyramidal Apical at various temperatures for  $\text{PrBaCo}_2\text{O}_{5.50}$ .

*distortion*. Furthermore an anomaly in resistivity data at 150 K and the hysteresis between warming and cooling cycles of both magnetization and resistivity measurements is seen in  $100 \text{ K} \leq T \leq 200 \text{ K}$  range.

XANES and EXAFS studies presented here provide important clues in understanding the above transitions and the role of  $\text{Co}3d\text{-O}2p$  hybridization in inducing them. Firstly, EXAFS studies at the Co  $K$  edge show that octahedral Co-O bond distances has very little or no variation as a function of temperature. Thermal evolution of Co-O bond distance of square pyramidal Co ion and interpolyhedral Co-O-Co bond angle exhibits features which agree well with observed transitions in magnetic and transport properties. These two parameters along with behaviour of pre-edge peak in the Co  $K$  edge XANES spectra indicate the possible mechanism responsible for various transitions in the insulating phase of  $\text{PrBaCo}_2\text{O}_{5.5}$ .

The increase in Co-O bond distance along  $b$  axis of the  $\text{CoO}_5$  polyhedra, the corresponding decrease of the bond length along  $c$  axis below 300 K accompanied by lowering of the Co-O-Co interpolyhedron bond angle results in tilting of the  $\text{CoO}_5$  square pyramids. As a result the hybridization between  $\text{Co}3d$  and  $\text{O}2p$  orbitals increases. The tilting of the square pyramids and the lowering of bond distance along  $c$  axis facilitates anti-ferromagnetic ordering of the Co spins along  $c$  axis at 246 K as has been proposed by neutron diffraction [10]. The increase in hybridization is also reflected in the pre-edge feature wherein the height of the  $t_{2g}$  peak becomes greater than that of  $e_g$  peak at 250 K. For a  $\text{Co}^{3+}$  ion in any spin state, the  $e_g \downarrow$  orbitals are normally vacant and therefore

the transition corresponding to these orbitals has higher intensity compared to the other peak which represents a transition to  $t_{2g} \downarrow$  and  $e_g \uparrow$ . A lowering of intensity of  $e_g \downarrow$  peak can be construed to imply a charge transfer from  $e_g \uparrow$  orbitals of the square pyramidal Co ion to  $e_g \downarrow$  orbitals of octahedral Co ion via the O2p orbitals. This results in occurrence of magnetic moment on the LS Co ion at the octahedral site as seen from neutron diffraction studies [10]. Furthermore, neutron diffraction studies on other  $\text{RBaCo}_2\text{O}_{5.5}$  also propose existence of magnetic moment on  $\text{Co}^{3+}$  ions in octahedral coordination [18]. Charge transfer induced changes in structural, magnetic and transport properties have also been reported in other perovskite compounds [38, 39, 40]. We propose here that the fractional charge transfer between IS  $\text{Co}^{3+}$  at square pyramidal site and LS  $\text{Co}^{3+}$  at the octahedral site as the cause of spontaneous magnetic moment seen in antiferromagnetic state of  $\text{PrBaCo}_2\text{O}_{5.5}$ . Below 250 K there is further tilting of the  $\text{CoO}_5$  pyramids which results in stronger antiferromagnetic interaction and another magnetic transition at 200 K. With further decrease in temperature, though the Co-O-Co bond angle decreases, the Co-O bond distance increases. This implies that there is an upper threshold for the Co-O hybridization beyond which the polyhedra go away from each other. Both, the Co-O bond distance and Co-O-Co bond angle have a local maxima around 150 K. This increase in bond distance and bond angle changes the Co3d-O2p hybridization and can induce a rearrangement of Co spin structure. In absence of a SSO transition that results in another AFM transition, inevitable magnetic frustration sets in which explains the hysteresis observed between FCC and FCW magnetization curves in the  $100 \text{ K} \leq T \leq$

200 K region.

## 5.8 Conclusions

Unlike in the case of heavier rare-earths where a pure antiferromagnetic ordering has been observed, the phase below  $T_N$  in  $\text{PrBaCo}_2\text{O}_{5.5}$  is a mixture of antiferromagnetic and ferromagnetic order. In addition to  $T_C$  and  $T_N$ , the compound undergoes another magnetic transition at  $T_{R1}$ . XAFS studies at the Co K edge in  $\text{PrBaCo}_2\text{O}_{5.5}$  indicate a strong hybridization between  $\text{Co}3d$  and  $\text{O}2p$  orbitals. An increase in Co-O bond distance causes the  $\text{CoO}_5$  square pyramids to tilt resulting in antiferromagnetic ordering. An increase in  $\text{Co}3d$ - $\text{O}2p$  hybridization, as seen from the drastic change in  $t_{2g}/e_g$  peak height ratio, results in a charge transfer from the square pyramidal Co  $e_g \uparrow$  orbitals to octahedral Co  $e_g \downarrow$  orbitals via O  $2p$  orbitals which reflects as a magnetic moment on LS  $\text{Co}^{3+}$  ion. Further tilting at lower temperatures, pushes the polyhedra away from each other. This changes the  $p - d$  hybridization and reorients the antiferromagnetic Co spins giving rise to anomalies in magnetic and transport properties of this double perovskite.

# References

- [1] Maignan A, Martin C, Pelloquin D, Nguyen N, and Raveau B 1999 *J. Solid State Chem.* **142** 247
- [2] Martin C, Maignan A, Pelloquin D, Nguyen N, and Raveau B 1997 *Appl. Phys. Lett.* **71** 1421
- [3] Moritomo Y, Akimoto T, Takeo M, Machida A, Nishibori E, Takata M, Sakata M, Ohoyama K, and Nakamura A 2000 *Phys. Rev. B* **61** R13325
- [4] Respaud M, Frontera C, García-Muñoz, Aranda A G M, Raquet B, Broto J, Rakoto H, Goiran M, Llobet A, and Carvajal J 2001 *Phys. Rev. B* **64** 214401
- [5] Vogt T, Woodward P M, Karen P, Hunter B A, Henning P, and Moodenbaugh A R 2000 *Phys. Rev. Lett.* **84** 2969
- [6] Suard E, Fauth F, Caignaert V, Mirebeau I, and Baldinozziet G 2000 *Phys. Rev. B* **61** R11871
- [7] Troyanchuk I, Kasper N, and Khalyavin D D 1998 *Phys. Rev. Lett.* **80** 3380



- [8] Streule S, Podlesnyak A, Mesot J, Medared M, Conder K, Pomjakushina E, Mitberg E, and Kozhevnikov V 2005 *J. Phys: Condens. Matter* **17** 3317
- [9] Diaz-Fernandez Y, Malavasi L, and Mozzati M C 2008 *Phys. Rev. B* **78** 144405
- [10] Frontera C, García-Muñoz, A. Carrillo, M. A. G. Aranda, I. Margiolaki and A. Caneiro 2006 *Phys. Rev. B* **74** 054406
- [11] Frontera C, García-Muñoz J and A. Carrillo *Phys. Rev. B* **70** 184428
- [12] Luetkens H, Stingaciu M, Pashkevich Y, Conder K, Pomjakushina E, Gusev A, Lamonova K, Lemmens P, and Klauss H 2008 *Phys. Rev. Lett.* **101** 017601
- [13] Frontera C, García-Muñoz, Llobet A, and Aranda M 2002, *Phys. Rev. B* **65**, 180405
- [14] Khalyavin D D, Barilo S, Shiryayev S, Bychkov G, Troyanchuk I, Furrer A, Al-lenspach P, Szymczak S, and Szymczak R 2003 *Phys. Rev. B* **67** 214421
- [15] Pomjakushina E, Conder K, and Pomjakushin V 2006 *Phys. Rev. B* **73** 113105
- [16] Jarry A, Luetkens H, Pashkevich Y, Stingaciu M, Pomjakushina E, Conder K, Lemmens P, and Klaus H 2009 *Physica B* **404** 765
- [17] Fauth F, Suard E, Caignaert V, and Mirebeau I 2002 *Phys. Rev. B* **66** 184421
- [18] Khalyavin D D, Argentiou D N, Amann U, Yaremchenko A A, and Kharton V V 2007 *Phys. Rev. B* **75** 134407

- [19] Plakhty V, Chernenkov P, Barilo S, Podlesnyak E, Pomjakushina E, Moskvina E, and Gavrilov S 2005 *Phys. Rev. B* **71** 214407
- [20] Kundu A K, Reveau B, Caignaert V, Rautama E-L and Pralong V 2009 *J. Phys. Condens. Matter* **21** 056007
- [21] Flavell W, Thomas A, Tsoutsou D, Mallick A, North M, Seddon E, Cacho C, Malins A, Patel S, Stockbauer R, Kurtz R, Sprunger P, Barilo S, Shiryaev S, and Bychkov G 2004 *Phys. Rev. B* **70** 224427
- [22] Wu H 2001 *Phys. Rev. B* **64** 92413
- [23] Wu H 2003 *J. Phys.: Condens. Matter* **15** 503
- [24] Pandey S K, Ashwani Kumar, Patil S, Medicherla V R R, Singh R, Maiti K, Prabhakaran D, Boothroyd A, and Pimpale A V 2008 *Phys. Rev. B* **77**, 045123
- [25] Wu Z Y, Benfatto M, Pedio M, Cimino R, Mobilio S, Barman S R, Maiti K, and Sarma D D 1997 *Phys. Rev. B* **56**, 2228
- [26] Barman S, and Sharma D D 1994 *Phys. Rev. B* **49**, 13979
- [27] Pandey S K, Patil S, Medicherla V, Singh R, and Maiti K 2008 *Phys. Rev. B* **77**, 115137
- [28] Zhitlukhina E, Lamonova K, Orel S, Lemmens P and Pashkevich Y 2007 *J. Phys. Condens. Matter* **19**, 156216

- [29] Chang J Y, Lin B N, Hsu Y Y, and Ku H C 2003 *Physica B* **329-333** 826
- [30] Haas O, Struis R P W J, and McBreen J M 2004 *J. Solid State Chem* **177** 1000
- [31] Pandey S K, Khalid S, Lalla N P, and Pimpale A V 2005 *J. Phys: Condens. Matter* **18** 10617-10630
- [32] Conder K, Pomjakushina E, Soldatov A, and Mitberg E 2005 *Mater. Res. Bull.* **40** 257
- [33] Ganorkar S, Priolkar K R, Sarode P R, and Banerjee A 2011 *J. Appl. Phys.* **110** 053923
- [34] Ganorkar S, and Priolkar K R 2010 *Solid State Comm.* **150** 1963
- [35] Ren Y, Yan J-Q, Zhou J-S, Goodenough J B, Jorgensen J D, Short S, Kim H, Proffen Th, Chang S, and McQueeney R J 2011 *Phys. Rev. B* **84** 214409
- [36] Huang S L, Fan Z C, Yi J B, Zhao B C, Wu Y, Ruan K Q, Li M, Ding J, and Wang L 2008 *J. Phys.: Condens. Matter* **20** 395213
- [37] Chang J Y, Lin B N, Hsu Y Y, and Ku H C 2003 *Physica B* **329-333** 826 2995
- [38] Liu S-H, Huang J-C A, Qi X, Lin W-J, Siao Y-J, Lin C-R, Chen J-M, Tang M-T, Lee Y-H, and Lee J-C, *AIP Advances* **1** 032173 (2011)
- [39] Sarma D D, Mahadevan P, Saha-Dasgupta T, Ray S, and Kumar A 2000 *Phys. Rev. Lett.* **85** 2549

- [40] Long Y W, Hayashi N, Saito T, Azuma M, Muranaka S and Shimakawa Y 2009

*Nature* **458** 60

# Chapter 6

## Influence of local structure on magnetic properties of Layered Cobaltites $\text{PrBaCo}_2\text{O}_{5+\delta}$ , $\delta > 0.5$

### 6.1 Introduction

Partial substitution of alkaline-earth metals for rare-earth metals in  $\text{RCoO}_3$  (R - rare-earth element) and their subsequent ordering of results in double layered perovskites. One such Ba substituted layered perovskites is  $\text{RBaCo}_2\text{O}_{5+\delta}$ , ( $\leq \delta \leq 1$ ). The ionic size difference between Ba and R and the resultant valance of Co due to oxygen non-stoichiometry make cobaltites more complex to study. They are of very special interest for their unique properties like metal insulator transition (MIT), spin state transition, charge ordering and giant magnetoresistance (MR) [1, 2, 3, 4, 5, 6, 7]. These properties have their origin in the strong interplay between crystallographic, magnetic and transport properties. A property that distinguishes the cobaltites from other transition metal perovskites is the crystal field splitting of the  $3d$  energy level of the Co ion. It is of the same order of magnitude as the Hund's rule intra-atomic exchange energy. Spin state transition can therefore be easily provoked by varying temperature, pressure, magnetic field or chemical composition

(oxygen content or rare earth ion) of the material. These spin state transitions are believed to be responsible for their unique properties. The transport properties of the layered cobaltites are found to be very sensitive due to the coexistence of ferromagnetic (FM) and antiferromagnetic (AFM) states. A giant negative magnetoresistance (MR) (of about 10%) coinciding with FM-AFM transition has been observed in  $\text{GdBaCo}_2\text{O}_{5.5}$  [2], whereas  $\text{LaBaCo}_2\text{O}_{5.5}$  exhibits a strongly irreversible MR near FM-AFM transition [8].

Oxygen non-stoichiometry is one of the important aspect in these layered cobaltites. Tailoring of oxygen content realizes in different valance states of cobalt ion ( $2^+$ ,  $3^+$ ,  $4^+$ ) and different local environments, both of which play a crucial role in their magnetic properties [9, 10, 11]. The structure of Co based double perovskites also depends on the oxygen content ( $5 + \delta$ ). In general, the lower and higher oxygen content compounds crystallize in tetragonal structure with 112 type unit cell while the intermediate members crystallize in orthorhombic 122 type unit cell [10, 11]. The magnetic properties are found to be correlated to oxygen content and crystal structure. While the compounds with lower  $\delta$  have an AFM ground state, FM dominates in compounds richer in oxygen. When  $\delta = 1$ , the FM order is associated with metallic behaviour due to double exchange interaction [12]. With the decrease in oxygen content, a transition from metallic to insulating state occurs in the paramagnetic state and further as the number of trivalent Co ions increase FM order changes to AFM ordering. Neutron diffraction studies on  $\text{PrBaCo}_2\text{O}_{5.75}$  reveal a paramagnetic to FM and an incomplete FM to AFM transition [13]. Furthermore, in these oxygen rich compounds, the  $\text{Co}^{3+}$  ions in octahedral coordination are found to be in

HS state as compared to LS state in  $\text{PrBaCo}_2\text{O}_{5.5}$  [14]. It is therefore not clear if the HS to LS spin state transition of octahedral  $\text{Co}^{3+}$  ions is responsible for the transition from FM to AFM ground state or if it is the delocalization of  $pd\sigma$  holes that are responsible for the AFM to FM transition in these double perovskites [15]. Our recent studies have shown that local structure around Co ions plays an important role in deciding the magnetic properties of these hole doped cobaltites [16]. Hence it would be worthwhile to exploring the local structure around Co ions in these layered cobaltites and correlating them with their magnetic properties. In particular, it would be interesting to examine the changes in local structure of Co ions as the ground state changes from FM to AFM.

Extended X-ray Absorption Fine Structure (EXAFS) spectroscopy is known to be a valuable tool to probe the local structure. EXAFS has been effectively used to understand the local atomic structural distortions and the spin state of Co ion in the parent  $\text{RCoO}_3$  compounds [17, 18, 19, 20, 21, 22, 23]. In comparison to  $\text{RCoO}_3$ , the oxygen cage around Co ion is more distorted in  $\text{RBaCo}_2\text{O}_{5+\delta}$  [24, 25]. It is suspected that the deformation of polyhedra modify the hybridization between outer orbits of cation (R,Ba,Co) and  $2p$  orbitals of oxygen ion which affect electric and magnetic properties of double perovskites [26]. Furthermore, the difference between the ionic radii of R and Ba along with deformed polyhedra will affect the crystal field splitting of the  $3d$  band [27]. In this chapter we report the results of investigations carried out on three oxygen rich  $\text{PrBaCo}_2\text{O}_{5+\delta}$ , ( $\delta = 0.80, 0.67$  and  $0.58$ ) compounds. The sample was prepared as described in section 2.1 and the oxygen content was determined by iodometric titration as mentioned in Table

2.1.

## 6.2 Structural Study : XRD

The structure of Co based double perovskites is known to depend on the oxygen content  $5 + \delta$ . In general there are three structural regimes reported [9]. The hole doped region ( $0.7 \leq \delta \leq 1$ ) wherein the structure is tetragonal, the intermediate region ( $0.3 \leq \delta \leq 0.7$ ) which is characterized by doubling of  $b$  axis due to ordering of the Co ions and orthorhombic structure and the electron doped region ( $0 \leq \delta \leq 0.3$ ) with the compounds having tetragonal structure. The limits of structural transition are not strict and often depend on the rare-earth ion. With the change in oxygen content, the coordination geometry around Co ions also changes from octahedral ( $\delta \approx 1$ ) to square pyramidal ( $\delta \approx 0$ ).

Rietveld refinement of room temperature XRD patterns of  $\text{PrBaCo}_2\text{O}_{5+\delta}$  for  $\delta = 0.67$  and  $0.80$  confirm the formation of single phase samples with 112 type tetragonal unit cell belonging to  $P4/mmm$  space group. As can be seen from Figure 6.1 compounds having  $\delta = 0.67$  and  $0.80$  show the presence of very minor impurity phases ( $\sim 1\%$ ) with peaks around  $2\theta \sim 29^\circ$  and  $31^\circ$  which can be ascribed to unreacted Pr-oxides ( $\text{Pr}_2\text{O}_3$ ,  $\text{Pr}_6\text{O}_{11}$ ). Sample with oxygen content  $\delta = 0.58$  crystallize in orthorhombic structure with  $Pmmm$  space group and 122 type unit cell. This change in structural symmetry is reflected by the splitting of (200) peak at  $2\theta \approx 46^\circ$  as can be seen in Fig. 6.2. Due to tetragonal to orthorhombic transition and subsequent doubling of unit cell along the  $b$ -axis, the (200)



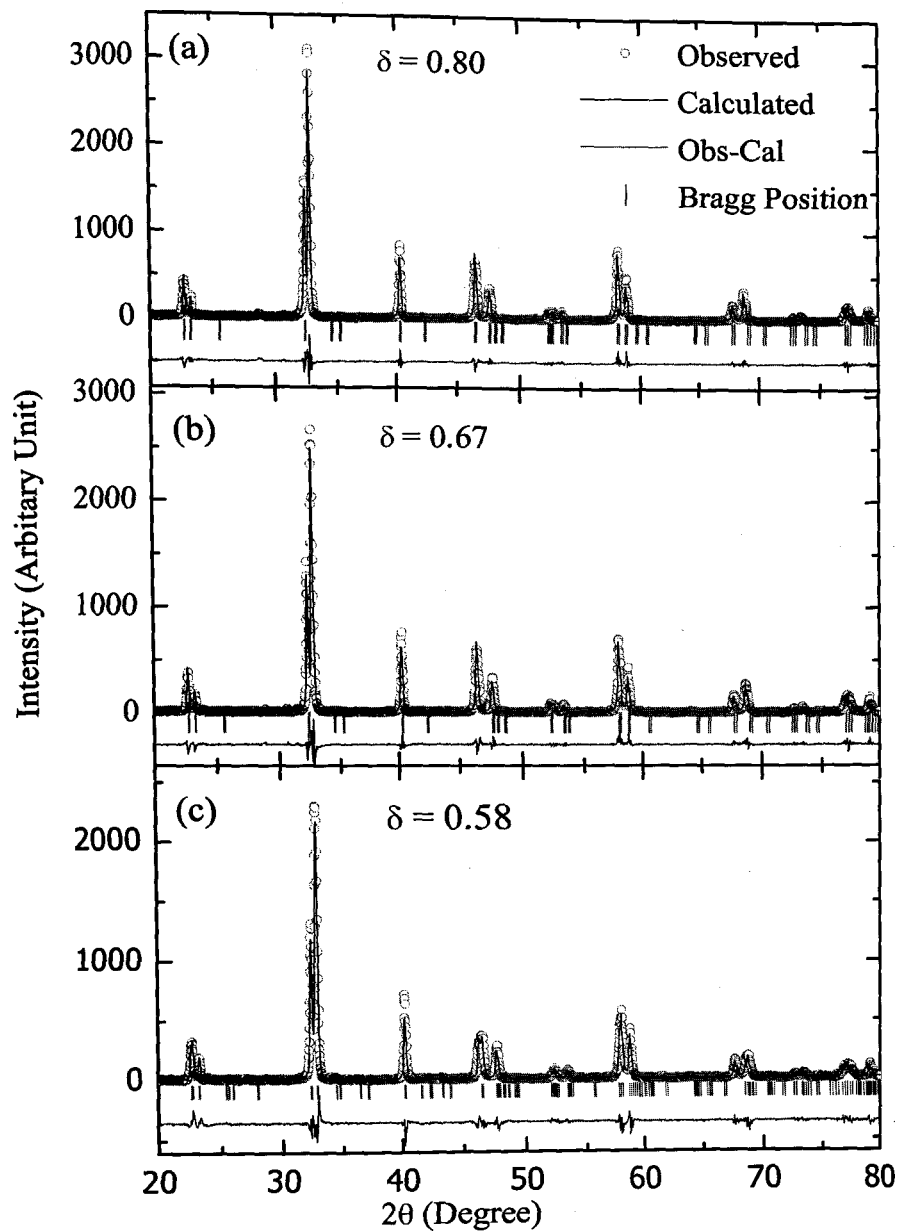


Figure 6.1: Rietveld refinement of XRD patterns of  $\text{PrBaCo}_2\text{O}_{5+\delta}$ , (a)  $\delta = 0.80$ , (b)  $\delta = 0.67$  and (c)  $\delta = 0.58$ . Circles represent experimental data, the continuous line through data is the fitted curve, vertical line indicate Bragg's position and the difference pattern is shown at the bottom as solid line.

reflection splits into two distinct (200) and (040) Bragg peaks.

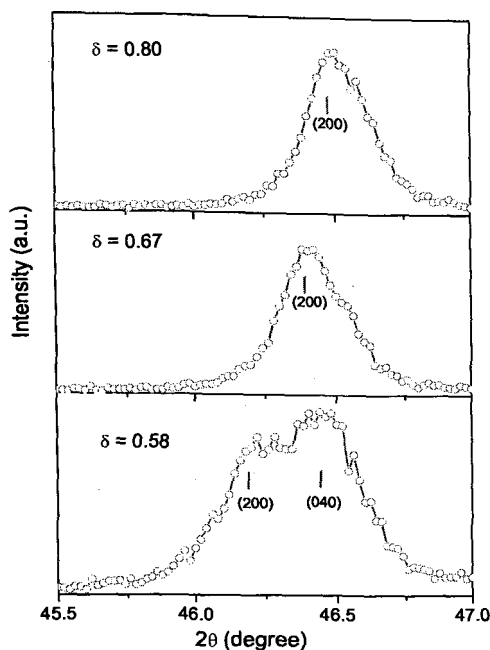


Figure 6.2: The (200) Bragg reflection and its splitting to (200) and (040) upon tetragonal to orthorhombic transition in  $\text{PrBaCo}_2\text{O}_{5.58}$ .

The lattice parameters obtained from Rietveld refinement are given in Table 6.1. The parameters obtained are in good agreement with the neutron diffraction results on  $\text{PrBaCo}_2\text{O}_{5.75}$  [11, 13]. However, high resolution synchrotron XRD measurements on similar composition reveal that the structure belongs to orthorhombic unit cell with  $Pmmm$  space group [28]. In the present case no splitting of (200) reflection as expected for an orthorhombic structure was seen. It must be noted here that a structural crossover from tetragonal to orthorhombic unit cell is reported for oxygen concentration around  $\delta = 0.6$ . [11, 16].

Table 6.1: Lattice parameters for  $\text{PrBaCo}_2\text{O}_{5+\delta}$ .

$\delta$	a(Å)	b(Å)	c(Å)	V(Å <sup>3</sup> )
0.80	3.9045(1)	3.9045(1)	7.6355(2)	116.410(7)
0.67	3.9085(7)	3.9085(7)	7.6311(2)	116.579(5)
0.58	3.9276(1)	7.8142(3)	7.6363(2)	234.37(1)

### 6.3 Magnetization Measurements

The temperature dependence of magnetization  $M(T)$  measured at 100 Oe is shown in Figure 6.3(a)-(c). The ZFC and FC magnetization curves of all samples except  $\delta = 0.80$  show PM to FM transition followed by a decrease in magnetization which, based on neutron diffraction results [14], is ascribed to a FM to AFM transition. The compound with  $\delta = 0.80$  exhibits a PM to FM transition at  $T_C = 148$  K. There is however, a large difference between ZFC and FC magnetization curves of this compound. Studies on oxygen rich  $\text{PrBaCo}_2\text{O}_{5+\delta}$  indicate that compounds with  $\delta = 0.9$  and  $0.85$  order ferromagnetically while that with  $\delta = 0.75$  orders antiferromagnetically at 175 K which can be transformed to FM state under magnetic field [28]. Hence the difference between ZFC and FC magnetization curves for  $\delta = 0.8$  sample can be ascribed to the presence of competing magnetic interactions. A closer examination of  $M(T)$  curves indicates presence of few more magnetic transitions at low temperatures. For  $\delta = 0.80$  apart from the PM to FM transition another transition is visible at  $T_{R1} \sim 50$  K which has not been hitherto reported. This transition is also present in other compounds (see insets (i) in Figure 6.3 (a-c) and insets therein). Muon spin relaxation ( $\mu\text{SR}$ ) studies on  $\text{NdBaCo}_2\text{O}_{5.5}$  attribute

the transition around 50 K to a magnetic phase transition [27].

In case of  $\delta = 0.67$ , a small rise in magnetization, akin to a PM to FM transition is noticed at 150K. However, the small value of magnetic moment and the subsequent sharp decrease in magnetization at  $T = 100$  K prompts us to ascribe both these transitions at  $T_{N1} = 150$  K and  $T_{N2} = 100$  K to an AFM ground state. In  $\text{PrBaCo}_2\text{O}_{5.5}$ , where magnetization has similar behaviour, neutron diffraction studies have reported antiferromagnetic spin alignment [14]. The structural transition from tetragonal to orthorhombic for  $\delta = 0.58$  shifts  $T_{N1}$  and  $T_{N2}$  at higher temperatures.

Second aspect that stands out is the low values of magnetization in compounds with  $\delta < 0.8$ . Different hypotheses have been considered to explain the low value of the magnetic moment. Firstly, it could be due to presence of low spin ( $S = 0$ )  $\text{Co}^{3+}$  ions as majority species. However, optical studies on Eu based double perovskites discounts this possibility [29]. The resulting small total magnetization observed at low temperature could be due to ferrimagnetic ordering or mutually orientated moments of  $\text{Co}^{2+/3+}$  ions in the non equivalent pyramidal and octahedral sites. A third hypothesis is based on the coexistence of ferromagnetic and an antiferromagnetic phase or on segregation of a FM phase in the antiferromagnetic matrix in the form of ferromagnetic domains. This phase separation scenario is also observed for  $\text{GdBaCo}_2\text{O}_{5+\delta}$  [30]. In this case, the application of the magnetic field continuously transforms the antiferromagnetic state into ferromagnetic state.

$M(T)$  have been recorded at 1000 Oe and 1 T during FCC and FCW cycles for the

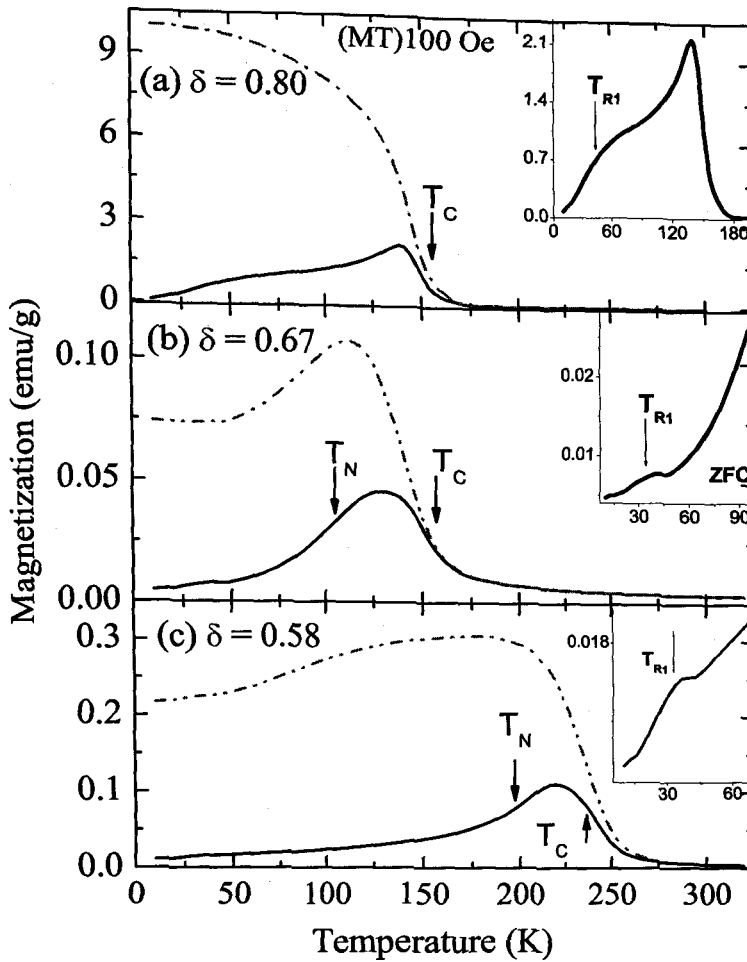


Figure 6.3: Temperature dependent magnetization  $M(T)$  (a) 100 Oe ZFC and FC cycle indicated by solid line and dashed lines. Inset shows transition at 50 K ( $T_{R1}$ ) by arrow.

samples with  $\delta = 0.80, 0.58$  as depicted in Figure 6.4(a) and (b). It is clear from the

Figure 6.4 ferromagnetism seems to be strengthened with the application of field. This

lends weight to the hypothesis of electronic phase separation in these compounds. A small

amount of thermal hysteresis that increases with decreasing  $\delta$  is still observed below  $T_C$

even in fields of 1 T confirming the presence of a complex magnetic ground state as was

evident from magnetization curves at 100 Oe. For  $\delta = 0.58$  one can also notice a crossover

between FCC and FCW magnetization curves at around 176.4 K. At lower temperature

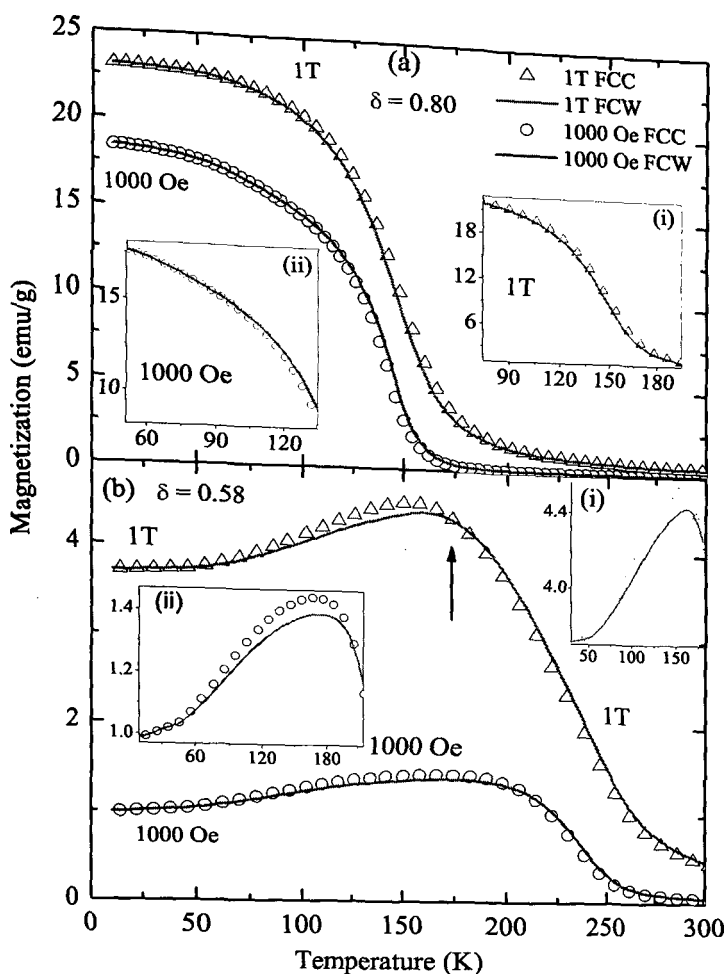


Figure 6.4: Temperature dependance of magnetization recorded at 1000 Oe and 1 T for FCC and FCW cycles. The crossing FCC and FCW curves is presented more clearly in the insets.

( $50 \text{ K} \leq T \leq 180 \text{ K}$ ), the FCW magnetization curve lies below the FCC curve while above  $T \geq 176.4 \text{ K}$ , the FCW curve lies above FCC curve. While no such feature is observed for  $\delta = 0.80$ . It has been shown that oxygen deficient compound has a complex magnetic ground state with competing magnetic interactions present right down to 10 K [16].

Magnetic susceptibility  $\chi = M/H$  calculated from magnetization also reveals important clues about magnetic ordering in these two compounds with  $\delta = 0.80$  and 0.67. In the case of  $\text{PrBaCo}_2\text{O}_{5.80}$ , a plot of  $\chi^{-1}$  vs T exhibits a Curie-Weiss (linear) behaviour

almost down to its  $T_C$  as shown in Figure 6.5(a). The values of paramagnetic Curie temperature,  $\theta_p$  and effective magnetic moment  $\mu_{eff}$  are 150 K and  $5.34 \mu_B/f.u.$  respectively and are in good agreement with those reported for  $\text{PrBaCo}_2\text{O}_{5.75}$  [13].

Deviation from Curie-Weiss fit is noted at temperature as high as 250 K (Figure 6.5(b)) in case the of  $\text{PrBaCo}_2\text{O}_{5.67}$ . The deviation and the behaviour of susceptibility can be ascribed to the presence of weak antiferromagnetic correlations well above its ordering temperature. Though  $\theta_p$  obtained from Curie-Weiss fit is positive, there is a decrease in its value from 150 K for  $\delta = 0.80$  to 92 K for  $\delta = 0.67$ .

Canting of magnetic spins due to different local environment of Co ions and/or their spin states could be the reason for positive values of  $\theta_p$ . Neutron diffraction studies have indicated AFM ordering at  $T_N = 220$  K in  $\text{PrBaCo}_2\text{O}_{5.5}$  [14]. This ordering is a result of interaction between IS  $\text{Co}^{3+}$  ions in square pyramidal coordination. A possibility  $\text{Co}^{3+} - \text{O} - \text{Co}^{3+}$  pairs giving rise to weak antiferromagnetic correlations in  $\text{PrBaCo}_2\text{O}_{5.67}$ , well above its magnetic ordering temperature cannot be ruled out. The value of  $\mu_{eff}$  obtained from Curie-Weiss fit is  $5.41 \mu_B/f.u.$

Based on the similarities of  $\mu_{eff}$  values and their agreement with that of reported for  $\text{PrBaCo}_2\text{O}_{5.75}$  prompts us to assign LS state for  $\text{Co}^{4+}$  ions and HS/IS state for  $\text{Co}^{3+}$ . It may also be noted that a simple calculation of magnetic moment of Co ions assuming all  $\text{Co}^{4+}$  to be in LS state and octahedral  $\text{Co}^{3+}$  ions in HS while square pyramidal  $\text{Co}^{3+}$  in IS state gives a value of  $5.47 \mu_B/f.u.$  which is in good agreement with that obtained from Curie Weiss fit. With a decrease in  $\delta$ , the concentration of  $\text{Co}^{3+}$  ions will increase giving

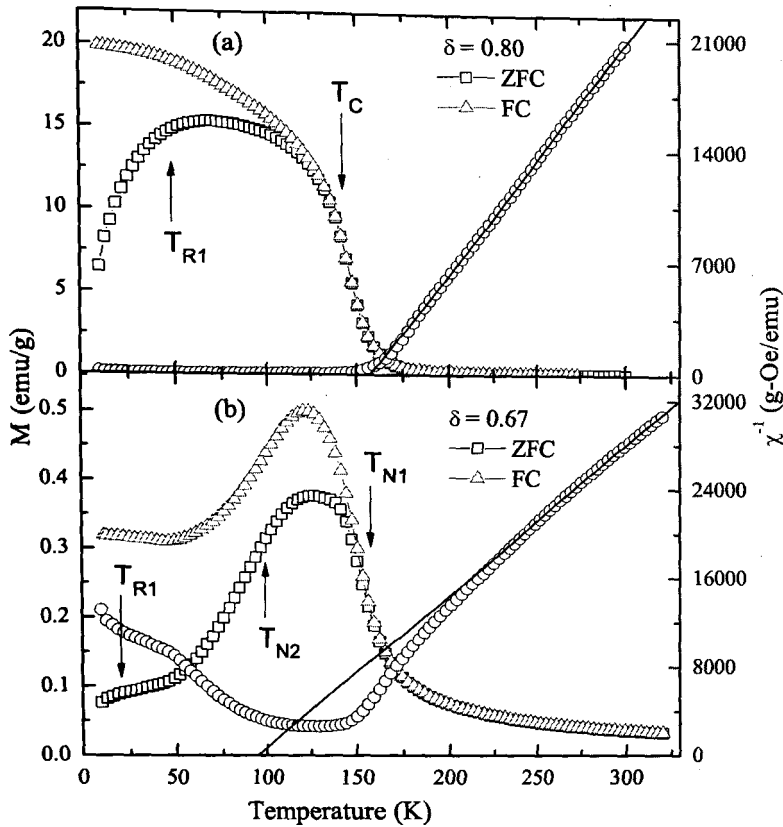


Figure 6.5: Temperature dependent magnetization  $M(T)$  in the field of 1000 Oe for ZFC and FC cycle indicated by open squares and triangles respectively. The magnetic transitions are indicated by arrows. Plot of  $1/\chi$  Vs temperature where in circles denote the experimental data along with Curie-Weiss fit indicated by solid line. (a)  $\delta = 0.80$  (b)  $\delta = 0.67$

rise to a higher possibility of  $\text{Co}^{3+} - \text{O} - \text{Co}^{3+}$  pairs. Clusters of square pyramidal  $\text{Co}^{3+}$  ions can influence antiferromagnetic interactions at higher temperatures.

The isothermal magnetization  $M(H)$  recorded at 10 K and in the vicinity of  $T_C$  and  $T_N$  for compounds having  $\delta = 0.80, 0.58$ . The  $M(H)$  for  $\delta = 0.80$  is presented in Figure 6.6. A clear hysteresis loop signifying the presence of ferromagnetism is observed at 10 K. The magnetization however, does not saturate even up to 14 T indicating a presence of strong



magnetic anisotropy or a competing AFM state. The hysteretic behaviour persists up to 150 K though the coercive field decreases with increasing temperature before vanishing at  $T_C = 150$  K (top left inset of Figure 6.6(c)).  $M(H)$  curve at 300 K shown in the bottom left inset of Figure 6.6(c) indicates the sample to be paramagnetic at this temperature. Another notable feature in the hysteresis curves is that the virgin curve lies outside the loop at 100 K and 150 K.

This can be attributed to presence of two different Co ions in the matrix. Due to the presence of  $\text{Co}^{3+}$  and  $\text{Co}^{4+}$  ions there is an electronic phase separation. The ferromagnetism can be attributed to majority  $\text{Co}^{3+} - \text{O} - \text{Co}^{4+}$  superexchange interactions in agreement with Goodenough-Kanamori rule [31]. While AFM can be due to minority  $\text{Co}^{3+} - \text{O} - \text{Co}^{3+}$  superexchange interaction. In this case, the application of the magnetic field continuously transforms the AFM state into FM state. This leads to coercive field being strongly temperature dependent. Since the coercive field of the ferromagnetic component is smaller than the field of the metamagnetic transition which transforms the AFM state into FM state, the virgin curve appears outside the hysteresis loop.

$M(H)$  recorded for  $\delta = 0.58$  at various temperature is presented in Figure 6.7. The main point is that although the samples are reported to undergo AFM transition, ferromagnetic hysteresis loop is observed at all temperatures below  $T_C$ .

Further, isothermal magnetization measured at 300 K (Inset in Figure 6.7) shows a slight curvature indicating presence of short range ferromagnetic interactions well above  $T_C$ . In the case of both samples, coercive field increases with decrease in temperature

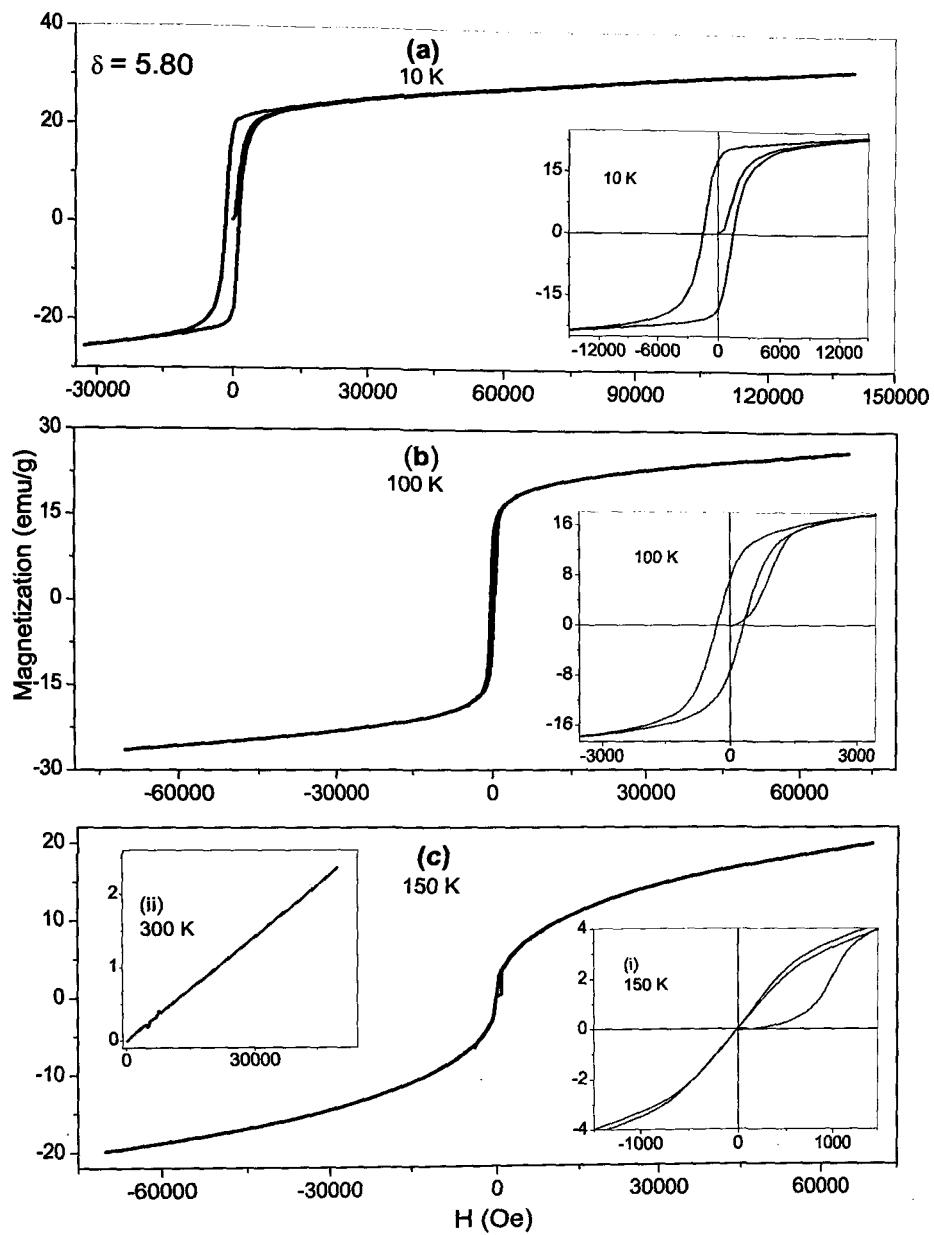


Figure 6.6: Hysteresis loops for  $\text{PrBaCo}_2\text{O}_{5.80}$  recorded at (a) 10 K, (b) 100 K and (c) 150 K. The same data on a magnified scale is shown in the insets.  $M$  vs  $H$  data at 300 K is presented in inset(ii).

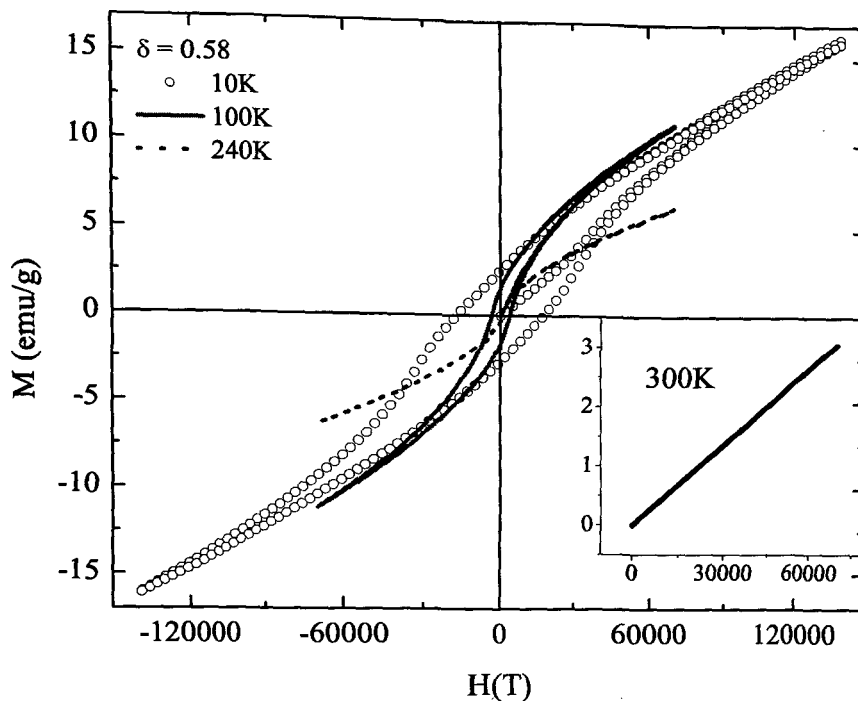


Figure 6.7: Isothermal magnetization curves of  $\text{PrBaCo}_2\text{O}_{5.58}$ , recorded at 10 K, 100 K, and 240 K. The initial magnetization curve at 300 K is shown in inset.

indicating strengthening of FM interactions. However, no saturation of magnetization is observed even at lowest temperature and maximum field of measurement in the case of these compounds. The continuous increase in magnetization with field could also be attributed to paramagnetic contribution of Pr ions. However, this contribution would have been reversible, in contrast to the obtained result. The hysteresis loop at 10 K shows a clear irreversibility right up to fields = 14T. This indicates presence of competing ferro and antiferromagnetic interactions in the two samples. Moreover, it is clear that the magnetization is induced by the applied field rather than being of spontaneous nature.

## 6.4 Transport Properties : Electrical Resistivity Measurements

Electrical resistivity exhibits semiconducting behaviour in the entire temperature range (10 K - 330 K) for the compounds,  $\delta = 0.8$ , 0.67 and 0.58 (Figure 6.8(a)). Data was recorded for cooling and warming cycles. A comparison of resistivity curves shows that resistivity as well as the change in resistivity are much higher for  $\text{PrBaCo}_2\text{O}_{5.67}$  and  $\text{PrBaCo}_2\text{O}_{5.58}$ . For  $\delta = 0.67$  and 0.58 the resistance changes by almost 5 orders of magnitude from  $\sim 10^{-1}\text{Ohm-cm}$  at 300 K to  $\sim 5 \times 10^3\text{Ohm-cm}$  at 25 K while in case of  $\delta = 0.8$ , it changes from  $\sim 10^{-3}\text{ Ohm-cm}$  to  $10^{-1}\text{ Ohm-cm}$  in  $300\text{ K} \geq T \geq 25\text{ K}$ . A plot of  $\ln \rho$  v/s  $T^{-1/4}$  presented in Figure 6.8(b) and (c) exhibits a linear variation for a large temperature range indicating variable range hopping (VRH) to be the dominant mechanism of conduction in all the compounds. However, the hopping temperature is much higher for  $\delta = 0.67$  and 0.58 as compared to that in  $\delta = 0.8$ . Hysteresis between the cooling and warming curves of  $\delta = 0.58$  can be seen in the temperature region between 100 K and 200 K which coincides with the difference in magnetization seen in FCC and FCW curves in Figure 6.4(b). This is a clear indication of coupling between spin and charge degrees of freedom.

## 6.5 Magneto-Transport Properties : Measurements of Magnetoresistance

Resistivity measured in applied field of 8T had a similar temperature dependency with very little difference from the zero field value in the entire temperature range. No notice-

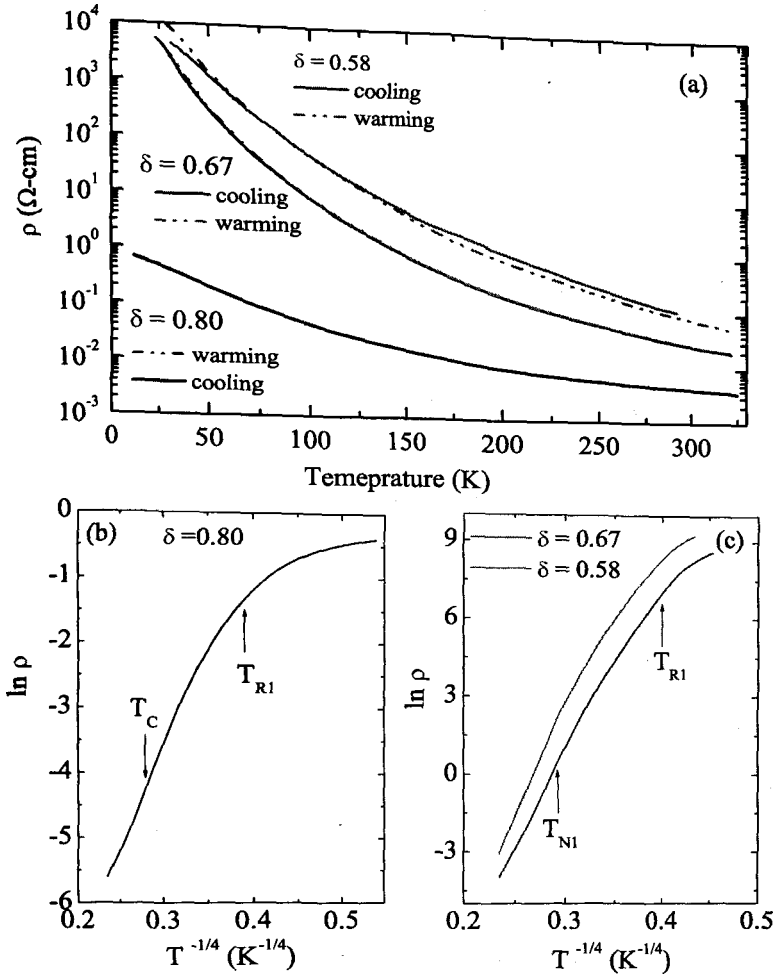


Figure 6.8: (a) Plot of resistivity with temperature during cooling and warming cycles. (b) Logarithm of the resistivity versus  $T^{-1/4}$  plot with arrows indicating different transitions.

able change has been observed in resistivity.

Isothermal magnetoresistance (MR) for  $\text{PrBaCo}_2\text{O}_{5.80}$  measured at various temperatures in the field range of  $\pm 8\text{T}$  are shown in Figure 6.9. MR is quite large ( $\sim 40\%$  at 10 K and 8T) and negative at  $T \leq 100$  K as expected for a ferromagnetically ordered sample. An interesting feature to be noted is the irreversibility of MR measured while ramping the magnetic field in both directions. This irreversibility of MR gives rise to "butterfly-like" pattern below 50 K. Normally such an effect is observed near magnetic

phase boundary or due to presence of competing magnetic interactions [8]. This observation augers well with the observation of  $T_{R1}$  at 50 K in  $\text{PrBaCo}_2\text{O}_{5.80}$ . It may also be noted that hysteresis recorded at 10 K and in the field of  $\pm 14\text{T}$  fails to show saturation of magnetic moment Figure 6.7. Hence, even though the compound shows bulk ferromagnetic character below its  $T_C$ , there could be weak competing magnetic interactions present due to minority  $\text{Co}^{3+}\text{-O-Co}^{3+}$  pairs.

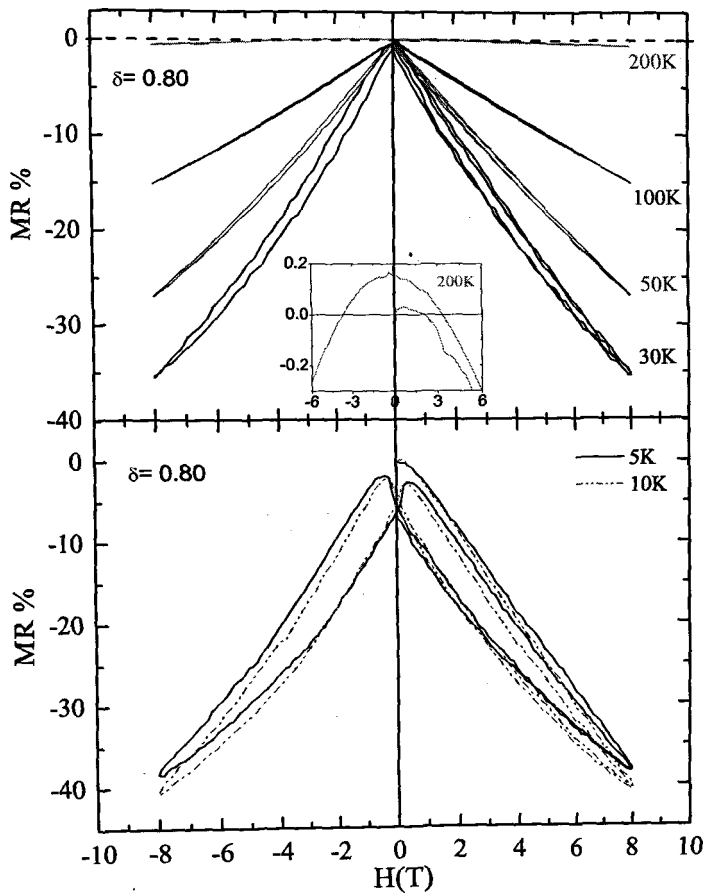


Figure 6.9: Magnetic-field-dependent isothermal magnetoresistance at various temperatures for  $\delta = 0.80$ . Inset shows enlarge view of positive going MR at 200 K.

In the case of  $\delta = 0.67$  MR is negative but small ( $\sim 3\%$  at 8T) and for  $T \leq 50$  K,

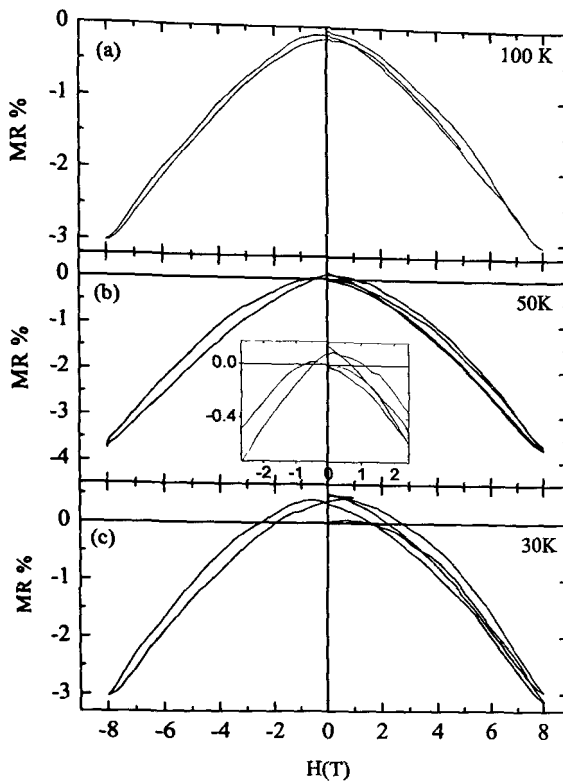


Figure 6.10: Magnetic-field-dependent isothermal magnetoresistance at various temperatures for  $\delta = 0.67$ , (a) 100 K, (b) 50 K; Inset shows an enlarged view of positive going MR at 50 K, (c) 30 K.

exhibits positive values at low fields (see Figure 6.10). The positive values of MR indicate antiferromagnetic ground state. However, the crossover to negative values at low fields and butterfly-like effect hints at the presence of competing magnetic interactions or even field induced magnetization. This is in general agreement with inferences drawn from magnetization results which show presence of antiferromagnetic correlations at higher temperatures as well as large difference in ZFC and FC values at low temperatures. Attempts were made to measure MR at higher temperatures but no specific trend could be made out as the values were very small.

MR for  $\delta = 0.58$ , found to be very similar to that of  $\delta = 0.67$  with some changes. The

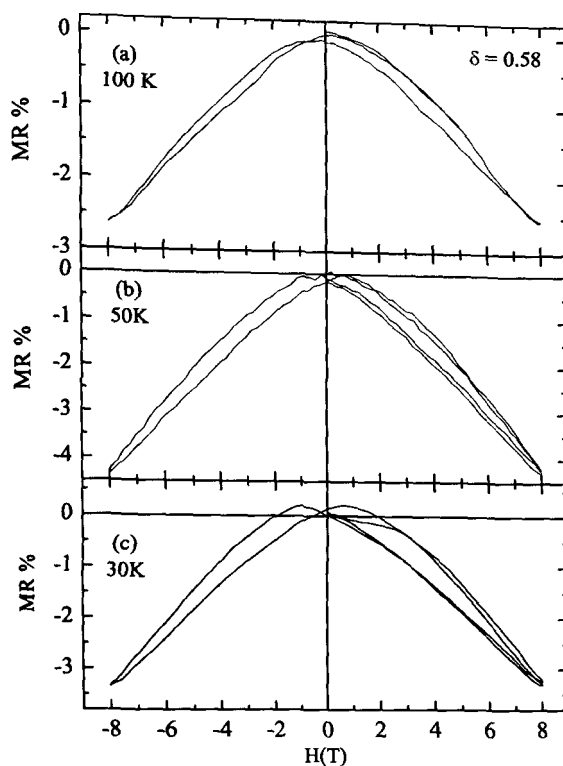


Figure 6.11: Magnetic-field-dependent isothermal magnetoresistance at various temperatures for  $\delta = 0.58$ , (a) 100 K, (b) 50 K (c) 30 K.

MR lobes generally cross each other at 0T, but for  $\delta = 0.58$ , MR lobes cross each other at  $-0.9T$  for 100 K as shown in Figure 6.11(a). The MR lobes at 50 K and 30 K are shifted slightly to non-zero position indicates strong AFM-FM competition in this compound.

MR at 30 K shows butterfly-like effect.

## 6.6 X-ray Absorption Spectroscopic Measurements

$\text{PrBaCo}_2\text{O}_{5+\delta}$  shows the presence of competing magnetic interactions. To understand the role of  $\text{Co}^{3+}$  spin state and local coordination around it in the transport and magnetic properties of  $\text{PrBaCo}_2\text{O}_{5+\delta}$ , XANES and EXAFS measurements at the Co  $K$  edge have been studied at several temperatures in the range  $20 \text{ K} \leq T \leq 300 \text{ K}$ .



### 6.6.1 Extended X-ray Absorption Fine Structure (EXAFS)

The presence of competing magnetic interactions, short range correlations at temperatures much above ordering temperature and irreversibility in isothermal magnetoresistance make it evidently clear that the local structure around Co and its spin state play an important role in governing magnetic and transport properties of these layered double perovskites. EXAFS measurements at Co  $K$  edge and at various temperatures can give an insight of changes in local structure and spin state of Co ions. The temperature dependant EXAFS spectra recorded at various temperatures were treated as per given in Chapter 2 and modelled as describe in Chapter 5. Figure 6.12 (a) and (d) presents magnitude of FT of  $k^3$  weighted  $\chi(k)$  data for the two compounds  $\delta = 0.8$  and  $0.67$  respectively. EXAFS spectra in the range 1-4 Å were fitted with Co-O, Co-Co and Co-Pr/Ba single scattering and Co-O-Co multiple scattering correlations. The fitting parameters were defined using relations based on lattice parameters to reduce interdependency and number of variables. The solid lines in Figure 6.12 (a) and (d) respectively depict the best fit obtained to experimental data at 20 K. The variations of Co-O bond distances and Co-O-Co bond angle obtained from fitting are presented in Figure 6.12 (b) and (c) for  $\delta = 0.80$  and (e) and (f) for  $\delta = 0.67$  respectively.

In the case of  $\delta = 0.8$ , it can be seen that the Co-O planar bond length (Figure 6.12(b)) decreases steadily with temperature followed by an increase around 150 K which coincides with the  $T_C$  of the compound. A similar behaviour is also noted for the planar Co-O-Co bond angle (Figure 6.12(c)). On the other hand, the Co-O apical bond distance

exhibits a step-like behaviour with an increase around 240 K. This elongation of CoO polyhedra along *c*-axis and the concomitant shrinkage in Co-O planar bond length and the Co-O-Co bond angle corresponds to the tilting of CoO polyhedra towards each other. Further, at lower temperatures ( $\sim 150$  K) the polyhedra rotate about *c* axis resulting in increase of Co-O planar bond length and the planar Co-O-Co bond angle.

A similar variation of bond distances can be seen in the case of  $\delta = 0.67$ . The elongation along *c*-axis and tilting of Co-O polyhedra can be seen to happen around 300 K (Figure 6.12(e), (f)). At lower temperatures, the apical Co-O bond distance is found to remain nearly constant while the planar Co-O bond distance and Co-O-Co bond angle exhibit identical variation with temperature. In particular, the planar Co-O bond distance and bond angle show two minima centred at about 250 K and 100 K and a maxima at around 150 K. Interestingly these temperatures respectively correspond to onset of magnetic correlations as seen from Curie-Weiss analysis of susceptibility, and the antiferromagnetic ordering temperatures,  $T_{N1}$  and  $T_{N2}$  of the compound.

Figure 6.13(a) shows Fourier transform (FT) of EXAFS data recorded at 20 K along with the corresponding best fit. The variation of Co-O bond lengths for the octahedra and square pyramids along with Co-O-Co inter-polyhedron bond angle are plotted in Figure 6.13(b-f). As can be seen from Figure 6.13(f) there appears to be hardly any change in planar Co-O bond distances of the square pyramidal site in the entire temperature range. However, in case of octahedra, although the Co-O bond distance along *a* axis remains nearly constant in the entire temperature range, that along *b* axis shows a strong

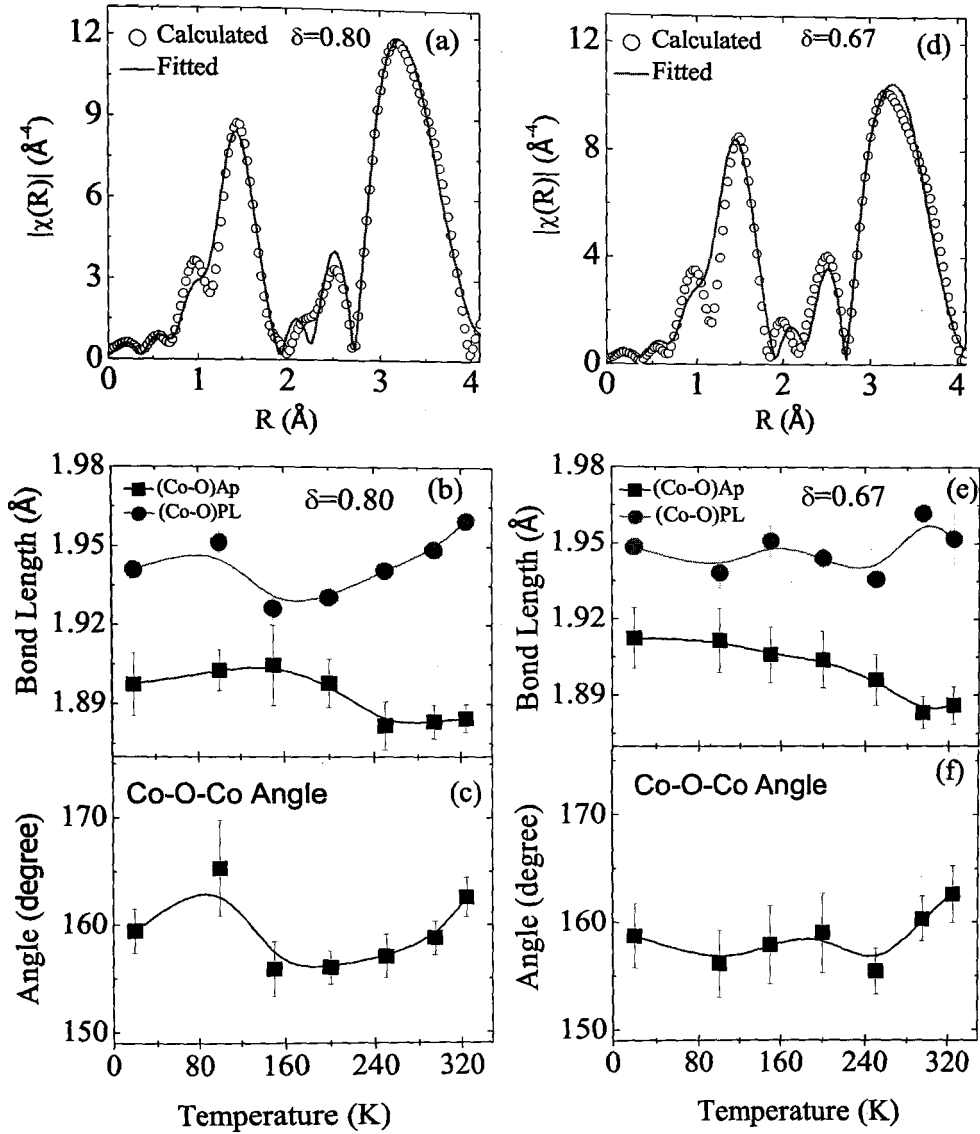


Figure 6.12: (a) and (d) EXAFS  $\chi(k)$  data and best fit, (b) and (e) variation of average Co-O bond distances planer and apical (c) and (f) Co-O-Co bond angle at various temperatures for  $\text{PrBaCo}_2\text{O}_{5.80}$  and  $\text{PrBaCo}_2\text{O}_{5.67}$  respectively.

temperature dependence (see Figure 6.13(b)). It must be mentioned here that amongst the lattice parameters,  $a$  shows the least change as a function of temperature [14]. It can be seen that the changes octahedral in Co-O bond distance and Co-O-Co bond angle around  $T_{N1}$  and 150 K.

## 6.7 Discussion

It is quite evident from the above studies that  $\delta$  has a great influence on magnetic transition temperatures. Though the magnetization of sample with  $\delta = 0.8$  does not show presence of an antiferromagnetic transition, the wide separation between ZFC and FC magnetization curves and the nature of magnetic hysteresis loops clearly show presence of competing AFM and FM interactions. It is also seen that all the compounds undergo another magnetic transition  $T_{R1}$  at lower temperatures. This transition appears to be related to orthorhombic distortion.

The two compounds  $\text{PrBaCo}_2\text{O}_{5+\delta}$  with  $\delta = 0.67$  and  $0.80$  crystallize in tetragonal unit cell with  $P4/mmm$  structure. However, they exhibit contrasting magnetic behaviour. While  $\text{PrBaCo}_2\text{O}_{5.8}$  orders ferromagnetically below 147 K,  $\text{PrBaCo}_2\text{O}_{5.67}$  has an antiferromagnetic ground state. In the case of  $\text{PrBaCo}_2\text{O}_{5.80}$ , charge balance demands 30% Co ions to be in tetravalent state while the rest 70% to be in trivalent state.

The value of  $\mu_{eff}$  obtained from Curie-Weiss analysis of susceptibility and its agreement with that reported for  $\text{PrBaCo}_2\text{O}_{5.75}$  [13] indicates that  $\text{Co}^{4+}$  ion are in LS state while  $\text{Co}^{3+}$  ions are in HS/IS state. Therefore the observed FM ordering can be ascribed

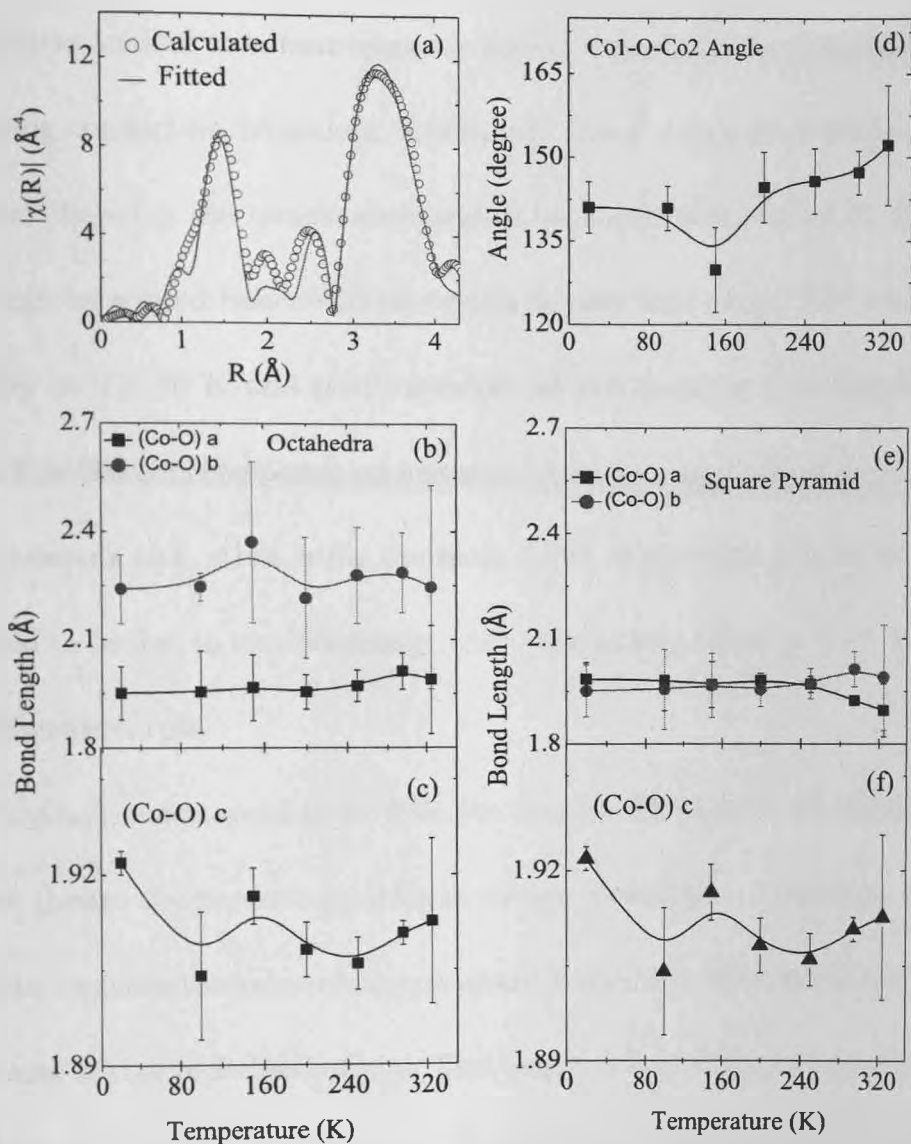


Figure 6.13: (a) EXAFS  $\chi(k)$  data and best fit at 20 K, variation of Co-O bond distances (b) Octahedra Planer (c) Octahedra apical, (d) Co-O-Co bond angle, Co-O bond distances (e) square pyramidal planer (f) square pyramidal apical at various temperatures for  $\text{PrBaCo}_2\text{O}_{5.58}$ .

to double exchange (DE) interaction between LS  $\text{Co}^{4+}$  ( $t_{2g}^5, e_g^0$ ) and HS/IS  $\text{Co}^{3+}$  ( $t_{2g}^5, e_g^1$  or  $t_{2g}^4, e_g^2$ ) ions. These DE interactions are facilitated by tilting and the rotation of  $\text{Co}^{3+}\text{O}$  and  $\text{Co}^{4+}\text{O}$  polyhedra towards each other about the  $c$  axis. This increases the  $\text{Co}(3d) - \text{O}(2p)$  hybridization leading to a ferromagnetic order. The change in hybridization also promotes hopping conduction behaviour resulting in lower values of resistivity. Mott's VRH law is best obeyed in the temperature region between 200 K and 50 K. Deviations from linearity can be noticed below and above this temperature range. MR also exhibits irreversibility at  $T \leq 50$  K and positive values at low fields at  $T = 200$  K. It may be noted that  $T = 200$  K corresponds approximately to the temperature at which Co-O polyhedra tilt towards each other while the weak AFM interactions noticed below 50 K could be implied to be due to superexchange (SE) interactions between  $\text{Co}^{3+}$  ions as per Goodenough-Kanamori rule.

For  $\text{PrBaCo}_2\text{O}_{5.67}$ , the properties are found to be very different. With the decrease in oxygen content though the percentage of Co in square pyramidal coordination and those in trivalent state increases the value of  $\mu_{eff}$  obtained from Curie Weiss fit to susceptibility is nearly the same as that in  $\text{PrBaCo}_2\text{O}_{5.80}$ . This implies that  $\text{Co}^{3+}$  ions continue to be in HS/IS state and the  $\text{Co}^{4+}$  ions in LS state. Therefore antiferromagnetic superexchange interaction can be expected between neighbouring CoO polyhedra containing trivalent cobalt ions while the  $\text{Co}^{3+}\text{-O-Co}^{4+}$  pairs will interact via double exchange mechanism. EXAFS studies indicate that the antiferromagnetic SE interactions are a result of the outward rotation of  $\text{Co}^{3+}$  polyhedra about the  $c$ -axis. The presence of competing ferro-

magnetic interactions arising due to DE interactions can give rise to canting of Co spins resulting in an increase in magnetization at about 150 K. The antiferromagnetic order localizes the charge carriers leading to a much higher resistivity as compared to  $\delta = 0.8$  compound and a much lower MR even near the AFM transition.

The double perovskite  $\text{PrBaCo}_2\text{O}_{5.58}$  crystallises in orthorhombic structure with  $Pmmm$  space group. The properties of this sample are found to be very similar to that of  $\delta = 0.67$ . Magnetization depicts a PM to FM like transition at 246 K followed by another transition to AFM state at 200 K. EXAFS studies shows that there is hardly any change in square pyramids, the major changes are observed in octahedral site.

## 6.8 Conclusions

In summary, there exists a transition from tetragonal to orthorhombic structure with decrease in oxygen content. All the samples have a complex magnetic ground state due to competing ferromagnetic and antiferromagnetic interactions. In the case of  $\delta = 0.80$  the inward rotation and tilting of the neighbouring  $\text{Co}^{3+}\text{O}$  and  $\text{Co}^{4+}\text{O}$  polyhedra about the c-axis facilitates DE mechanism between LS  $\text{Co}^{4+}$  and HS/IS  $\text{Co}^{3+}$  ions leading to ferromagnetic order. While in case of  $\delta = 0.67$  the tilting and outward rotation of the neighbouring  $\text{Co}^{3+}\text{O}$  polyhedra away from each other supports  $\text{Co}^{3+} - \text{O} - \text{Co}^{3+}$  superexchange mediated antiferromagnetic ordering. EXAFS studies on  $\delta = 0.58$  shows that there is hardly any change in square pyramids, the major changes are observed in octahedral site.

# References

- [1] Maignan A, Martin C, Pelloquin D, Nguyen N, and Raveau B 1999 *J. Solid State Chem.* **142** 247
- [2] Martin C, Maignan A, Pelloquin D, Nguyen N, and Raveau B 1997 *Appl. Phys. Lett.* **71** 1421
- [3] Moritomo Y, Akimoto T, Takeo M, Machida A, Nishibori E, Takata M, Sakata M, Ohoyama K and Nakamura A 2000 *Phys. Rev. B* **61** R13325
- [4] Respaud M, Frontera C, García-Muñoz J, Aranda A G M, Raquet B, Broto J, Rakoto H, Goiran M, Llobet A, and Carvajal J 2001 *Phys. Rev. B* **64** 214401
- [5] Vogt T, Woodward P M, Karen P, Hunter B A, Henning P, and Moodenbaugh A R 2000 *Phys. Rev. Lett.* **84** 2969
- [6] Suard E, Fauth F, Caignaert V, Mirebeau I and Baldinozziet G 2000 *Phys. Rev. B* **61** R11871
- [7] Troyanchuk I, Kasper N, and Khalyavin D D 1998 *Phys. Rev. Lett.* **80** 3380



- [8] Kundu A K, Reveau B, Caignaert V, Rautama E-L and Pralong V 2009 *J. Phys. Condens. Matter* **21** 056007
- [9] Streule S, Podlesnyak A, Mesot J, Medared M, Conder K, Pomjakushina E, Mitberg E and Kozhevnikov V 2005 *J. Phys: Condens. Matter* **17** 3317
- [10] Diaz-Fernandez Y, Malavasi L and Mozzati M C 2008 *Phys. Rev. B* **78** 144405
- [11] Frontera C, Carrillo A, Oró-Solé J and García-Muñoz J L 2005 *Chem. Mater*, **17**, 5439-5445
- [12] Nakajima T, Ichihara M and Ueda Y 2005 *J. Phys. Soc. Jpn.* **74** 1572
- [13] Frontera C, García-Muñoz J L and Carrillo A 2004 *Phys. Rev. B* **70** 184428
- [14] Frontera C, García-Muñoz J L, Carrillo A, Aranda M A G, Margiolaki I and Caneiro A 2006 *Phys. Rev. B* **74** 054406
- [15] Wu H 2003 *J. Phys.: Condens. Matter* **15** 503
- [16] Ganorkar S, Priolkar K R, Sarode P R, and Banerjee A 2011 *J. Appl. Phys.* **110** 053923
- [17] Pandey S K, Kumar A, Patil S, Medicherla V R R, Singh R, Maiti K, Prabhakaran D, Boothroyd A, and Pimpale A V 2008 *Phys. Rev. B* **77** 045123
- [18] Wu Z Y, Benfatto M, Pedio M, Cimino R, Mobilio S, Barman S R, Maiti K and Sarma D D 1997 *Phys. Rev. B* **56** 2228

- [19] Berman S and Sarma D D 1994 *Phys. Rev. B* **49**, 13979
- [20] Pandey S K, Patil S, Medicherla V R R, Singh R and Maiti K 2008 *Phys. Rev. B* **77** 115137
- [21] Chang J Y, Lin B N, Hsu Y Y and Ku H C 2003 *Physica B* **329-333** 826-828
- [22] Haas O, Struis R P W J and McBreen J M 2004 *J. Solid State Chem* **177** 1000-1010
- [23] Pandey S K, Khalid S, Lalla N P and Pimpale A V 2005 *J. Phys: Condens. Matter* **18** 10617-10630
- [24] Khalyavin D D, Barilo S, Shiryaev S, Bychkov G, Troyanchuk I, Furrer A, Al-lenspach P, Szymczak S and Szymczak R 2003 *Phys. Rev. B* **67** 214421
- [25] Pomjakushina E, Conder K and Pomjakushin V 2006 *Phys. Rev. B* **73** 113105
- [26] Hidaka M, Soejima M, Soda M, Sato M, Choi S H, Sung N E, Kim M and Lee J M 2005 *Phys. Stat. Sol (b)* **242** 1422-1430
- [27] Jarry A, Luetkens H, Pashkevich Y, Stingaciu M, Pomjakushina E, Conder K, Lemmens P and Klaus H 2009 *Physica B* **404** 765
- [28] Garc J Lía-Muñoz, Frontera C, Llobat A, Carrillo A E, Caneiro A, Aranda M A G, Ritter C and Dooryee E 2004 *Physica B* **350** e277-e279
- [29] Makhnev A A, Nomerovannaya L V, Tashlykov A O, Barilo S N and Shiryaev S V 2007 *Phys. Solid State* **49** 894

[30] Taskin A, Lavrov A, Ando Y 2005 *Phys. Rev. B* **71** 134414

[31] Goodenough J 1963 *Magnetism and the Chemical Bond* Wiley-Interscience:New

York

## Chapter 7

# Magnetic and Spectroscopic Studies of Oxygen Deficient Layered Cobaltites $\text{PrBaCo}_2\text{O}_{5+\delta}$ ( $\delta = 0.43, 0.35$ )

### 7.1 Introduction

$\text{RCoO}_3$  (R = rare earth element) type perovskites and their derivatives stimulated tremendous interest due to their physio-chemical properties. One of such derivatives is  $\text{RBaCo}_2\text{O}_{5+\delta}$  type layered perovskite. Non-stoichiometry and doping makes these layered cobaltites to show a variety of physical phenomena like metal insulator transition (MIT), spin state transition, charge ordering and giant magnetoresistance (MR) etc. [1, 2, 3, 4, 5, 6, 7]. Strong electron correlations are intensely shown in these systems. "Oxygen Engineering" or control of oxygen content is one of the important concept in these layered perovskites that not only controls the formal valence state of the metal ion but also its local environment. Furthermore, the spin state transitions of Co ions can also be triggered easily by varying oxygen content. Therefore controlling oxygen content can be a prime factor in realising tailor made materials for desired applications.

$\text{RBaCo}_2\text{O}_{5.5}$  perovskites ( $\delta = 0.5$ ) have singly valent cobalt ( $3+$ ) ion surrounded by alternate octahedral and square pyramidal oxygen environment. The competition between crystal field, on-site Coulomb correlation and the inter atomic exchange energy results in three possible spin states  $\text{Co}^{3+}$  : the low spin state (LS,  $t_{2g}^6 e_g^0$ ,  $S=0$ ), the intermediate spin state (IS,  $t_{2g}^5 e_g^1$ ,  $S=1$ ) and high spin state (HS,  $t_{2g}^4 e_g^2$ ,  $S=2$ ) [8]. These spin state transitions are known to play an important role in their unique properties. A change in the value of  $\delta$  either on lower or higher side induces mix valence and therefore new magnetic interactions.

Although there are a large number of studies on oxygen content variation in  $\text{RBaCo}_2\text{O}_{5+\delta}$ , the members with lighter rare-earths and  $\delta < 0.5$  have not been explored much. In particular, the influence of oxygen content on the local structure and its correlation with magnetic and transport properties of these layered perovskites is missing in literature. Recently we have shown that such a correlation exists in oxygen rich compounds with  $\delta > 0.5$  [9]. Studies on magnetic properties of  $\text{PrBaCo}_2\text{O}_{5+\delta}$  as a function of oxygen content showed that the samples with lower oxygen content  $5 + \delta$  have a larger orthorhombic distortion and more complex magnetic properties.

Spectroscopy is an important tool to investigate the local lattice distortions around metal ions. IR spectroscopy and its complementary technique Raman spectroscopy have been effectively used to understand the local lattice distortion in  $\text{RBaCo}_2\text{O}_{5.5}$  [10, 11, 12], while X-ray absorption fine structure spectroscopy (XAFS) can precisely probe the local structure and has been effectively used in case of the parent  $\text{RCoO}_3$  compounds [13, 14,

15, 16, 17, 18, 19]. It is contemplated in literature that the deformation of CoO polyhedra affects the crystal field which in turn modifies the hybridization between outer orbits of cations (R, Ba, Co) and  $2p$  orbitals of oxygen ion thereby affecting electric and magnetic properties of layered perovskites [20, 21]. The aim of this work is to correlate spectroscopic properties (IR, Raman and XAFS) of  $\text{PrBaCo}_2\text{O}_{5+\delta}$ , where  $\delta = 0.43$  and  $0.35$  with their magnetic and transport properties in order to develop a better understanding of complex magnetic ground states. The sample was prepared as described in section 2.1 and the oxygen content was determined by iodometric titration as mentioned in Table 2.1.

## 7.2 X-ray Diffraction Measurements

Rietveld refinement of room temperature XRD pattern of  $\text{PrBaCo}_2\text{O}_{5+\delta}$  for  $\delta = 0.43$  and  $0.35$ , presented in Figure 7.1, confirms the formation of single phase sample with 122 type orthorhombic unit cell belonging to  $Pmmm$  space group. A very minor ( $\sim 1\%$ ) impurity phase is detected with peaks around  $2\theta \sim 29^\circ$  and  $31^\circ$  which can be ascribed to unreacted Pr-oxides ( $\text{Pr}_2\text{O}_3$ ,  $\text{Pr}_6\text{O}_{11}$ ). The lattice parameter obtained from Rietveld refinement are given in Table 7.1. The unit cell volume decreases with decrease in oxygen concentration which is due to decrease in cell parameters  $a$  and  $b$ . The parameter  $c$  however, shows a slight increase as the oxygen content is reduced from 5.43 to 5.35. The orthorhombic distortion,  $O_s = (a - b)/(a + b)$  found higher for  $\delta = 0.43$  ( $O_s = 0.00397$ ) than that of  $\delta = 0.35$  ( $O_s = 0.00355$ )

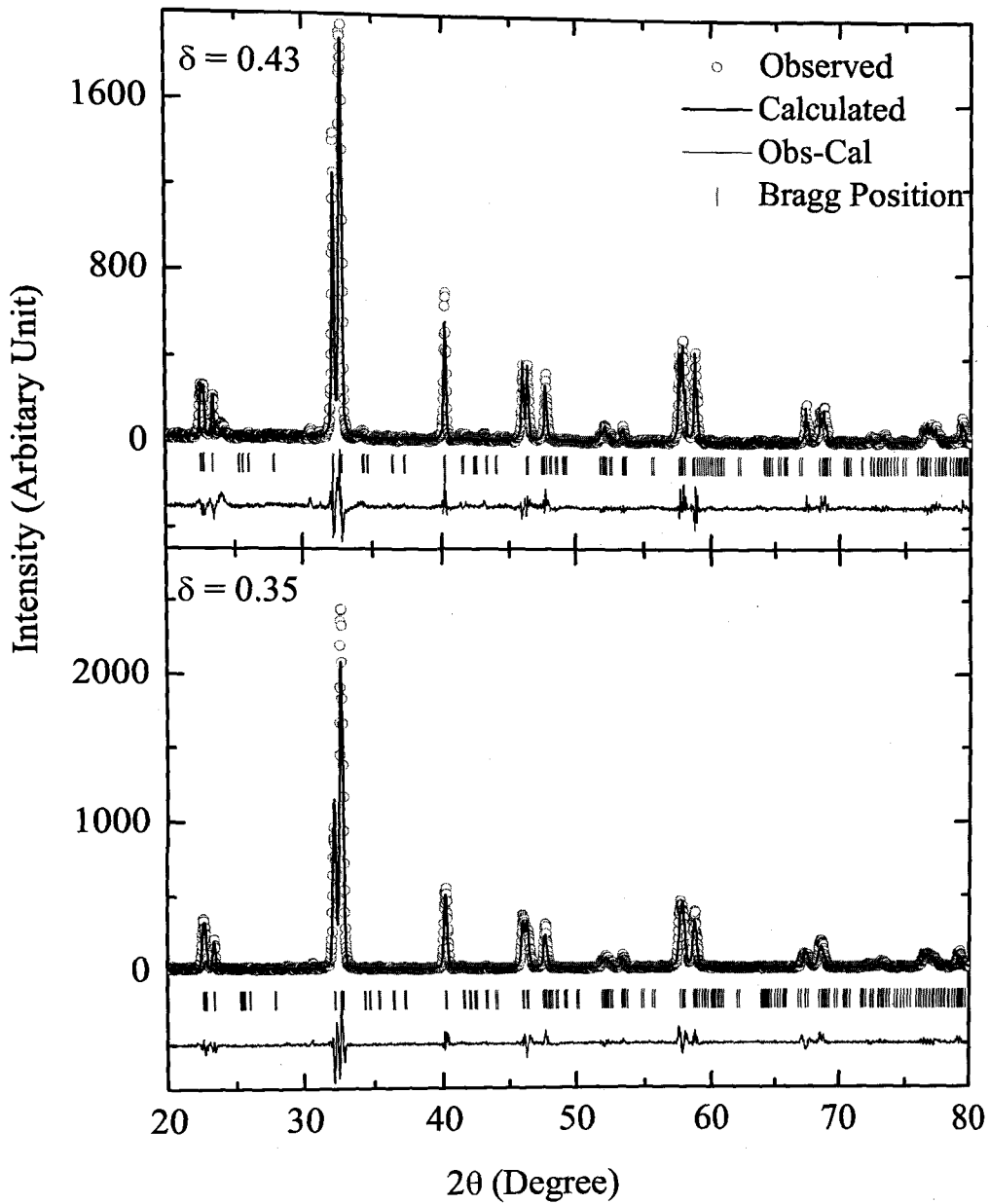


Figure 7.1: Rietveld refinement of XRD patterns of  $\text{PrBaCo}_2\text{O}_{5+\delta}$  for  $\delta = 0.43$  and  $0.35$ . Circles represent experimental data, the continuous line through the data is the fitted curve, vertical lines shows Bragg's reflections and the difference pattern is shown at the bottom as solid line.

Table 7.1: Lattice parameters and magnetic transition temperatures for  $\text{PrBaCo}_2\text{O}_{5+\delta}$ .

$\delta$	$a(\text{\AA})$	$b(\text{\AA})$	$c(\text{\AA})$	$V(\text{\AA}^3)$	$T_{N1}(\text{K})$	$T_{N2}(\text{K})$	$T_{R1}(\text{K})$	$T_{R2}(\text{K})$
0.43	3.9435(1)	7.8246(2)	7.6103(2)	234.83(1)	260	200	302	140
0.35	3.9360(2)	7.8163(5)	7.6148(4)	234.27(2)	240	180	299	60

### 7.3 Magnetization Measurements

Magnetization  $M(T)$  as a function of temperature for  $\text{PrBaCo}_2\text{O}_{5.43}$  measured at 100 Oe and 1000 Oe are shown in Figure 7.2(a) and (b) respectively. The curves show PM-FM like transition characterized by an increase in magnetization at  $T_{N1} = 260$  K followed by a decrease in magnetization which is designated as FM-AFM transition at  $T_{N2} = 200$  K. Based on neutron diffraction studies on  $\text{PrBaCo}_2\text{O}_{5.5}$  [8], both these transitions have been ascribed as transitions to antiferromagnetic ground state. The important things to note are a weak magnetic transition,  $T_{R1}$  at about 300 K and the double hump structure near  $T_{N1}$  in the magnetization curves. Although the transition at  $T_{R2}$  is also noticed in other oxygen rich  $\text{PrBaCo}_2\text{O}_{5+\delta}$ , its transition temperature at 140 K in compound with  $\delta = 0.43$  is unusually high. Muon spin relaxation ( $\mu\text{SR}$ ) studies on  $\text{NdBaCo}_2\text{O}_{5.5}$  attribute the transition around 50 K to a magnetic phase transition [21].

For  $\delta = 0.35$ , magnetization curve shows similar transitions with a shift towards lower temperatures as can be seen for Figure 7.3.

$M(T)$  have been recorded at 1000 Oe and 1 T during ZFC, FCC and FCW cycles Figure 7.3(b). Ferromagnetism dominates with the application of field. A small amount of thermal hysteresis that increases with decreasing  $\delta$  is still observed below  $T_{N1}$  even in



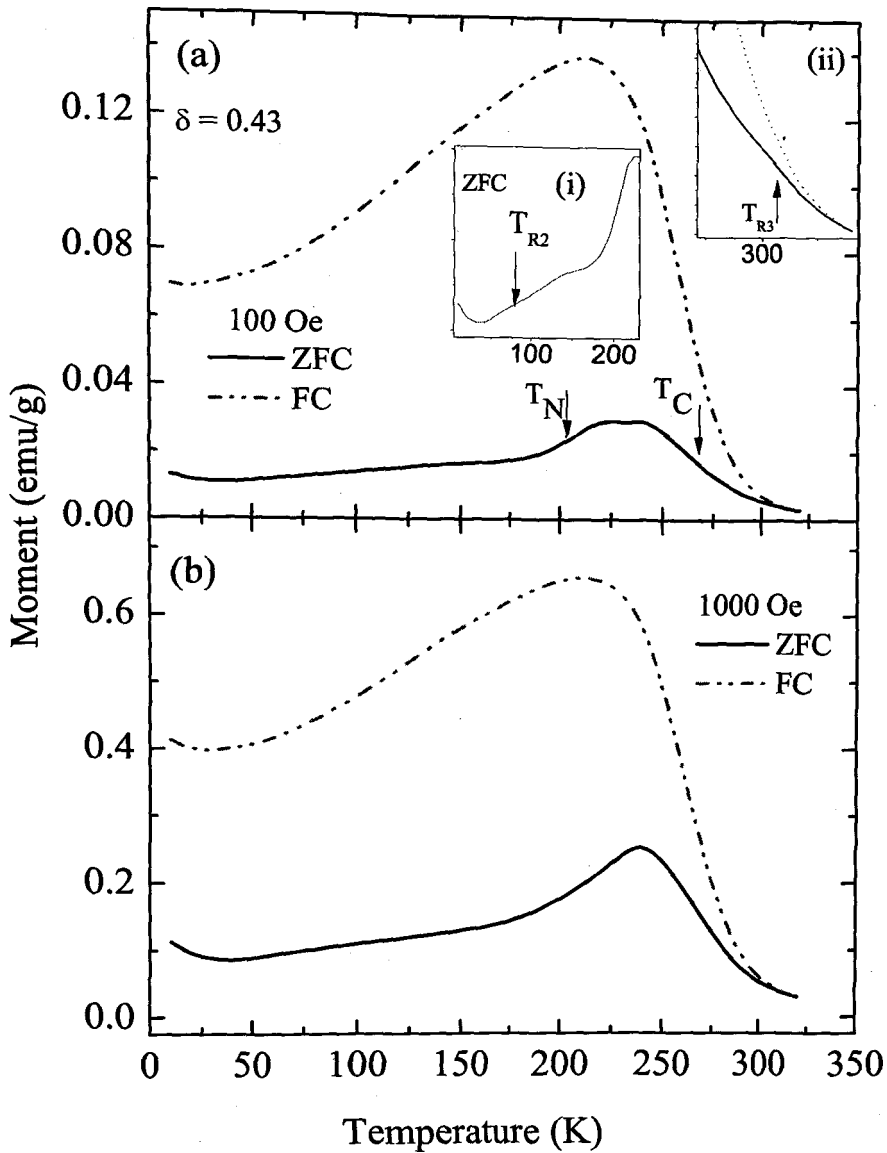


Figure 7.2: Temperature dependent magnetization  $M(T)$  for  $\text{PrBaCo}_2\text{O}_{5.43}$  (a) 100 Oe ZFC and FC cycle indicated by solid line and dashed lines. Inset (i) shows transition at 140 K ( $T_{R2}$ ) by arrow (ii) shows transition at 300 K ( $T_{R1}$ ) by arrow (b) 1000 Oe ZFC and FC cycle indicated by solid line and dashed lines respectively.

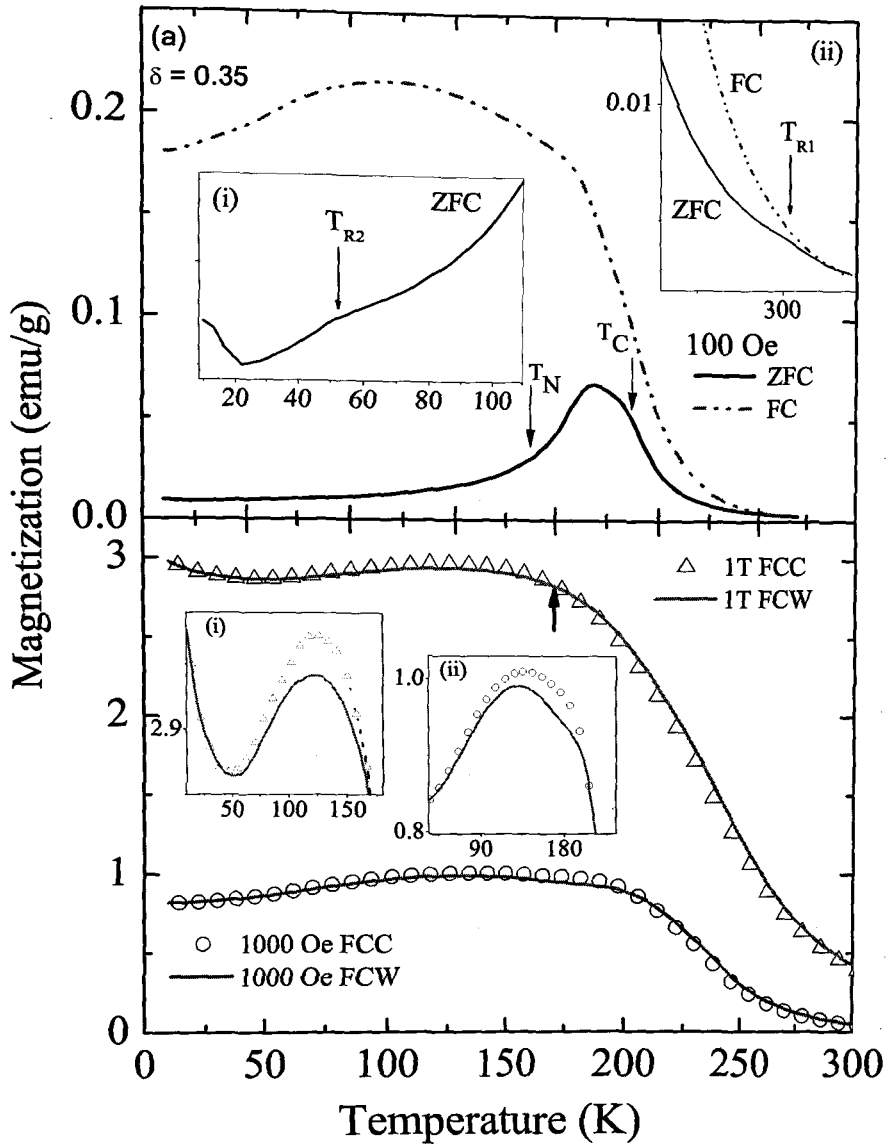


Figure 7.3: Temperature dependent magnetization  $M(T)$  for  $\text{PrBaCo}_2\text{O}_{5.35}$  (a) 100 Oe ZFC and FC cycle indicated by solid line and dashed lines. Inset (i) shows transition at 60 K ( $T_{R2}$ ) by arrow (ii) shows transition at 300 K ( $T_{R1}$ ) by arrow (b)  $M(T)$  recorded at 1000 Oe and 1 T for FCC and FCW cycles. The crossing FCC and FCW curves is presented more clearly in the insets(i) and (ii).

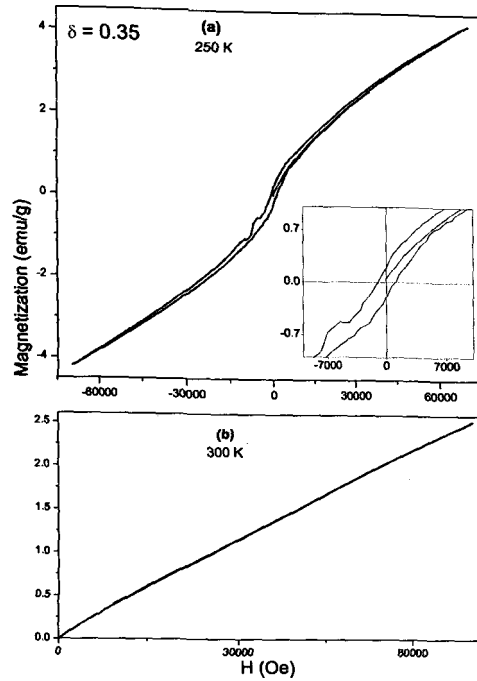


Figure 7.4: Magnetization as a function of magnetic field for  $\text{PrBaCo}_2\text{O}_{5.35}$  recorded at (a) 250 K with the inset showing expanded view of the hysteresis loop and (b) the data recorded at 300 K.

fields of 1 T confirming the presence of a complex magnetic ground state as was evident from magnetization curves at 100 Oe. A closer look at Figure 7.3(b) indicates a presence of a crossover between FCC and FCW curves (see insets (i) and (ii) of Figure 7.3(b)). At low temperatures the FCC curves lie below the FCW curves. As the temperature is increased, the FCC curves cross over and lie above the FCW curves. This cross over temperature is seen to be dependent on oxygen content. One can also notice a crossover between FCC and FCW magnetization curves at around 174 K.

Isothermal magnetization  $M(H)$  recorded at at 250 K and 300 K for  $\delta = 0.35$  is presented in Figure 7.4(a)-(b). It may be noted that both temperatures are above its  $T_{N1}$ . The magnetization curve at 300 K exhibits a curvature towards the horizontal axis. Such

a behaviour can be attributed to presence of short range ferromagnetic interactions. Furthermore, the  $M(H)$  curve at 250 K exhibits a narrow hysteresis loop ( $m_0 \simeq 0.21$  emu/g,  $H_C \simeq 856$  Oe). This observation clearly indicates the transition  $T_{R3}$  to be ferromagnetic in nature. This weak FM ordering could arise due to  $Co^{2+} - O - Co^{3+}$  interactions.

## 7.4 Transport Properties : Electrical Resistivity Measurements

Electrical resistivity recorded in zero field for the both samples exhibits semiconducting behaviour in the entire temperature range (10 K - 330 K) as presented in Figure 7.5(a) and (b). One notices a narrow hysteresis in values of resistance measured during warming and cooling cycles in the temperature range 300 K - 90 K. The irreversibility in resistivity begins at about  $T_{R1}$  and continues till about  $T_{R2}$  indicating a coupling between charge and spin degrees of freedom. It may be mentioned here that the transition at  $T_{R2}$  is believed to be due to structural rearrangement [21]. A similar hysteresis is also noted in case of resistivity measured in 8T magnetic field. A plot of  $\ln \rho$  v/s  $T^{-1/4}$  presented in Figure 7.5(c) and (d) exhibits a linear variation for a large temperature range indicating variable range hopping (VRH) to be the dominant mechanism of conduction in these compounds. Change in slope had been observed at  $T_{R2}$  as indicated by arrow.

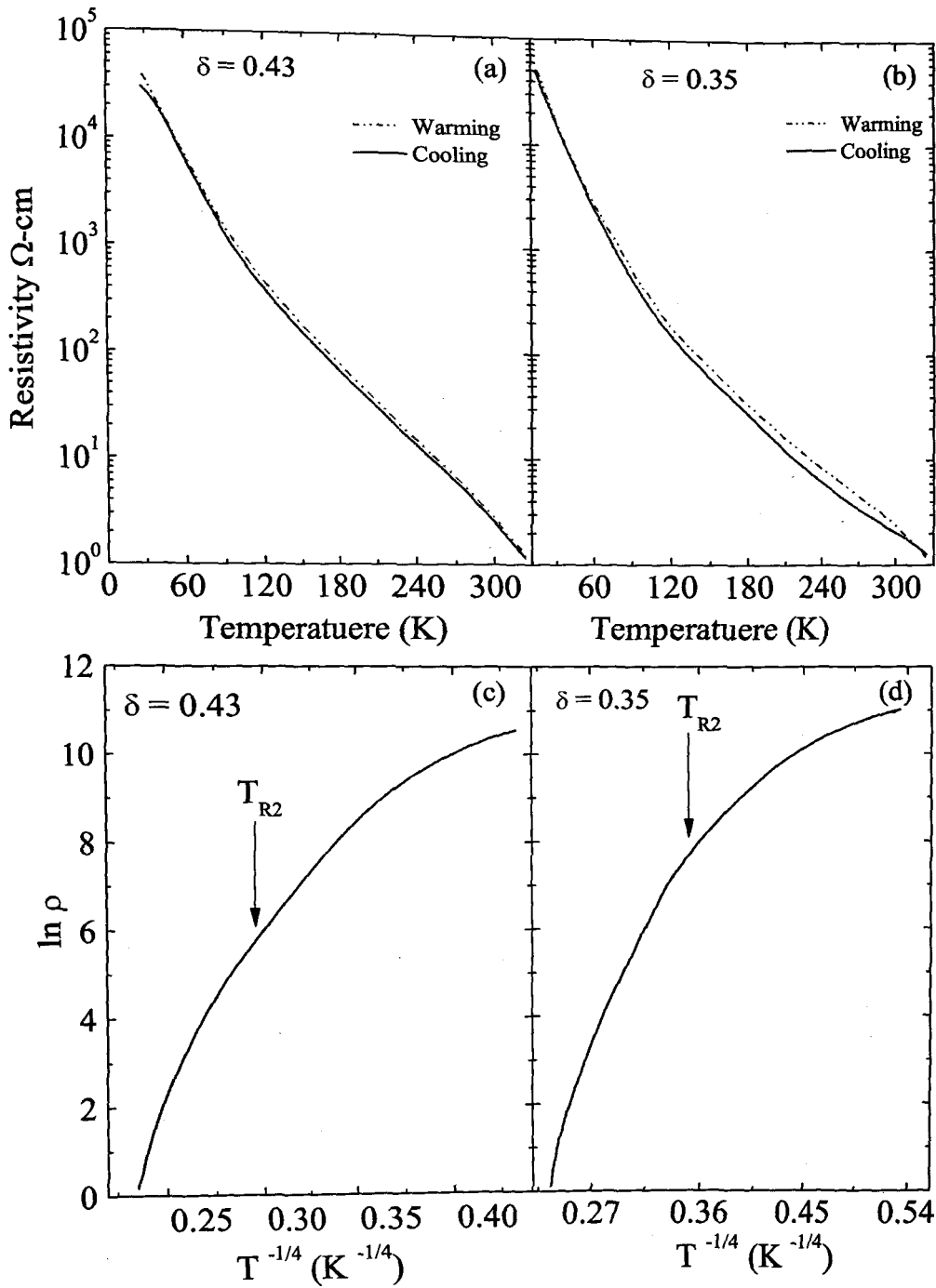


Figure 7.5: (a)-(b) Plot of electrical resistivity versus temperature in  $H = 0T$  during cooling and warming cycles for samples having  $\delta = 0.43$  and  $0.35$  respectively. (c)-(d) A plot of  $\log \rho$  versus  $T^{-1/4}$ . The arrow points to a anomaly indicating change in transport mechanism around  $T_{R2}$ .

## 7.5 Magneto-Transport Properties : Magnetoresistance Measurements

Isothermal magnetoresistance (MR) for measured at several temperatures in the field range of  $\pm 8\text{T}$  are shown in Figure 7.6. MR for  $\delta = 0.43$  recorded at 200 K shows positive going MR as can be seen for Figure 7.6 (a). Usually MR is positive for AFM compounds and negative MR is a signal for ferromagnetic interactions.

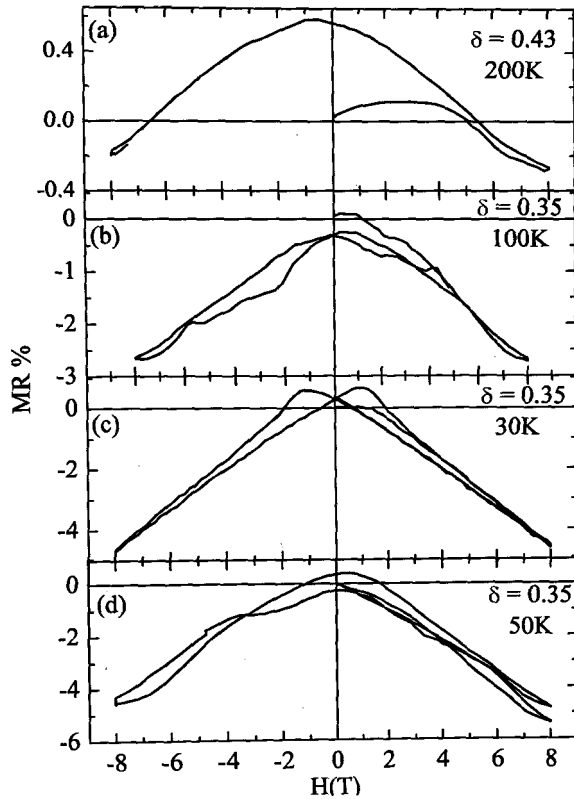


Figure 7.6: Magnetic-field-dependent isothermal magnetoresistance at (a) 200 K for samples having  $\delta = 0.43$  (b) 100 K, (c) 50 K and (d) 30 K for  $\delta = 0.35$ .

The observed negative MR could therefore be either due to presence of both FM and AFM interactions or due to a magnetic frustration resulting from a reorientation of AFM Co spins. MR could not be measured at any further lower temperatures due large values

of resistance. MR for samples having  $\delta = 0.35$  was recorded at 100 K, 50 K and 30 K. The variation of MR is typical of a spin disorder scattering and indicates a presence of competing magnetic interactions. MR at all temperatures is negative but small and increases with decreasing temperature. The irreversibility of MR measured while ramping the magnetic field in both directions giving rise to "butterfly-like" pattern below 50 K indicates presence of competing magnetic interactions [23].

## 7.6 Infra-Red Spectroscopic Measurements

In order to investigate the role of local structure around Co ions in the magnetic and transport properties of these layered perovskites, infra-red and Raman spectroscopic measurements have been performed. Factor group analysis for the orthorhombic structure of these compounds predicts 56 vibrational modes of which 32 modes are infra-red (IR) active ( $11B_{1u}+11B_{2u}+10B_{3u}$ ) and 24 modes Raman active ( $8A_g+3B_{1g}+5B_{2g}+8B_{3g}$ ) [24].

In Figure 7.7(a), IR absorption spectra for compound having  $\delta= 0.43$ , recorded at 80 K and 375 K are presented. Two broad structures corresponding to optical phonon bands appear in the range  $400\text{ cm}^{-1}$  to  $650\text{ cm}^{-1}$ . The bands around  $400\text{cm}^{-1}$  are ascribed to Co-O bending modes while those around  $600\text{cm}^{-1}$  are due to Co-O stretching vibrations.

The IR spectra at 80 K can be fitted with four Gaussian peaks centring at 606, 570, 531 and  $498\text{cm}^{-1}$  as shown in inset of Figure 7.7(a). Similar IR vibrational modes are also observed for  $\text{GdBaCo}_2\text{O}_{5.5}$  [24]. According to lattice dynamical calculations of IR modes [24], the stretching mode at  $606\text{ cm}^{-1}$  denotes vibration of octahedral Co-O bond along

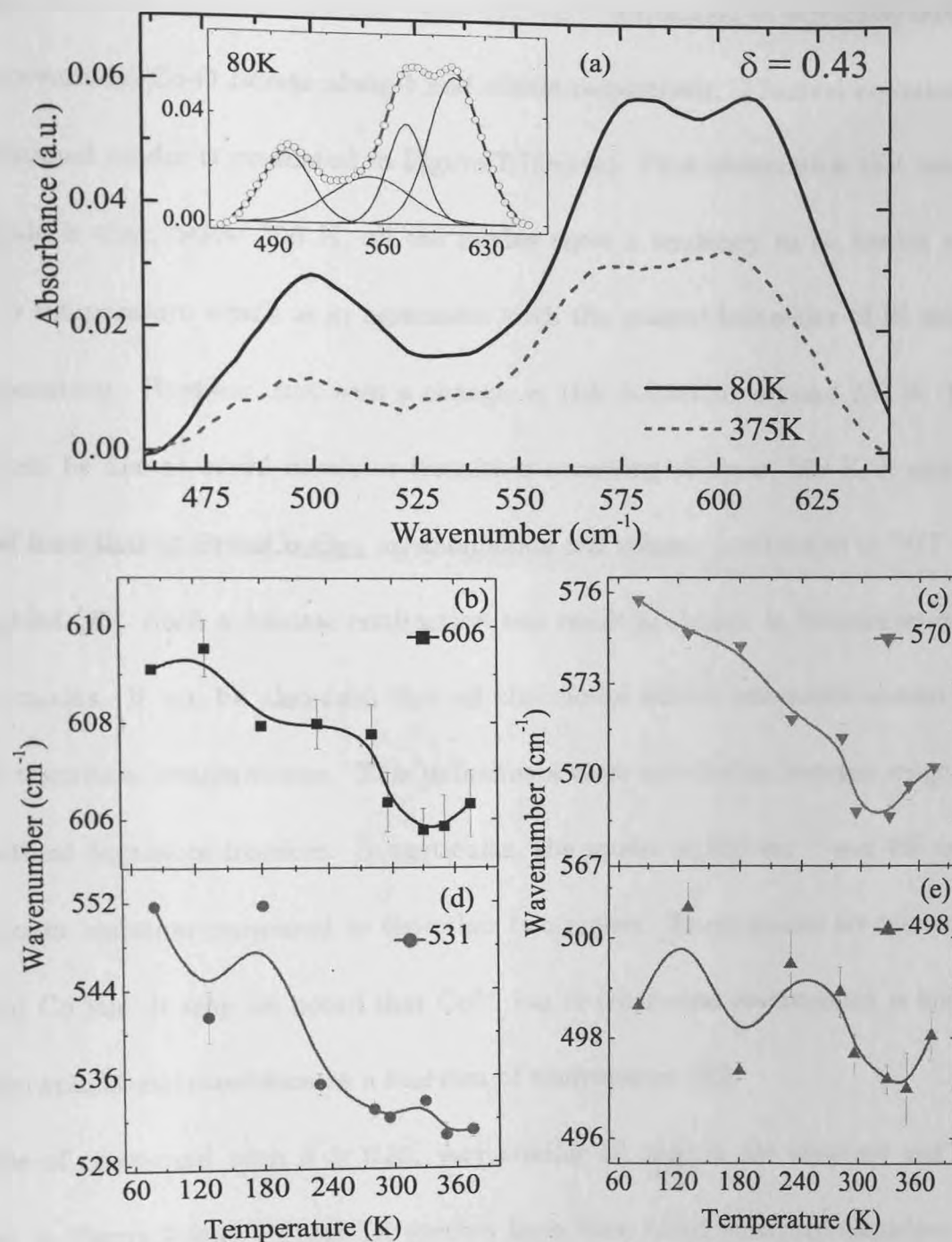


Figure 7.7: (a) Fourier transform IR absorption spectra of  $\text{PrBaCo}_2\text{O}_{5.43}$  at 80 K and 375 K. Inset shows best fitted curve (solid line) which is a sum of four constituent Gaussian peaks. (b)-(e) Temperature evolution of IR stretching modes.



*c*-axis, while the mode at  $498\text{ cm}^{-1}$  denotes octahedral Co-O stretching motion in the a-b plane. The other two modes at  $570\text{ cm}^{-1}$  and  $531\text{ cm}^{-1}$  correspond to stretching motion of square pyramidal Co-O bonds along *b* and *c* axis respectively. Thermal evolution of these vibrational modes is presented in Figure 7.7(b)-(e). First observation that can be readily made is that, below 300 K, all the modes show a tendency to be harden with decrease in temperature which is in agreement with the general behaviour of IR modes with temperature. However, one sees a change in this behaviour around 330 K. This change could be due to metal insulator transition occurring at about 350 K. It may be mentioned here that in  $\text{PrBaCo}_2\text{O}_{5.5}$  an anomalous cell volume contraction at MIT has been reported [25]. Such a volume contraction can result in change in frequencies of IR vibration modes. It can be also seen that all the modes exhibit anomalies around the magnetic transition temperatures. This indicates a close correlation between magnetic and structural degrees of freedom. In particular, the modes at  $606\text{ cm}^{-1}$  and  $498\text{ cm}^{-1}$  show stronger variation compared to the other two modes. These modes are related to octahedral Co ion. It may be noted that  $\text{Co}^{3+}$  ion in octahedral environment is known to undergo spin state transitions as a function of temperature [25].

In case of compound with  $\delta = 0.35$ , very similar IR spectra are observed and are presented in Figure 7.8(a). These IR spectra have been fitted with five Gaussians as shown in inset of Figure 7.8(a) centring at  $596, 565, 532, 500$  and  $490\text{ cm}^{-1}$ . Temperature evolution of these IR modes is presented in Figure 7.8(b). Here too similar conclusions like in case of compound with  $\delta = 0.43$  can be drawn. Especially the emergence of

a vibration mode at  $500\text{ cm}^{-1}$  below  $350\text{ K}$  supports this. This mode arises due to vibration of octahedral Co-O bond along the  $a - b$  plane. Barring two modes at  $596$  and  $565\text{ cm}^{-1}$  all other modes exhibit a very different behaviour with strong anomalies around  $T_{N1}$  and  $T_{N2}$ . Such strong variation of IR modes indicates a role of local lattice distortions in magnetic transitions.

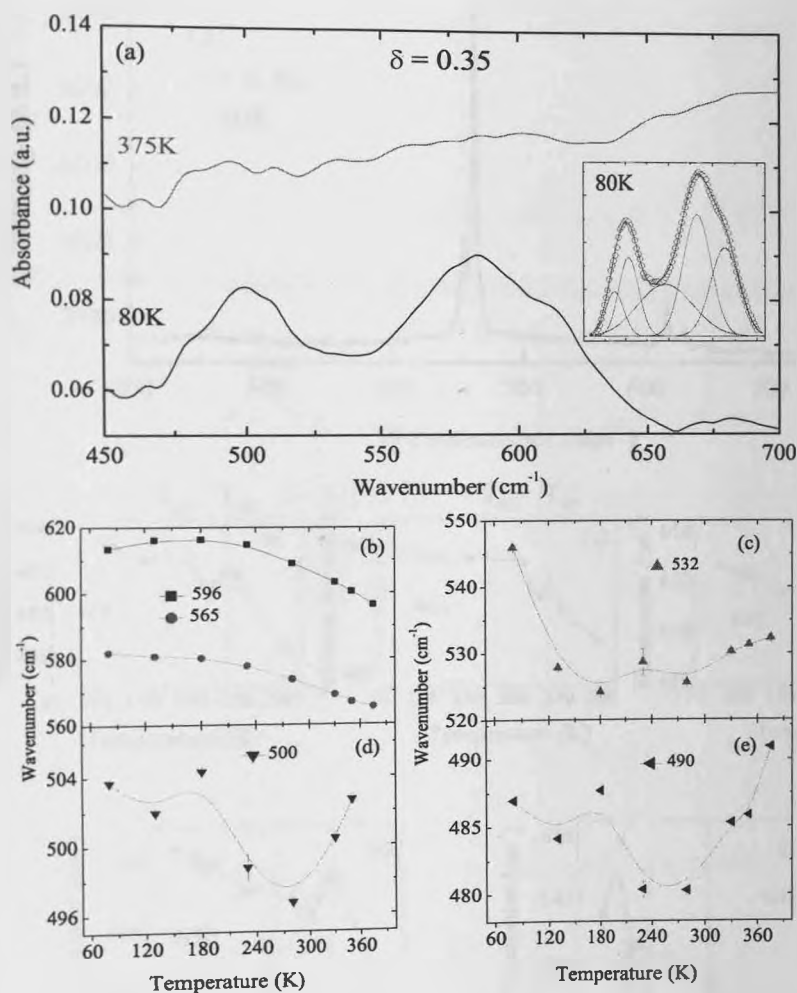


Figure 7.8: (a) Fourier transform IR absorption spectra of  $\text{PrBaCO}_2\text{O}_{5.35}$  at  $80\text{ K}$  and  $375\text{ K}$ . Inset shows best fitted curve (solid line) which is a sum of five constituent Gaussian peaks. (b)-(e) Temperature evolution of IR stretching modes.

## 7.7 Raman Spectroscopic Measurements

Raman spectra recorded at various temperatures for  $\text{PrBaCo}_2\text{O}_{5.35}$  are presented on Figure 7.9(a). The non central position of Co ions provoke strong anharmonicity of vibrations along the  $c$  axis.

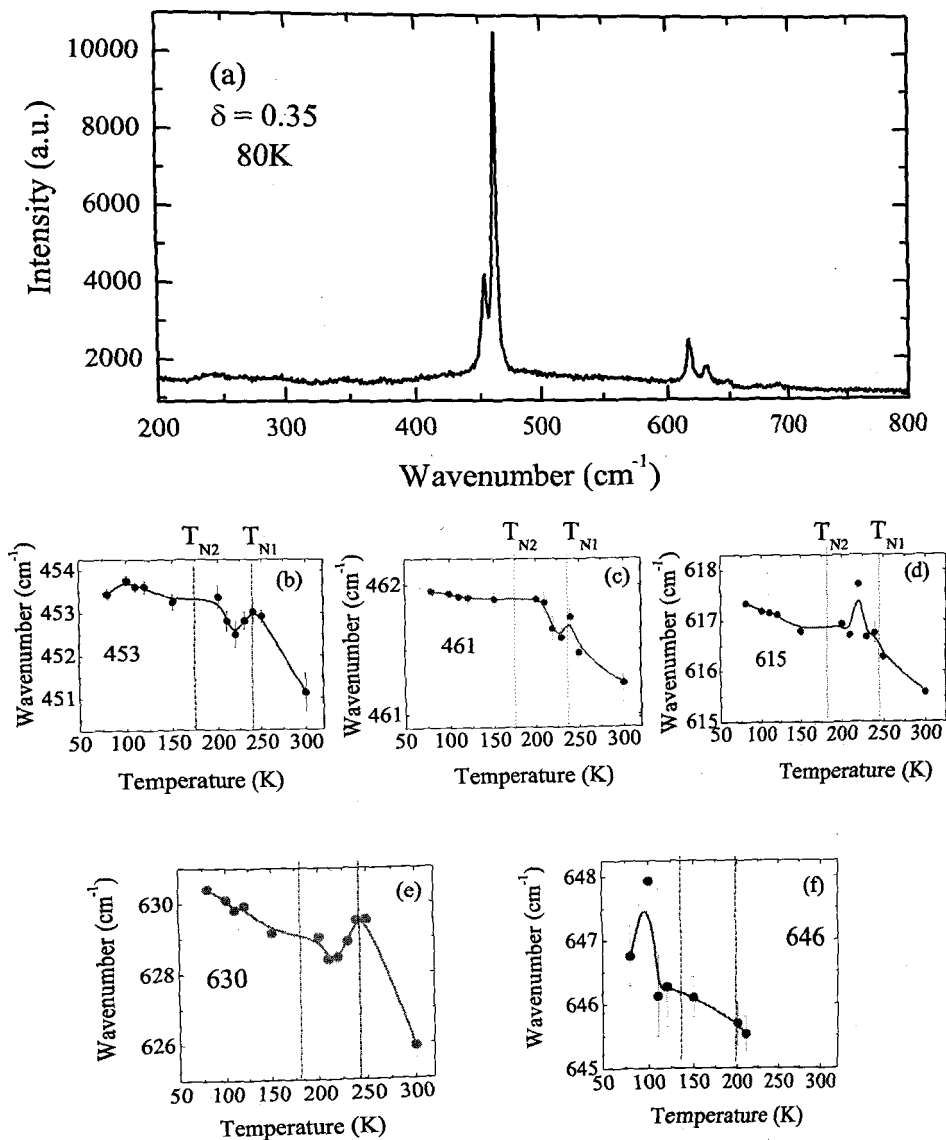


Figure 7.9: (a) Raman spectra of  $\text{PrBaCO}_2\text{O}_{5.35}$  at 80 K. (b)-(f) Temperature evolution of Raman modes of different frequencies.

Raman spectra of this compound reveals that modes from  $400\text{cm}^{-1}$  to  $600\text{cm}^{-1}$  are responsible for basal octahedral and square pyramidal Co-O bond stretching motion, shows unusual softening near magnetic transitions, while a new mode at  $646\text{cm}^{-1}$  appears below 200 K coinciding with transition  $T_{N2}$ . These observations clearly point out that the role of local structural interactions are dominant in inducing the magnetic transitions in these layered perovskites. Therefore a thorough study of local structure around Co ion is warranted.

## 7.8 X-ray Absorption Spectroscopic Measurements

IR and Raman spectroscopic measurements indicates that local lattice distortion around magnetic transition temperatures. To understand local coordination around Co ion and its role in the transport and magnetic properties of  $\text{PrBaCo}_2\text{O}_{5+\delta}$ , XANES and EXAFS measurements at the Co K edge have been carried out at several temperatures in the range  $20\text{ K} \leq T \leq 300\text{ K}$ .

### 7.8.1 X-ray Absorption Near Edge Structure (XANES)

Co K edge XANES spectra at room temperature for compounds with  $\delta = 0.43$  and  $0.35$  are shown in Figure 7.10. The spectra are quite similar with a main resonance peak followed by a broad structure consisting of a doublet extending from 10 to 20 eV beyond the main peak. There is also a pre edge structure which arises from  $1s \rightarrow 3d$  transition made allowed due to admixture of oxygen  $2p$  orbitals.

A comparison of XANES spectra in the two compounds shows that there is a small

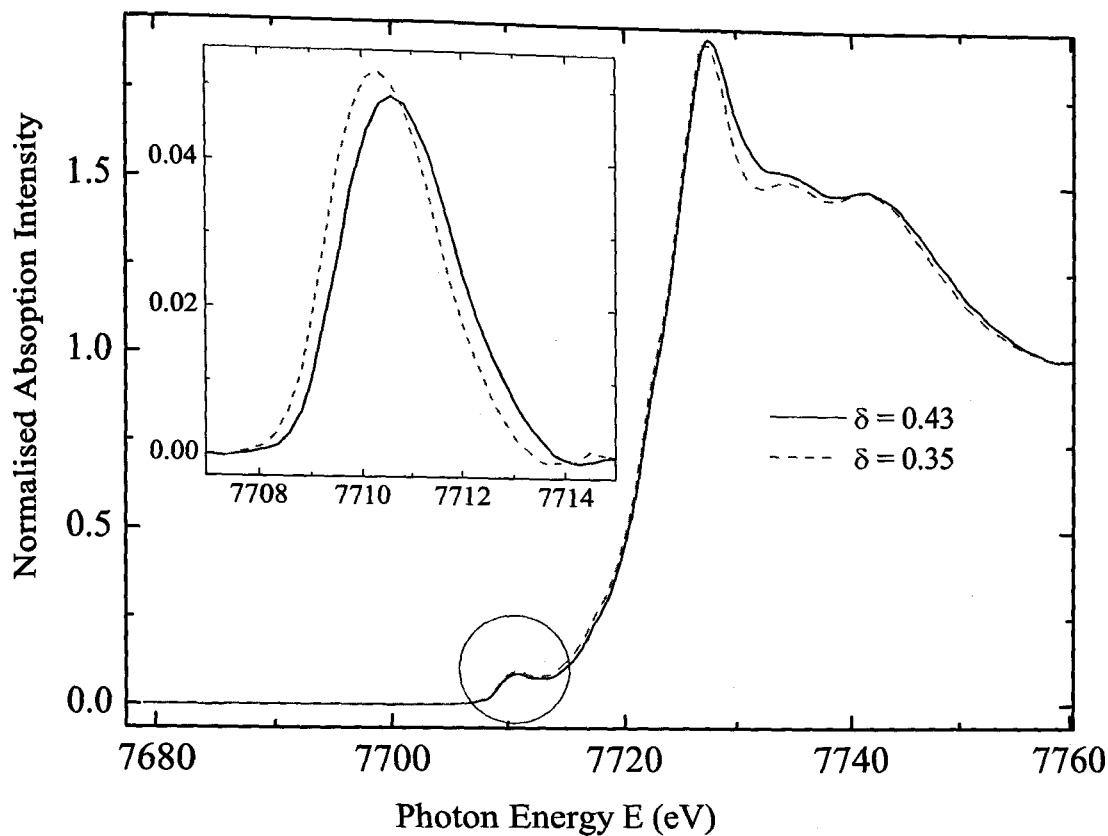


Figure 7.10: Normalized, Co K edge XANES for  $\delta = 0.43$  (solid lines) and for  $\delta = 0.35$  (dashed line), recorded at room temperature; inset (left top) shows pre-edge excluded region from baseline fitting.

shift in the position of the absorption edge towards higher energy in compound with  $\delta = 0.43$ . Such a shift can be ascribed to increase in average Co valence in this compound.

Further, the XANES features in  $\text{PrBaCo}_2\text{O}_{5.43}$  are broader suggesting the presence of higher degree of disorder in the local structure around Co ion in this compound. It may be mentioned here that the same material exhibited highest orthorhombic distortion [22].

The inset of Figure 7.10 shows the pre-edge region in the energy range 7708 eV to 7714 eV. A shift in the pre-edge structure and a reduction in the intensity of the pre-edge peak is noticed in case of compound with  $\delta = 0.43$  as compared to that with  $\delta = 0.35$ .

This relative shift and the decreased intensity of the pre-edge peak could be due to a change in crystal field splitting of the 3d state in  $\text{PrBaCo}_2\text{O}_{5.43}$ . The calculated crystal field splitting from deconvolution of the pre-edge structure into two peaks corresponding to a transition of the core electron to  $e_g \uparrow$  and  $e_g \downarrow$  states indicates that it increases from 0.93 eV in  $\text{PrBaCo}_2\text{O}_{5.35}$  to 1.02 eV in  $\text{PrBaCo}_2\text{O}_{5.43}$ . It must be mentioned here that in  $\text{RCoO}_3$  compounds, a decrease in intensity of pre-edge peak has been attributed to increased hybridization of the Co  $e_g$  states with O 2p orbitals [26]. This could also be a probable cause of decreased relative intensity of the pre-edge peak in compound with  $\delta = 0.43$ . Both, the increased crystal field and higher degree of hybridization in  $\text{PrBaCo}_2\text{O}_{5.43}$  can be related to higher orthorhombic distortion, which results in a greater overlap of the Co 3d and O 2p orbitals.

### 7.8.2 Extended X-ray Absorption Fine Structure (EXAFS)

In order to obtain quantitative information about the local structure around Co ion, EXAFS data collected in the temperature range 20 K-325 K were analysed as described in Chapter 2. The data fitted to a model as described in Chapter 5. Figure 7.11(a) shows magnitude of Fourier transform (FT) of EXAFS data recorded at 20 K in  $\text{PrBaCo}_2\text{O}_{5.43}$  along with the corresponding best fit. The variation of Co-O bond lengths in the octahedra and square pyramids along with Co1-O-Co2 inter-polyhedron bond angle are plotted in Fig 7.11(b-f). From Figure 7.11(b) there appears a major change in planar Co-O bond distances at the octahedral site but the error bars are also very large. The planar Co-O bond distances obtained for the square pyramidal Co are well behaved and show features

around magnetic transition temperatures. These features are also present in distances obtained from octahedral site but with much larger amplitude as well as error bars. Possible reason for large variations in octahedral distances could be the presence of larger disorder as seen from XANES as well as from the orthorhombic distortion estimated from XRD. It could also be due to high degree of correlations between various parameters but as has been shown later, the variation in distances is much more well behaved in case of  $\text{PrBaCo}_2\text{O}_{5.35}$ . In the thermal variation of Co-O planar distances, one can notice a maximum separation between the two at around 260 K and 140 K which respectively correspond to  $T_{N1}$  and  $T_{R2}$ . At around 260 K, while the Co-O-Co interpolyhedral bond angle (Figure 7.11(d)) shows a local maxima, the Co-O apical distances exhibit a minimum (Figure 7.11(c) and (f)). Almost a reverse behaviour is noticed at about 200 K which corresponds to  $T_{N2}$ . Here the separation between planar distances decreases, the Co-O-Co bond angle shows a minimum while there is elongation of polyhedra along the  $c$  axis. This behaviour correlates well with the measured magnetization of the sample. Magnetization exhibits maxima around  $T_{N1}$  and  $T_{R2}$  while it sharply decreases to a minimum around  $T_{N2}$ .

Magnitude of FT of Co K EXAFS recorded at 20 K along with the fitted curve for compound with  $\delta = 0.35$  is depicted in Figure 7.12(a) while the plots in Figure 7.12(b-f) show temperature variation of various Co-O bond distances and Co-O-Co bond angle. The Co-O bond distances obtained from EXAFS are, on an average, larger but show nearly similar variation as in case of  $\delta=0.43$ . However, unlike in earlier case, the changes

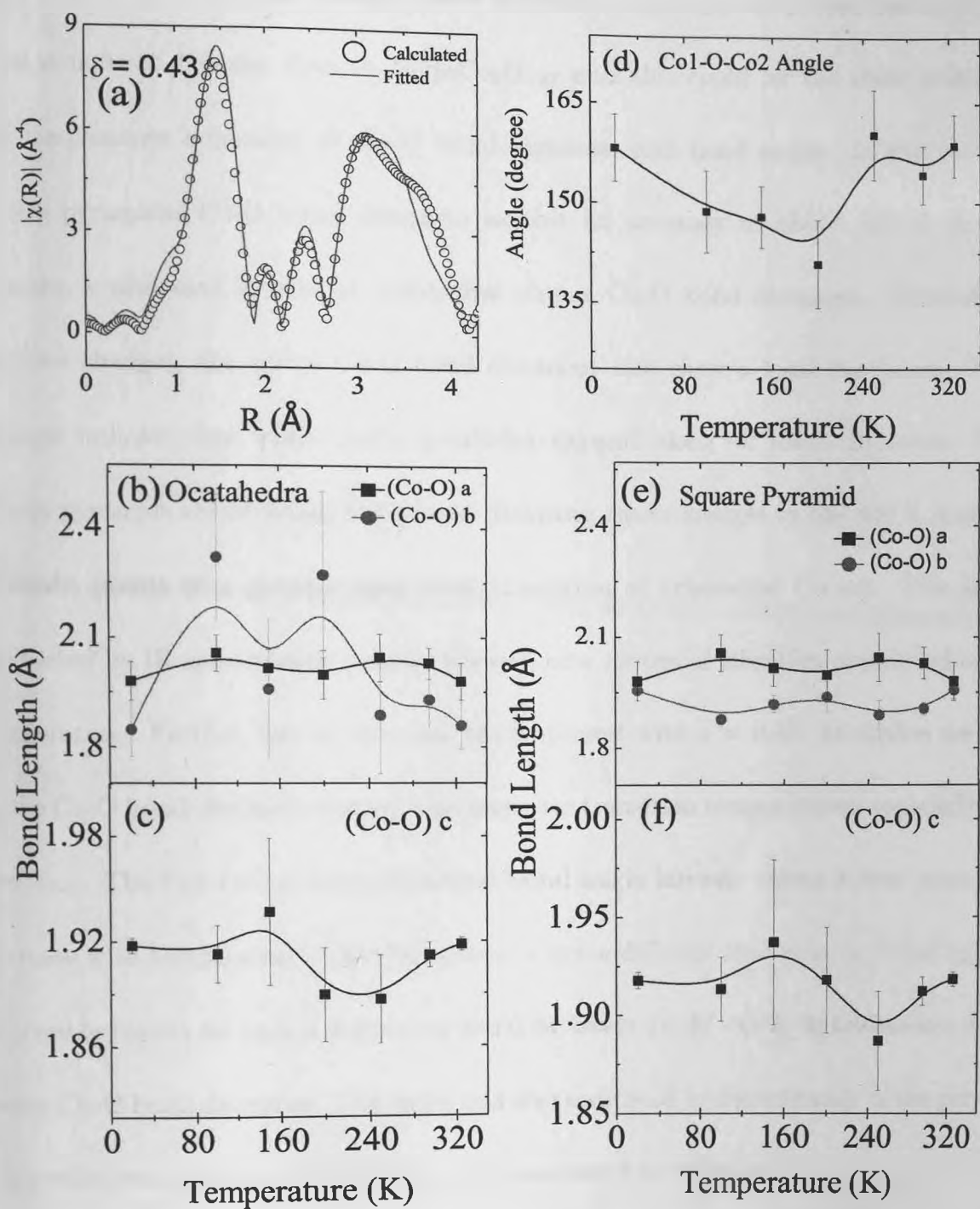


Figure 7.11: (a) EXAFS  $\chi(k)$  data and best fit at 325 K, variation of Co-O bond distances (b) Octahedra Planer (c) Octahedra Apical, (d) Co1-O-Co2 bond angle, Co-O bond distances (e) square pyramidal Planer (g) square pyramidal Apical at various temperatures for  $\text{PrBaCo}_2\text{O}_{5.43}$ .



in both octahedral and square pyramidal Co-O bond distances in  $\text{PrBaCo}_2\text{O}_{5.35}$  are small and comparable. XANES features have indicated that this compound has much less local structural disorder than in  $\text{PrBaCo}_2\text{O}_{5.43}$  and this could be the main reason for the temperature behaviour of Co-O bond distances and bond angle. In this case the square pyramidal Co-O bond distances exhibit an anomaly at about 300 K. A local maxima is also seen in case of octahedral planar Co-O bond distances. Concomitant to these changes, the apical Co-O bond distances also show a local maximum. These changes indicate that while  $\text{CoO}_6$  octahedra expand along all three directions,  $\text{CoO}_5$  square pyramids shrink along the  $y$  axis. Relating these changes to the 300 K magnetic anomaly, points to a possible spin state transition of octahedral Co ion. This is also supported by IR spectroscopy results wherein new modes of vibration appear below this temperature. Further, like in the case of compound with  $\delta = 0.43$ , anomalies are seen in the Co-O bond distances around the magnetic transition temperatures, especially  $T_{N1}$  and  $T_{N2}$ . The Co1-O-Co2 interpolyhedral bond angle however shows a near monotonic decrease with temperature. This behaviour is quite different that seen in  $\text{PrBaCo}_2\text{O}_{5.43}$ . A possible reason for such a behaviour could be lower Co  $3d$  - O  $2p$  hybridization due to longer Co-O bond distances. The same was also indicated by the intensity of the pre-edge peak which was higher in  $\text{PrBaCo}_2\text{O}_{5.35}$  as compared to  $\text{PrBaCo}_2\text{O}_{5.43}$ .

The variation of Co-O bond distances in both compounds is more or less quite similar. An increase in all bond distances at about 300 K indicates that the magnetic transition at  $T_{R2}$  is likely due to a spin state transition of Co ion occupying the octahedral site. These

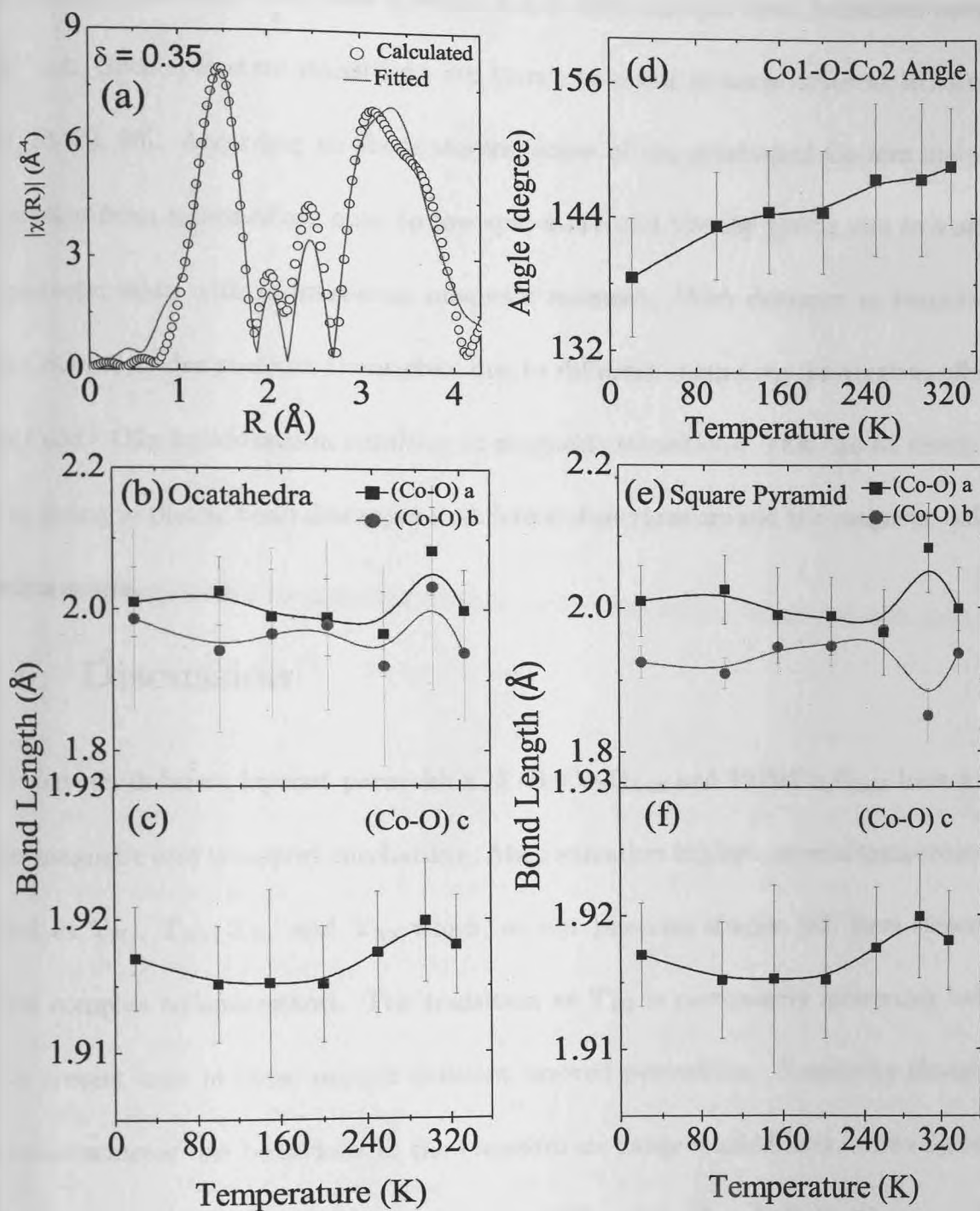


Figure 7.12: (a) EXAFS  $\chi(k)$  data and best fit at 325 K, variation of Co-O bond distances (b) Octahedra planer (c) Octahedra apical, (d) Co1-O-Co2 bond angle, Co-O bond distances (e) square pyramidal planer (g) square pyramidal apical at various temperatures for  $\text{PrBaCo}_2\text{O}_{5.35}$ .

compounds have a mixture of  $\text{Co}^{3+}$  and  $\text{Co}^{2+}$  ions. If we assume  $\text{Co}^{2+}$  to largely occupy the square pyramidal sites, then it would imply that the spin state transition occurs in  $\text{Co}^{3+}$  ion. Such spin state transitions are known to occur in many different  $\text{RBaCo}_2\text{O}_{5.5}$  [27, 28, 29, 30]. According to these studies, some of the octahedral Co ions undergo a transition from intermediate spin to low spin state and thereby giving rise to an antiferromagnetic state with spontaneous magnetic moment. With decrease in temperature, the CoO polyhedra readjust themselves due to different competing interactions affecting the  $\text{Co}3d - \text{O}2p$  hybridization resulting in magnetic transitions. This can be clearly seen from change in planar bond distances in different directions around the magnetic ordering temperatures.

## 7.9 Discussion

The oxygen deficient layered perovskites,  $\text{PrBaCo}_2\text{O}_{5.43}$  and  $\text{PrBaCo}_2\text{O}_{5.35}$  have a complex magnetic and transport mechanism. Magnetization exhibits several transitions classified as  $T_{N1}$ ,  $T_{N2}$ ,  $T_{R1}$  and  $T_{R2}$  which, as our previous studies [22] have shown, are quite complex to understand. The transition at  $T_{R2}$  is particularly interesting because it is present only in these oxygen deficient layered perovskites. Resistivity though has a semiconductor like behaviour in the temperature range studied here, shows hysteretic behaviour during cooling and warming cycles. MR measured on  $\text{PrBaCo}_2\text{O}_{5.35}$  also shows irreversibility as ramping of magnetic field resulting in butterfly-like pattern which is indicative of complex magnetic interactions present in the system. Such irreversibilities are

visible at all temperatures down to 30 K implying thereby that both competing magnetic interactions are strong and present at all temperatures. This leads one to believe that the magnetic interactions have their origin in structural instabilities more so in local structural instabilities that these compounds might undergo as a function of temperature. Infra-red absorption and Raman scattering experiments indeed give weight to the above assumption wherein the Co-O vibration modes show distinct anomalies at around magnetic transition temperatures. In particular, the Co-O vibration modes corresponding to octahedral cobalt ion show much larger variations as compared to the other modes. The anomalies in vibration modes at 300 K and 180 K are also clearly seen in Co-O bond distance variations obtained from EXAFS.

Co K edge XAFS studies further highlight the role of local structural distortions in these layered perovskites.  $\text{PrBaCo}_2\text{O}_{5.43}$  which has a higher orthorhombic distortion as compared to  $\text{PrBaCo}_2\text{O}_{5.35}$  exhibits broader XANES features indicating that the disorder is more pronounced in the local environment of Co ions. This disorder is perhaps responsible for a stronger hybridization between Co  $3d$  and O $2p$  orbitals. This is more clearly evidenced by the lower intensity of the pre-edge peak in  $\text{PrBaCo}_2\text{O}_{5.43}$ . The disorder is also reflected in Co-O bond distances. In  $\text{PrBaCo}_2\text{O}_{5.43}$ , the Co-O bond distances, especially those of octahedral Co ion vary widely as a function of temperature. These wide variations of bond distances though read with large error bars, seem credible because they correspond well with anomalies exhibited by Co-O vibration modes in infra-red spectroscopy. Such wide variations can induce changes in hybridization between Co ion

and its nearest neighbours. Interestingly even in  $\text{PrBaCo}_2\text{O}_{5.35}$ , which has comparatively a lower disorder, the Co-O bond distances show variations and more specifically around the magnetic transition temperatures. This clearly indicates that magnetic transitions in these oxygen deficient layered perovskites are a manifestation of changing Co  $3d$  -  $2p$  hybridization. These changes in hybridization occur due to a competition between the Jahn teller interaction energy and the crystal field energy which are affected by the spin state transition of Co ions.

## 7.10 Conclusion

Study of local structure around Co ions in layered perovskites  $\text{PrBaCo}_2\text{O}_{5.43}$  and  $\text{PrBaCo}_2\text{O}_{5.35}$  using XAFS, IR absorption and Raman scattering studies have been carried out to understand the mechanism of magnetic interactions in these compounds. Our studies indicate importance of local structural disorder and Co  $3d$  - O  $2p$  hybridization in inducing several magnetic transitions in these oxygen deficient layered perovskites.

# References

- [1] Maignan A, Martin C, Pelloquin D, Nguyen N, and Raveau B 1999 *J. Solid State Chem.* **142** 247
- [2] Martin C, Maignan A, Pelloquin D, Nguyen N, and Raveau B 1997 *Appl. Phys. Lett.* **71** 1421
- [3] Moritomo Y, Akimoto T, Takeo M, Machida A, Nishibori E, Takata M, Sakata M, Ohoyama K and Nakamura A 2000 *Phys. Rev. B* **61** R13325
- [4] Respaud M, Frontera C, García-Muñoz J, Aranda A G M, Raquet B, Broto J, Rakoto H, Goiran M, Llobet A, and Carvajal J 2001 *Phys. Rev. B* **64** 214401
- [5] Vogt T, Woodward P M, Karen P, Hunter B A, Henning P, and Moodenbaugh A R 2000 *Phys. Rev. Lett.* **84** 2969
- [6] Suard E, Fauth F, Caignaert V, Mirebeau I and Baldinozziet G 2000 *Phys. Rev. B* **61** R11871
- [7] Troyanchuk I, Kasper N, and Khalyavin D D 1998 *Phys. Rev. Lett.* **80** 3380

- [8] C. Frontera, J. García-Muñoz, A. Llobet, and M. Aranda, *Phys. Rev. B* **65**, 180405 (2002)
- [9] Ganorkar S, Priolkar K R, Sarode P R, Banerjee A, Rawat R and Emura S 2012 *J. Phys: Condens. Matter* **24** 476003
- [10] Kasper N, Troyanchuk I, Khalyavin D, Hamad N, Haupt L, Froebel P, Baerner K, Gmelin E, Huang Q, and Lynn J W 1999 *Phys. Stat. Sol. (b)* **215** 697
- [11] Ganorkar S, Priolakar K R 2010 *Solid State Comm.* **150** 1963-66
- [12] Fauluques E C et al 2004 *Spectroscopy of Emerging Materials* (Kluwer Academic Publisher, The Netherlands) p 195
- [13] Pandey S K, Kumar A, Patil S, Medicherla V R R, Singh R, Maiti K, Prabhakaran D, Boothroyd A, and Pimpale A V 2008 *Phys. Rev. B* **77** 045123
- [14] Wu Z Y, Benfatto M, Pedio M, Cimino R, Mobilio S, Barman S R, Maiti K and Sarma D D 1997 *Phys. Rev. B* **56** 2228
- [15] Berman S and Sarma D D 1994 *Phys. Rev. B* **49**, 13979
- [16] Pandey S K, Patil S, Medicherla V R R, Singh R and Maiti K 2008 *Phys. Rev. B* **77** 115137
- [17] Chang J Y, Lin B N, Hsu Y Y and Ku H C 2003 *Physica B* **329-333** 826-828
- [18] Haas O, Struis R P W J and McBreen J M 2004 *J. Solid State Chem* **177** 1000-1010

- [19] Pandey S K, Khalid S, Lalla N P and Pimpale A V 2005 *J. Phys: Condens. Matter* **18** 10617-10630
- [20] Hidaka M, Soejima M, Soda M, Sato M, Choi S H, Sung N E, Kim M and Lee J M 2005 *Phys. Stat. Sol (b)* **242** 1422-1430
- [21] Jarry A, Luetkens H, Pashkevich Y, Stingaciu M, Pomjakushina E, Conder K, Lemmens P and Klaus H 2009 *Physica B* **404** 765
- [22] Ganorkar S, Priolkar K R, Sarode P R, and Banerjee A 2011 *J. Appl. Phys.* **110** 053923
- [23] Kundu A K, Reveau B, Caignaert V, Rautama E-L and Pralong V 2009 *J. Phys. Condens. Matter* **21** 056007
- [24] Yasodha P, Premila M, Bharathi A, Valsakumar M C, Rajaraman R and Sundar C S 2010 *J Solid Stat Chem* **183** 2602-08
- [25] Frontera C, García-Muñoz J L, Carrillo A, Aranda M A G, Margiolaki I and Caneiro A 2006 *Phys. Rev. B* **74**
- [26] Pandey S K, Khalid S, Lalla N P and Pimpale A V 2006 *J. Phys: Condens. Matter* **18** 10617
- [27] Flavell W, Thomas A, Tsoutsou D, Mallick A, North M, Seddon E, Cacho C, Malins A, Patel S, Stockbauer R, Kurtz R, Sprunger P, Barilo S, Shiryaev S, and Bychkov G 2004 *Phys. Rev. B* **70** 224427



- [28] Plakhty V, Chernenkov P, Barilo S, Podlesnyak E, Pomjakushina E, Moskvina E and Gavrilov S 2005 *Phys. Rev. B* **71** 214407
- [29] Taskin A, Lavrov A N and Ando Y 2003 *Phys. Rev. Lett.* **90** 227201
- [30] Soda M, Yasui Y, Ito M, Iikubo S and Sato M 2003 *J. Phys. Soc. Japan* **72** 1729

# Chapter 8

## Summary and Conclusions

### 8.1 Summary and Conclusion

The detailed study of magnetization has been carried out with the aim to investigate the factors responsible for unique properties of cobaltites. It has been found that all cobalt based layered perovskites, irrespective of the rare-earth ion exhibit multiple magnetic transitions below room temperature. To further illustrate this point we present the magnetic phase diagram for two families  $\text{SmBaCo}_2\text{O}_{5+\delta}$  and  $\text{PrBaCo}_2\text{O}_{5+\delta}$  in Figures 8.1 and 8.2 respectively.

The only distinguishing point is the existence of antiferromagnetic transition for oxygen rich  $\text{SmBaCo}_2\text{O}_{5+\delta}$  and additional magnetic transitions in oxygen deficient  $\text{PrBaCo}_2\text{O}_{5+\delta}$ .

To understand the effect of rare-earth ionic radius on magnetic and transport properties of these compounds a series of double perovskites  $\text{RBaCo}_2\text{O}_{5.5}$  (Pr, Nd, Sm, Gd and Y) type has been studied. It is seen that though the variation of cell volume follow Vegard's law with ionic radii, the compound with  $\text{R}=\text{Sm}$  has anomalies in orthorhombic distortion as well as interpolyhedron bond angle. The transport and magnetic properties

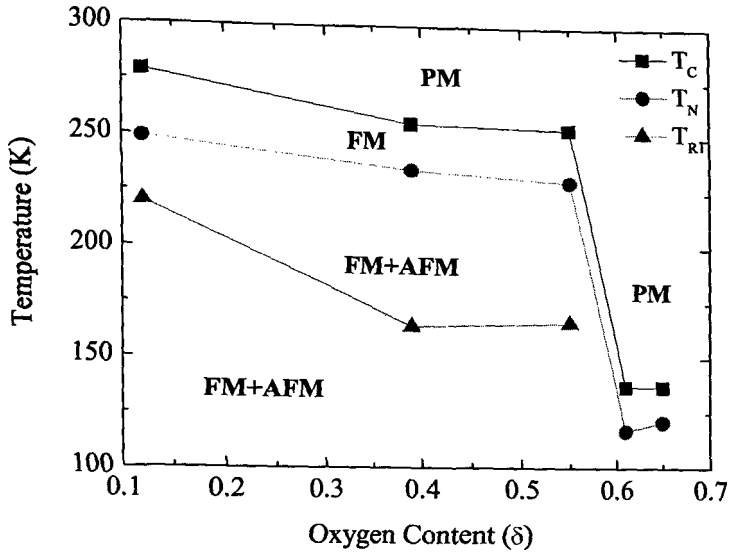


Figure 8.1: Phase diagram constructed from magnetic transition observed in magnetization curves recorded at 100 Oe for  $\text{SmBaCo}_2\text{O}_{5+\delta}$ .

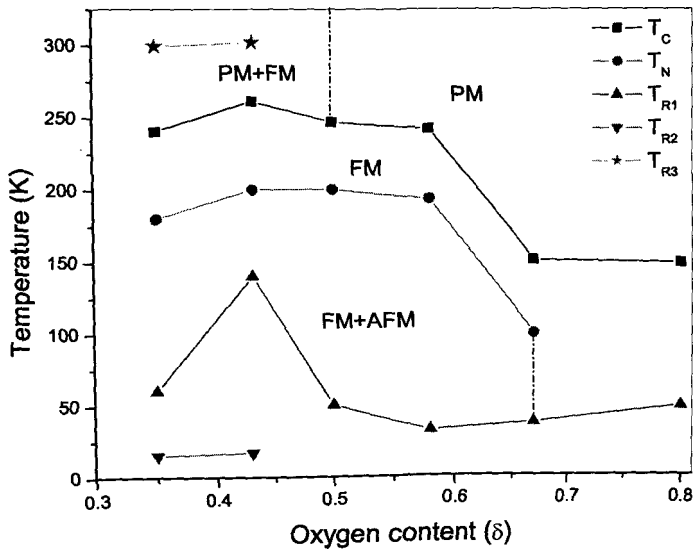


Figure 8.2: Phase diagram constructed from magnetic transition observed in magnetization curves recorded at 100 Oe for  $\text{PrBaCo}_2\text{O}_{5+\delta}$ .

for R=Sm compound are also found to be different than that of other members of the cobaltite family. Magnetization studies indicates increasing dominance of ferromagnetic interactions with increase in size of the rare-earth ion. It is observed that, though there is a similarity in the nature of magnetic interactions exhibited by different  $\text{RBaCo}_2\text{O}_{5.5}$ , the strength of these magnetic interactions depend on the structural distortions around the Co caused by the varying the size of the rare-earth ion.

In order to further understand the anomalous behaviour of  $\text{SmBaCo}_2\text{O}_{5.5}$  systematic investigation of magnetic, transport and X-ray spectroscopic properties of  $\text{SmBaCo}_2\text{O}_{5+\delta}$  ( $0.12 \leq \delta \leq 0.65$ ) have been carried out. Variation of oxygen content on either side of  $\text{SmBaCo}_2\text{O}_{5.5}$  induces a transition from orthorhombic to tetragonal structure. Further variation in oxygen content also results in strong competition between ferromagnetic and antiferromagnetic interactions which manifests in magnetic compensation. This structural symmetry influences the crystal field splitting of the Co 3d states as well as the Co 3d - O 2p hybridization. This perhaps has an effect on the spin state of Co ions and therefore the magnetic properties. Our studies therefore show that oxygen content greatly influences the local structure around Co ions which in turn plays an important role in magnetic and transport properties of these layered perovskites.

It is not possible to probe local structure of Co in all rare-earth based cobaltites due to interfering L edges of the rare-earth ion. Pr L edges occur at much lower energies as compared to Co K edge, hence Co K edge EXAFS studies have been carried out in the  $\text{PrBaCo}_2\text{O}_{5+\delta}$  ( $0.35 \leq \delta \leq 0.80$ )

compared to Co K edge, hence Co K edge EXAFS studies have been carried out in the  $\text{PrBaCo}_2\text{O}_{5+\delta}$  ( $0.35 \leq \delta \leq 0.80$ )

XAFS studies at the Co *K* edge in  $\text{PrBaCo}_2\text{O}_{5.5}$  indicate a strong hybridization between Co3*d* and O2*p* orbitals. It has been seen that there is a possibility of charge transfer from the square pyramidal to octahedral Co ion which reflects as a magnetic moment on LS Co<sup>3+</sup> ion. Further local lattice distortion changes the *p* – *d* hybridization and reorients the antiferromagnetic Co spins giving rise to anomalies in magnetic and transport properties of this double perovskite.

$\text{PrBaCo}_2\text{O}_{5.80}$  shows dominant ferromagnetism which is due to the inward rotation and tilting of the neighbouring Co<sup>3+</sup>O and Co<sup>4+</sup>O polyhedra about the *c*-axis facilitating double exchange mechanism. While in case of  $\delta = 0.67, 0.58$  compounds antiferromagnetic superexchange interactions dominate.

$\text{PrBaCo}_2\text{O}_{5.43}$  and  $\text{PrBaCo}_2\text{O}_{5.35}$  show more complex magnetic properties. Infra-red absorption and Raman scattering experiments show signatures of the local lattice distortion near magnetic transition temperatures. The changes in Co 3*d* - O2*p* hybridization occur due to a competition between the Jahn-Teller interaction energy and the crystal field energy which is affected by the spin state transition of Co ions.

In conclusion, the XAFS studies reveals that the local structure plays an important role in magnetic properties of these materials. The Co-O local structure is strongly influenced by oxygen content which primarily decides the valence state and coordination of the Co ion.

## 8.2 Future Work

In the above concluding section, we mention a few suggestions which can be further pursued in relation with the double perovskites. Double perovskites are found to be more important in technological applications. Hence, it is necessary to understand the physical properties in more detail. These properties can be easily tuned as per requirement with varying chemical composition, synthesis method, temperature, pressure and magnetic field.

With the results presented in this thesis, it will be worth looking at overall structural aspect of these materials at low temperatures. Similarly the magnetic structure of  $\text{SmBaCo}_2\text{O}_{5+\delta}$  is not clear. Full polarisation analysis of resonant X-ray magnetic scattering (RXMS) is known to advance the determination of magnetic moment directions of complex magnetic structures which will help to determine magnetic structure will shed light on magnetic compensation and reversal in this particular member of double perovskites.

It is clear that all octahedral Co is not in IS state, hence the investigation of spin state of cobalt needs to be carried out. In this case Co L<sub>2,3</sub> edge studies could prove useful as they directly probe the 3d band which participates in bonding as well as magnetic interactions.

# Chapter 9

## List of Publications

### Journal Publications

1. Infrared spectroscopic studies of  $\text{GdBaCo}_2\text{O}_{5.5}$

**S. Ganorkar** and K.R. Priolkar

Solid State Communications, 150, 19631966 (2010)

2. Effect of Oxygen Content on Magnetic Properties of Layered Cobaltite

$\text{PrBaCo}_2\text{O}_{5+\delta}$

**S. Ganorkar**, K. R. Priolkar, P. R. Sarode and A. Banerjee

Journal of Applied Physics 110, 053923 (2011)

3. Influence of local structure on magnetic properties of layered cobaltites

$\text{PrBaCo}_2\text{O}_{5+\delta}$  ( $\delta > 0.5$ )

**S. Ganorkar**, K. R. Priolkar, P. R. Sarode, A. Banerjee, R. Rawat and S. Emura

J. Phys.: Condens. Matter 24 476003 (2012)

4. Magnetic and Spectroscopic Studies of Oxygen Deficient Layered Cobaltites

$\text{PrBaCo}_2\text{O}_{5+\delta}$  ( $\delta = 0.43, 0.35$ )

- S. Ganorkar**, K. R. Priolkar, P. R. Sarode, A. Banerjee, V. G. Sathe and S. Emura  
Communicated to J. Phys.: Condens. Matter (March 2013)
5. Correlation between rare earth ionic radius, structure and magnetic properties of  $\text{RBaCo}_2\text{O}_{5.5}$
- S. Ganorkar**, K. R. Priolkar, P. R. Sarode, A. Banerjee, R. Rawat and S. Emura  
Communicated to J. Appl. Phys. (March 2013)
6. Effect of  $\text{Co}3d\text{-O}2p$  Hybridization on Magnetic and Transport Properties of  $\text{PrBaCo}_2\text{O}_{5.5}$  : EXAFS Study
- S. Ganorkar**, K. R. Priolkar, P. R. Sarode, A. Banerjee, R. Rawat and S. Emura  
(Manuscript ready)
7. Unusual magnetic properties of  $\text{SmBaCo}_2\text{O}_{5+\delta}$  ( $0.12 \leq \delta \leq 0.65$ )
- S. Ganorkar**, K. R. Priolkar, P. R. Sarode, A. Banerjee, and S. Emura  
(Manuscript ready)

### Conference Publications

1. Spin State Transitions in  $\text{RCoO}_3$  ( $\text{R} = \text{La, Pr, Nd}$ )
- S. Ganorkar**, K. R. Priolkar, and P. R. Sarode  
Proc. DAE Solid State Physics Symposium, 53, 201-202 (2008)
2. Effect of Oxygen Content On Properties of  $\text{PrBaCo}_2\text{O}_{5+\delta}$  **S. Ganorkar**,  
K.R.Priolkar and P.R.Sarode Proc. DAE Solid State Physics Symposium, 54, 839-  
840 (2009)





3. Magnetic, Transport and Spectroscopic Properties of  $\text{PrBaCo}_2\text{O}_{5.35}$

**S. Ganorkar**, K. R. Priolkar, P. R. Sarode, A. Banerjee and V. G. Sathe

AIP Conf. Proc. 1349, 1129-1130 (2011)

4. Effect of rare earth size on structural, magnetic and transport properties of

$\text{RBaCo}_2\text{O}_{5.5}$

**S. Ganorkar**, K. R. Priolkar, P. R. Sarode, and A. Banerjee

AIP Conf. Proc. 1447, 1141-1142 (2012)

T- 583